Forschungszentrum Karlsruhe
Technik und Umwelt

Wissenschaftliche Berichte
FZKA 5928

Pre-oxidised PWR Test CORA-29: Test Results

S. Hagen, P. Hofmann, V. Noack, L. Sepold, G. Schanz, G. Schumacher

Hauptabteilung Ingenieurtechnik
Institut für Materialforschung
Institut für Neutronenphysik und Reaktortechnik
Projekt Nukleare Sicherheitsforschung

August 1997

Forschungszentrum Karlsruhe
Technik und Umwelt
Wissenschaftliche Berichte

FZKA 5928

Pre-oxidised PWR Test CORA-29: Test Results

S. Hagen, P. Hofmann, V. Noack, L. Sepold,
G. Schanz, G. Schumacher

Hauptabteilung Ingenieurtechnik
Institut für Materialforschung
Institut für Neutronenphysik und Reaktortechnik
Projekt Nukleare Sicherheitsforschung

Forschungszentrum Karlsruhe GmbH, Karlsruhe
1997

Forschungszentrum Karlsruhe GmbH
Postfach 3640, 76021 Karlsruhe

Mitglied der Hermann von Helmholtz-Gemeinschaft
Deutscher Forschungszentren (HGF)

ISSN 0947-8620

Abstract

Pre-oxidized PWR Test CORA-29: Test Results

The CORA-Out-of-pile experiments are part of the international Severe Fuel Damage (SFD) program. They should provide information on the damage development of Light Water Reactor (LWR) fuel elements in the temperature range 1200°C to 2400°C.

In all tests with the exception of CORA-28 and CORA-29 the cladding was used in the as-received state. Test CORA-28 (BWR) and CORA-29 (PWR) were performed with pre-oxidized bundle components. The pre-oxidation should simulate oxide layers that have formed during normal operation in a reactor. The pre-oxidation was performed in the CORA test facility at 800°C (1073 K) for 2000 s with a steam flow rate of 6 g/s. The resulting oxide layer thickness of the cladding surfaces of test bundle CORA-29 varied between about 4 μm at the lower end of the bundle and about 12 μm maximum at the upper end. This was less than computed (25 μm) on the basis of the existing rate equations.

With a pre-oxidation of this extent the physico-chemical behaviour of the test bundle CORA-29 was comparable with the other PWR related tests without any pre-oxidation. The same temperature and damage behaviour was found. No influence on the onset (temperature and time) of the temperature escalation and the maximum temperatures was registered. There was only a tendency for the melt to relocate to slightly lower elevations in the CORA-29 bundle (about 100 mm lower). The relocation behaviour is partially determined by wetting conditions of the solid surface. The wetting becomes less pronounced if the solid substrate is ceramic and the molten material is metallic in nature.

CORA-29 resulted in a higher amount of total hydrogen (225 g) compared with the other PWR-type experiments performed under comparable test conditions. The enhanced oxidation of the pre-oxidized bundle in comparison with an unoxidized one indicates the remarkable possibility of an induced growth of less protective scales during the test transient.

Kurzfassung

PWR Test CORA-29 mit voroxidiertem Bündel, Test Ergebnisse.

Die CORA-Out-of-pile Experimente wurden im Rahmen des internationalen „Severe Fuel Damage" Programms durchgeführt. Sie sollten Informationen über die Schadensmechanismen an Leichtwasser-Reaktor (LWR) Brennelementen bei Kühlmittelverlust-Störfällen im Temperaturbereich 1200 °C bis 2400 °C liefern.

Der Versuch CORA-29 wurde mit voroxidierten Bündelkomponenten durchgeführt. Die Voroxdidation sollte die Oxidschichten simulieren, die sich während des normalen Reaktorbetriebs ausbilden. Beim Versuch CORA-29 wurde die Voroxidation in der CORA-Anlage bei 800 °C (1073 K) bei einem Dampfstrom von 6 g/s durchgeführt. Die entstandene Oxidschicht hatte eine Stärke von 4 μm am unteren Ende und maximal 12 μm am oberen Ende des Bündels. Vorgesehen war eine Oxidschicht von 25 μm.

Mit der erreichten Voroxidation war das Verhalten des Testbündels CORA-29 vergleichbar mit denjenigen der analog durchgeführten PWR-Versuchen ohne Voroxidation. Es wurde das gleiche Temperatur- und Schadensverhalten gefunden. Insbesondere hat sich kein Einfluß der Voroxidation auf das Einsetzen der Temperatureskalation und die maximal erreichte Temperatur ergeben.

Lediglich eine etwas stärkere Verlagerung der Schmelzen von ca. 100 mm konnte im Bündel CORA-29 festgestellt werden. Das Verlagerungsverhalten wird durch die Benetzungsbedingungen der Oberflächen bestimmt. Die Benetzung wird schwächer, wenn die Oberfläche von keramischer Natur ist und die herabfließende Schmelze metallischen Charakter hat.

CORA-29 ergab eine deutlich höhere integrale Wasserstofferzeugung (225 g) als bei den anderen unter vergleichbaren Bedingungen durchgeführten Experimenten. Das bemerkenswerte Ergebnis einer verstärkten Oxidation des voroxidierten Bündels im Vergleich zu einem nichtoxidierten ist ein Hinweis darauf, daß während der Testransiente das induzierte Wachstum von Schichten mit verminderter Schutzwirkung auftreten kann.

Contents

1. Introduction

The TMI-2 accident has demonstrated that a severe fuel damage transient will not necessarily escalate to an uncontrolled core melt down accident if the design basis accident limits are exceeded. Therefore, comprehensive research programs have been initiated in various countries to investigate the relevant fuel rod bundle damage mechanisms, that occur in an uncovered core after an increase of temperature.

In the Federal Republic of Germany at the Forschungszentrum Karlsruhe (FZK) the Severe Fuel Damage (SFD) Program is now co-ordinated by the Project Nuclear Safety Research (PSF) as successor of Project Nuclear Safety (PNS) and LWR Safety Project Group (PRS). As part of this program, out-of-pile experiments (the CORA-Program) were conducted at the Hauptabteilung Ingenieurtechnik (HIT), These experiments have been designed to provide information on the behaviour of Light Water Reactor (LWR) fuel elements under Severe Fuel Damage (SFD) conditions up to meltdown. The results of the out-of-pile experiments can be used for the assessment of the SFD computer codes.

Within the frame work of international co-operation the out-of-pile experiments are contributing confirmatory and complementary information to the results obtained from the limited number of inpile tests. The investigation of the basic phenomena of the damage process is supported by separate-effect tests.

The most important aspects concerning fuel rod failure and subsequent core degradation are the chemical interactions amongst the fuel element components in competition with the oxidation of the cladding in steam, which causes also the temperature escalation. Melt formation starts around 1200 °C by chemical interactions of the Inconel spacer grids and absorber materials - (Ag, In, Cd) for PWRs and B_4C/stainless steel for BWRs - with the Zircaloy cladding. The dissolution of the UO_2 pellets by liquid Zircaloy starts far below the UO_2 melting point.

Melt relocation, blockage formation and finally fragmentation of fuel elements during reflooding characterise the degraded core and the potential of long term coolability. Furthermore the influence of internal pressure of the fuel rods (ballooning and

bursting) and external pressure of the system (solid contact between pellets and cladding) on the bundle meltdown behaviour was investigated. Further on, the investigation of the influence of pre-oxidation, inital heat-up rate, steam availability, water level in the bundle and bundle size was included in the program. The damage behaviour of WER fuel elements was the subject of the last two CORA-tests.

The tests performed in the CORA-facility are listed in the test matrix (Table 1). The original test matrix was directed towards the behaviour of PWR fuel elements only. In 1988 discussion showed that in most countries using nuclear energy, information on the behaviour of BWRs in severe accident conditions was needed. In consequence, five planned PWR experiments were replaced by BWR tests in the revised test matrix. Also the original sequence of tests was changed, as one can see from the test numbers.

In this report PWR test CORA-29 is discussed. In all tests with the exception of CORA-28 and CORA-29 the Zry cladding was used as received. During normal operation however an oxide layer of about 25 μm is formed in dependence of operating time and conditions. In CORA-29 therefore the influence of preoxidation of the Zry cladding on the damage behaviour of PWR bundle should be investigated.

The pre-oxidation was performed in the CORA facility at 1073 K for 9000 s with a steam flow rate of 6 g/s. The resulting oxide layer thickness on the cladding tube surfaces varied between 4 μm at the lower end of the bundle and about 12 μm at the upper end. This was much less than the precalculated value. The results of this test showed, that the physico-chemical behaviour of test bundle CORA-29 was comparable with other PWR related tests without any pre-oxidation (see for example test CORA-5). The thin oxide layers only had a minor influence on the relocation of molten material. The relocation behaviour is partially determined by the wetting conditions of the solid surface. The wetting becomes poorer if the solid substrate is ceramic and the molten relocating material metallic in nature.

2. Description of the CORA test facility

The CORA out-of-pile facility was designed to investigate the behaviour of LWR fuel elements under severe fuel damage accident conditions. In the experiments the decay heat was simulated by electrical heating. Great emphasis was placed on the fact that the test bundles contain the original materials used in light-water reactor fuel elements to investigate the different material interactions.

Pellets, cladding, grid spacers, absorber rods and channel box walls were typical of those of the investigated LWRs with respect to their compositions and radial dimensions. In test CORA-29 the following PWR components were used: Original UO_2 pellets, Zry-4 cladding, Zry-4 and Inconel-718 spacer, and (80 Ag, 15 In, 5 Cd) absorber rods in stainless steel cladding and Zry-4 guide tubes.

Figure 1 gives a simplified flow diagram of the facility. The geometrical arrangement of the different CORA components is given in Figure 2. The central part of the facility was the fuel rod bundle. The bundle was enclosed in a Zry shroud with ZrO_2 fibre insulation. A high temperature radiation shield surrounded the bundle and shroud assembly, leaving an annular space for introduction of the quench cylinder. The bundle was connected to the power supply system at the upper and lower ends.

Below the bundle was the quench unit with a water filled quench cylinder, which can be raised around the bundle at a controlled speed. The cylinder was guided by three rods, which also connect the electric power to the bundle lower end.

The bundle upper end was fixed in the bundle head plate. The plate was connected by a funnel shaped tube to the surge condenser. The surge condenser was double-walled, leaving access to the bundle end fittings above the bundle head funnel.

The steam was produced in the steam generator, superheated and guided to the lower end of the bundle. The steam not consumed within the bundle was condensed in two parallel condensers and the hydrogen produced was fed into the off-gas system after dilution by air to a low H_2 concentration.

Bundle design:

The bundle and its surroundings are shown in Figure 3 and 4. The bundle horizontal arrangement is given in Figure 5 and the bundle components in Figure 6. Characteristic data of the bundle are presented in Tables 2, 3 and 4. The bundle consisted of 16 heated rods, 8 unheated rods and 2 absorber rods inside the Zry guide tube.

The heated fuel rod simulator was sheathed with standard Zry-4 cladding tube, containing UO_2 annular pellets with a central heater. The heater consisted of a 1024 mm long tungsten rod (6 mm diameter), the upper electrode (300 mm molybdenum; 689-770 mm copper) and the lower electrodes (300 mm molybdenum; 183-219 mm copper). The electrodes have a diameter of 9 mm. The electrodes are flame-sprayed with 0.2 mm thick layer of ZrO_2. Large flexible copper cables provided the connection to the electrical system. The resistance of the flexible cables to the points of voltage measurement for the determination of the power was less than 1 mΩ per rod (recommended value: 0.5 mΩ).

The resistivities R of tungsten, molybdenum and copper are given respectively in the following three equations:

$$R_W = 2.61 \bullet 10^{-2} + 2.63 \bullet 10^{-4} T_W + 2.20 \bullet 10^{-8} T^2_W$$

$$R_{Mo} = 2.29 \bullet 10^{-2} + 5.36 \bullet 10^{-5} T_{mo} + 1.38 \bullet 10^{-7} T^2_{Mo} - 2.22 \bullet 10^{-11} T^3_{Mo}$$

$$R_{cu} = 7.89 \bullet 10^{-3} + 9.90 \bullet 10^{-5} T_{cu} - 5.49 \bullet 10^{-8} T^2_{Cu} + 3.16 \bullet^{-11} T^3_{Cu}$$

with T in [Kelvin] and R in [$\Omega mm^2/m$].

The unheated fuel rod simulators consisted of solid UO_2 pellets and Zry cladding. The unheated rods extended to about -200 mm elevation, i.e. to about 20 mm above the initial water level of the quench cylinder (-220 mm). Zry-4 spacers were used at 880 mm and -5 mm elevation and an Inconel 718 spacer at + 496 mm (Figure 3).

The absorber rods (Figure 6) were built from original components (80 Ag, 15 In, 5 Cd; wt%) absorber alloy in 10,2/11,2 mm stainless steel cladding. The rod was surrounded by the 12,2/13,8 mm Zry-4 guide tube.

The fuel rod simulators and the absorber rods were screwed into the bundle head plate sealing it hermetically. The bundle head plate thus gave the fixed elevation for the axial thermal movement of the rods.

For upper end bundle cooling the heated rods (the copper electrode inside the Zry-4 cladding) and the connectors for the pressure capillaries and the thermocouples of the unheated rods were surrounded by water. The water was cooled by a heat exchanger. Argon was blown against the lower surface of the plate to protect the sealing in the bundle head plate.

At the lower end the heated fuel rod simulators were cooled by the water of the quench cylinder. The initial water level was at the -220 mm elevation. The unheated rods were in contact with the water of the quench cylinder only by the thermocouple connections. The gross volume of water inside the quench cylinder (230 mm ID) was about 70 l.

The bundle was surrounded by a Zry-4 shroud of 1.22 mm thickness. The shroud conducted the steam through the bundle. The steam entered at an orientation of 180° into the lower end (0 mm elevation). To minimise the heat losses from the shroud, it was surrounded by a 19 mm (0.75 inch) thick insulating layer of ZrO_2 fibre. On account of the low heat conductivity and heat capacity of the ZrO_2 fibre the shroud temperature could follow the bundle temperature closely. The shroud participated in the interaction with steam. The resulting oxidation energy contributed substantially to bundle heat-up.

In contrast to most other tests in CORA-29 no windows were cut into the shroud. With regard to radiation losses the area of the windows amounts to about 3% of the shroud. In addition no cross flow is assured by a closed window.

The connection between steam inlet at 0 mm elevation and shroud was made by a stainless steel steam distribution tube. This tube extended down into the water of the quench cylinder thus forming a lower closure. The time history of the water level in the quench cylinder showed that there is no net condensation of steam in the quench cylinder.

At an elevation of 36 mm the steam distribution tube joined into the shroud. From here the shroud extended in vertical direction for 1231 mm and the insulation for 1036 mm.

The annuli between the shroud and the high-temperature shield on one hand and high temperature shield and pressure containment on the other hand were closed at the upper end by fibre ceramic layers of 38 mm thickness.

High temperature shield:

To keep the heat losses as low as possible, the bundle was surrounded by an additional high temperature shield (HTS). The vertical and the horizontal cross-sections of the high temperature shield are given in Figures 3 and 4. The high temperature shield consisted mainly of ceramic fibre plates. The inner layer of plates consisted of ZrO_2, and the outer layer of Al_2O_3. The fibre ceramics were excellent insulators and had a low density which resulted in a low heat capacity. The thermal shock behaviour of the fibre ceramics was also excellently low.

The mechanical strength of the high temperature shield was ensured by external walls of stainless steel (0.9 mm). The fibre ceramic plates were attached to the stainless steel cover by ceramic nails. The inner ZrO_2 layer was 38 mm thick, and the outer Al_2O_3 layer was 76 mm. They were separated by a gap of 23 mm. The distance from the inner insulation surface to the centre of the bundle was 153 mm.

The high temperature shield was located within the pressure tube. In the pressure tube a large number of flanges allowed access to the bundle. Through these holes and their extensions in the temperature shield, the bundle could be inspected during the test with the help of the videoscope systems.

Heating system:

In CORA-29 16 rods were heated. The rods could be individually connected to three power systems available. In this test the intended power input was the same for all rods. Since the voltages and currents of the individual rods were measured, the power input for each rod could be determined. The power input was controlled by a computer. The time dependent power history was programmed before the test. The

power was controlled by measurement of the currents of the groups, and by setting the voltage necessary to obtain the desired power.

3. Test conduct

3.1 Pre-oxidation

CORA-29 should investigate for a PWR type bundle the influence of pre-oxidation. During normal operation an oxide layer of about 25 μm is formed in dependence of operation time and conditions. Therefore a pre-oxidation of test bundle CORA-29 was foreseen in the CORA-facility. The bundle was heated to about 800 °C for 9000s at a steam flow of 6 g/s. Power and steam input and the resulting temperature of the different components are presented in appendix C. The resulting oxide layer is given in Figure 8. As is shown in the cross section of Figure 8, 2 segments, cut from an original Zry cladding tube and a Zircaloy wire were used to measure the oxidation profile. The different type of stringers were used, to make sure that there is no significant difference between the oxidation of rod surface and a wire at different radial positions of the bundle.

As can seen from Figure 8 the preoxidation of the bundle increases from 4 μm at the bottom to about 12 μm at the top.

3.2 Test conduct of main test

In the CORA experiments the following phases for the test sequence were generally distinguished (Figure 9):

1. 0-3000 s: pre-heating
2. 3000-4900 s: transient
3. > 4900: cooldown.

The pressure in the system was controlled as in all tests to 0.22 Mpa. The argon input is separated in two parts: 8g/s Argon is preheated and is entering together with the steam at the lower end into the bundle (0 mm elevation).
The second amount of 6 g/s is not flowing through the bundle and is mainly used for the protection of the bundle head plate. It is marked with the label „videoscopes"

though in this test no videoscopes are included. Booth amounts contribute to the dilution of the hydrogen leaving the facility.

The flow of 8 g/s preheated argon through the bundle and a low constant electric power input of about 0.52 kW increase the temperature to a level high enough to avoid condensation of 6 g/s steam added after 3300 sec.

During the transient phase the initial temperature increase of about 1 K/s was produced by raising the electric power input from 4.5 to 23 kW (Figure 9). The test was terminated by turning off the electric power at 4900 s (slow cooldown by heat losses). The steam input was stopped at the same time.

The boundary conditions during the test are given in detail in Figures 10 to 24. Figure 12 shows the total electric power input, which was produced by the voltage inputs to the three groups of rods (Figure 13) and the resulting total current (Figure 15). The electric power input is controlled by measurement of the voltages of the rod groups and the currents of the individual rods. Then the computer sets the voltages to give the power required. The total electric energy input corresponds to the time integral of the power input (Figure 14). The nearly constant current (Fig. 15) for the linear increasing voltage (Fig. 13) is caused by the strong increase of the resistance (Fig. 16) due to increasing temperature.

The regular increase of the voltage in Figure 13 is disturbed at about 4200 s. The irregularities are produced by melt formation allowing flow of current in neighbouring unheated rods as well. This effect can be seen more pronounced in Figure 17, showing the currents of the single rods. The relocation of the melt can produce a bypass by surrounding unheated rods.

The resistance of the bundle, the three rod groups and the single rods are given in Figure 16, Figure 18 and Figure 19 to 21. The sharp spikes during power shutdown are artificial due to measurement of voltage and current at not exactly the same times.

In Figure 22 the water temperatures in the quench cylinder at -250 mm and -300 mm are given (initial water level at - 220 mm). The decrease of the temperature at

-250 mm and the increase at -300 mm is caused by melt falling into the quench cylinder and disturbing the stratification of quench water heated from the top.

The temperatures measured at -50 mm elevation (Figure 23) show partly the irregularities caused by relocated melt produced in the upper part of the bundle. As shown in the schematic drawings in the same figure, the measurements are made on the steam tube at 165° orientation (slot 268) and stretching 15 mm into the steam tube at 345° orientation (slot 267).

The temperature of the incoming argon at the steam inlet is measured with two thermocouples (Figure 24). The resulting measurements are practically the same. The slow increase of the steam inlet temperature is caused by the heatup of the walls of the connecting tube from superheater to the entrance of the bundle, due to the additional heat capacity of the steam.

4. Temperature measurements

The temperatures in the bundle were measured by high-temperature thermocouples of WRe5/WRe26 wires and HfO_2 insulating material. The sheath was made of tantalum and Zircaloy. Thermocouples with „Ker" in the name were additionally shielded with a ZrO_2 sheath. The measurements in the high temperature shield were performed with NiCrNi-thermocouples sheathed with stainless steel. Also the compensation cables were sheathed with stainless steel. The positions of the thermocouples in the bundle are given in Table 5 and Figure 25 and those in the high temperature shield in Figures 48 and 49.

The temperature measurements of the bundle are presented as function of time in the following way: on one hand, the temperatures of the components (heated rods, unheated rods, channel box walls, absorber blade, etc.) are given in Figures 26 - 36. On the other hand - for comparison reasons - the temperature measurements for different components are grouped by axial elevations (Figures 37 - 45). The temperature measurements of the high temperature shield are given in Figures 50 - 68.

4.1 Temperatures in the bundle

Due to the bundle arrangement with the Zircaloy shroud - participating in the exothermal reaction of Zircaloy with steam - and the good ZrO_2 fibre insulation a flat radial temperature profil was reached.

The measurements at the same elevation have therefore been combined to give a representative temperature for the bundle. Due to the failure of some thermocouples after the escalation these best-estimated temperatures are more reliable before this event. The results of this combination of measurements are given in Figure 46 as best-estimated temperatures of the bundle as function of time for different elevations. In Figure 47 these values are rearranged as axial temperature distributions for different times in the test sequence:

Before 3400 s the temperature in the bundle is mainly determined by the temperature of the incoming „gas" of about 550 °C. We have a decreasing axial temperature profile with the maximum at the lower end. With increasing power input and temperature level the incoming steam and gas is cooler than the bundle and acts as coolant. The maximum of the temperature moves to the upper end of the bundle.
At 4000 s for 750 mm to 950 mm elevation the temperature has reached values high enough to start the escalation. The escalation at 750 mm and 850 mm elevation reached its turnaround point first at about 30 s earlier than at 950 mm. Then the escalation moved up and down the bundle. At 1050 mm and 550 mm the escalation started about 100 s later followed by the escalation at 450 mm within the next 100 s. The escalation at 1150 mm and 350 mm had a delay of about 300 s.

The final maximum reached between 350 mm and 950 mm elevation was about 2000 °C. At 1050 mm and 1150 mm elevation only a maximum temperature of about 1900 °C and 1800 °C was reached.

For the axial region not showing a temperature escalation we got at 1250 mm and 150 mm elevation steadily increasing temperatures reaching the maximum at the end of the test with about 1600 °C and 1200 °C.

At 1350 mm elevation (Figure 37; lower picture) a maximum temperature of 800 °C is reached at the end of the test.

At 150 mm elevation (Figure 44 upper picture) the sudden rises of the temperature are caused by relocated melt. Also at 50 mm elevation (Figure 44; lower picture) the sudden increase of the temperature on the heated and unheated rod may be caused by relocating melt. Besides the short spike at 4300 s the maximum temperature at this elevation amounts to 800 to 900 °C. In the region 0 to - 50 mm a maximum temperature of 600 to 700 °C is found.

At the start of the test the water level in the quench cylinder is set to -220 mm. The temperatures in the quench cylinder at -250 mm and -300 mm (Figure 22) increase during the test from 65 °C to 100 °C and from 50 °C to 80 °C. The irregularities in the temperatures after 4200 s are caused by melt dropping into the quench cylinder and disturbing the stratification of its water.

In the bundle head plate (Figure 37; upper picture) the maximum temperature increases from about 100 °C at the upper surface (1511 mm) to about 300 °C at the lower surface (1471 mm). The maximum temperature was reached at about 300 s after shutdown of the power.

In Figure 46a the bundle temperature is compared to the hydrogen production. One can clearly recognise the correlation of the temperature escalation and the hydrogen produced.

In Figure 70 the chemical power calculated from the measured hydrogen of Figure 69 is compared to the electric power input. During its maximum the chemical power is nearly twice as large as the maximum of the electric power.

4.2 Temperatures of the High Temperature Shield

To reduce the radial heat losses, the insulated bundle is surrounded by the additional fibre insulation of the high temperature shield. The position of thermocouples on the inner surface (153 mm radius), inside the insulation and on the outer surface (293 mm radius) are given in Figures 48 and 49. Results of the measurement of temperatures are given in Figures 50 to 68.

The maximum temperature of the inner surface (153 mm radius) increases from about 250 °C at 90 mm elevation to about 1300 °C at 990 mm elevation (Figure 50). The azimuthal variation of the temperature at the inner surface is shown in Figures 54 to 56. The maximum deviation amounts to about 100 °C. While at 990 mm the comparison of the 345 ° side to the 165 ° side gives no remarkable difference, at 390 mm the 345° side has a maximum temperature of about 100 °C lower.
Comparing the 255° side against the 75° side at 89 mm and 390 mm elevation the 255° side has the lower temperature. Exactly the same behaviour was found in CORA-12, the test run before CORA-29. Also test CORA-31, performed after CORA 29 showed the same behaviour. This means that the azimuthal temperature deviation from a symmetric distribution must be connected to the arrangement of the test.

In Figure 51 the temperatures inside the high temperature insulation shield at 192 mm radius are given and compared for different azimuthal positions in Figures 57 and 58. The differences seen for the symmetric positions, especially the strong deviation of the temperature at 550 mm at 345°, reproduce the same behaviour as in tests CORA-13 and CORA-31.

In Figure 59 - 62 the temperatures are given for special radial distances. The results clearly show the movement of the temperature maximum from about 5000 s - the end of the heating period - at the radius of the inner wall to about 7000 s at the outer region of the high temperature shield.

In Figures 63 to 68 the time dependent temperatures at different radii inside the HTS grouped for fixed elevations show the strong decrease of temperature from the inside to the outside wall and from top to bottom.

5. Hydrogen generation

The hydrogen produced during the test by the steam/zirconium reaction is measured with mass spectrometer systems installed at two positions, i.e. above the test section, and in the mixing chamber after the gas has passed the condenser (see Figure 1). The gas at the test section outlet can contain a high steam partial pressure

and has therefore to be diluted by helium before it enters the analyser through the capillary tube. For this purpose a dilution chamber with flow meters is installed.

A schematic diagram of the probes, gas lines, and gas analysis system is provided in Figure 7. The off-gas mixture which contains hydrogen among other gases is transported to the spectrometer via capillary tubes. It is analysed by quadruple mass spectrometers of the type Leibold PQ 100. The ion currents representing the concentration of the respective gases are determined. The production rate of a gas component is calculated with the ratio of the partial pressure oft the particular gas to that of argon (carrier gas) and multiplied by the argon flow rate through the test bundle. The hydrogen generation rate is evaluated as follows:

$R_m = 2 \bullet p_H F_{Ar} / (22.4 \bullet p_{Ar})$ [g/s]

with

R_m = mass production rate of hydrogen [g/s]

p_H = partial pressure of hydrogen

p_{AR} = partial pressure of argon

F_{ar} = volumetric argon flow through mixing chamber [l/s]

Based on a calibration test with bundle CORA-7, in which a mixture of argon and 30 % hydrogen was radially injected into the test section, the delay time of monitoring the gas was estimated to be 80 s. This time was taken into account for the measured hydrogen production in all CORA experiments. The same calibration tests, however, show lower increases in the rate of hydrogen production than would be expected from the injected gas flow. For this reason the measured data were corrected based on the actual gas concentration, i.a. on the gas input during the calibration test. A transfer function was determined and applied to the measured data. The result is a corrected curve that better represents the H2 production rate in the test section.

The hydrogen production rate during test CORA-29 is given in Figure 69. The corrected data are based on the transfer function of the CORA-7 calibration test. The

corrected curve shows a steeper increase. The small peaks in the corrected curve are a consequence of the correction method and should be therefore not taken into account. The maximum production rate of about 300 mg/s is reached at about 4500s. The total hydrogen produced during the tests amounts to 225 g. This was the highest value measured in all CORA tests.

In the exothermic Zircaloy/steam reaction the formation of hydrogen is correlated with the production of energy. Using the corrected values of the hydrogen the resulting chemical power is shown in Figure 70. In the same figure the electric power input is given for comparison. The maximum value of the chemical power is nearly twice as large as the maximum of the electric power. The total amount of hydrogen produced was 225 g. This corresponds to an oxidation energy of 34.2 MJ. The total electric input amounted to 34.1 MJ. The same amount of chemical energy was produced as the electric input. But the exothermic reaction is concentrated not only in time on the second half of the test, but also the escalation is concentrated on a short region of the bundle. This means for the period of escalation in the region of escalation the exothermic energy production is much larger than the electric input in this region.

To calculate the percentage of Zr oxidation from the hydrogen production the bundle length is used, that had experienced temperature above 1430 °C. For PWR bundle mass of cladding and shroud and for BWR bundle mass of cladding, shroud and channel box wall was taken into account. With these assumptions we get for CORA 29 a total Zr oxidation of 75%. The fraction of steam consumed compared to the total input was 38%.

For CORA-28 /15/, a BWR test with preoxidation of about 55 μm ZrO_2 oxide layer in the upper part of the bundle we got from 104 g total hydrogen production the following results: The exothermic energy corresponded to 55 % of the electric input. We got a total oxidation of 30 %. A fraction of 79 % of the steam introduced into the bundle was consumed. In CORA-28 only 2 g/s steam flow was used, compared to 6 g/s for CORA-29.

6. Post test appearance of the bundle

The post test appearance of the bundle CORA-29 is shown in Figures 84-122. The state of the insulation can be seen in Figure 84, which gives the bundle, at different orientations. These photographs show the bundle after the test, still in its test position. Only the surrounding high temperature shield was moved down, to give access to the bundle. The pieces of insulation missing in the photographs are broken away after the test. The outer appearance of the ZrO_2 fibre boards in Figure 84 shows an overall smooth surface. In Figures 85 the inner surfaces of the fibre insulation are presented, showing the strong interaction between shroud and insulation preferentially in the upper part of the bundle in consistence with the axial temperature profil.
In Figures 86 and 87 the inner surfaces are compared to their outer surfaces. The outer surface shows the bundle after the test without any handling, the inner surfaces could only be photographed after dismantling.

In Figures 88 to 90 details of the inner surfaces are shown at different elevations. Figure 88 shows the region above the upper Zry spacer (880 mm). One can recognize the strong deformation of oxidized remnants of the Zry shroud. The oxidation process has bent the original shroud plane. From earlier separate effect tests with optical inspection during the experiment (NIELS-tests) we know that in the high temperature region, the deformation developed without fragmentation. The fragmentation of the oxided Zircaloy took place during the cooldown phase. From the material distribution in the cross section it is assumed, that in this upper region no interaction between bundle and shroud has taken place. Compared to the middle region (Figure 89) the surface in this upper region has the appearance of less complete oxidation and interaction with molten Zry coming from the upper end. In the region from 350 mm to 650 mm (Figure 90) the surface shows additional relocated refrozen melt probably coming also from the bundle.

The damage of the bundle, as seen from the outside, is shown in Figures 91 to 108. Figures 91 and 92 present an overview of the bundle after removal of the shroud

insulation. During dismantling the strong embrittled shroud broke away in the upper half of the bundle. The region of strong damage between 450 mm and 1150 mm elevation is in agreement with the temperature distribution. The flowering of the oxidized claddings can be especially recognized in region between 500 mm and 800 mm elevation. Above the remnant of the oxidized Zry spacer (838 mm - 880 mm) a region of less oxidation can be seen.

In Figures 93 to 108 details of the damage are given by a set of photos taken in direction to the four sides of the bundle at four different elevations starting at the upper part of the bundle. In this figures in addition to elevation also the maximum temperatures reached are given. If the damage of the shroud at the upper end (Figures 93, 97, 202, 205) is now compared to the destruction at the lower end (Figures 96, 100, 104, 108) the following results are found:. The shroud survives in its original form about 1120 mm elevation which corresponds to a temperature of about 1880 °C. At the lower end the shroud survives in its original form below about 300 mm, with the exception of the wall in the 120° direction, where the wall probably is destroyed by the interaction with the adjacent absorber rod. The elevation of 300 mm corresponds to a temperature of 1750 °C. The shroud survives up to about 500 mm. At the lower end we have not a sharp boundary for the deformation, but an increasing destruction in the region from 300 mm to about 500 mm elevation. The maximum temperature increases in this region from 1750 °C to 1985 °C. The different behaviour may be caused by the stronger oxidation due to the later start of the temperature increase.

In the region from about 500 mm to 800 mm (Figures 95, 99, 103, 107) the outer appearance of the fuel rod simulators is dominated by flowering due to oxidation. If in Figure 95 the left side of the bundle with an unheated fuel rod simulator is compared to the right side with the absorber rod, the strong interaction of the absorber material can be recognised.

The region from 800 mm to 1100 mm is represented in Figures 94, 98, 102,106. In this region only in Figures 94 and 106 the stronger oxidation in form of the flowered claddings can be seen. Using Figure 5 one can identify that the rods with number

5.1, 3.1, 1.1 from Figure 94 and rods 1.1, 1.3, 1.5 from Figure 106 show the stronger oxidation. These are 5 adjacent rods. Of interest may be the fact, that their position is opposite to the entrance of the steam at the lower end at 180° direction. The other rods in this region show much less oxidation and with this survival of the cladding. In Figures 98 and 102 the structure of the pellets can be recognized on the rods. The Zircaloy must have been relocated. This appearance is most pronounced on the side of 210 ° direction, which has the strongest influence of the absorber rods.

The damage in the bundle can best be discussed by including the information from cross sections of the bundle. To enable the cutting of the cross sections a lucite box was set around the bundle for encapsulation with epoxy resin. The lower end of this box was closed by a paraffin layer, which was produced by refreezing paraffin floating on the water of the quench cylinder. Rütapox 0273 with the hardener LC (Bakelite GmbH, Iserlohn) was used as epoxy. This epoxy was chosen, as its reaction time was slow enough, that the shrinkage effect is negligible. The hardening time was one week. The bundle was filled, starting from the bottom through the steam inlet. A saw with 2.3 mm thick diamond blade of 500 mm OD (mean diamond grain size 138 μm) was used to cut the bundle at 3200 rpm.

The information coming from cross sections is presented in Figures 109 to 122. Horizontal cross sections are given in Figures 109, 110. The regions of the four rods surrounding the absorber rods 6.2 and 4.6 are given in Figures 111, 112. The vertical cross sections are presented in Figures 113 to 117. In Figures 118 to 122 test CORA-29 with two absorber rods and a small pre-oxidation is compared to test CORA-5 with one control absorber rod and rods as - received. A complete set of horizontal cross sections in given in appendix B (B1-B12).

From the post test photographs and the cross sections one can obtain the following information.

- In accordance with the temperature profile damage on the bundle is found between 120 mm (Figure 113) and 1225 mm (Figure B1). The cross section at 112 mm (Figures 109, 111, 112) shows no damage to the fuel rods or the

absorber rod. Only the gap between absorber rod and surrounding guide tube is filled with relocated absorber material. The temperature of this elevation was about 1000 °C.

- The absorber rod 4.6 has kept this melt up to about 120 mm elevation (Figure 113). Above 200 mm only the oxidized „skin" of the guide tube has partly survived at all higher elevations. Even in the highest horizontal cross section of the bundle (Figure B5) attack on the cladding can be recognized.

- The cross sections confirm, that within the bundle the damage starts from the absorber rods. The horizontal and vertical cross sections show that the gap between absorber rod and guide tube is blocked by the refrozen absorber melt, so that the mayor part of the absorber melt is distributed within the bundle to attack the Zry cladding after the Zry guide tube has failed by interaction with the absorber melt. This liquefaction of Zry cladding results in the initiation of dissolution of the UO_2 pellets far below the UO_2 melting point.

- As seen in the photographs of the bundle exterior (Fig. 94, 95, 99, 103, 106, 107) the cross sectiosn confirm the strong flowering of the oxidized cladding in the upper half of the bundle (Fig. 109, 110).

- The vertical and horizontal cross sections show that blockages have formed in two steps. Preferentially absorber material has formed a lower blockage between about 110 mm and 200 mm elevation (Fig. 109, 110, 114). A larger blockage, containing preferentially Zry and dissolved UO_2 has formed in the region between 300 mm and 430 mm elevation (Fig. 109, 110, 114, 116). This blockage has a porous structure, as can be seen from the cross sections (Fig. 109, 110, 114, 117).

- Test CORA-29 should investigate the influence of pre-oxidation on the damage behaviour of a PWR-type bundle. As discussed in section 3.1 only a small oxide layer from 4µm to 12µm had formed during the preoxidation phase in the facility. In Figure 118 to 122 therefore horizontal and vertical cross sections are compared from test CORA-29 to test CORA-5 which was performed with a bundle of Zry

claddings as received. From the comparison of the different cross sections no significant difference in the damage structure can be found. Fig. 118 shows the same flowering structure and also the same attack on the fuel rods in both tests. Fig. 119 demonstrates a very similar porous structure of the relocated melt. The similarity in the porous structure can also be seen clearly in the comparison of the vertical cross sections (Fig. 122). The only difference which could be found in melt relocation is the fact, that the melt in CORA-29 moves to lower elevations, as can be seen in Fig. 120, 122. More melt has formed in CORA-29. But this is due to the two absorber rods in the bundle, which is a more repesentative ratio of absorber rods to fuel rods, than the one rod in CORA-5.

- The strong relocation of absorber material from the upper part of the bundle means that in a reactor large regions could be left without absorber. During reflooding the consequences on the reactivity must be taken into account by using borated water.

7. Blockage formation and mass distribution

The relocation of molten material is also determined by measuring the axial distribution of the blocked area and bundle mass. These measurements were performed in connection with the epoxying process. As can be seen in Figure 79 the resin is poured into the Lucite mould from the bottom end. By weighing the resin left in the supply container after each step, i.e. when the resin level has raised in the bundle by 1 cm, the difference of mass allows the calculation of the void volume of the bundle as a function of axial height. The filling process is slow enough so that the reading at the scale can be taken per cm.

The error of this measured mass distribution amounts to about 15 %: 10 % with respect of the measurement of 1 cm increments of the epoxy level and 5% due to the error of mass measurement. The error, however, is alternating, i.e. epoxy not measured at one step is certainly included in the next reading at the scale. A filtering method using a Fourier transformation, where higher frequencies were cut off by a low pass filter, was performed to deal with these errors.

The data of the mass of resin as a function of elevation in Figure 80 demonstrate the scatter. The smoothed solid-line curve in Figure 80 was obtained from the data (crosses) by filtering. The axial distribution in Figure 80 is the distribution of the epoxy bundle fill-up, i.e. a complement to blockage in the bundle.

Using the density of the epoxy and the cross sectional area inside the Lucite mould the structural area of the bundle end state can be evaluated. Referred to the area of the shroud, it is given in Figure 82a as „relative blockage".

The Blocked area is defined as (cross section mould inside - cross section epoxy - cross-section of shroud remnants) referred to cross section of shroud inside.

As part of the shroud was removed together with the fibre insulation after the test, the remnants of the shroud which were present during the filling process were excluded in the evaluation by measuring their contribution to the cross section separately. The areas are given as percentages, where 100 % means complete blockage. To determine the axial mass distribution, the epoxy filled bundle was cut into horizontal slices and these bundle segments were weighed. The distribution is shown in Figure 81. Knowing the axial epoxy distribution, the contribution of the resin is subtracted from the measured weight, to give the mass distribution of the bundle. Also this distribution is corrected for the share of the shroud. The results are given in Figure 82b. These data represent the mass of the rods and spacer. The measured curve is compared with the mass distribution of the intact bundle.

The specific mass is defined as (mass of weighed samples - epoxy mass - mass of shroud remnants) referred to the pertinent axial segment.

If one compares the uncertainty of the axial mass distribution with the axial volume distribution, one can see, that the method using the weighed samples is the more accurate. The uncertainty of the measurement of the filled-in epoxy mass contains the same absolute error, however, the relative error is only one fifth, because the epoxy resin is referred to a 5 cm block compared with the reference of 1 cm for the volume method. Because of the lower density of the epoxy resin in comparison with the density of the structural material the relative error is further reduced. On the other hand in the mass distribution the resolution is reduced.

The axial distribution of blocked area and mass in the bundles (Figures 83) are very similar and in accordance with the results from the cross section. Material is reduced in the region about 450 mm and relocated to the lower part of the bundle, where the blockage can be seen in the region above 300 mm.

In Figure 83 the axial mass distribution is compared with the axial temperature distribution. One can recognize a strong correlation between the axial temperature profile and the melt relocation: The melt relocation to lower elevations corresponds to the expansion of high temperatures to the lower elevations. We have seen in all our tests that melt relocation and axial temperature distribution are coupled to each other. The melt relocation is determined by the axial temperature distribution, but the axial temperature distribution on the other side is influenced by the melt relocation and the exothermic steam/Zircaloy reaction triggered by the heat transported with the melt.

8. Summary and discussion of major results

Test CORA-29, a PWR-type test, was performed with pre-oxidized bundle components. The pre-oxidation should simulate conditions in the reactor, where oxide layers are formed during normal reactor operation. The pre-oxidation was performed in the CORA test facility at 800 °C for 9000 s. The steam flow rate was 6 g/s.

The resulting oxide layer thickness on the cladding surfaces varied between about 4 μm at the lower end of the bundle and about 12 μm at the upper end and was less than expected (25 μm) on the basis of separate effects tests /17/. Explanations for the smaller oxide layers may be the possible dependency of the onset of breakaway oxidation during the preoxidation on the surface conditions and the special batch of Zircaloy (etched or as-received, batch to batch variation). In CORA we used the Zircaloy as-received.

In general the physico-chemical behaviour of the test bundle CORA-29 was comparable with other PWR related tests without any preoxidation. The temperature

escalation starts in the upper part of the bundle at 850 mm elevation and proceeds in the lower part to 350 mm and in the upper part to 1150 mm elevations.

The damage development is initiated by the failure of the absorber rods. The eutectic interaction between silver from the absorber material starts the liquefaction of the Zry cladding. In consequence the liquefied Zry initiates the dissolution of the pellets far below the melting temperatures of UO_2.

The melt relocation and blockage formation was as in all other tests mainly determined by the axial temperature profile. A larger blockage of preferentially Zry with dissolved UO_2 formed between 300 and 430 mm. This blockage had a porous structure. A minor blockage of preferentially absorber material was found between 110 mm and 200 mm elevation. The absorber rod was destroyed above about 120 mm.

In CORA-29 the thin oxide layers had only a minor influence on the relocation of molten material. Axial elevations of about 100 mm lower where reached. The relocation behaviour is partially determined by the wetting conditions of the solid surface. The wetting becomes poorer if the solid substrate is ceramic and the molten relocating material metallic in structure.

The oxide layers on the cladding of CORA-29 did not have an influence on the onset (temperature and time) of the temperature escalation and the maximum temperature reached. It was therefore unexpected that in test CORA-29 the total hydrogen production 225 g was higher than in other PWR type experiments performed under comparable test conditions. The explanation for this effect is related with the possibility of a loss of the original protectiveness of thin oxide layers by defect formation during the subsequent temperature escalation, and beyond this the possibility of an induced quality degradation of the subsequently growing sublayers.

The total amount of hydrogen produced for the PWR test CORA-29 was 225 g. This corresponds to an oxidation energy of 34.2 MJ. In comparison the total electric input amounted to 34.1 MJ. For the BWR test CORA-28 the corresponding values amount to 104 g total hydrogen produced, equivalent to 15.8 MJ. The total electric input in test CORA-28 was 28.8 MJ. This means that in CORA-29 the exothermic energy corresponded to nearly 100 % of the electric input, compared to 55 % in CORA-28.

If we use for the determination of the Zr oxidation the bundle length, that had experienced temperature above 1430 °C, Zr oxidation in test CORA-29 amounts to 75% compared to the BWR-test CORA-28 with 30 %. The fraction of steam consumed in CORA-29 was 38 % compared to 79 % in CORA-28. This is the result of the much higher steam input of 6 g/s in PWR-test CORA-29 compared to 2 g/s in CORA-28.

9. References

1. J.M. Broughton; P. Kuan, D.A. Petti; "A Scenario of the Three Mile Island Unit 2 Accident", *Nuclear Technology*, Vol. 87, 34-53 (1989).

2. S. Hagen, K. Hain: "Out-of-pile Bundle Experiments on Severe Fuel Damage (CORA-Program)", *KfK* 3677 (1986).

3. S. Hagen, P. Hofmann, G. Schanz, L. Sepold; "Interactions in Zircaloy/UO_2 Fuel Rod Bundles with Inconel Spacers at Temperatures above 1200°C (CORA-2 and CORA-3)", *KfK* 4378 (1990).

4. S. Hagen, P. Hofmann, V. Noack, G. Schanz, G. Schumacher, L. Sepold; "Results of SFD Experiment CORA-13 (OECD International Standard Problem 31)" *KfK* 5054 (1993).

5. M. Firnhaber, K. Trambauer, S. Hagen, P. Hofmann, G. Schanz, L. Sepold:ISP-31, "CORA-13 Experiment on Severe Fuel Damage GRS-106", *KfK* 5287, NEA/CSNI/R (93) 17 (1993).

6. S. Hagen, P. Hofmann, V. Noack, G. Schanz, G. Schumacher, L. Sepold; "BWR Slow Heat-up Test CORA-31: Test Results", *KfK* 5383 (1994)

7. S. Hagen, P. Hofmann, V. Noack, G. Schanz, G. Schumacher, L. Sepold; "Dry Core BWR Test CORA-33: Test Results", *KfK* 5261 (1994).

8. S. Hagen, P. Hofmann, V. Noack, G. Schanz, G. Schumacher, L. Sepold; "Behaviour of a VVER Fuel Element Tested under Severe Accident Conditions in the CORA Facility (Test Results of Experiment CORA-W1)" *KfK* 5212 81994).

9. S. Hagen, P. Hofmann, V. Noack, G. Schanz, G. Schumacher, L. Sepold; "Behaviour of a VVER-1000 Fuel Element with Boron Carbide/Steel Absorber Tested under Severe Fuel Damage Conditions in the CORA Facility (Results of Experiment CORA-W2)", *KfK* 5363 (1994).

10. J. Burbach; "Results of SEM/EDX Microrange Analyses of the PWR Fuel Element Meltdown Experiment CORA-13", *KfK* 5162 (1993).

11. J. Burbach; "Results of SEM/EDX Microrange Analyses of the BWR Fuel Element Meltdown Experiment CORA-16", *KfK* 5282 (1994).

12. S. Hagen, P. Hofmann, V. Noack, L. Sepold, G. Schanz, G. Schumacher;" Comparison of the Quench Experiments CORA-12, CORA-13, CORA-17", *FZKA* 5679, (1996).

13. S. Hagen, P. Hofmann, V. Noack, L. Sepold, G. Schanz, G. Schumacher; "Impact of absorber rod material on bundle degradation seen in CORA experiments", *FZKA* 5680 (1996).

14. S. Hagen, P. Hofmann, V. Noack, L. Sepold, G. Schanz, G. Schumacher; "Cold Lower End Test CORA-10: Test Results"; FZKA 5572 (1997)

15. S. Hagen, P. Hofmann, V. Noack, L. Sepold, G. Schanz, G. Schumacher; "Pre-oxidised BWR Test CORA-28: Test Results"; FZKA 5571 (1997)

16. S. Hagen, P. Hofmann, V. Noack, L. Sepold, G. Schanz, G. Schumacher; "Slow Heatup PWR Test CORA-30: Test Results" FZKA 5929 (1997)

17. S. Leistikow and G. Schanz, „Oxidation kinetics and related phenomena of Zircaloy-4 fuel cladding exposed to high temperature steam and hydrogen-steam mixtures under PWR accident conditions; Nuclear Engineering and Design 103 (1987) 65-84

10. Acknowledgements

At the Forschungszentrum Karlsruhe a variety of support needed for preparation, conduct, and evaluation of the experiment is hereby gratefully acknowledged. The facility was designed by K. Hain and his team. The special bundle set up was designed by Mr. H. Junker. The test rods were assembled by Mr. E. Mackert, the test bundles by Messrs. H. Gießmann and R. Röder. The authors would like to thank Messrs. H. Benz, C. Grehl and H.J. Röhling for test preparations and conduct. Mr. K. P. Wallenfels was responsible for arrangement of camera and video systems and for the preparation of temperature measurements. Messrs. R. Huber and H. Malauschek prepared and conducted the on-line measurements of the off-gas composition.

Finally we would like to express our gratitude to Mrs. A. Stängle for the careful typing of this report.

List of tables

Tab. 1: CORA Test Matrix

Test No.	Max. Cladding Tempera-tures	Absorber Material	Other Test Conditions	Date of Test
2	≈ 2000°C	-	UO_2 refer., inconel spacer	Aug. 6, 1987
3	≈ 2400°C	-	UO_2 refer., high temperature	Dec. 3, 1987
5	≈ 2000°C	Ag, In, Cd	PWR-absorber	Febr. 26, 1988
12	≈ 2000°C	Ag, In, Cd	quenching	June 9, 1988
16	≈ 2000°C	B_4C	BWR-absorber	Nov. 24, 1988
15	≈ 2000°C	Ag, In, Cd	rods with internal pressure	March 2, 1989
17	≈ 2000°C	B_4C	quenching	June 29, 1989
9	≈ 2000°C	Ag, In, Cd	10 bar system pressure	Nov. 9, 1989
7	< 2000°C	Ag, In ,Cd	57-rod bundle, slow cooling	Febr. 22, 1990
18	< 2000°C	B_4C	59-rod bundle, slow cooling	June 21, 1990
13	≈ 2200°C	Ag, In, Cd	OECD/ISP; quench initiation at higher temperature	Nov. 15, 1990
29*	≈ 2000°C	Ag, In, Cd	pre-oxidized,	April 11, 1991
31*	≈ 2000°C	B_4C	slow initial heat-up (≈ 0.3 K/s)	July 25, 1991
30*	≈ 2000°C	Ag, In, Cd	slow initial heat-up (≈ 0.2 K/s)	Oct. 30, 1991
28*	≈ 2000°C	B_4C	pre-oxidized	Febr. 25, 1992
10	≈ 2000°C	Ag, In, Cd	cold lower end 2 g/s steam flow rate	July 16, 1992
33	≈ 2000°C	B_4C	dry core conditions, no extra steam input	Oct. 1, 1992
W1	≈ 2000°C	-	WWER-test	Febr. 18, 1993
W2	≈ 2000°C	B_4C	WWER-test with absorber	April 21, 1993

Initial heat-up rate: ≈ 1,0 K/s; Steam flow rate, PWR: 6 g/s, BWR: 2 g/s; quench rate (from the bottom) ≈ 1 cm/s

Tab. 2: Design characteristics of bundle CORA-29

Bundle type:		PWR
Bundle size:		25 rods
Number of heated rods:		16
Number of unheated rods:		7
Pitch:		14.3 mm
Rod outside diameter:		10.75 mm
Cladding material:		Zircaloy-4
Cladding thickness:		0.725 mm
Rod length:	- heated rods: (elevation - unheated rods (elevation	1960 mm - 489 to 1471 mm) 1672 mm - 201 to 1471 mm)
Heated pellet stack:		1000 mm
Heater material:		Tungsten (W)
Heater	- length - diameter	
Fuel pellets	- heated rods: - unheated rods:	UO_2 annular pellets UO_2 full pellets
Pellet stack	- heated rods: - unheated rods:	O to 1000 mm - 199 to 1295 mm
U-235 enrichment		0.2 %
Pellet outer diameter (nominal)		9.1 mm
Grid spacer	- material: - length: - location:	Zircaloy -4, Inconel 718 Zry 42 mm Inc 38 mm lower (Zry) -5 mm center (Inc) + 496 mm top (Zry) + 880 mm
Shroud	- material - wall thickness - outside dimensions - elevation	Zircaloy -4 1.2 mm 89.4 x 90.4 mm 36 mm to 1231 mm
Shroud insulation	 - insulation thickness - elevation	ZrO_2 fibre 19 mm 36 mm to 1036 mm

Tab. 2: (Continuation)

Mo electrode	- length	300 mm
	- diameter	8,6 mm
Cu electrode	- length	189 mm (lower end)
	- length	669 mm (upper end)
	- diameter	8,6 mm
Absorber rod	- number of rods	2
	- material and composition	80Ag,15In,5Cd (wt.%)
	- cladding	Stainless steel
	- cladding OD	11,2 mm
	- cladding ID	10,2 mm
	- length	1660 mm
	- absorber material	-189 mm to + 1300 mm
Absorber rod guide tube	- material	Zircaloy -4
	- OD	13,8 mm
	- wall thickness of tube	0,8 mm
Plenum Volume	- heated rods	$12 \cdot 10^{-6}$ m^3
	- unheated rods	$87 \cdot 10^{-6}$ m^3

Table 3: Total specific mass data of bundle CORA-29

Specific mass [kg/m]	
Tungsten heater elements	8.74
UO_2	10.85
Zircaloy in rods	3.45
Zircaloy in absorber rods	0.43
Stainless steel in absorber rods	0.26
Ag/In/Cd absorber	1.59
Inconel grid spacer	0.11
Zircaloy grid spacer	0.14
Zircaloy of shroud	2.77
Total zircaloy	6.65

Table 4: Areas of bundle CORA-29

Cross section areas [m^2]	
Tungsten	$4.524\ 10^{-4}$
UO_2	$1.043\ 10^{-3}$
Zircaloy cladding	$5.252\ 10^{-4}$
Absorber, Ag/In/Cd	$1.634\ 10^{-4}$
Absorber, Stainless steel cladding	$3.36\ 10^{-5}$
Absorber, Zircaloy guide tube	$6.54\ 10^{-5}$
Zircaloy shroud	$4.22\ 10^{-4}$
Total area inside the shroud	$7.535\ 10^{-3}$

Table 5: Positions of thermocouples

Positions of thermocouples in unheated rods (CORA 29)		
Slot Number	Elevation [mm]	Rod Number
131	1450	4,2
132	1350	2,6
101	1150	6,6
102	1050	2,2
103	950	6,4
104	850	2,4
105	750	4,4
221	550	2,6
222	550	6,6
223	550	2,2
224	450	4,2
225	350	6,4
231	150	2,4
232	50	4,4

Positions of thermocouples in absorber rods (CORA-29)		
Slot Number	Elevation [mm]	Rod Number
106	950	6,2
107	750	4,6
226	550	6,2
227	350	4,6

Positions of thermocouples at heated rods (CORA-29)		
Slot Number	Elevation [mm]	Rod Number
108	1150	5,3
109	950	5,5
110	750	3,5
228	550	5,5
229	350	5,3
230	150	3,3
233	50	3,5

Positions of thermocouples at guide tube (CORA-29)		
Slot Number	Elevation [mm]	Rod Number
111	1150	4,6
112	950	6,2
113	750	4,6
241	550	6,2
242	350	4,6
243	150	4,6
234	50	6,2

Positions of thermocouples at grid spacer (CORA-29)		
Slot Number	Elevation [mm]	Direction of TE
114	860	210°
115	860	30°
235	475	210°
236	475	30°
237	-26	210°
238	-26	30°

Positions of thermocouples in cer. tube,shroud+bundle		
Slot Number	Elevation [mm]	Direction of TE
116	950	30°
117	950	210°
118	750	30°
119	750	210°

Positions of thermocouples at shroud in cer. tube (C:-29)		
Slot Number	Elevation [mm]	Direction of TE
120	950	300°
121	750	300°
244	550	300
245	350	300°

Positions of thermocouples at shroud outer surface		
Slot Number	Elevation [mm]	Direction of TE
122	1150	210°
123	950	210°
124	750	210°
246	550	210°
247	350	210°
248	150	210°
239	50	210°

Positions of thermocouples at bundle flange (CORA-.29)		
Slot Number	Elevation [mm]	Direction of TE
134	1471	30°
135	1491	210°
136	1471	345°
137	1511	345°
138	1511	210°

Positions of thermocouples for gas (CORA-29)		
Slot Number	Elevation [mm]	Direction of TE
125	1350	120°
126	1250	300°

Positions of thermocouples in shroud insulation(CORA-29)		
Slot Number	Elevation [mm]	Direction of TE
133	1060	30°
127	950	30°
128	750	30°
249	550	30°
261	350	30
262	150	30°
269	50	210°

Positions of thermocouples steam distribution tube		
Slot Number	Elevation [mm]	Direction of TE
62	-300	180°
264	-250	300°
265	0	180°
266	0	180°
267	-50	345°
268	-50	165°
269	300°	300°

Table 6: List of cross sections for test bundle CORA-29

Probe	Proben-länge	Axiale Lage unten	Axiale Lage oben	Bemerkungen
29-a	140 mm	-185 mm	-45 mm	
Schnitt	2 mm			Unterer Abstandshalter
29-b	140 mm	-43 mm	97 mm	Mit Längsschnitt
Schnitt	2 mm			
29-01	13 mm	99 mm	112 mm	Querschnitt, oben poliert
Schnitt	2 mm			
29-c	140 mm	114 mm	254 mm	Mit 2 Längsschn., 29-c1-R poliert
Schnitt	2 mm			
29-02	13 mm	256 mm	269 mm	Querschnitt
Schnitt	2 mm			
29-d	140 mm	271 mm	411 mm	Mit 2 Längsschn., 29-d1-L poliert
Schnitt	2 mm			
29-03	13 mm	413 mm	426 mm	Querschnitt, oben poliert
Schnitt	2 mm			
29-e	140 mm	428 mm	568 mm	Mit Längsschnitt
Schnitt	2 mm			
29-04	13 mm	570 mm	583 mm	Querschnitt
Schnitt	2 mm			
29-f	140 mm	585 mm	725 mm	
Schnitt	2 mm			
29-05	13 mm	727 mm	740 mm	Querschnitt
Schnitt	2 mm			
29-g	130 mm	742 mm	872 mm	
Schnitt	2 mm			
29-06	13 mm	874 mm	887 mm	Oberer Abst.halter
Schnitt	2 mm			

Table 6: (continuation)

29-h	140 mm	889 mm	1029 mm	
Schnitt	2 mm			Oberhalb der Heizzone
29-i	140 mm	1031 mm	1171 mm	
Schnitt	2 mm			
29-j	52 mm	1173 mm	1225 mm	
Schnitt	2 mm			
29-k	xx mm	1227 mm	xxxx mm	Oberes Reststück

Table 7: Distribution of void volumes in unheated and heated rods

Void volume of one unheated rod

	elevation [mm]	volume [cm^3]	relative volume [cm^3/cm]
dishing of uranium pellets; gap between pellet stack and cladding	-201 to 1315	4.083	0.027
void volume above pellet stack	1315 to 1439	8.378	0.678
	1439 to 1456	0.711	0.419
	1456 to 1522	3.658	0.55
	1522 to 1531	0.387	0.43
	1531 to 1762	6.531	0.283
	1762 to 1764	0.084	0.419
system for pressure measurement		15.120	
total void volume		38.952	

Void volume of one heated rod

	elevation [mm]	volume [cm^3]	relative volume [cm^3/cm]
void volume below pellet stack	-369 to -334	0.826	0.236
	-334 to 0	1.391	0.0417
gap between pellet stack and cladding and between pellet stack and heater	0 to 1024	2.311	0.023
void above pellet stack	1024 to 1875	3.545	0.0417
	1875 to 1911	0.852	0.24
system of pressure measurement		10.860	
total void volume		19.785	

List of figures

29 : Temperatures between bundle and shroud

30 : Temperatures of the spacers

31 : Temperatures of the absorber rods and in the pertinent guide tubes

32 : Temperatures at the bundle head plate

33 : Location of the thermocouples at shroud and shroud insulation

34 : Temperatures of inner side of shroud measured with ceramic protected TCs

35 : Temperatures of outer side of shroud

36 : Temperatures of the shroud insulation

37 : Temperatures at elevations given (1511-1250 mm)

38 : Temperatures at elevations given (1150-1050 mm)

39 : Temperatures at elevations given (950 mm)

40 : Temperatures at elevations given (860 - 850 mm)

41 : Temperatures at elevations given (750 mm)

42 : Temperatures at elevations given (550 mm)

43 : Temperatures at elevations given (475 - 350 mm)

44 : Temperatures at elevations given (150 - 50 mm)

45 : Temperatures at elevations given (0 - -300 mm)

46 : Best-estimate bundle temperatures at different elevations

46a Comparison of hydrogen production rate and best estimate temperatures

47 : Axial temperature distribution during the transient of test CORA-29

48 : Locations of thermocouples in the high temperature shield (CORA-29)

49 : Position of thermocouples in the high temperature shield for test CORA-29

50 : Temperatures of HTS, Inner surface at 153 mm radius

51 : Temperatures of HTS, Temperatures in HT shield at 192 mm radius, 345°

52 : Temperatures of HTS, Temperatures in HT shield at 255 mm radius

53 : Temperatures of HTS, Temperatures in HT shield at 293 mm radius

54 : Temperatures of HTS, Comparison on inner surface at 153 mm radius

55 : Temperatures of HTS, Comparison on inner surface at 153 mm radius, 990 mm and 890 mm elevation

56 : Temperatures of HTS, Comparison on inner surface at 153 mm radius, 390 mm and 90 mm elevation

57 : Temperatures of HTS, Comparison in HT-shield at 192 mm radius, 950 mm and 750 mm elevation

58 : Temperatures of HTS, Comparison in HT-shield at 192 mm radius, 550 mm and 150 mm elevation

59 : Temperatures of HTS, Inner surface at 153 mm radius, 0 - 10000 s

60 : Temperatures of HTS, Temperatures in HT shield at 192 mm radius, 345°, 0 - 10000 s

61 : Temperatures of HTS, Temperatures in HT shield at 255 mm radius, 0 - 10000 s

62 : Temperatures of HTS, Temperatures in HT shield at 293 mm radius, 0 - 10000 s

63 : Temperatures of HTS, Radial dependence at about 950 mm elevation

64 : Temperatures of HTS, Radial dependence at about 550 mm elevation

65 : Temperatures of HTS, Radial dependence at about 100 mm elevation

66 : Temperatures of HTS, Radial dependence at about 950 mm elevation, 0 - 10000 s

67 : Temperatures of HTS, Radial dependence at about 550 mm elevation, 0 - 10000 s

68 : Temperatures of HTS, Radial dependence at about 100 mm elevation, 0 - 10000 s

69 : Hydrogen production in test CORA-29; production rate (top) and integral values (bottom)

70 : Comparison of chemical and electric power

71 : not used

72 : not used

73 : not used

74 : not used

75 : not used

76 : not used

77 : not used

78 : not used

79 : Epoxying process of the tested bundle

80 : Axial distribution of the bundle fill-up with epoxy resin

81 : Axial mass distribution of bundle segments filled with epoxy resin

82 : Comparison of axial mass distribution and axial volume distribution after the test

83 : Axial mass distribution after the test and axial temperature profiles during the test

84 : Posttest appearance of bundle, shroud and shroud insulation;
300°, 210°, 120°, 30° orientation

85 : Posttest view of the inner side of shroud insulation; 300°, 210°, 120°, 30° orientation

86 : Comparison of inner and outer side of shroud insulation; 300° and 210° orientation

87 : Comparison of inner and outer side of shroud insulation; 120° and 30° orientation

88 : Posttest view of the inner side of shroud insulation; 30° orientation,
850-1150 mm elevation

89 : Posttest view of the inner side of shroud insulation; 30° orientation,
550-950 mm elevation

90 : Posttest view of the inner side of shroud insulation; 30° orientation,
350-650 mm elevation

91 : Posttest view of bundle CORA-29 after partial removal of shroud;
300°, 210°, 120°, 30° orientation

92 : Posttest view of bundle CORA-29 after partial removal of shroud;
300°, 210°, 120°, 30° orientation; 200 - 1100 mm elevation

93 : Post test view of bundle, 300° partial view, 1050-1350 mm

94 : Post test view of bundle, 300° partial view, 750-1050 mm

95 : Post test view of bundle, 300° partial view, 500-750 mm

96 : Post test view of bundle, 300° partial view, 200-500 mm

97 : Post test view of bundle, 210° partial view, 1050-1350 mm

98 : Post test view of bundle, 210° partial view, 750-1050 mm

99 : Post test view of bundle, 210° partial view, 500-800 mm

100 : Post test view of bundle, 210° partial view, 200-500 mm

101 : Post test view of bundle, 120° partial view, 1050-1350 mm

102 : Post test view of bundle, 120° partial view, 750-1050 mm

103 : Post test view of bundle, 120° partial view, 500-800 mm

104 : Post test view of bundle, 120° partial view, 200-500 mm

105 : Post test view of bundle, 30° partial view, 1050-1350 mm

106 : Post test view of bundle, 30° partial view, 750-1050 mm

107 : Post test view of bundle, 30° partial view, 500-800 mm

108 : Post test view of bundle, 30° partial view, 200-500 mm

108a Refrozen melt at the lower end of the bundle seen in 120° direction

108b Refrozen melt at the lower end of the bundle seen in 210° direction

109 : Horizontal cross sections of bundle CORA-29, top view

110 : Horizontal cross sections of bundle CORA-29, bottom view

111 : Horizontal cross sections of the region of absorber rod 6.2, top view (1225 to -45 mm)

112 : Horizontal cross sections of the region of absorber rod 4.6, top view (1225 to -45 mm)

113 : Vertical cross sections through absorber rod 4.6, 120 - 410 mm

113a : Locations of the vertical cuts through sections CORA - 29-b, 29-c, 29-d, 29-e

114 : Vertical cross sections through absorber rod 4.6, 120 - 410 mm

115 : Vertical cross sections through absorber rod 4.6, -40 - 250 mm

116 : Vertical cross sections through absorber rod 4.6, both sides of the cut (420 - 570 mm)

117 : Vertical cross sections through unheated rods 2.2, 2.4 and 2.6;
both sides of the cut (270 - 410 mm)

118 : Comparison of horizontal cross sections CORA-29/ CORA-5 (725, 663 mm)

119 : Comparison of horizontal cross sections CORA-29/ CORA-5 (411, 408 mm)

120 : Comparison of horizontal cross sections CORA-29/ CORA-5 (112, 95 mm)

121 : Comparison of cross sections of region of one absorber rod in CORA-29/ CORA-5

122 : Comparison of vertical cross sections CORA-29/CORA-5

Appendix

A1 : Power input during pre-heat phase

A2 : Resistance of bundle during pre-heat phase

A3 : Argon input prior to test

A4 : Temperatures at steam inlet; pre-heat phase

A5 : Temperatures of heated rods; pre-heat phase

A6 : Temperatures of unheated rods; pre-heat phase

A7 : Temperatures between bundle and shroud measured with ceramic protected TCs; pre-heat phase

A7a : Temperatures of the spacers; pre-heat phase

A8 : Temperatures of the absorber rods and of the pertinent guide tubes; pre-heat phase

A9 : Temperatures between bundle and shroud; pre-heat phase

A10 : Temperatures of inner side of shroud measured with ceramic protected TCs; pre-heat phase

A11 : Temperatures of outer side of shroud; pre-heat phase

A12 : Temperatures of the shroud insulation; pre-heat phase

A13 : Temperatures at elevations given (1511-1250 mm); pre-heat phase

A14 : Temperatures at elevations given (1150-1050 mm); pre-heat phase

A15 : Temperatures at elevations given (950 mm); pre-heat phase

A16 : Temperatures at elevations given (860 - 850 mm); pre-heat phase

A17 : Temperatures at elevations given (750 mm); pre-heat phase

A18 : Temperatures at elevations given (550 mm); pre-heat phase

A19 : Temperatures at elevations given (475 - 350 mm); pre-heat phase

A20 : Temperatures at elevations given (150 - 50 mm); pre-heat phase

A21 : Temperatures at elevations given (0 - -300 mm); pre-heat phase

A22 : Temperatures of HTS, Inner surface at 153 mm radius; pre-heat phase

A23 : Temperatures of HTS, Temperatures in HT shield at 192 mm radius; pre-heat phase

A24 : Temperatures of HTS, Temperatures in HT shield at 255 mm radius; pre-heat phase

A25 : Temperatures of HTS, Temperatures in HT shield at 293 mm radius; pre-heat phase

B1 : Horizontal cross sections of bundle top view (1225 - 583 mm)

B2 : Horizontal cross sections of bundle top view (568 - -45 mm)

B3 : Horizontal cross sections of bundle bottom view (1173 - 570 mm)

B4 : Horizontal cross sections of bundle bottom view (428 - -185 mm)

B5 : Horizontal cross sections of bundle CORA-29 (1225 - 1171 mm)

B6 : Horizontal cross sections of bundle CORA-29 (1031 - 887 mm)

B7 : Horizontal cross sections of bundle CORA-29 (874 - 740 mm)

B8 : Horizontal cross sections of bundle CORA-29 (727 - 583 mm)

B9 : Horizontal cross sections of bundle CORA-29 (570 - 426 mm)

B10 : Horizontal cross sections of bundle CORA-29 (413 - 269 mm)

B11 : Horizontal cross sections of bundle CORA-29 (256 - 112 mm)

B12 : Horizontal cross sections of bundle CORA-29 (99 - -45 mm)

C1 : System pressure, argon flow, steam input and power during pre-oxidation (CORA-29 P)

C2 : Total electric power input during pre-oxidation (CORA-29 P)

C3 : Temperatures at steam inlet during pre-oxidation (CORA-29 P)

C4 : Temperatures of heated rods during pre-oxidation (CORA-29 P)

C5 : Temperatures of unheated rods during pre-oxidation (CORA-29 P)

C6 : Temperatures of the absorber rods during pre-oxidation (CORA-29 P)

C7 : Temperatures of the spacers during pre-oxidation (CORA-29 P)

C8 : Temperatures of the absorber rods and in the guide tubes during pre-oxidation (CORA-29 P)

C9 : Temperatures between bundle and shroud measured with ceramic protected Tcs during pre-oxidation (CORA-29 P)

C10 : Temperatures between bundle and shroud during pre-oxidation (CORA-29 P)

C11 : Temperatures of inner side of shroud measured with ceramic protected Tcs during pre-oxidation (CORA-29 P)

C12 : Temperatures of outer side of shroud during pre-oxidation (CORA-29 P)

C13 : Temperatures of the shroud insulation during pre-oxidation (CORA-29 P)

C14 : Temperatures of HTS, Inner surface at 153 mm radius during pre-oxidation (CORA-29 P)

C15 : Temperatures of HTS at 192 mm radius, 345° during pre-oxidation (CORA-29 P)

C16 : Temperatures of HTS at 255 mm radius during pre-oxidation (CORA-29 P)

C17 : Temperatures of HTS at 293 mm radius during pre-oxidation (CORA-29 P)

C18 : Temperatures of HTS, radial dependence at about 950 mm elevation during pre-oxidation (CORA-29 P)

C19 : Temperatures of HTS, radial dependence at about 550 mm elevation during pre-oxidation (CORA-29 P)

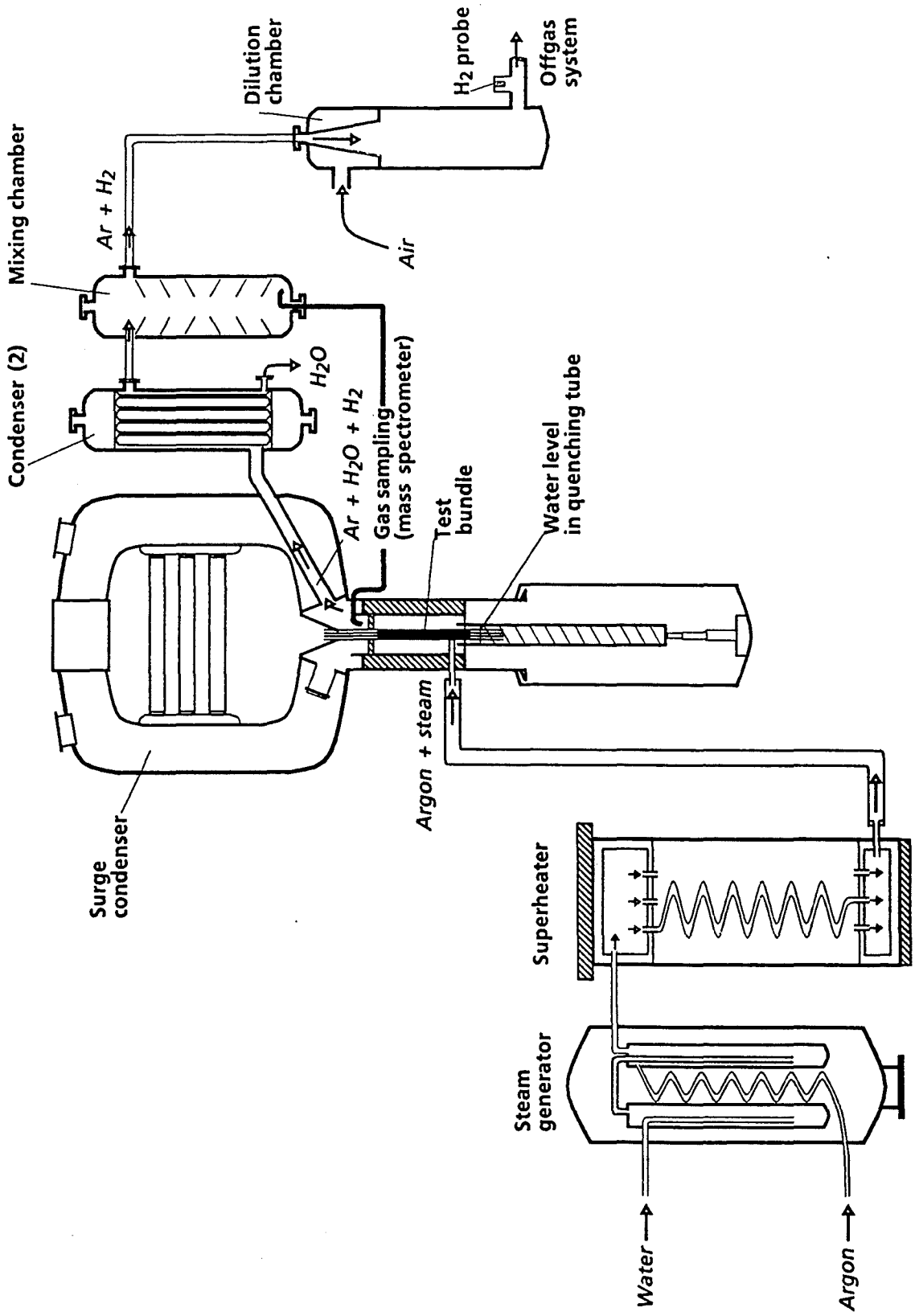

Fig. 1: SFD Test Facility (simplified flow diagram)

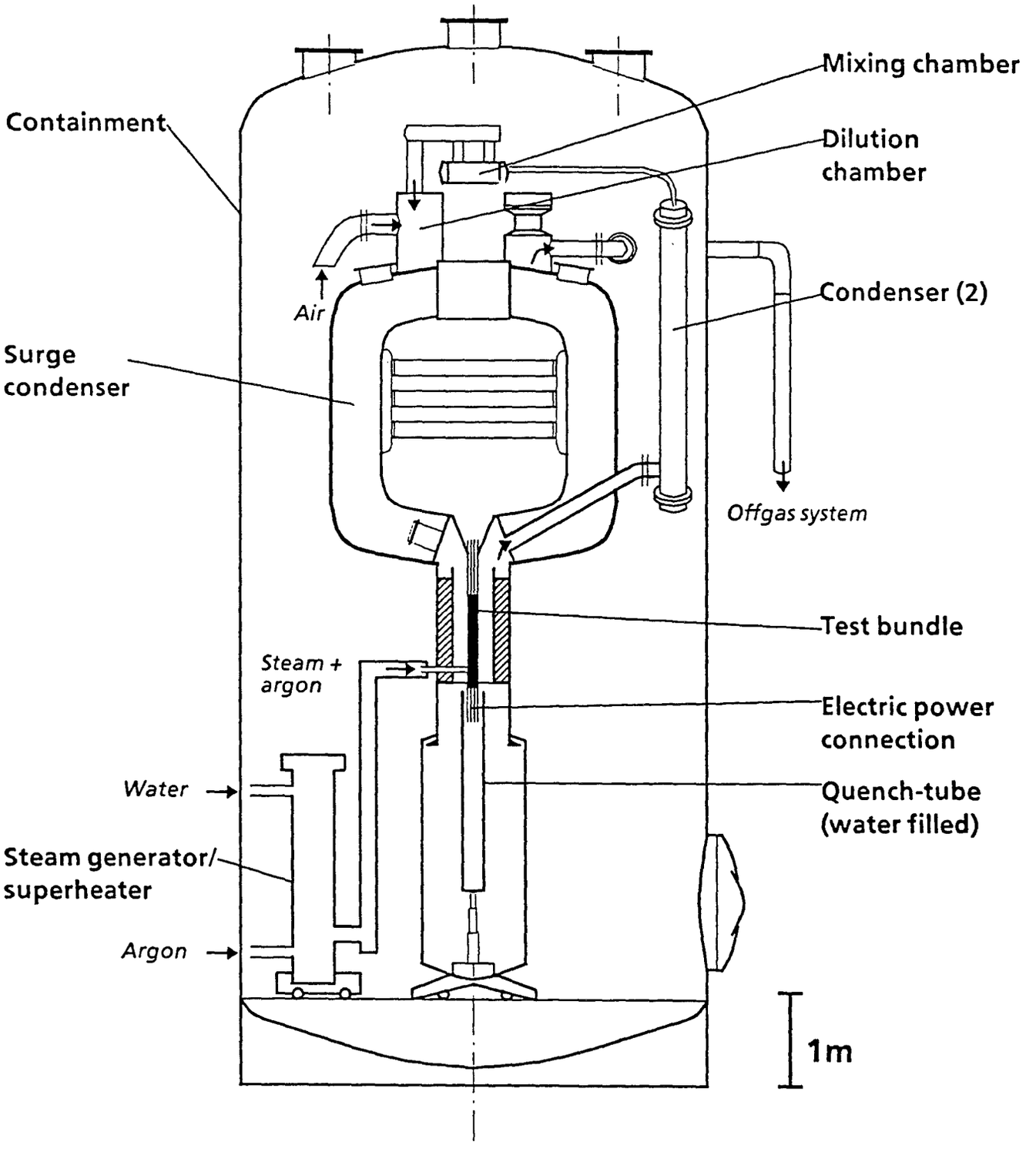

Fig. 2: SFD Test Facility CORA (Main Components)

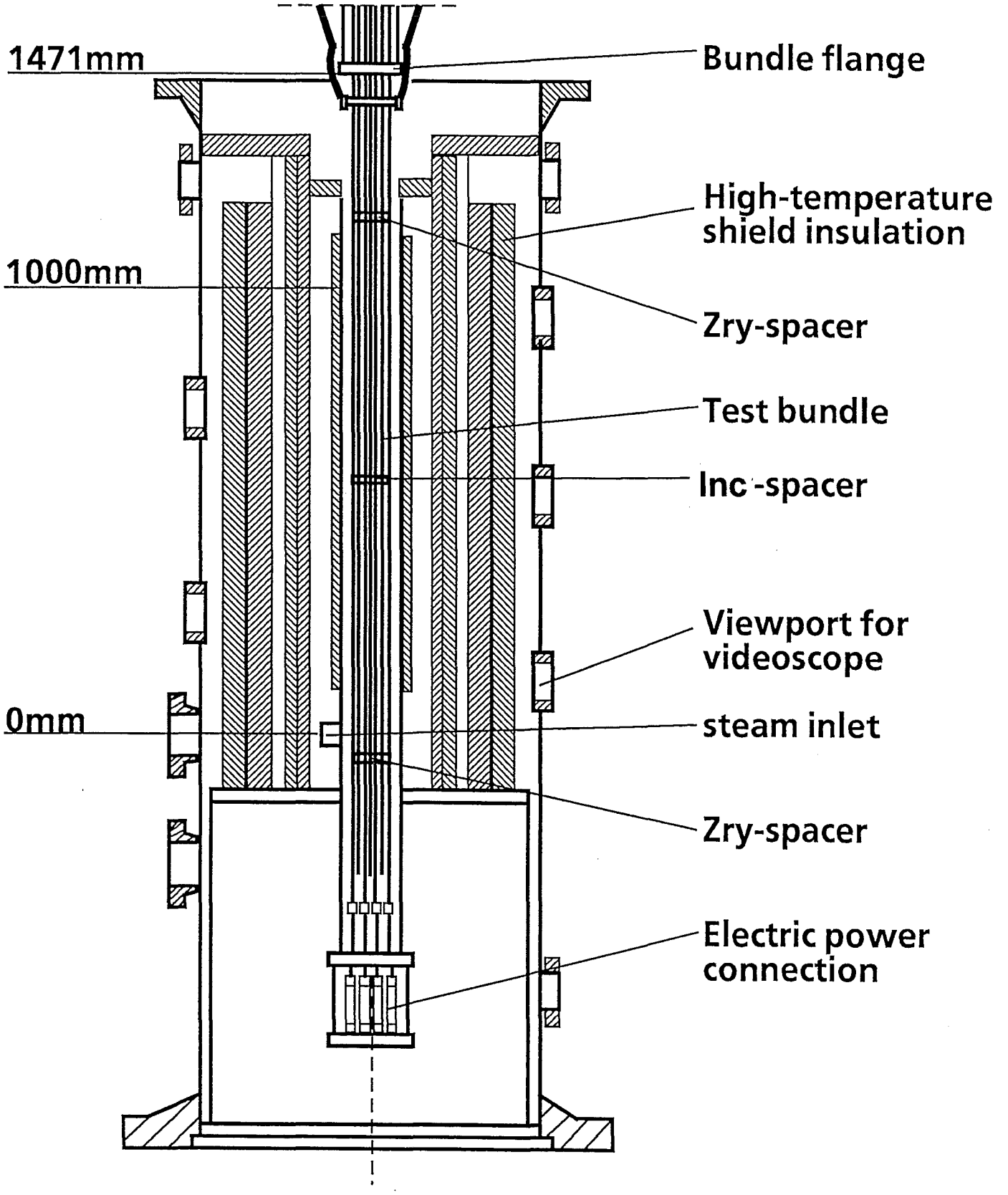

Fig. 3: CORA bundle arrangement

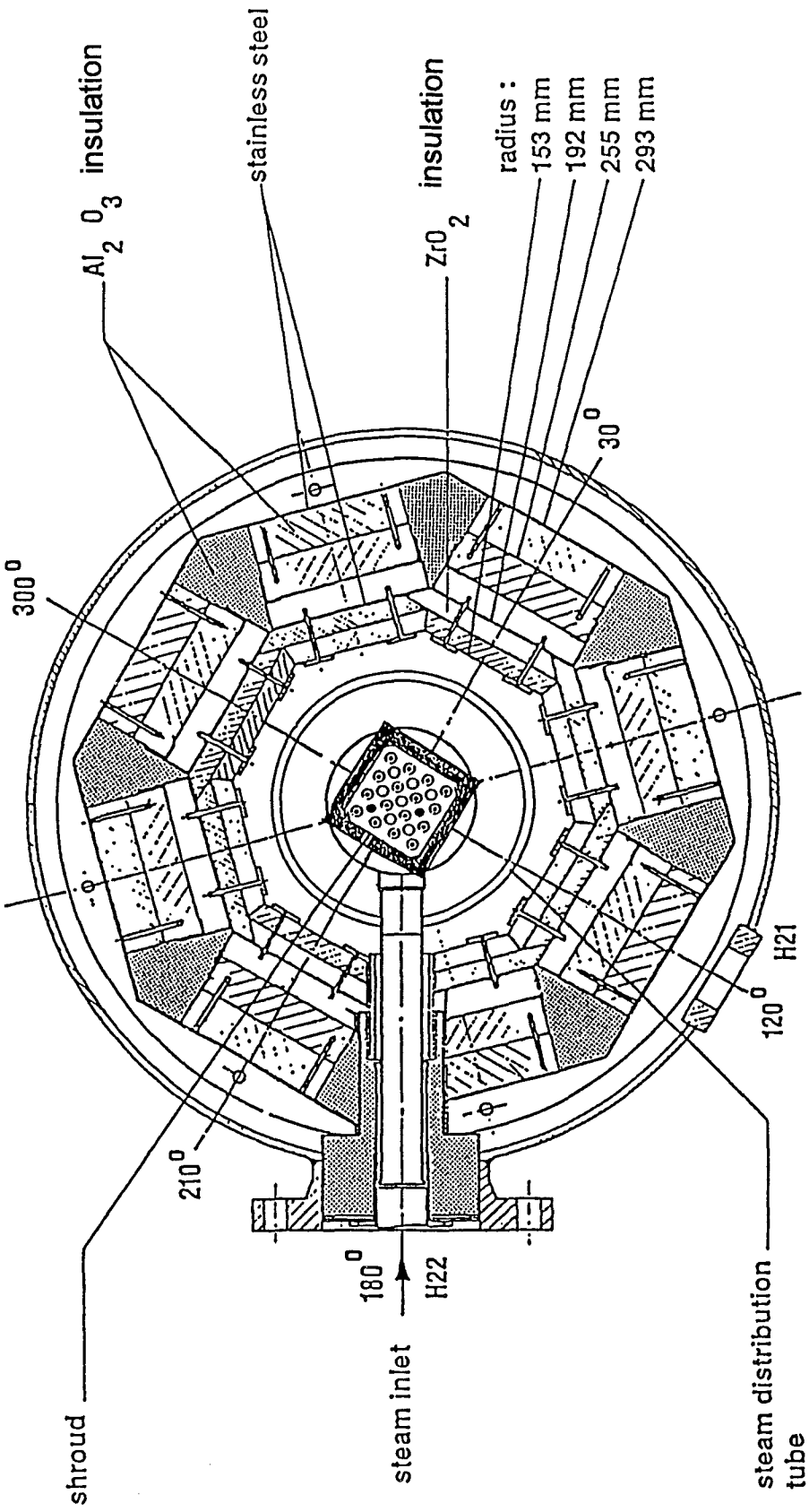

Fig. 4: Horizontal cross section of the high-temperature shield

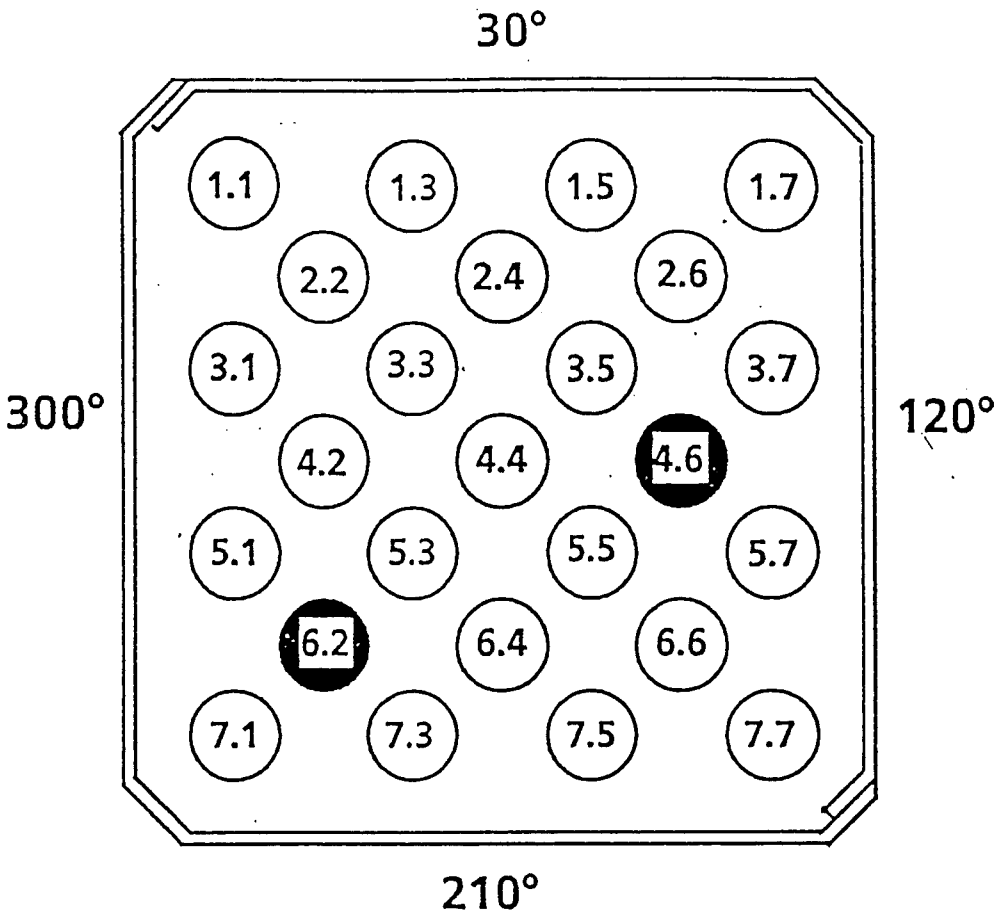

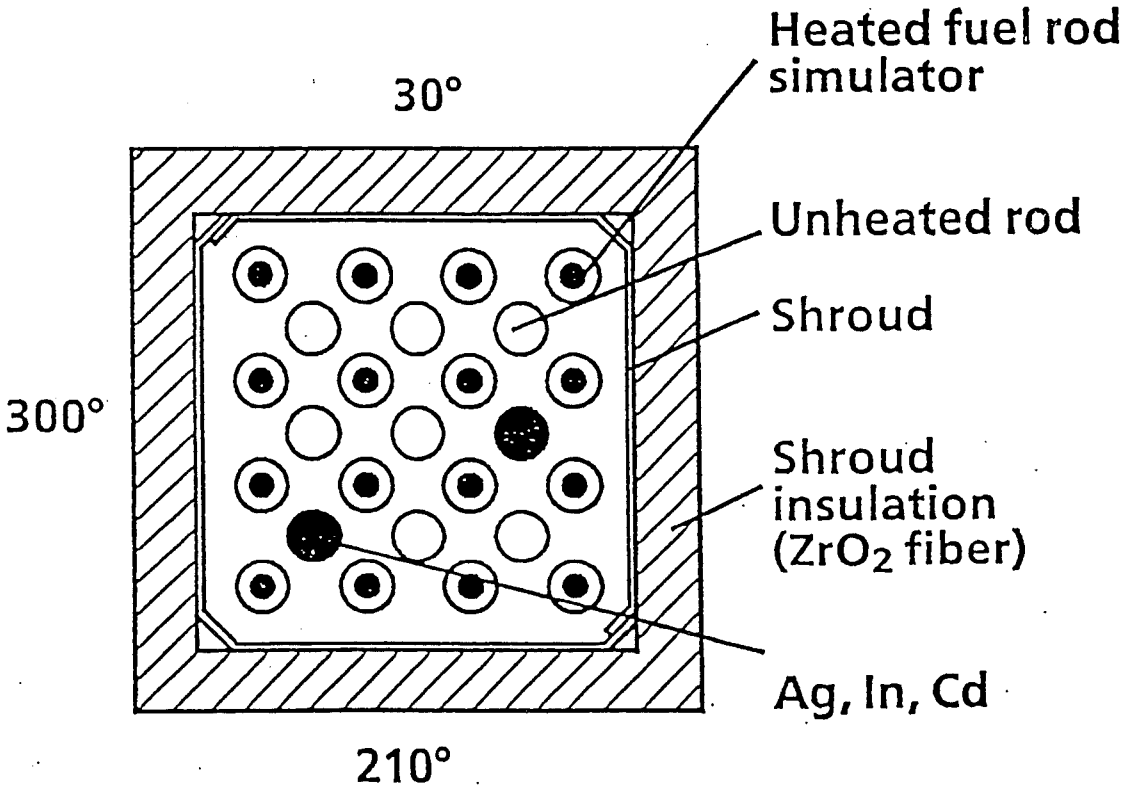

Fig. 5: Rod arrangement and test rod designation of bundle CORA-29

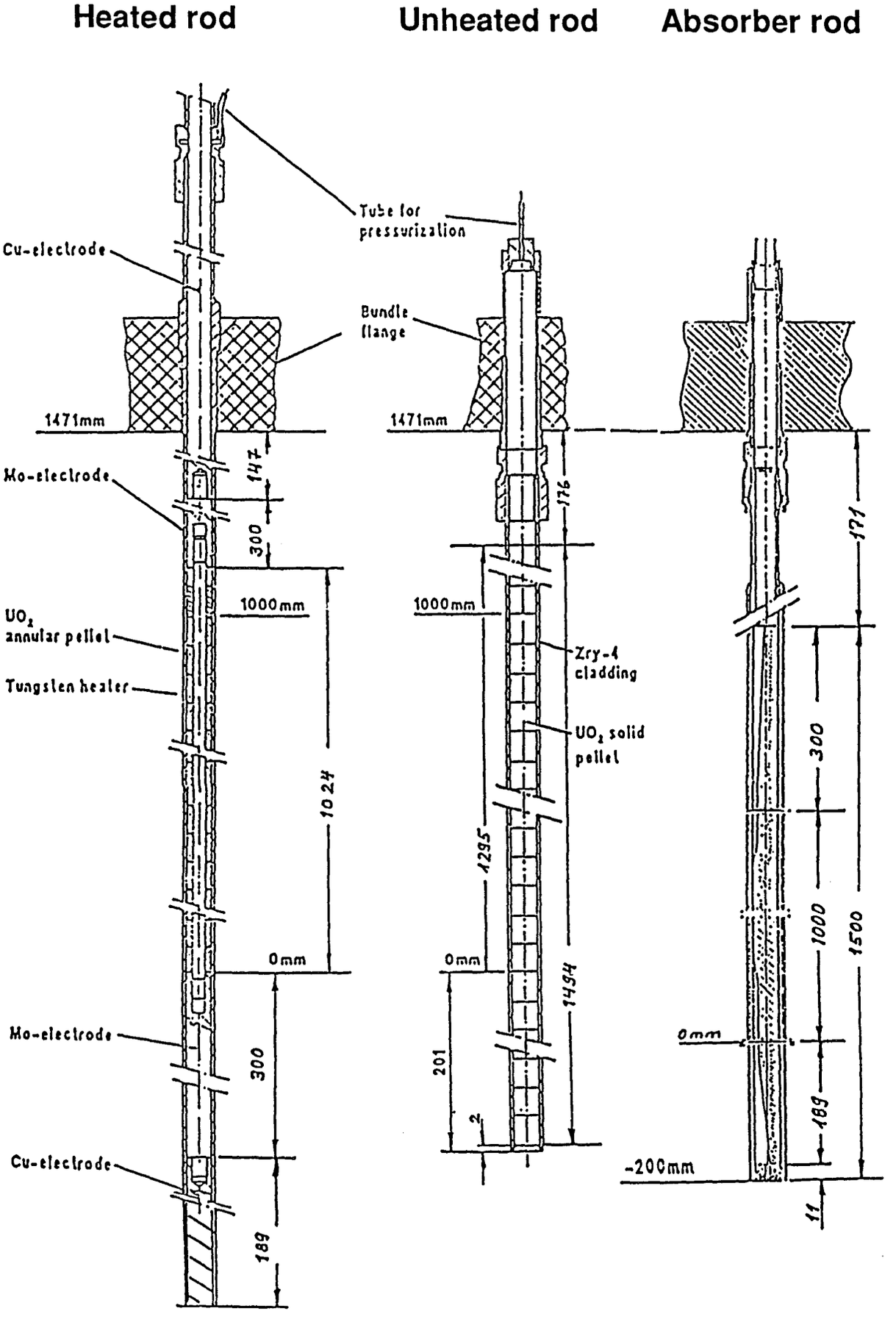

Fig. 6: Rod types used in the CORA experiments

(a)

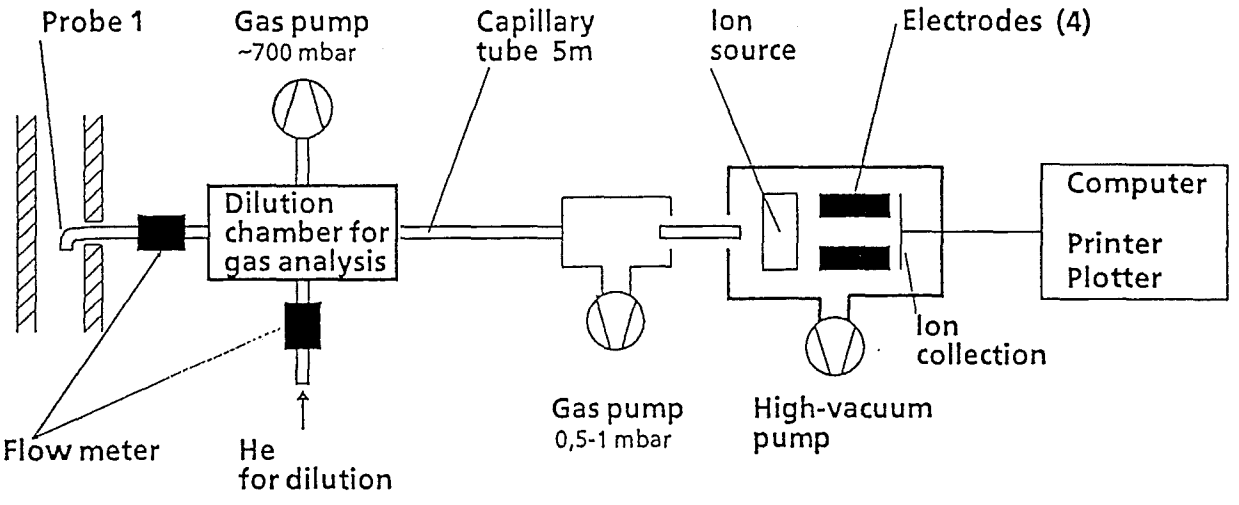

(b)

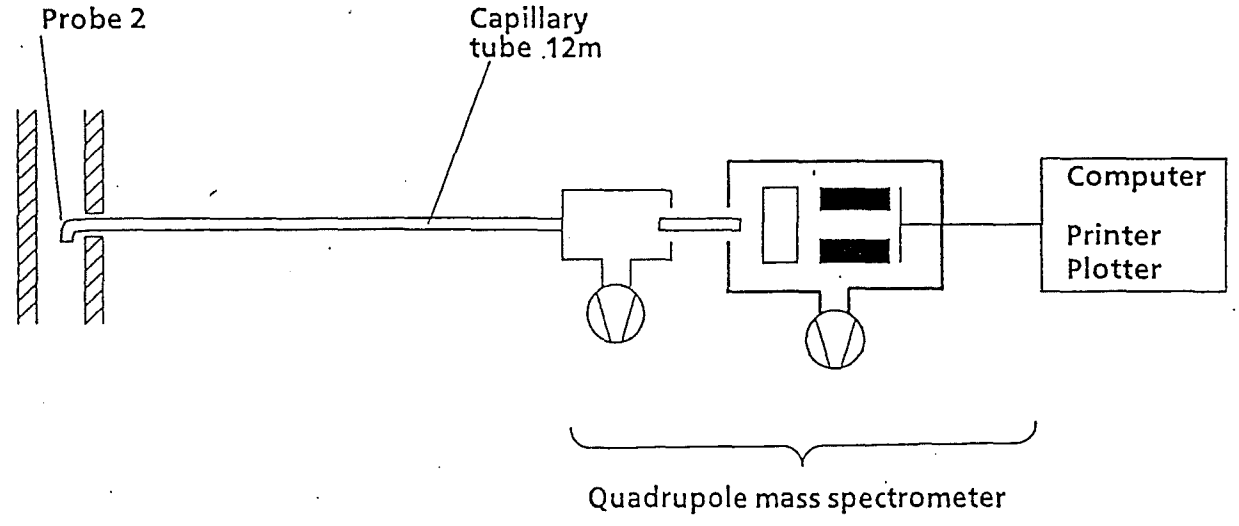

Location (a) : Outlet of test section

Location (b) : Mixing chamber

Fig. 7: Facility of hydrogen measurement

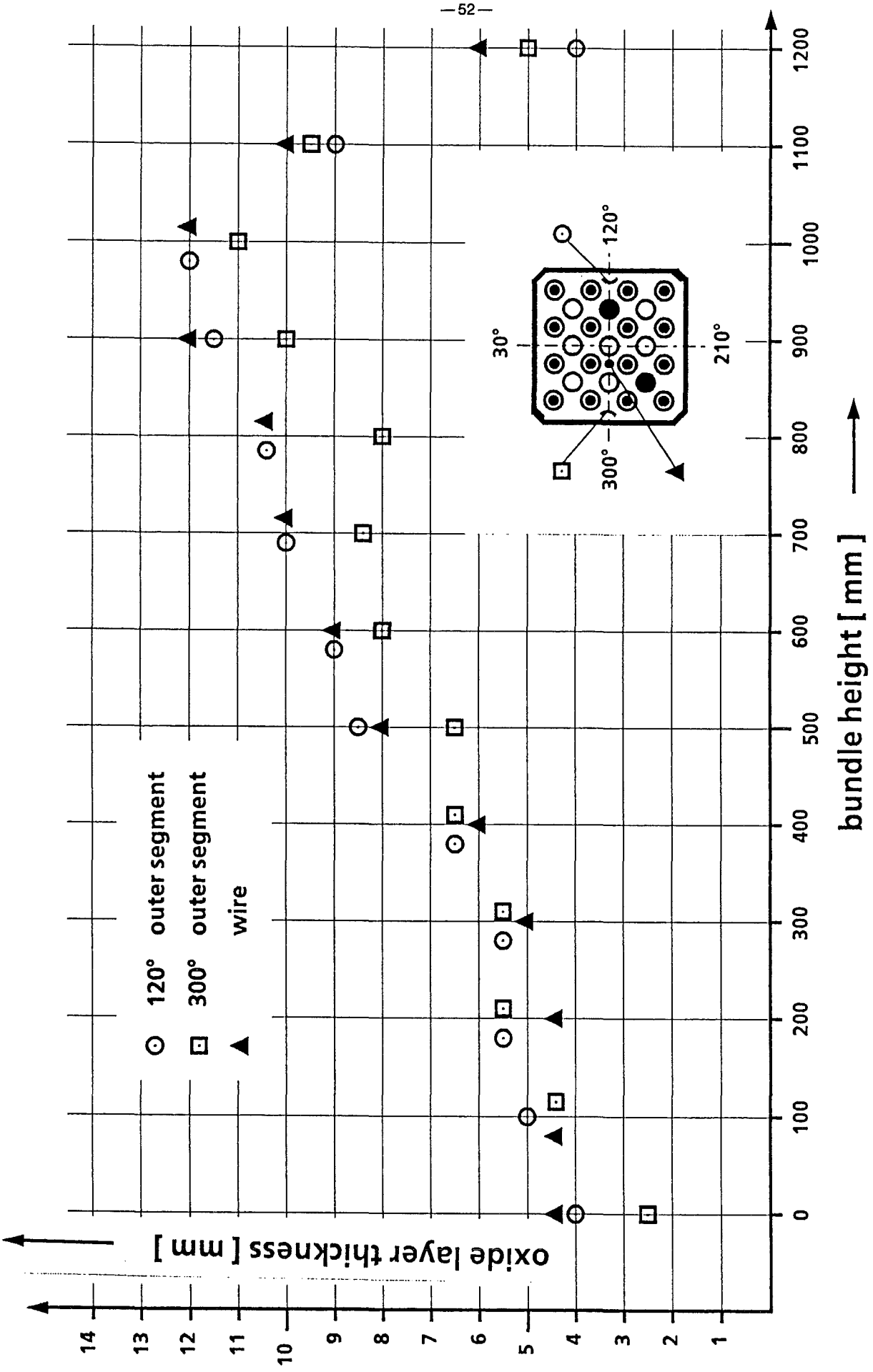

Fig. 8: Oxid layer resulting from pre-oxidation of test bundle CORA-29

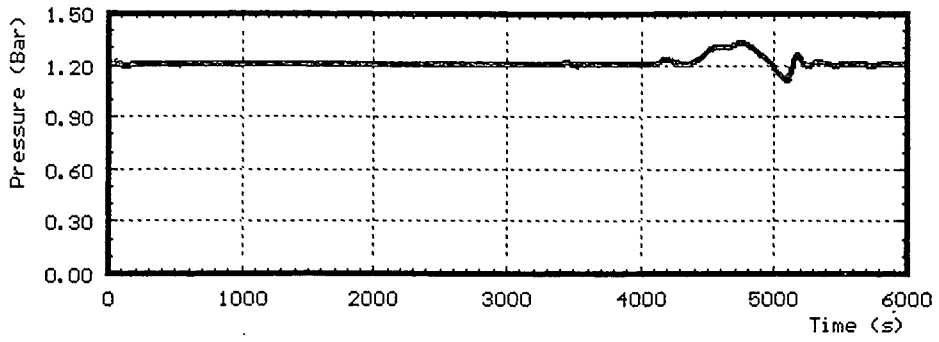

system pressure (gauge)

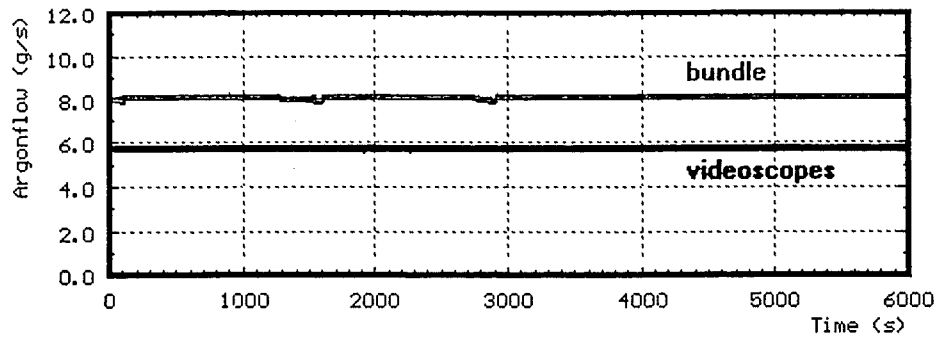

argon flow

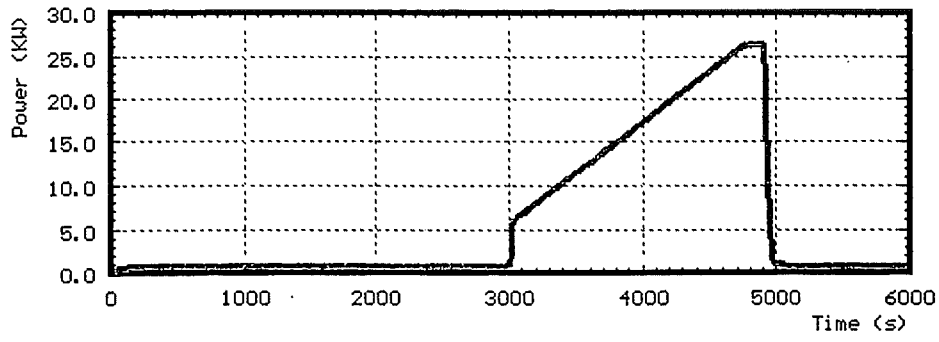

power

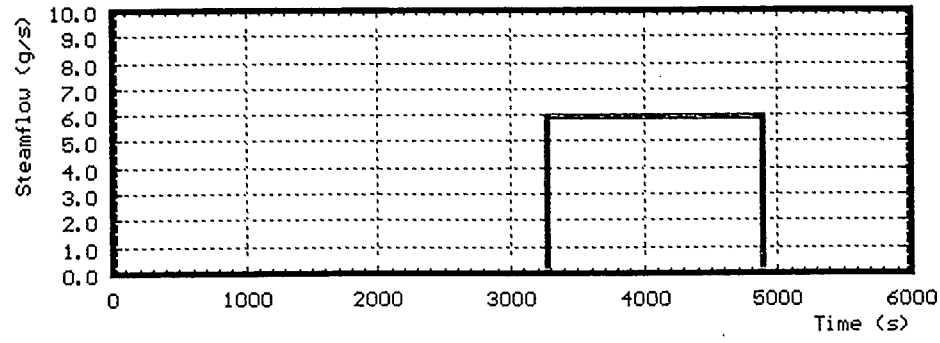

steam production

Fig. 9: CORA-29; System pressure, argon flow, steam input and power

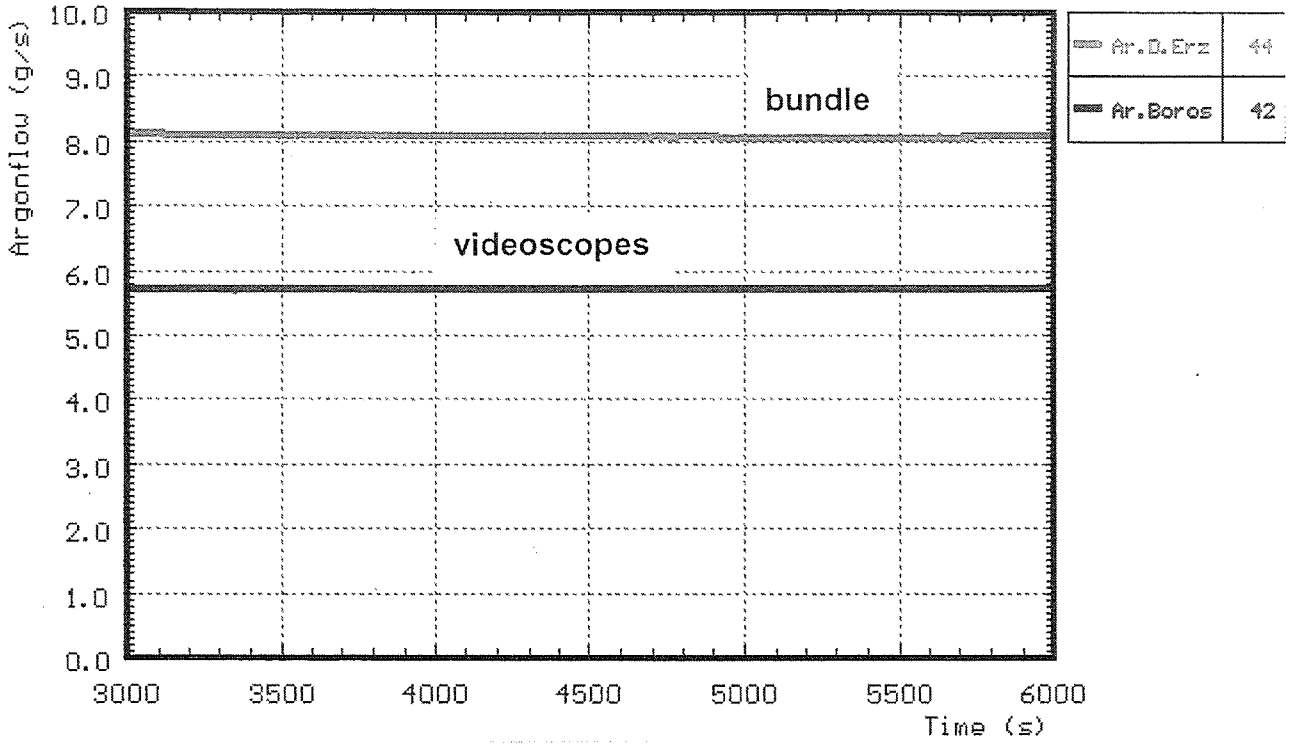

Fig. 10: CORA-29; Argon flow through bundle and videoscopes

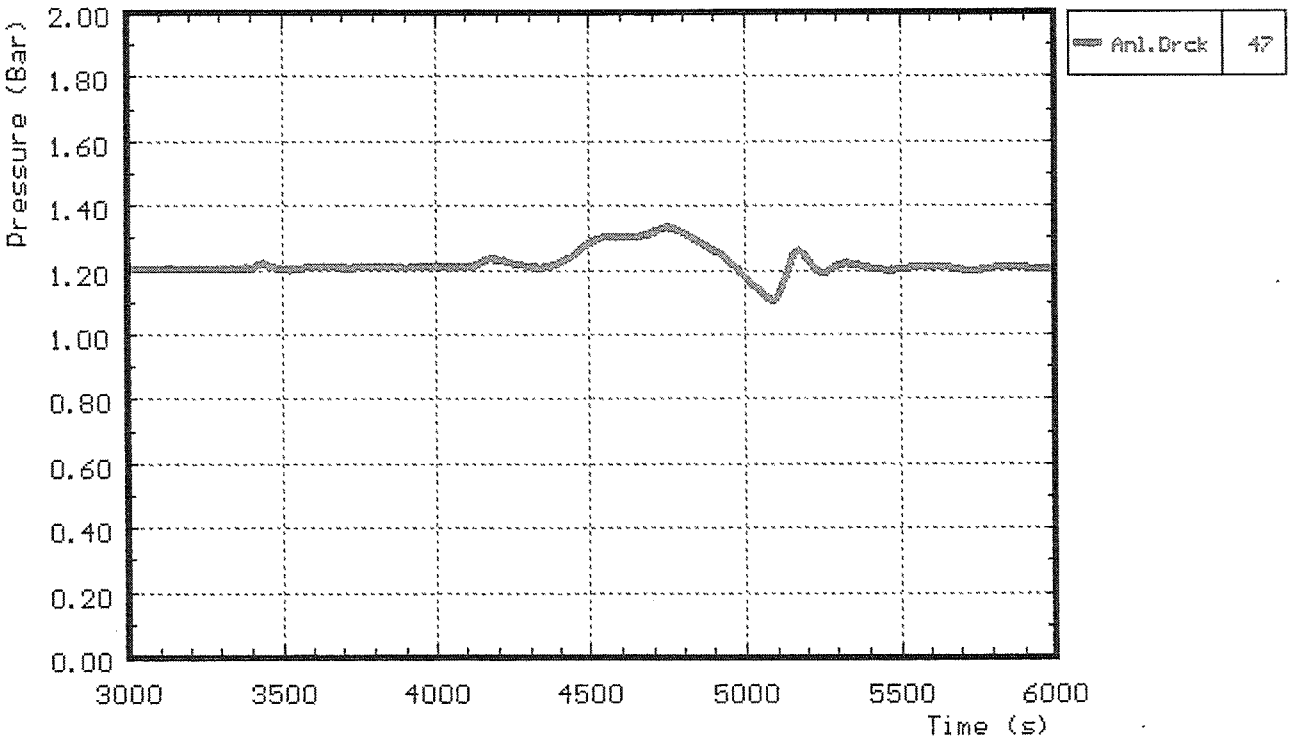

Fig. 11: CORA-29; System pressure (gauge)

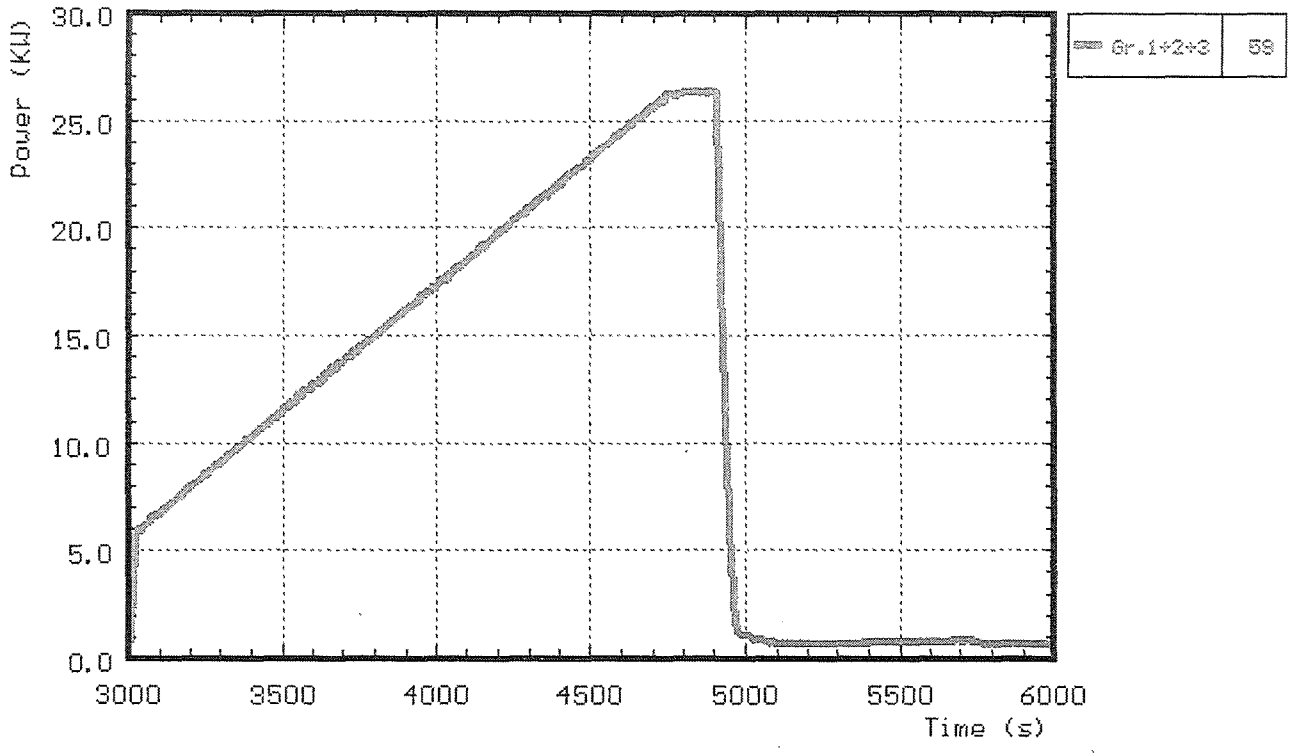

Fig. 12: CORA-29; Total electric power input

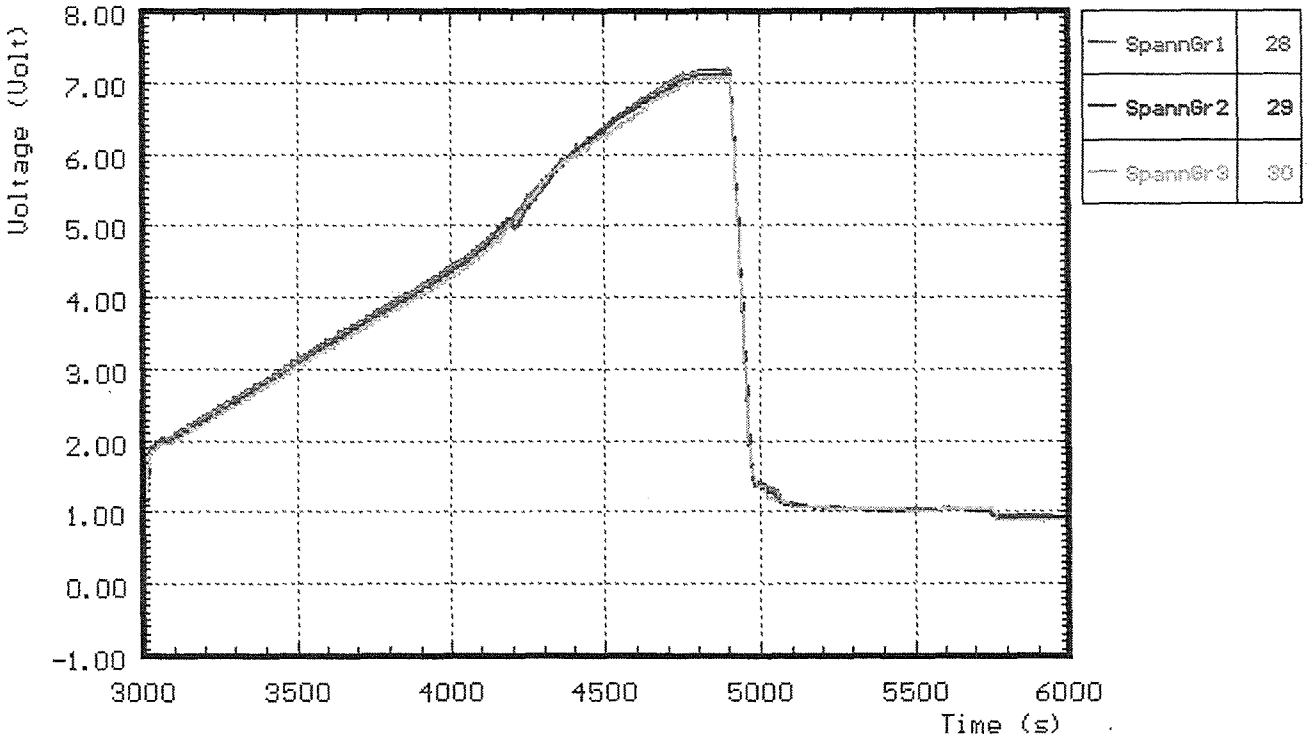

Fig. 13: CORA-29; Voltage input for the 3 rod groups

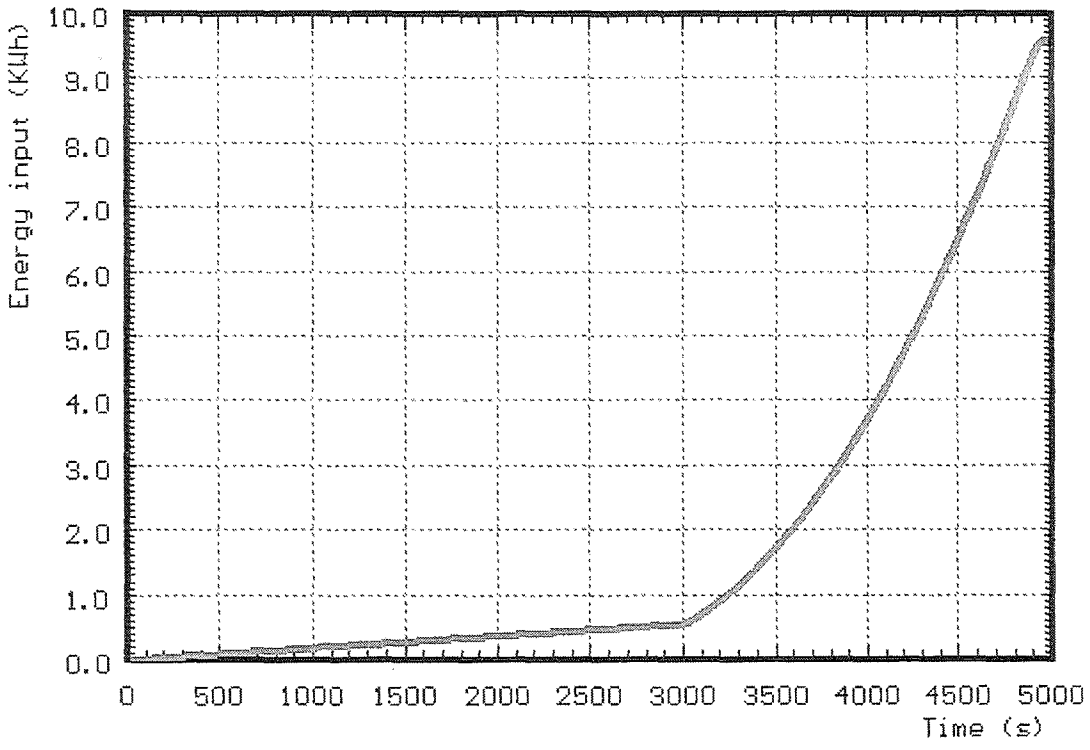

Fig. 14: CORA-29; Total electric energy input

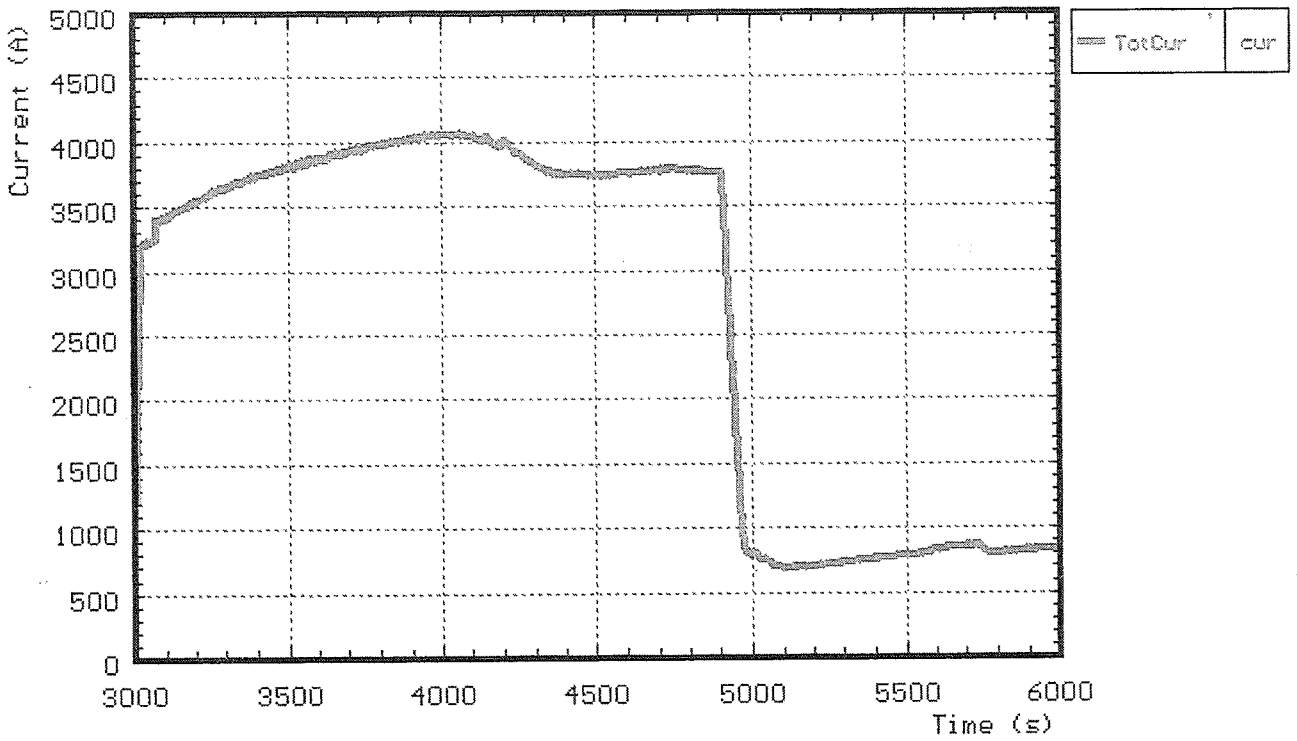

Fig. 15: CORA-29; Total current

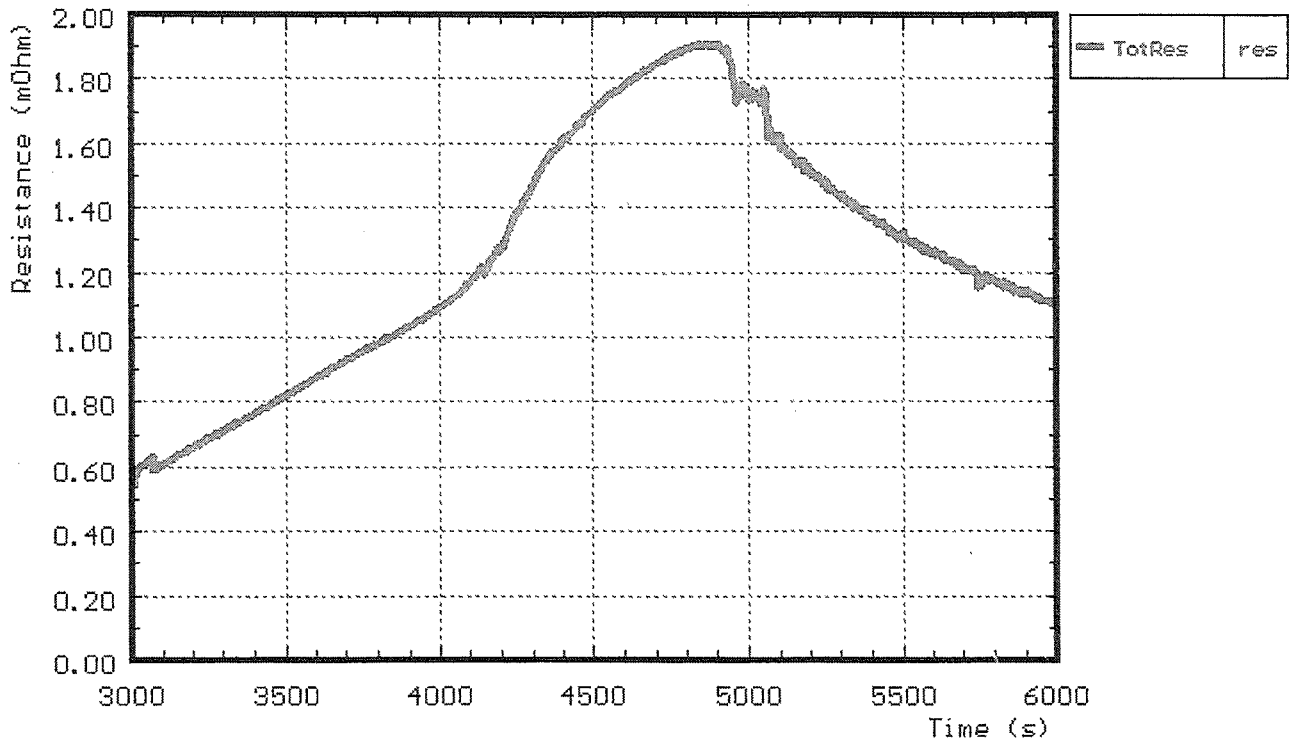

Fig. 16: CORA-29; Resistance of bundle
(Voltage group 1/total current)

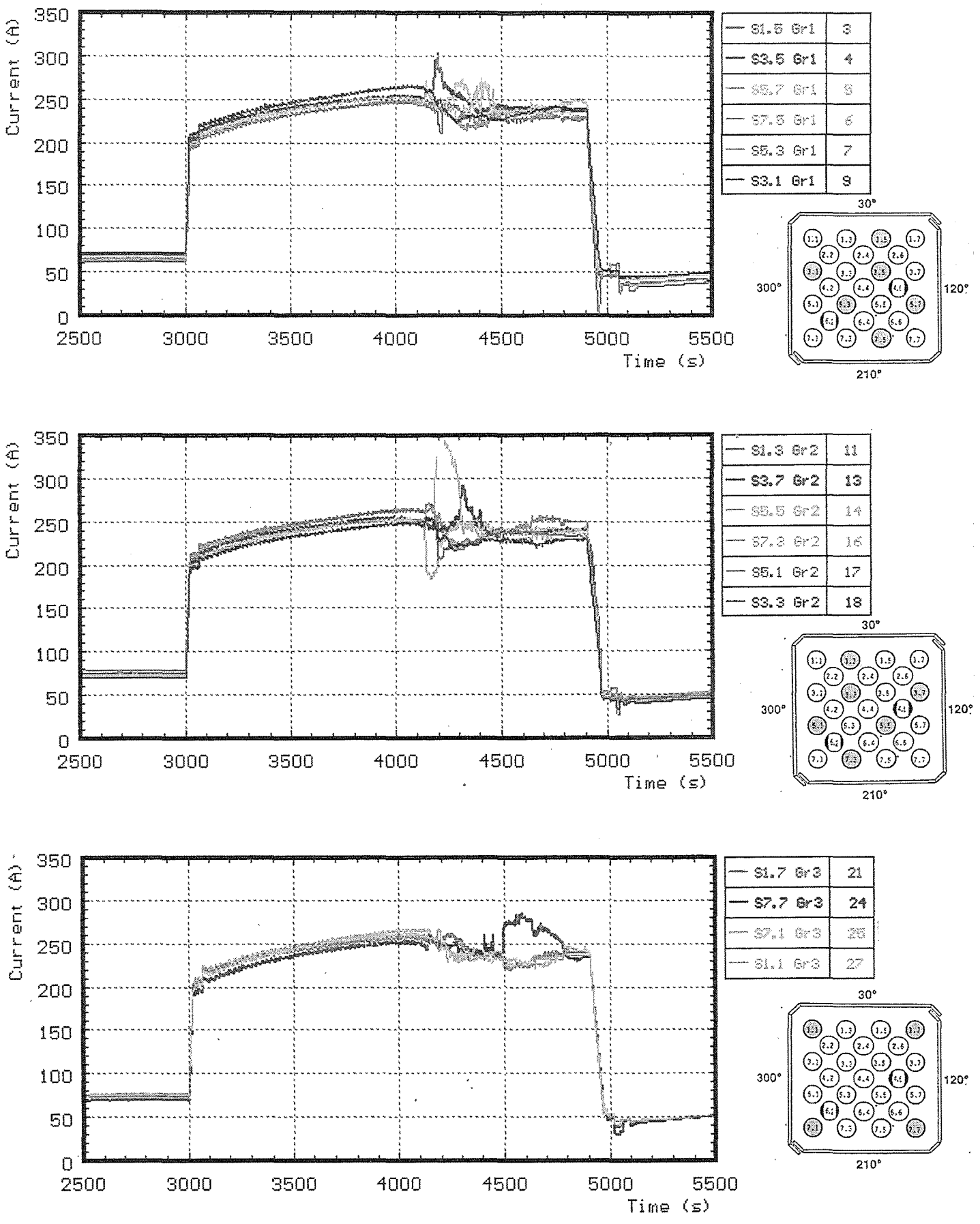

Fig. 17: CORA-29; Variations of currents within the rod groups

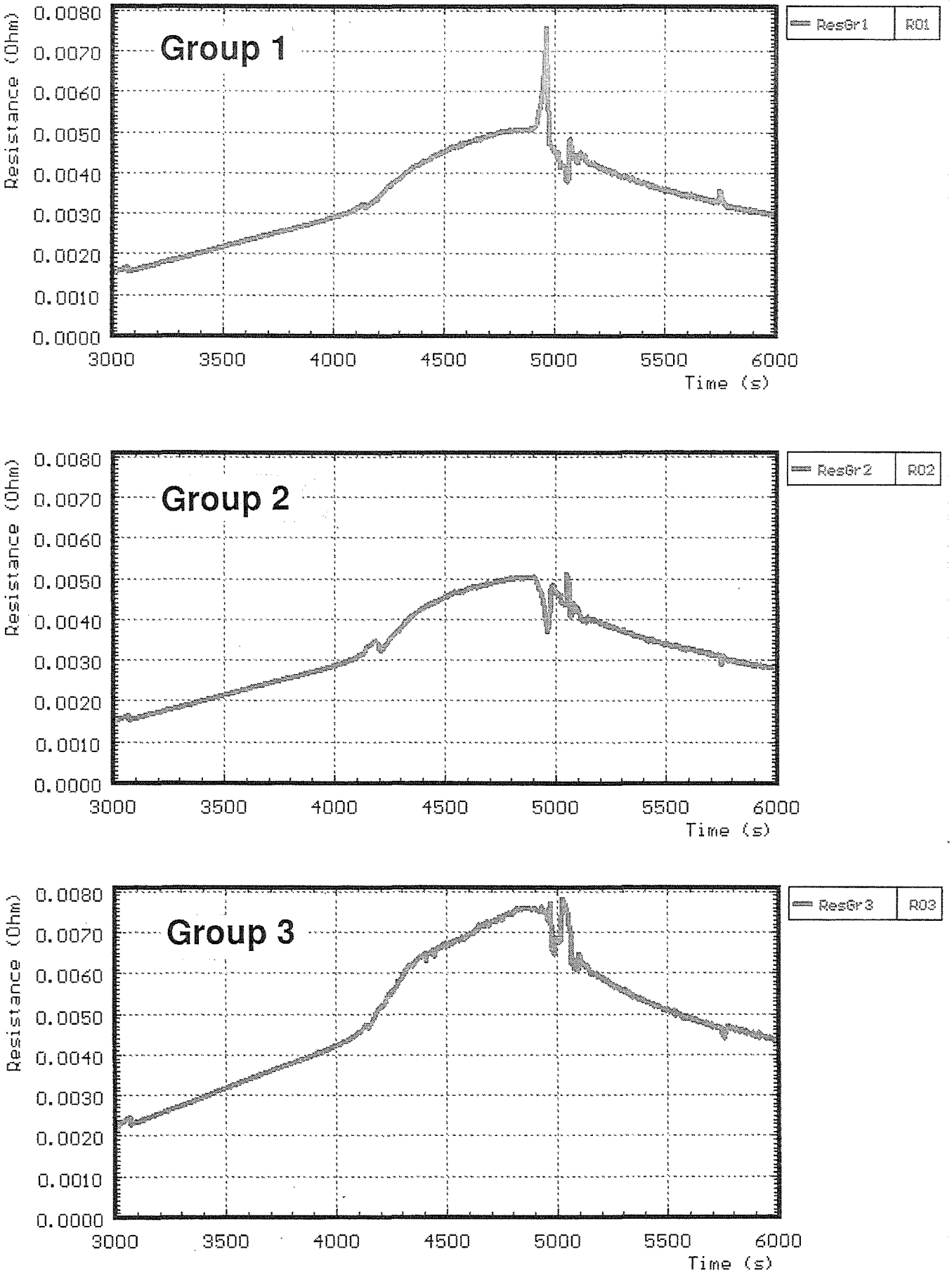

Fig. 18: CORA-29; Resistance of the rod groups

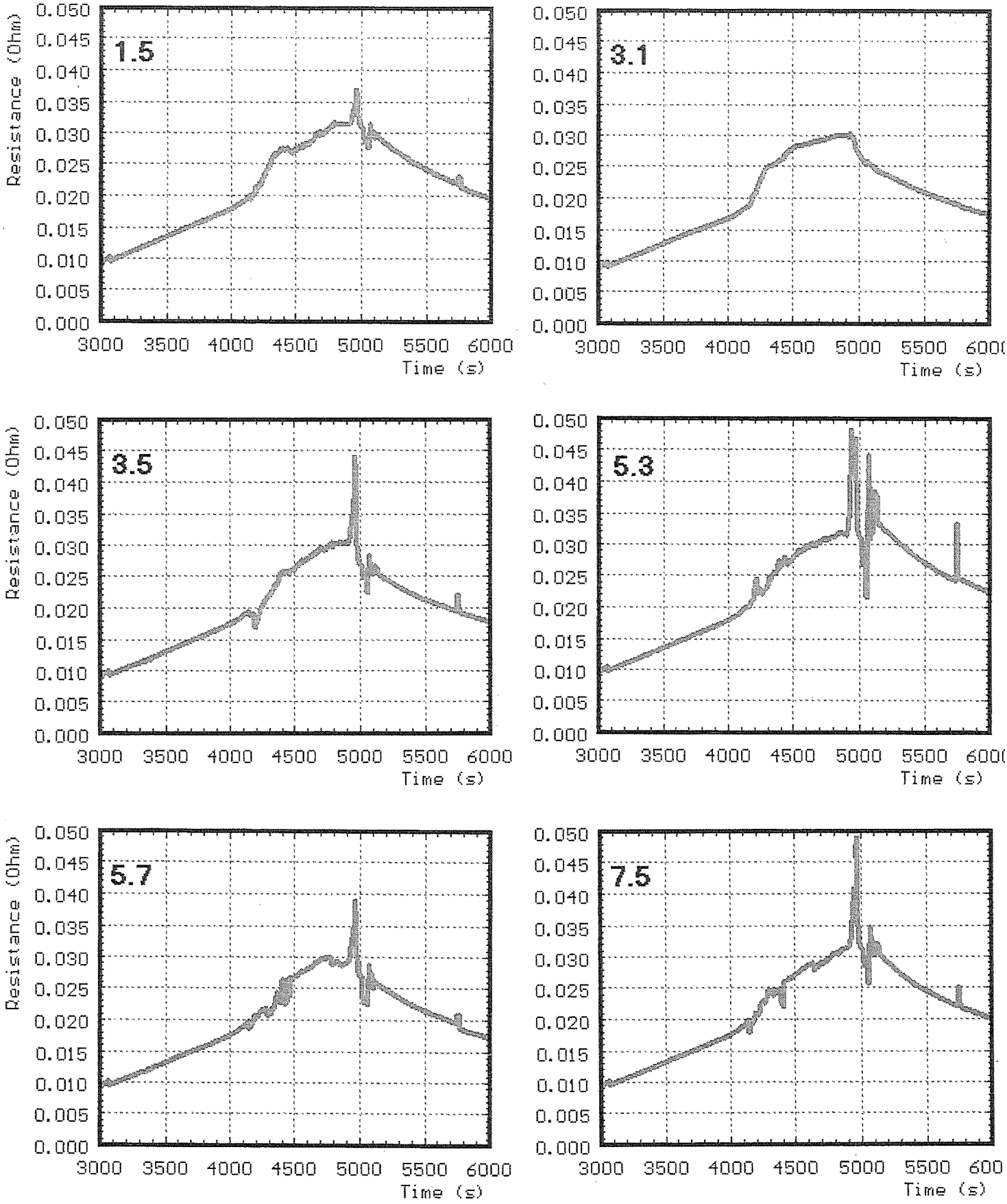

Fig. 19: CORA-29; Resistance of single rods group 1

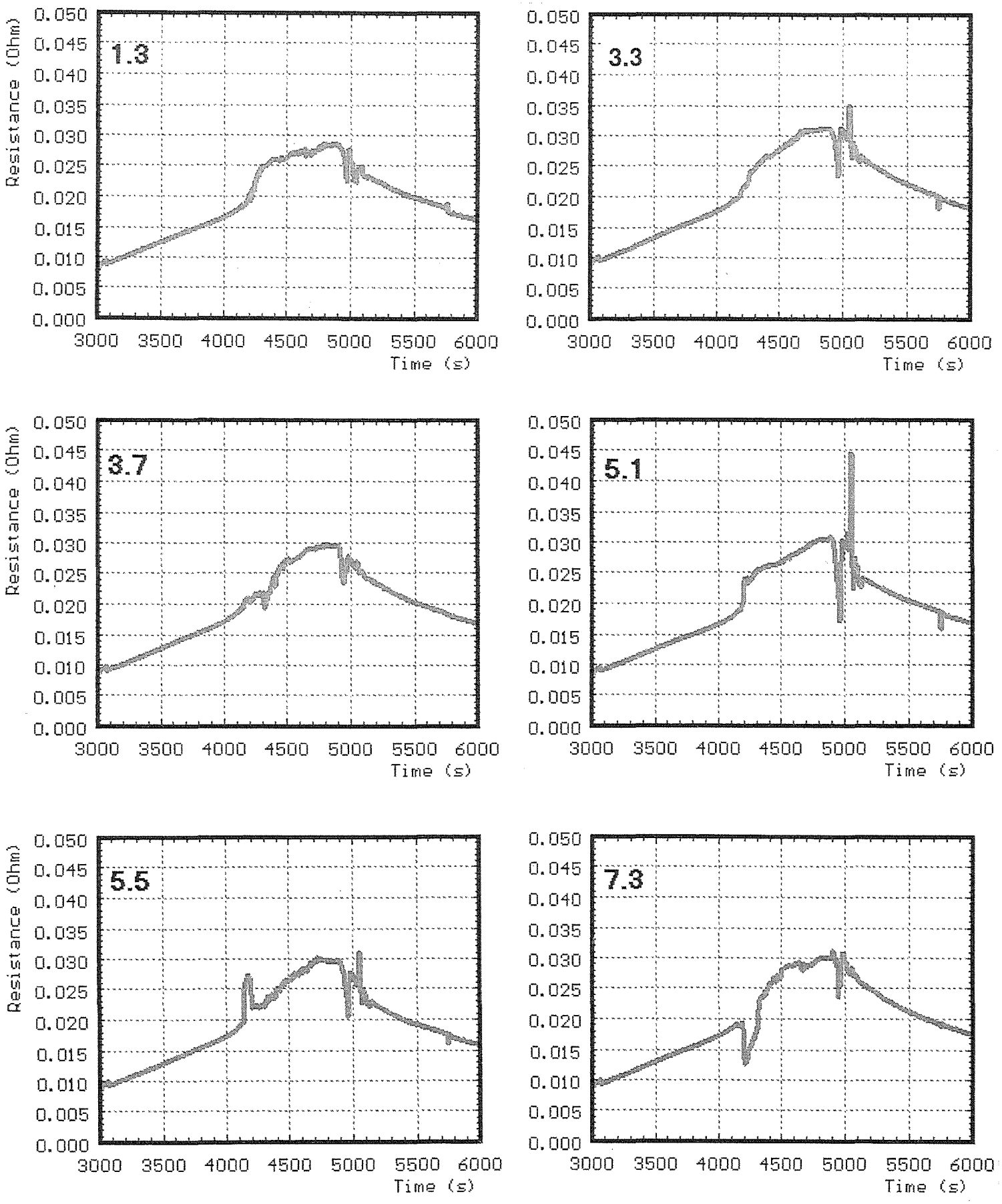

Fig. 20: CORA-29; Resistance of single rods group 2

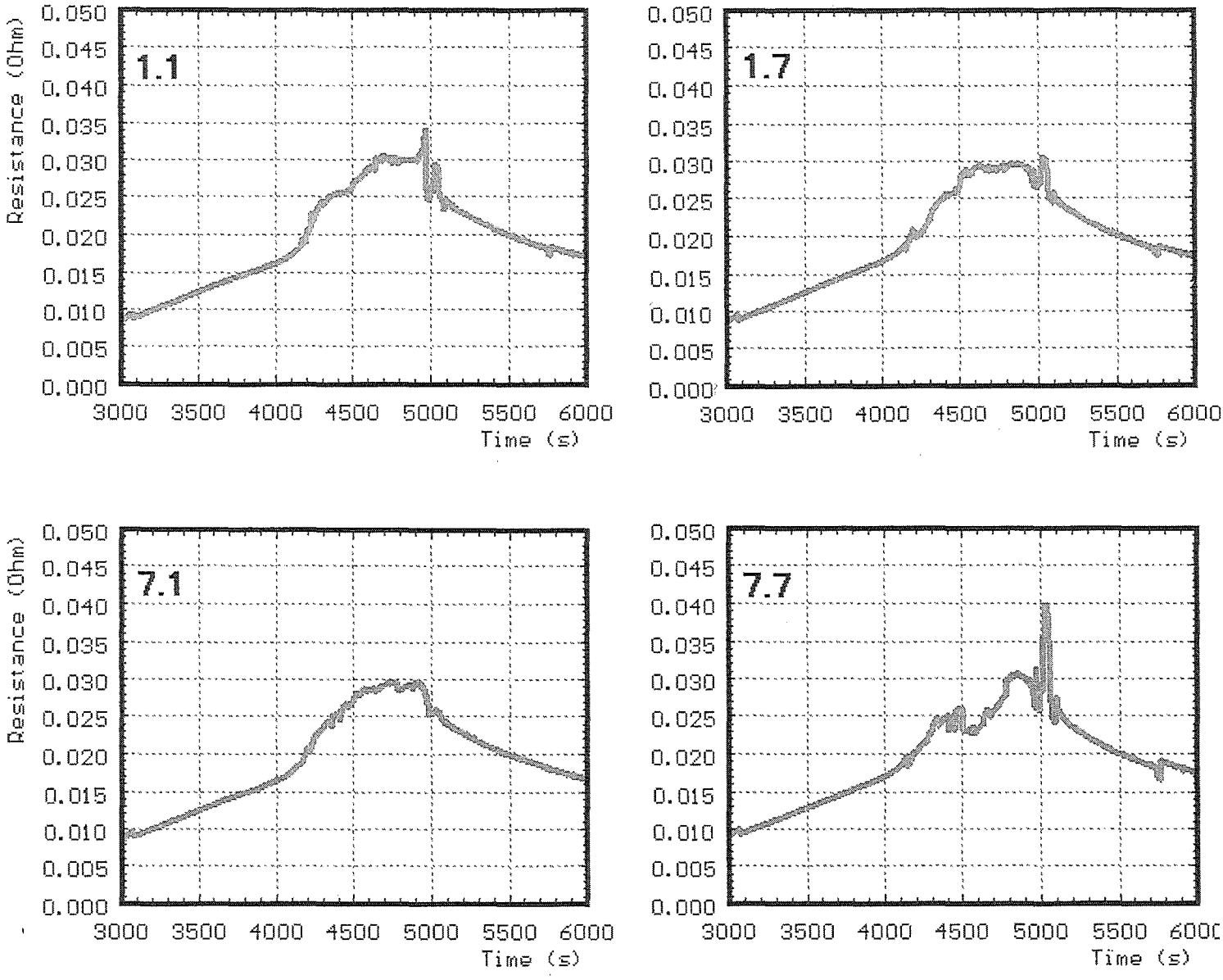

Fig. 21: CORA-29; Resistance of single rods group 3

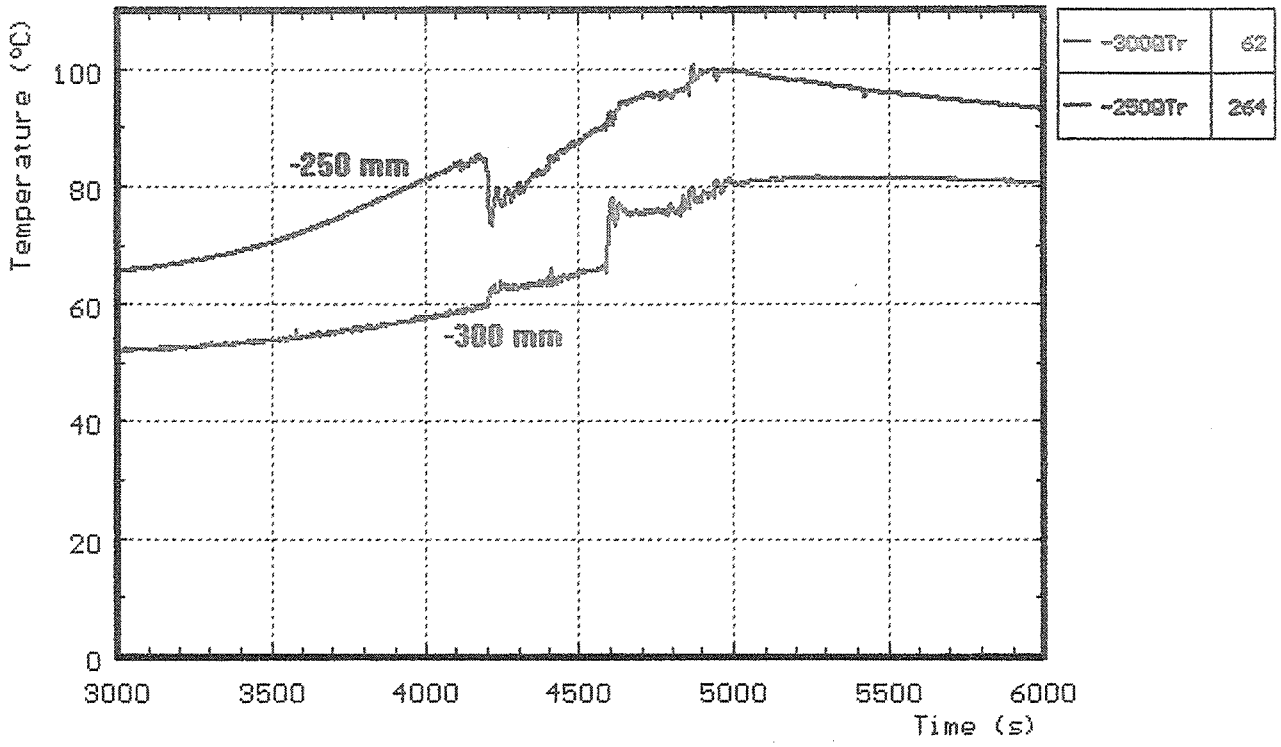

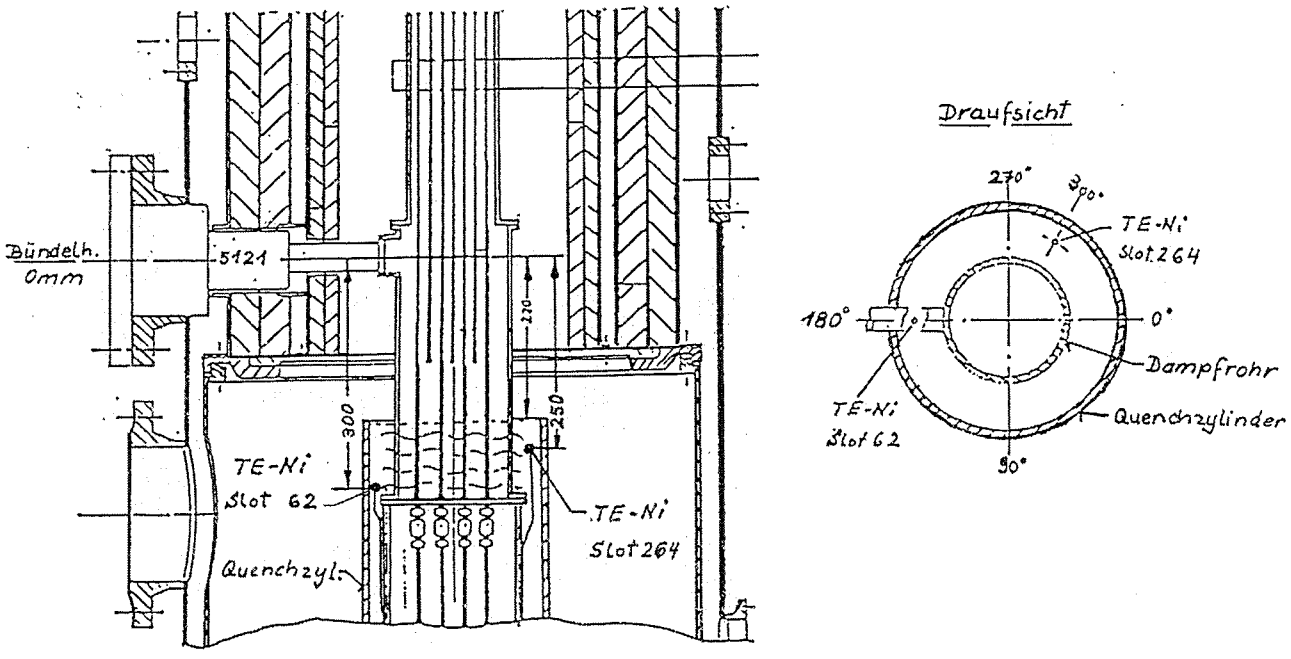

Fig. 22: CORA-29; Water temperature in the quench cylinder

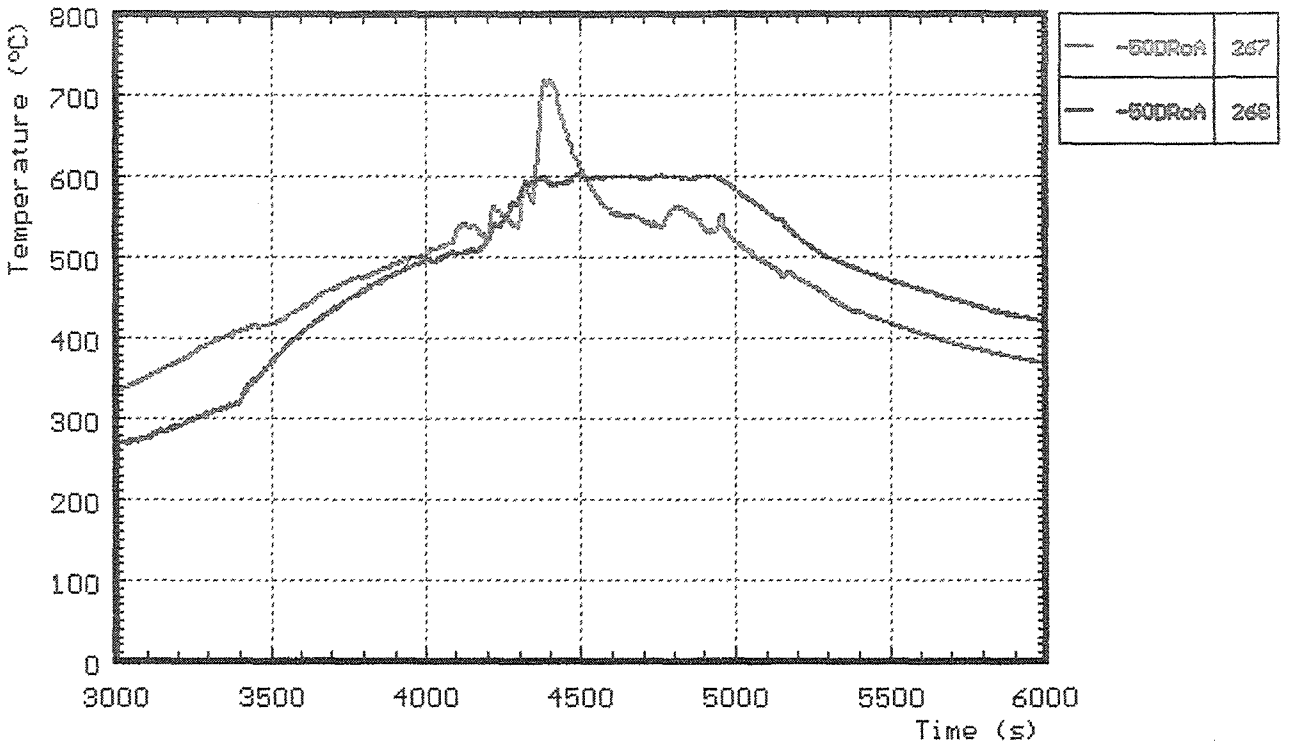

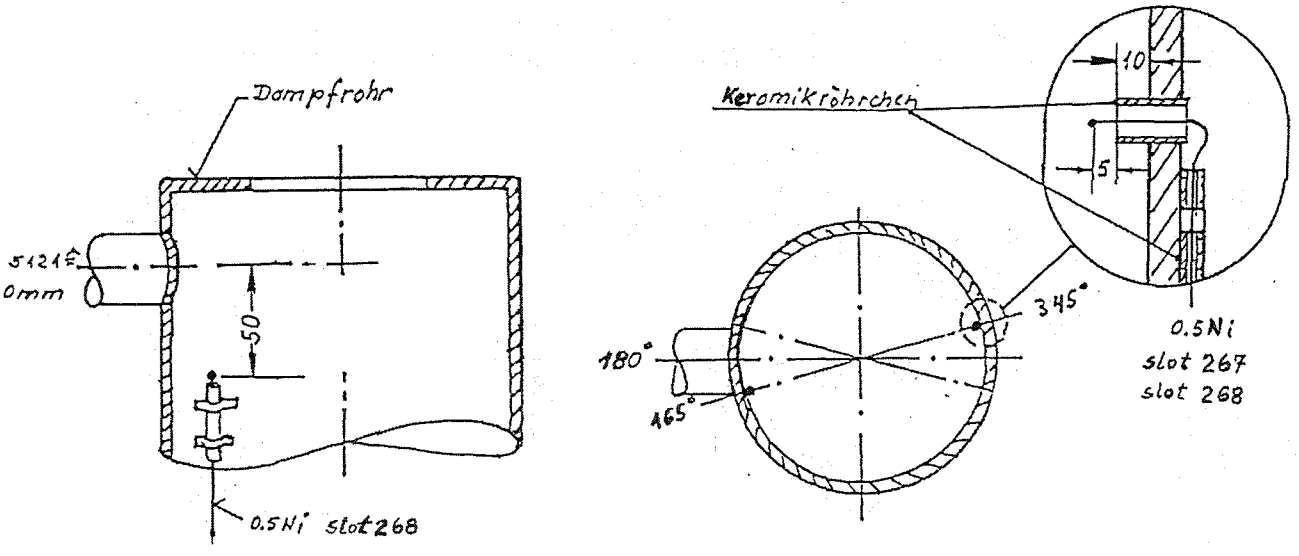

Fig. 23: CORA-29; Temperature in and on steam tube at -50mm elevation

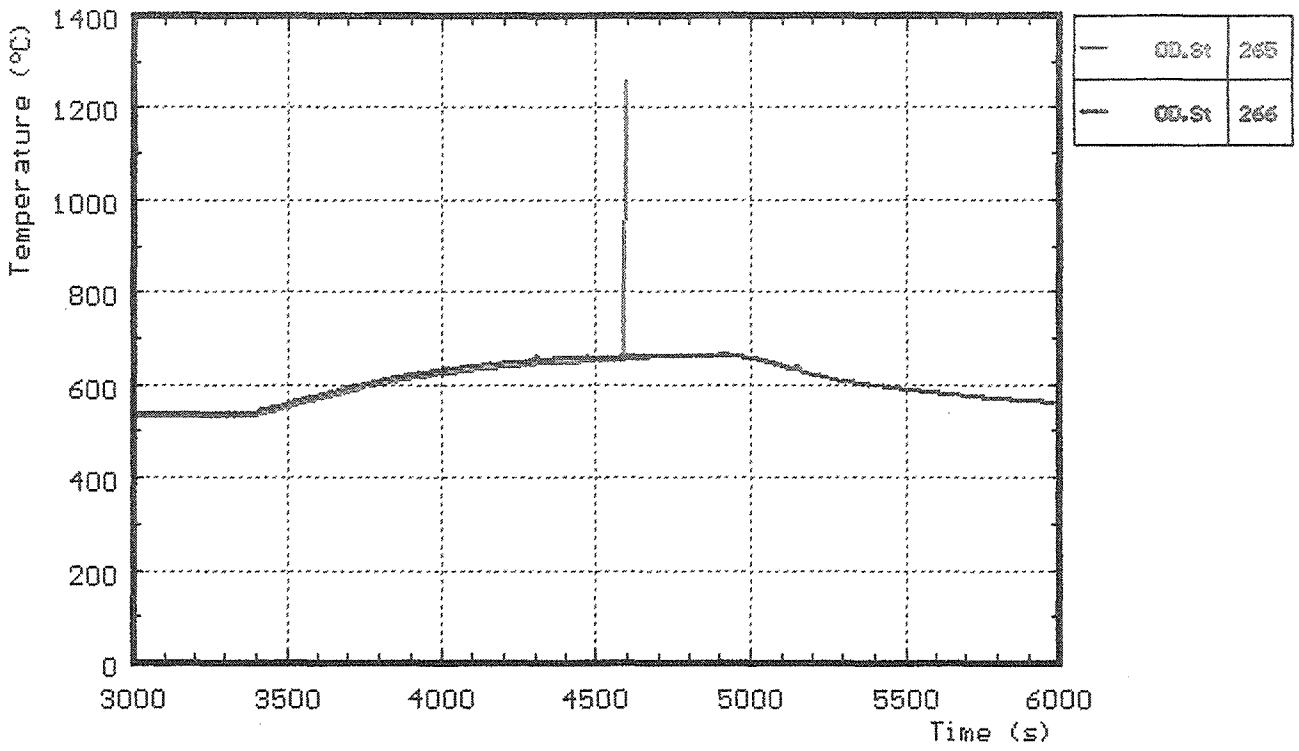

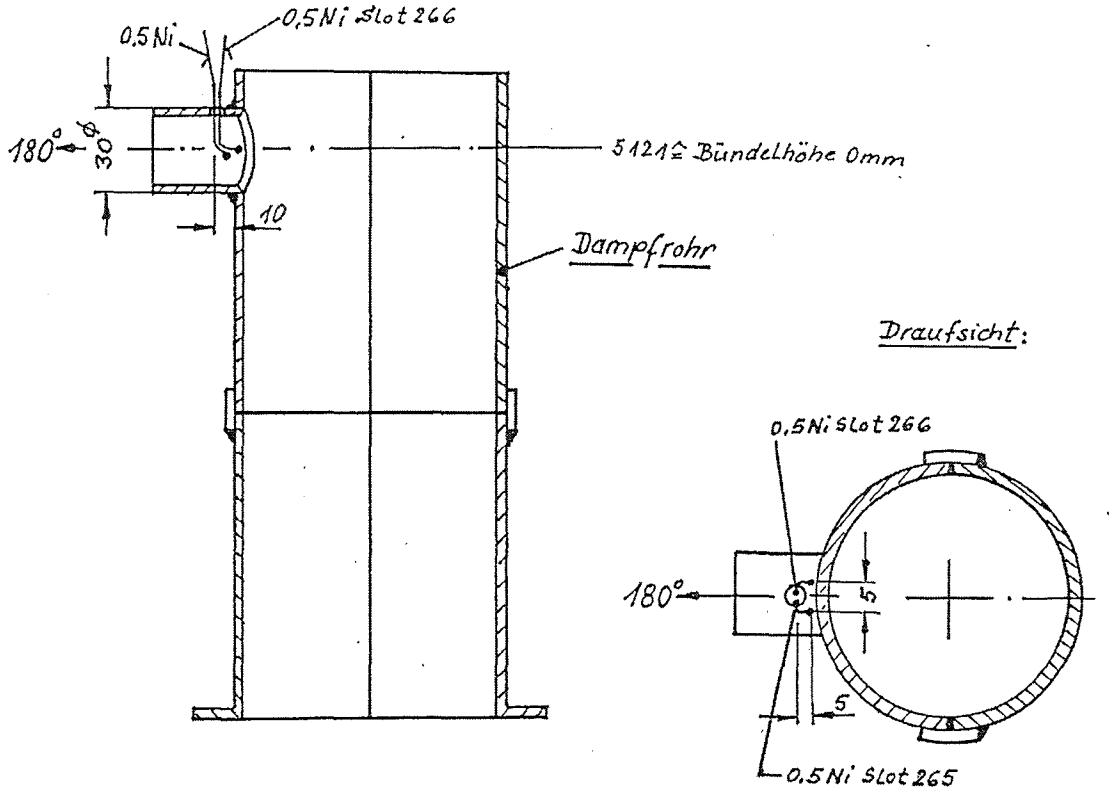

Fig. 24: CORA-29; Temperatures at steam inlet

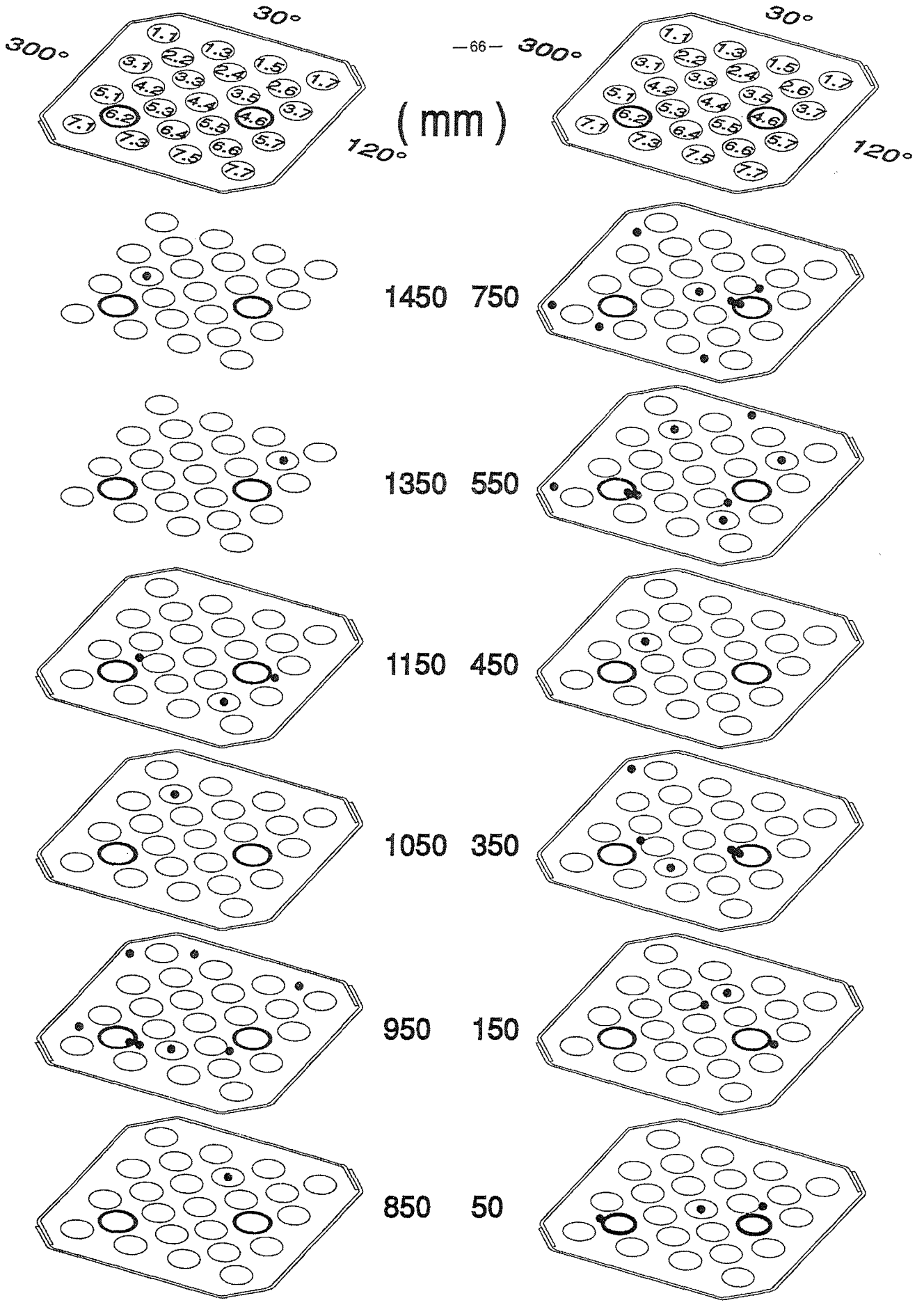

Fig. 25: Thermocouple locations within the bundle (CORA-29)

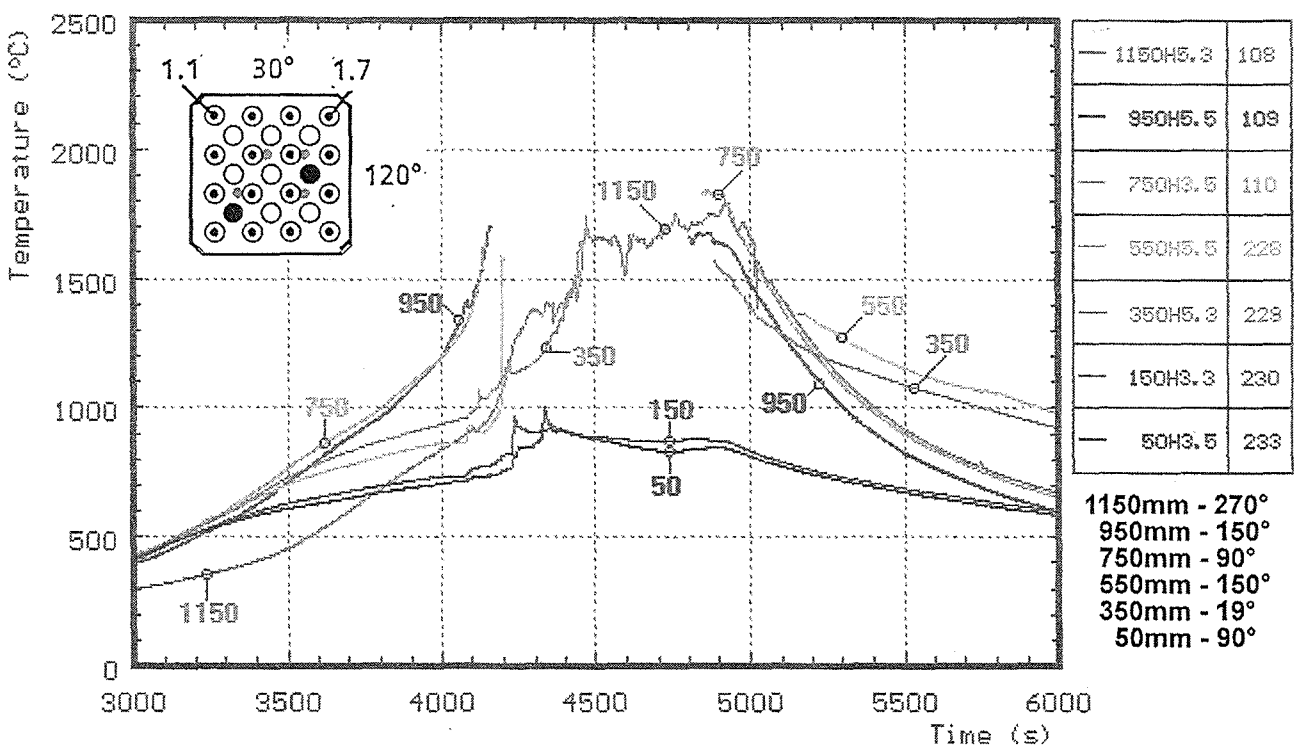

Fig. 26: CORA-29; Temperatures of heated rods

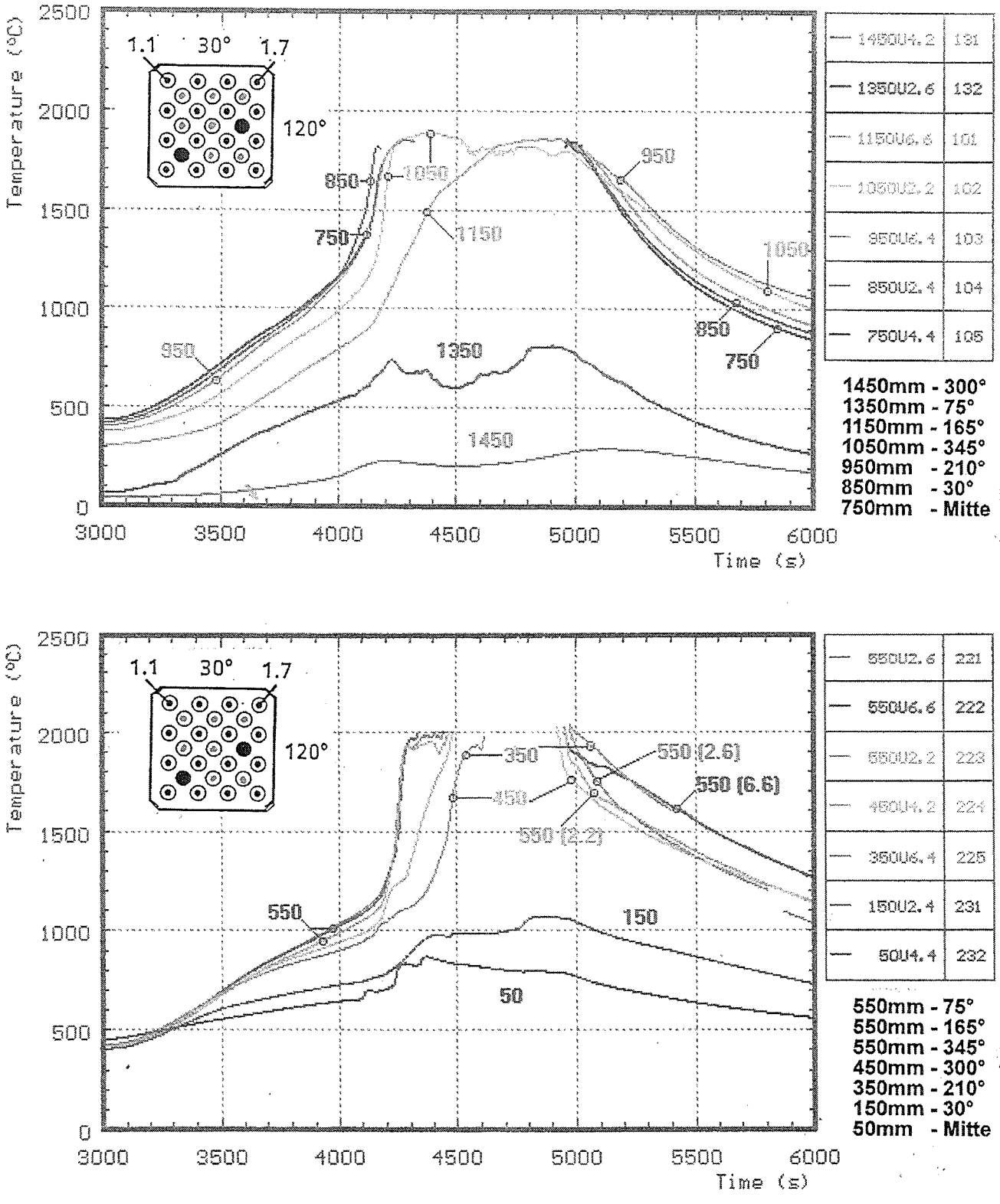

Fig. 27: CORA-29; Temperatures of unheated rods (TCs in central position)

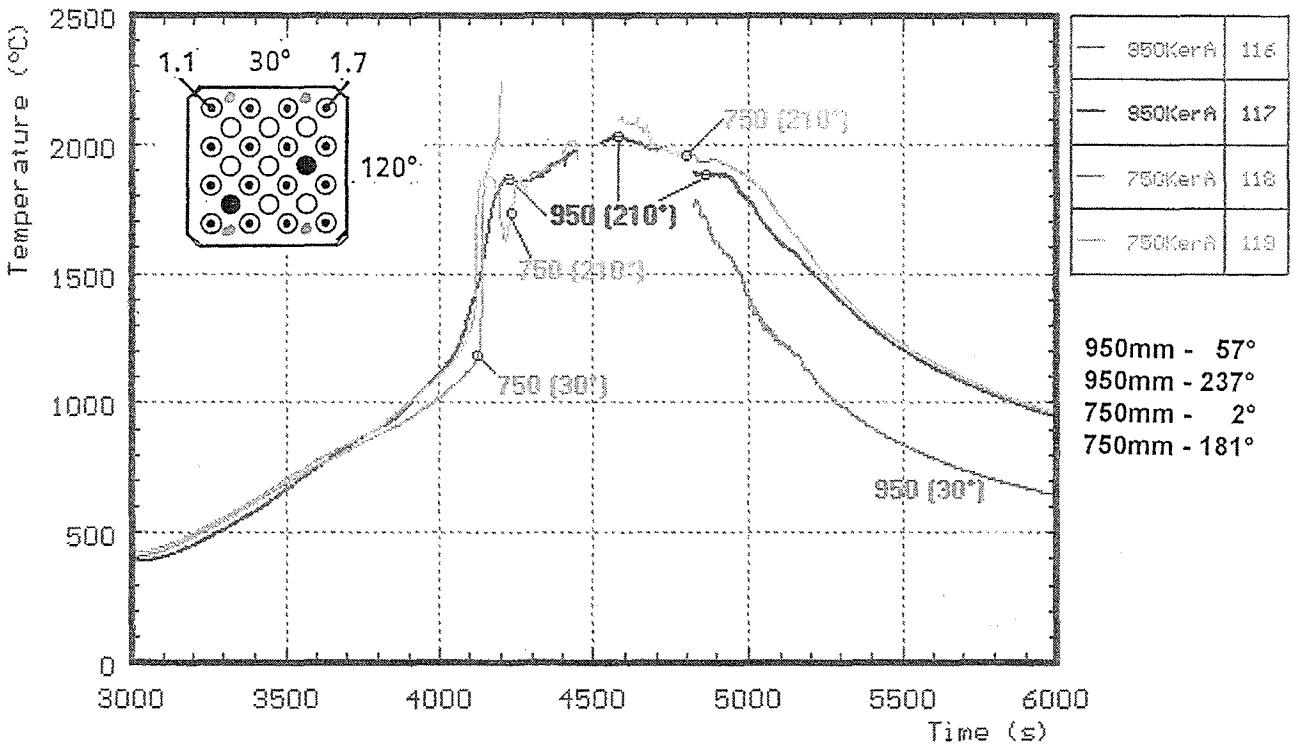

Fig. 28: CORA-29; Temperatures between bundle and shroud measured with ceramic protected TCs

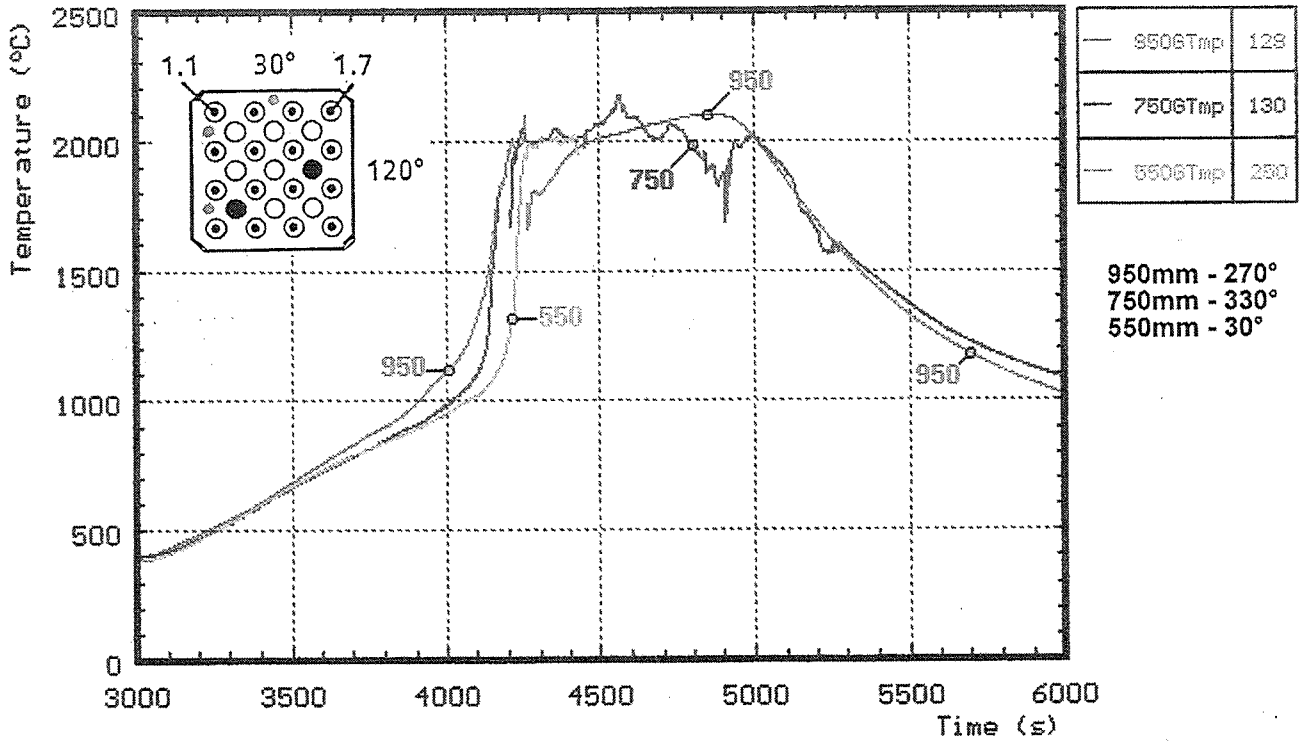

Fig. 29: CORA-29; Temperatures between bundle and shroud

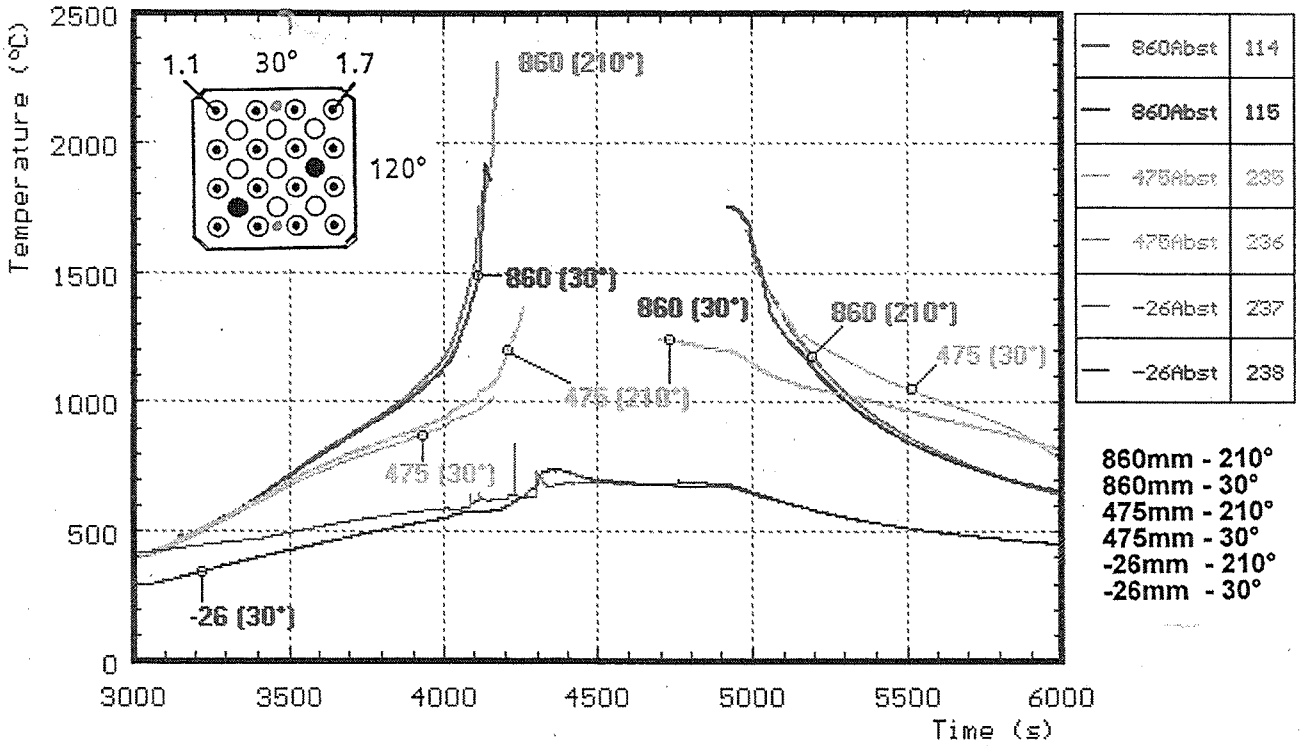

Fig. 30: CORA-29; Temperatures of the spacers

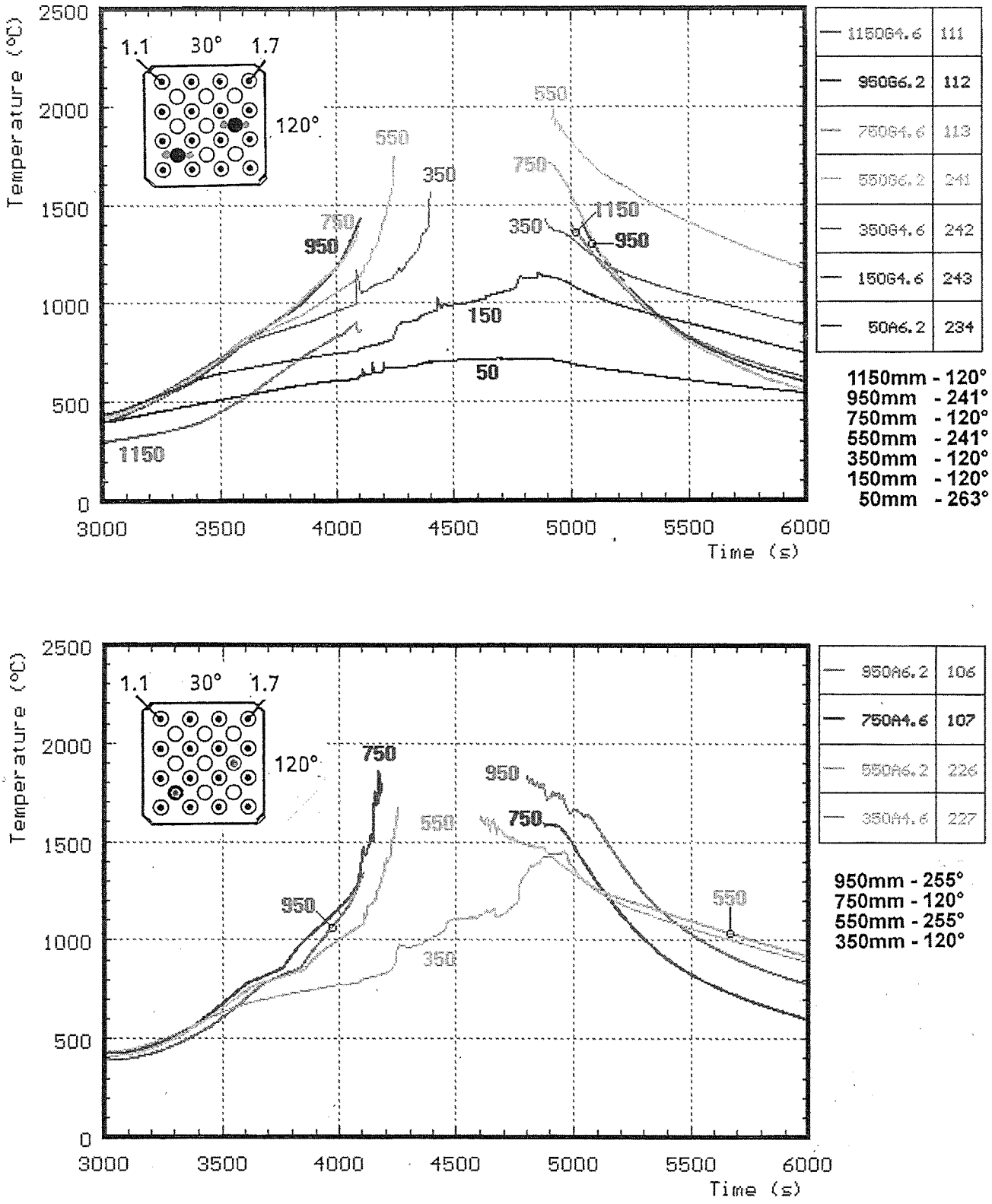

Fig. 31: CORA-29; Temperatures of the absorber rods and in the pertinent guide tubes

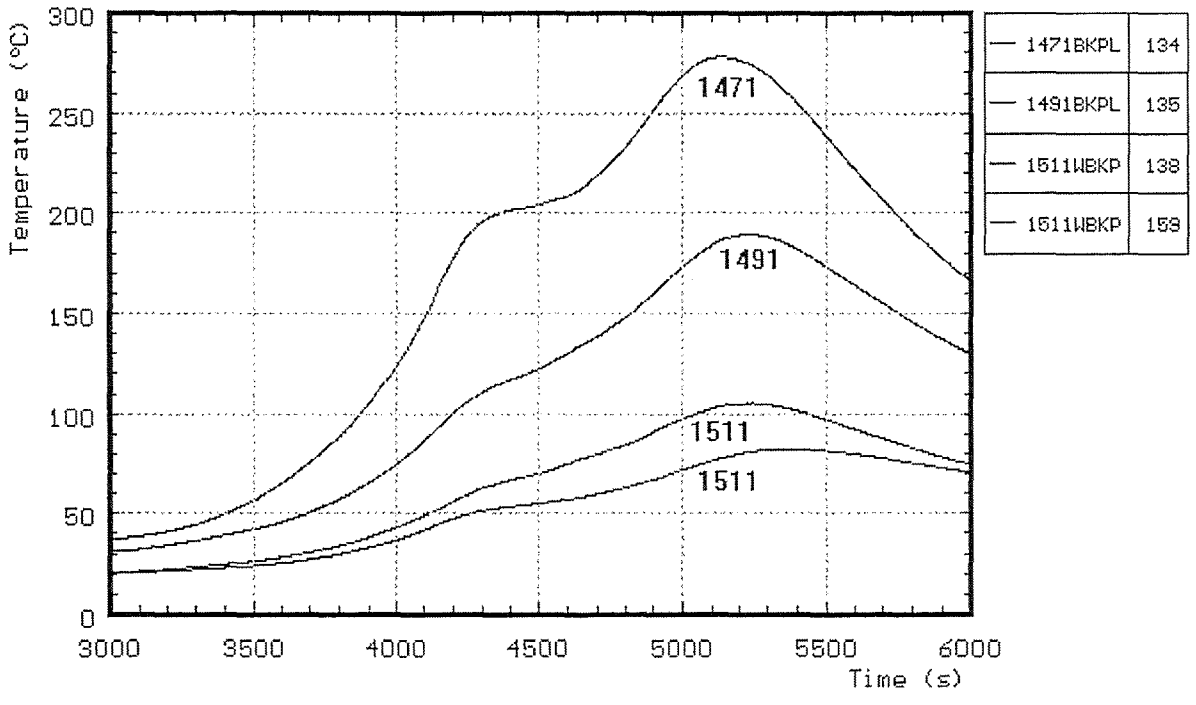

Fig. 32: CORA-29; Temperatures at the bundle head plate

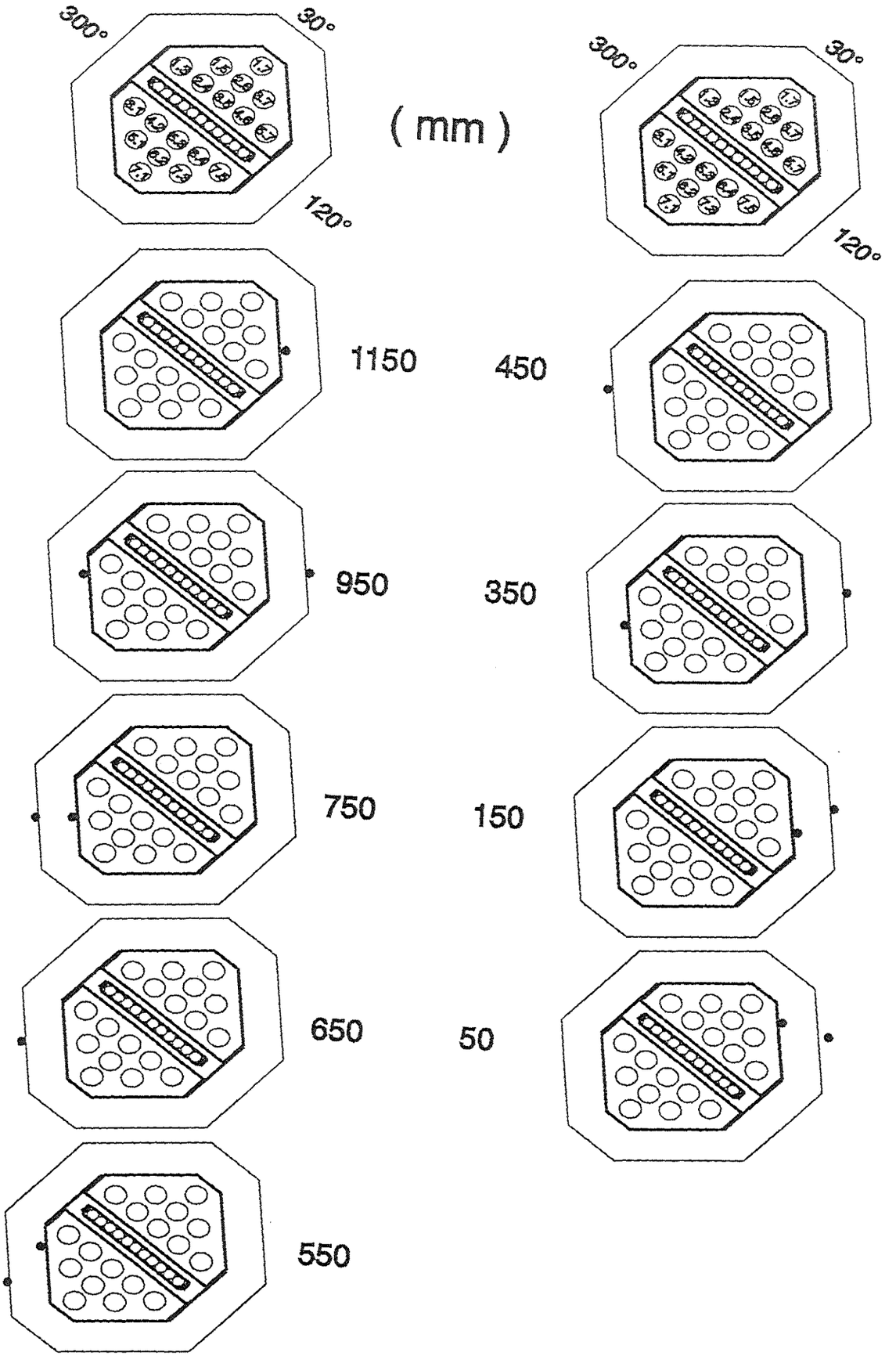

Fig. 33: Location of the thermocouples at shroud and shroud insulation (CORA-29)

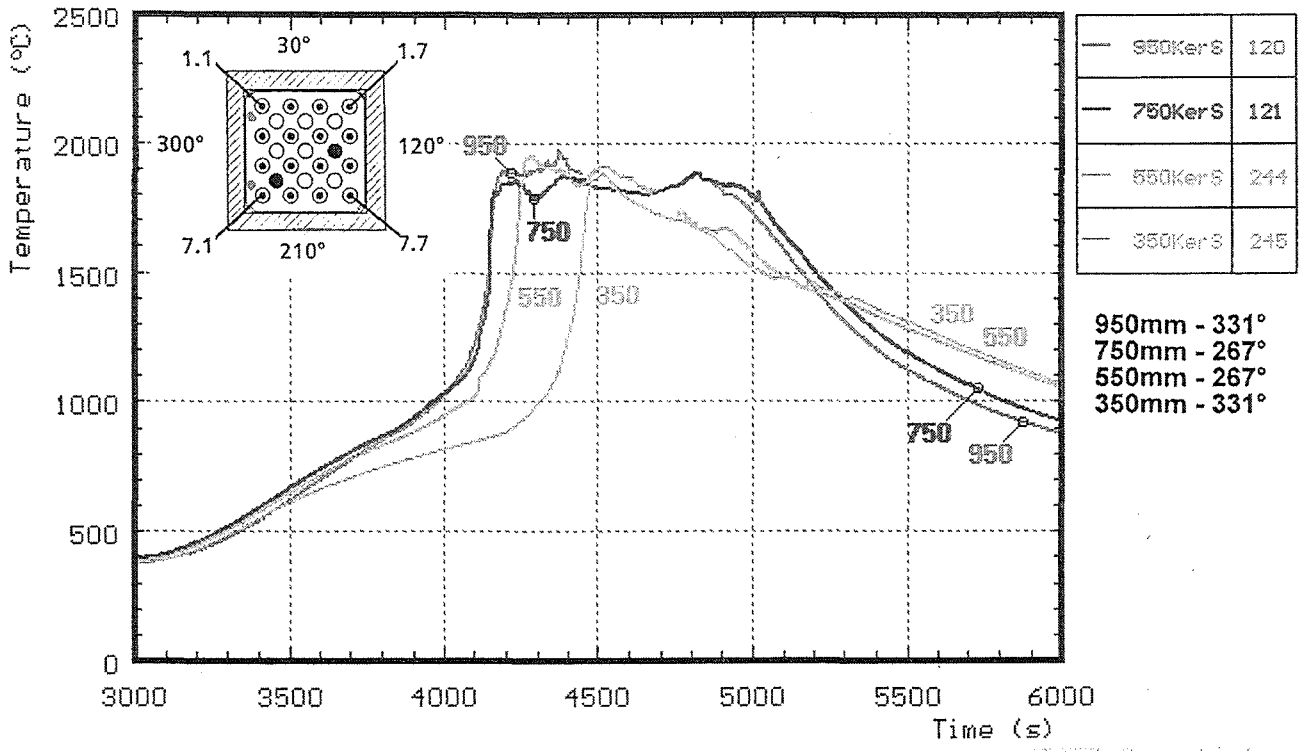

Fig. 34: CORA-29; Temperatures of inner side of shroud measured with ceramic protected TCs

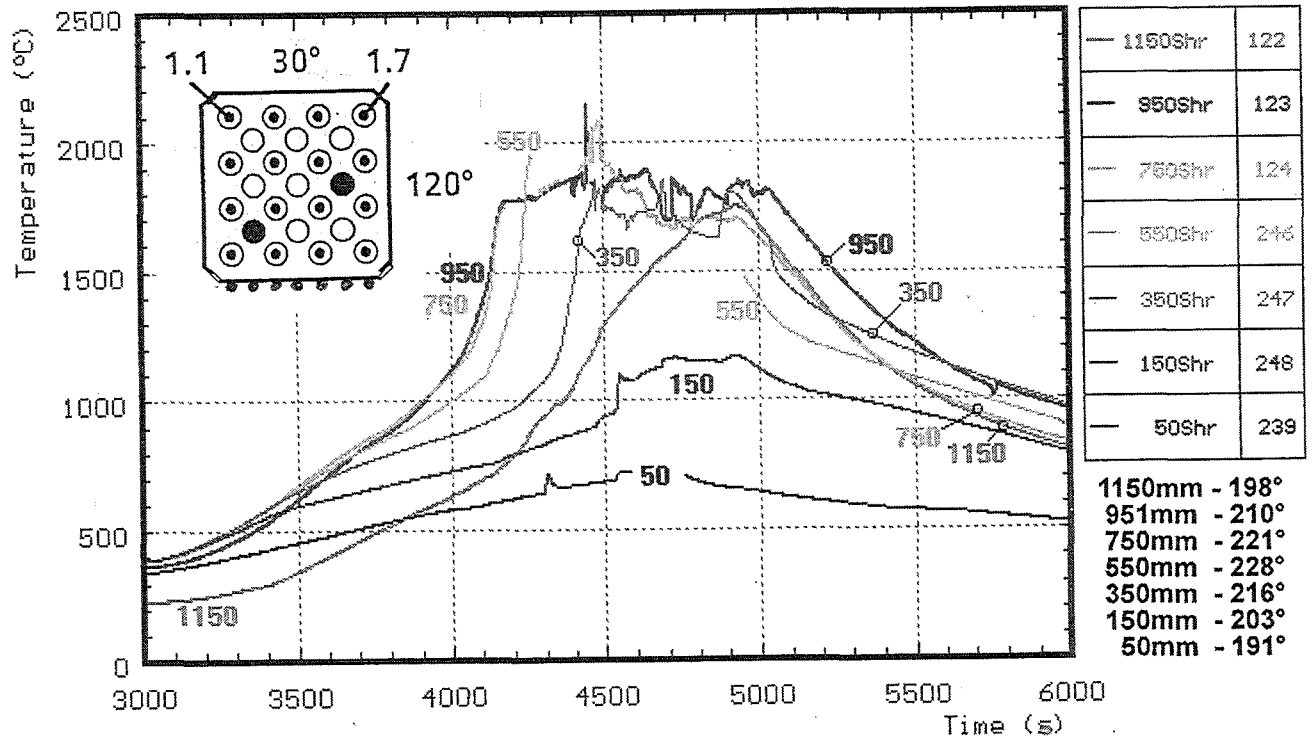

Fig. 35: CORA-29; Temperatures of outer side of shroud

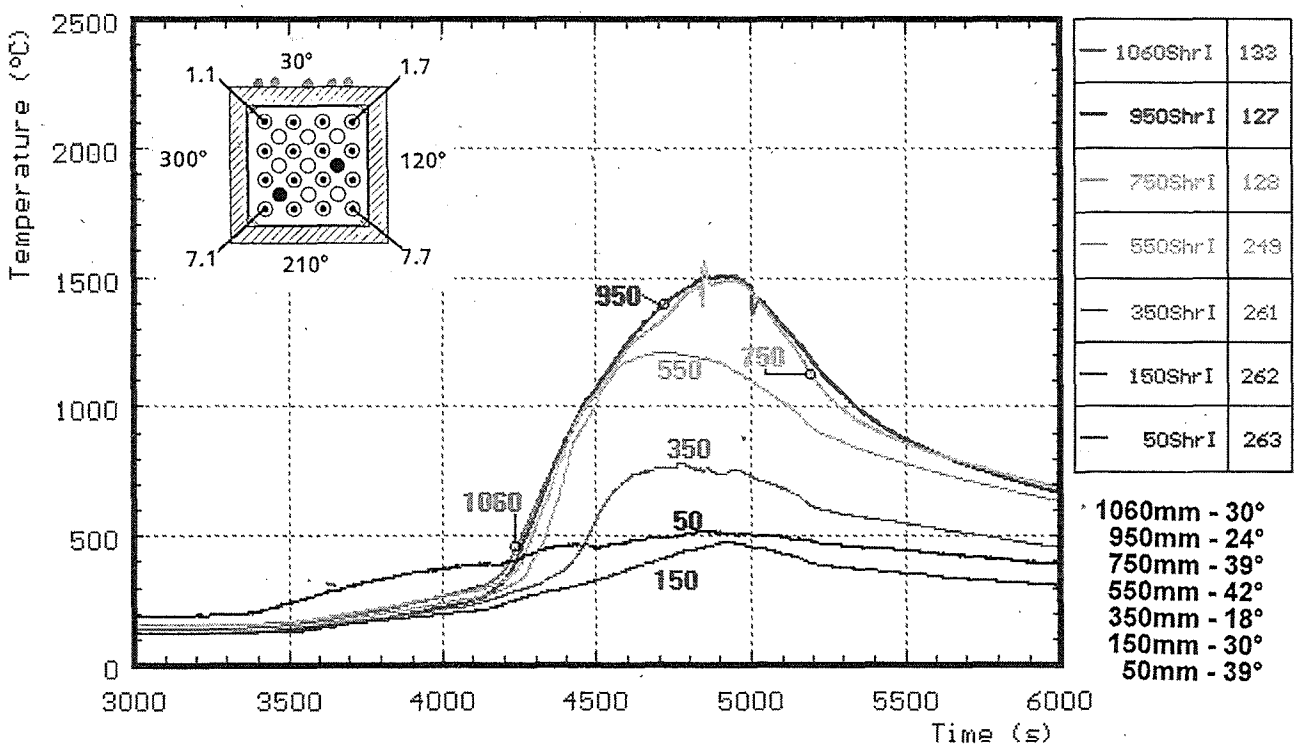

Fig. 36: CORA-29; Temperatures of the shroud insulation

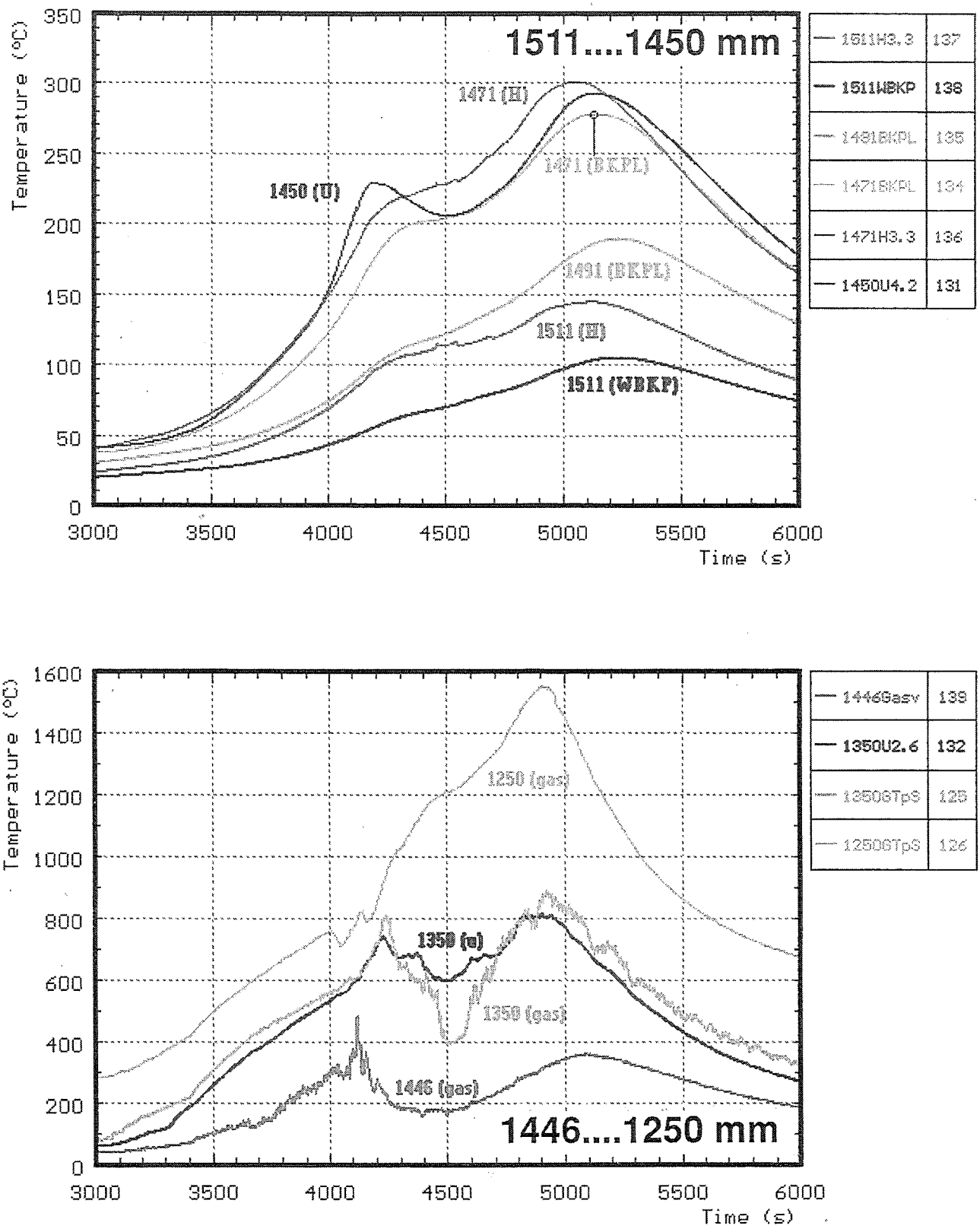

gas : gas temperature Bkpl : bundle heat plate
U : unheated rods WBKP : water temperature bundle head plate
H : heated rods

Fig. 37: CORA-29; Temperatures at elevations given (1511-1250 mm)

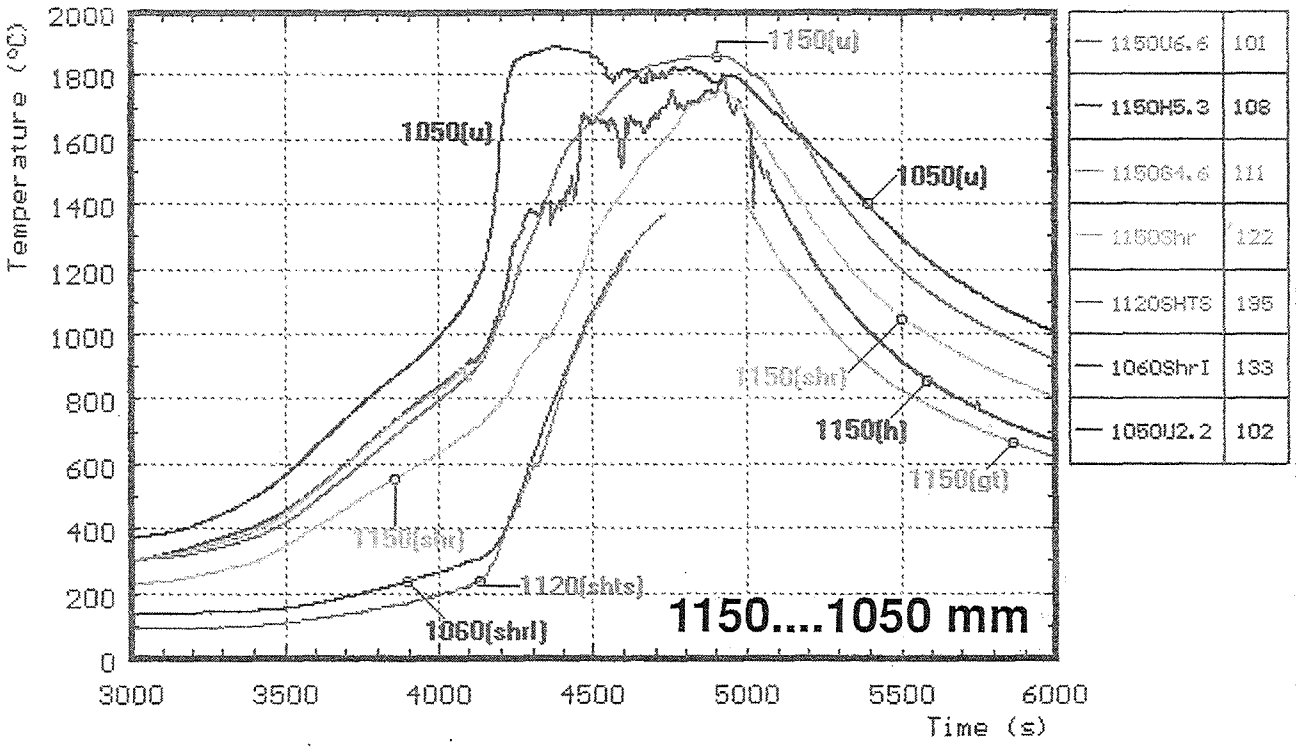

h	: heated rods	Shr	: on shroud
u	: unheated rods	SHTS	: between shroud and hts
gt	: guide tube	ShrI	: shroud insulation

Fig. 38: CORA-29; Temperatures at elevations given (1150 - 1050 mm)

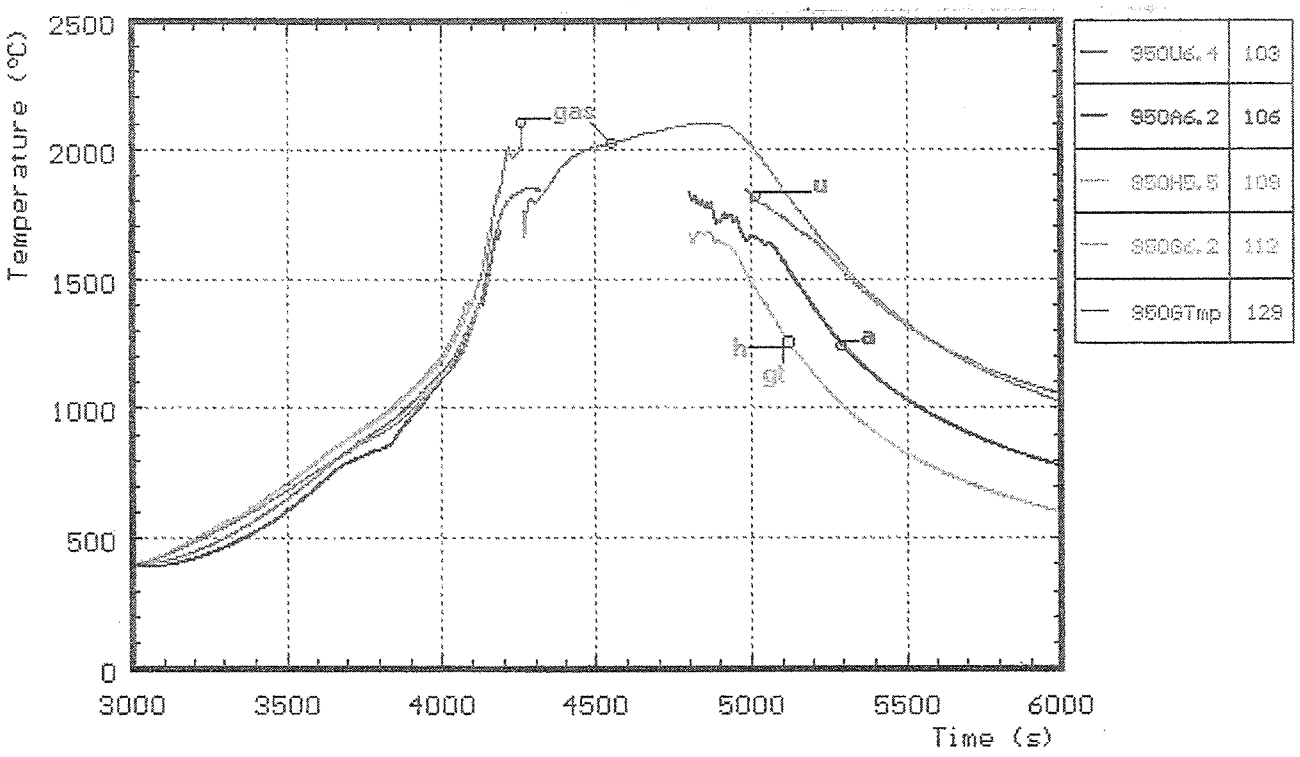

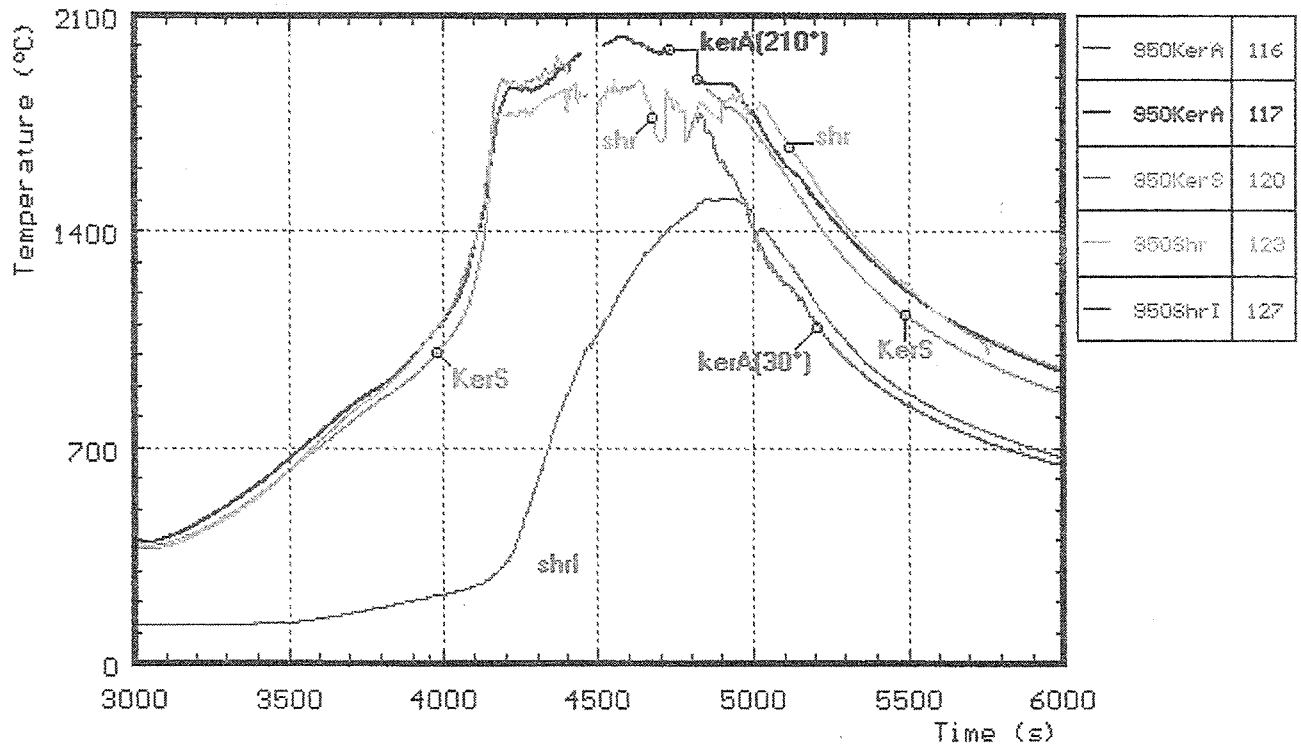

gas : gas temperature
a : in absorber
gt : guide tube
u : unheated rods
h : heated rods

KerA : gas temperature
KerS : inner side of shroud
shr : outer side of shroud
shrI : on shroud insulation

Fig. 39: CORA-29; Temperatures at elevations given (950 mm)

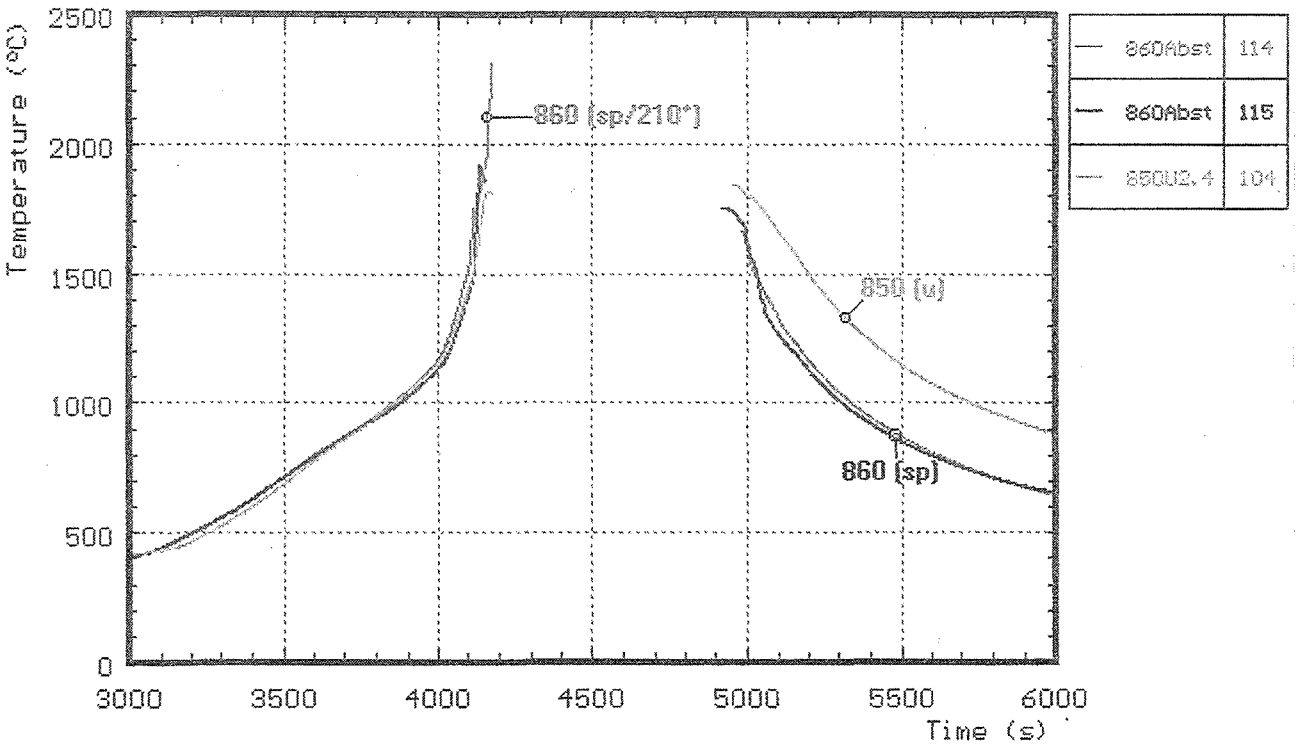

u : unheated rods sp : spacer

Fig. 40: CORA-29; Temperatures at elevations given (860 - 850 mm)

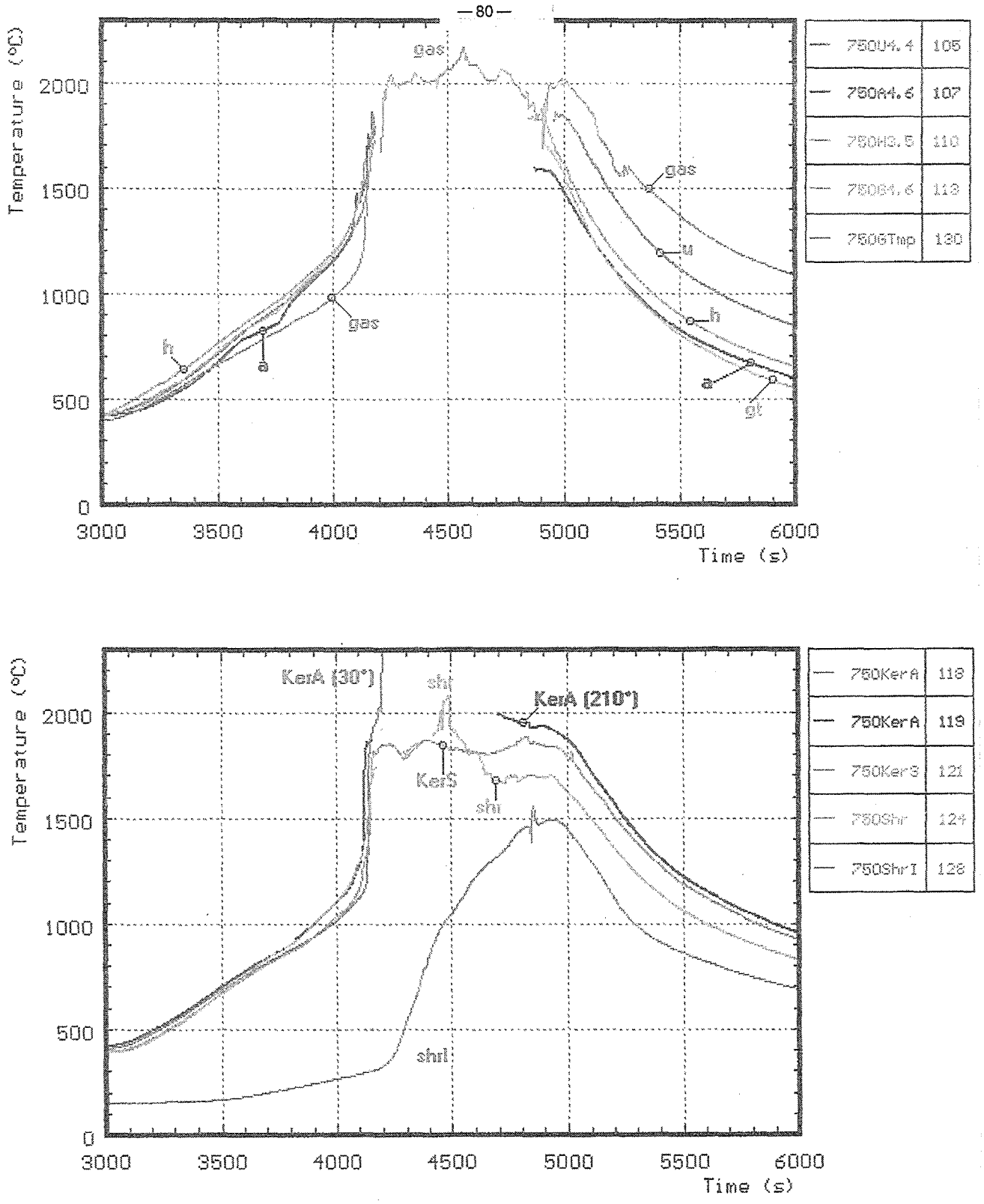

Shr	: on shroud	KerS	:inner side of shroud
ShrI	: shroud insulation	gt	: guide tube
a	: in absorber	h	: heated rods
u	: unheated rods	KerA	:gas temperature
gas	: gas temperature		

Fig. 41: CORA-29; Temperatures at elevations given (750 mm)

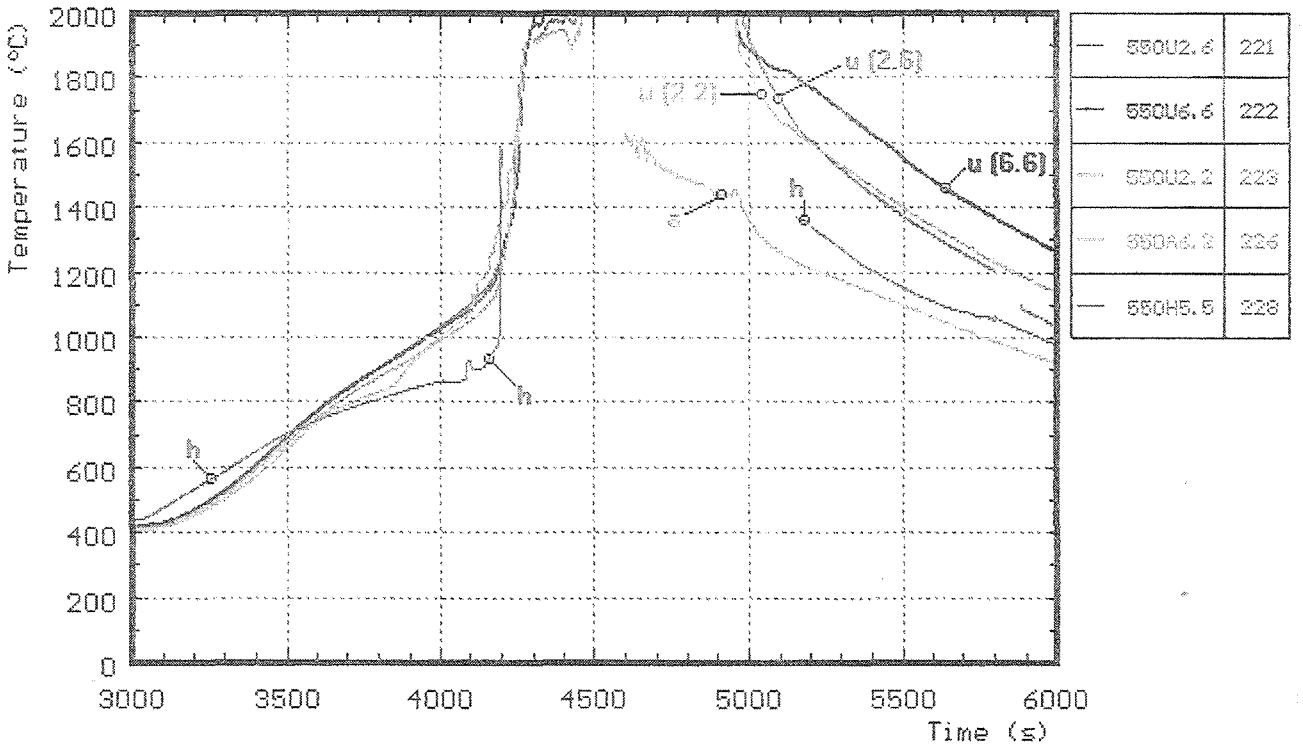

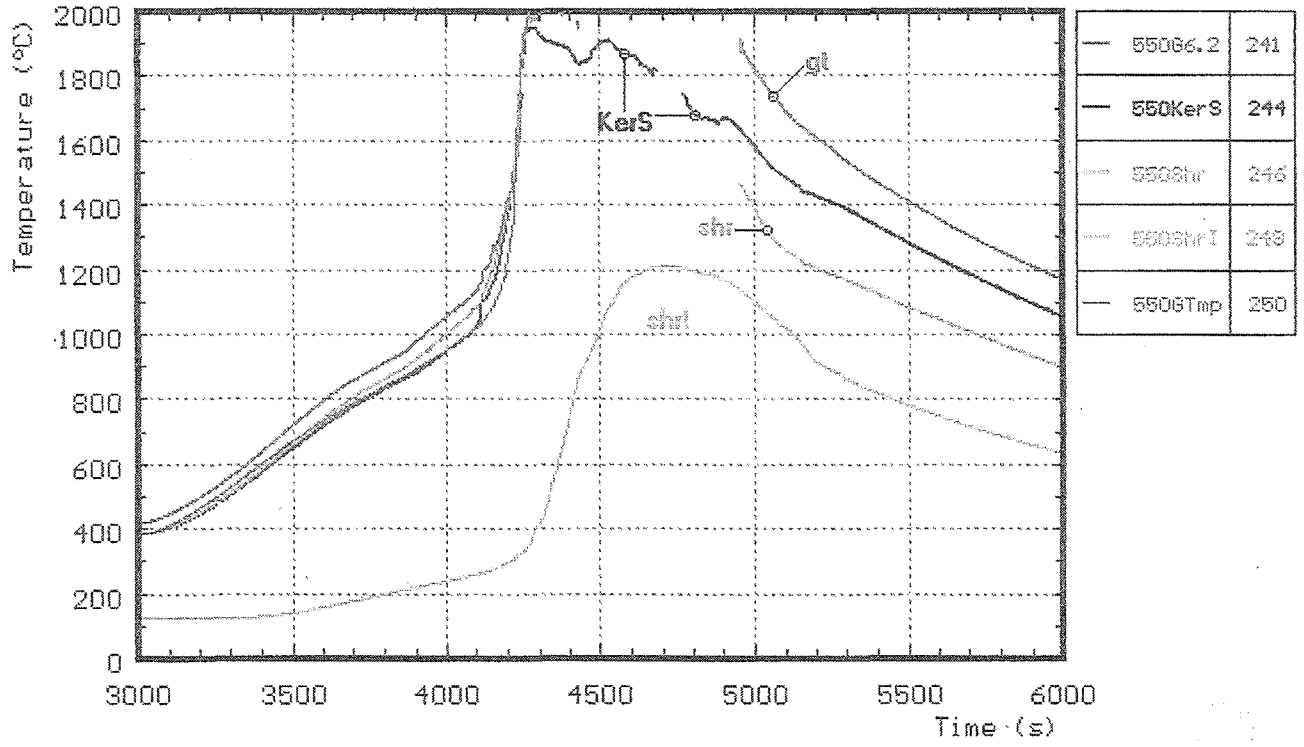

h	: heated rods	Shr	: on shroud
u	: unheated rods	ShrI	: shroud insulation
a	: in absorber	KerS	:inner side of shroud
gt	: guide tube		

Fig. 42: CORA-29; Temperatures at elevation given (550 mm)

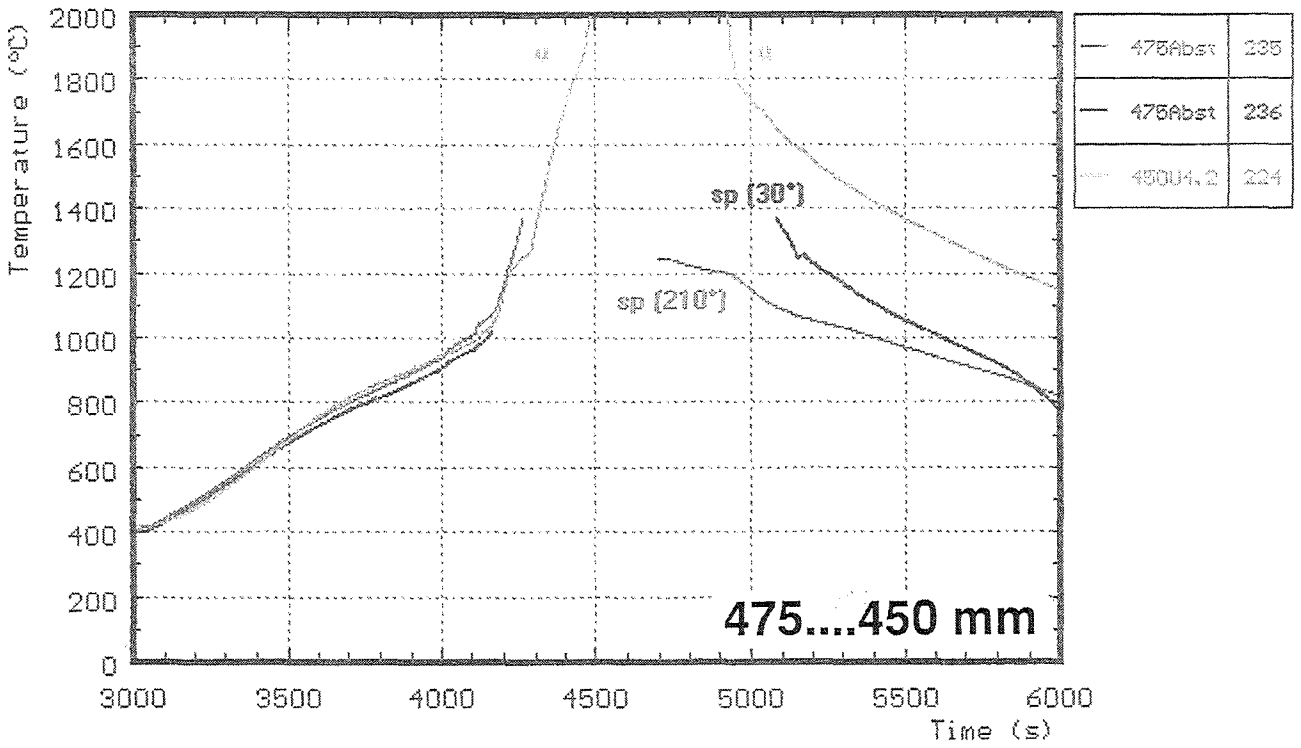

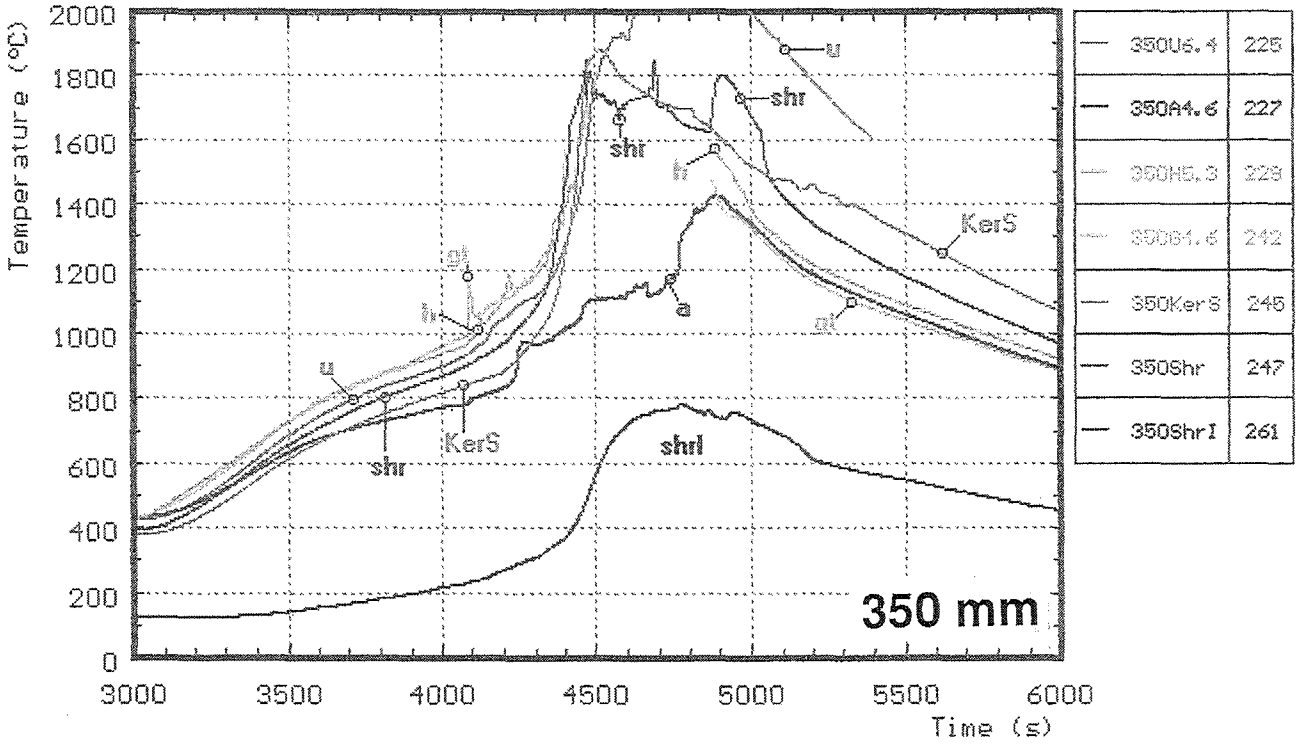

h	: heated rods	shr	: on shroud
u	: unheated rods	shrI	: shroud insulation
a	: in absorber	KerS	:inner side of shroud
gt	: guide tube	sp	: spacer

Fig. 43: CORA-29; Temperatures at elevation given (475 - 350 mm)

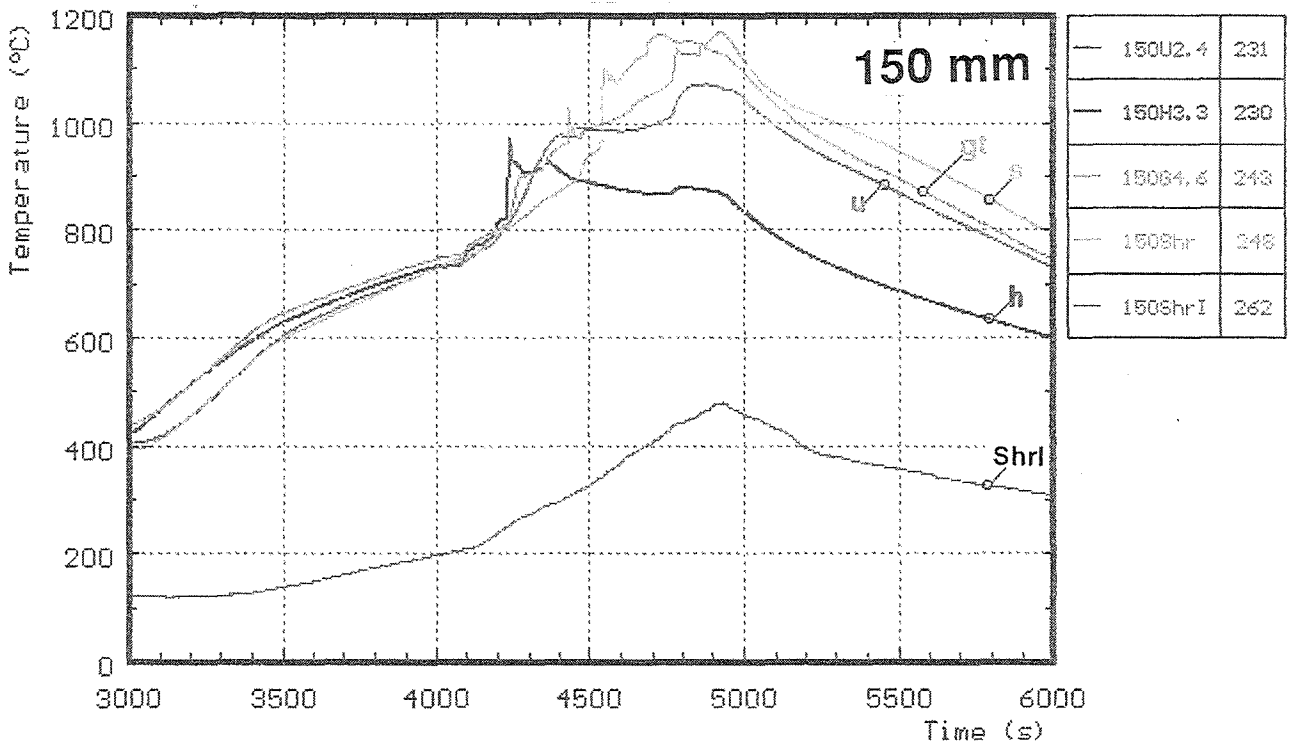

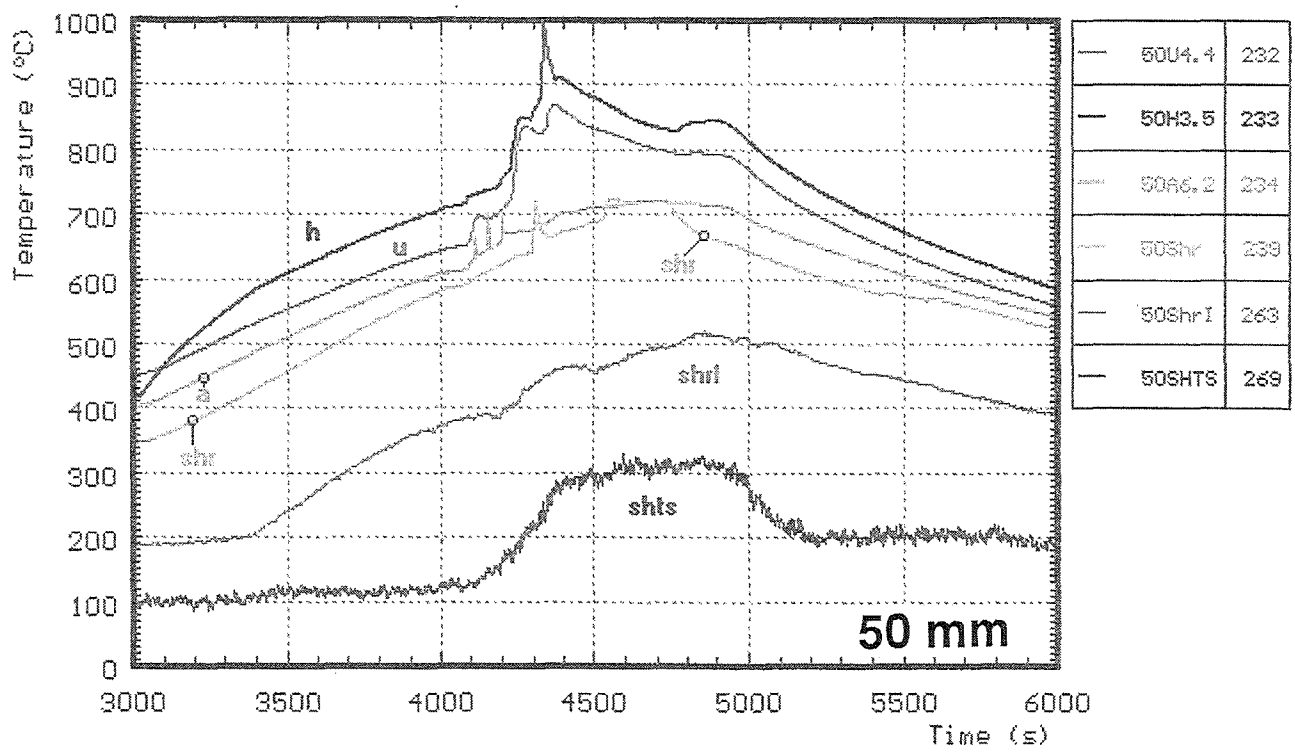

h : heated rods
u : unheated rods
a : in absorber
gt : guide tube

shr : on shroud
ShrI : shroud insulation
SHTS : between shroud and hts

Fig. 44: CORA-29; Temperatures at elevation given (150 - 50 mm)

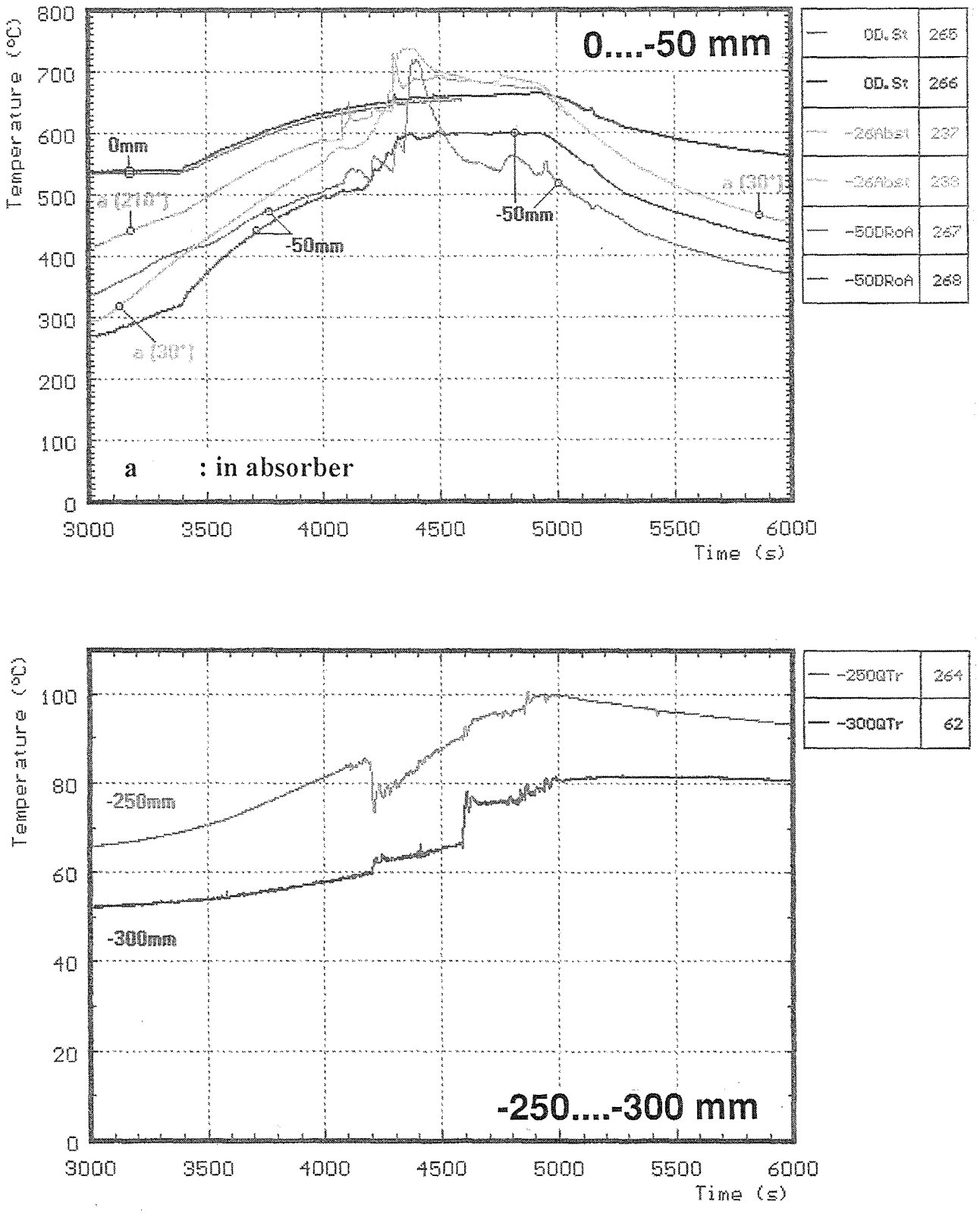

Fig. 45: CORA-29; Temperatures at elevations given (0 - -300 mm)

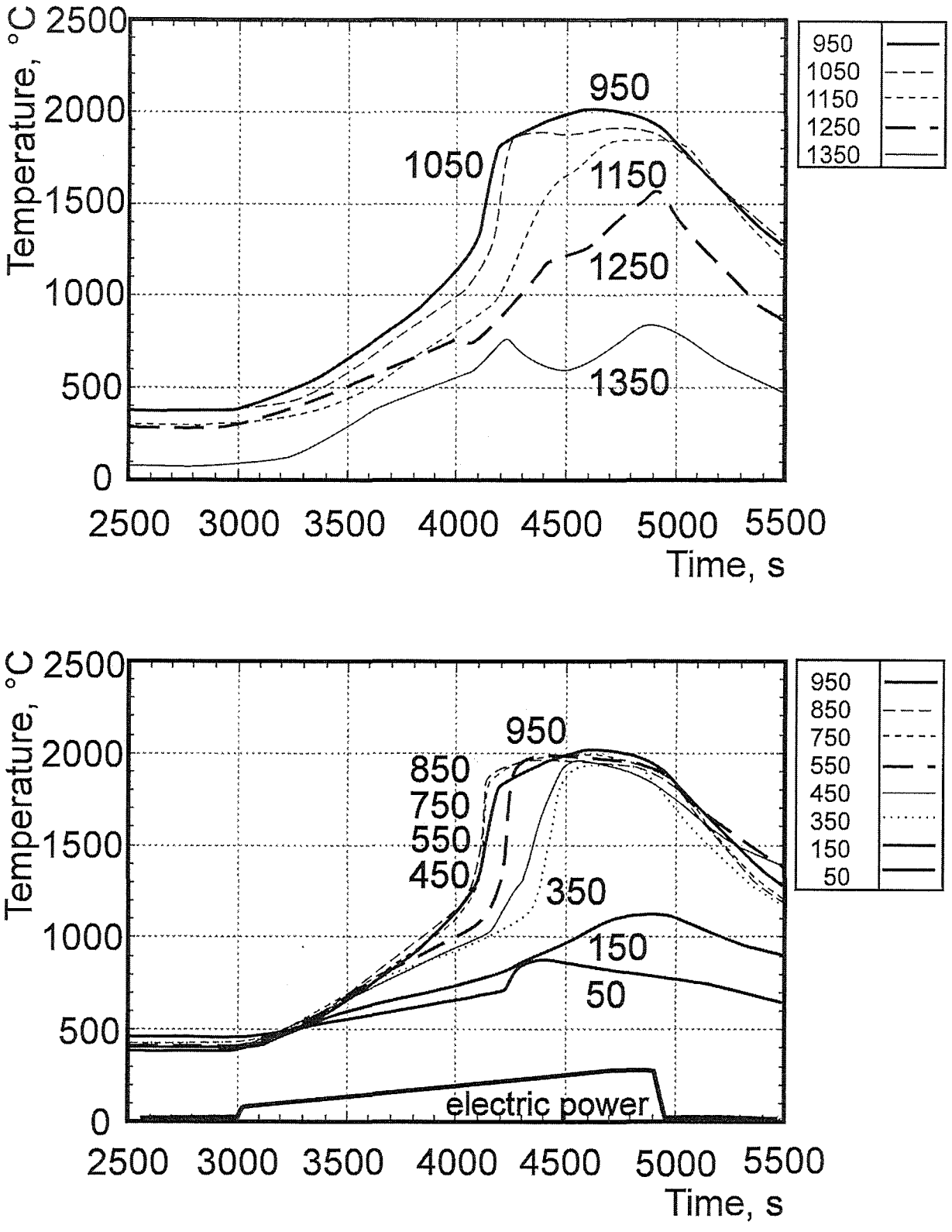

Fig. 46: CORA-29; Best-estimate bundle temperatures at different elevations

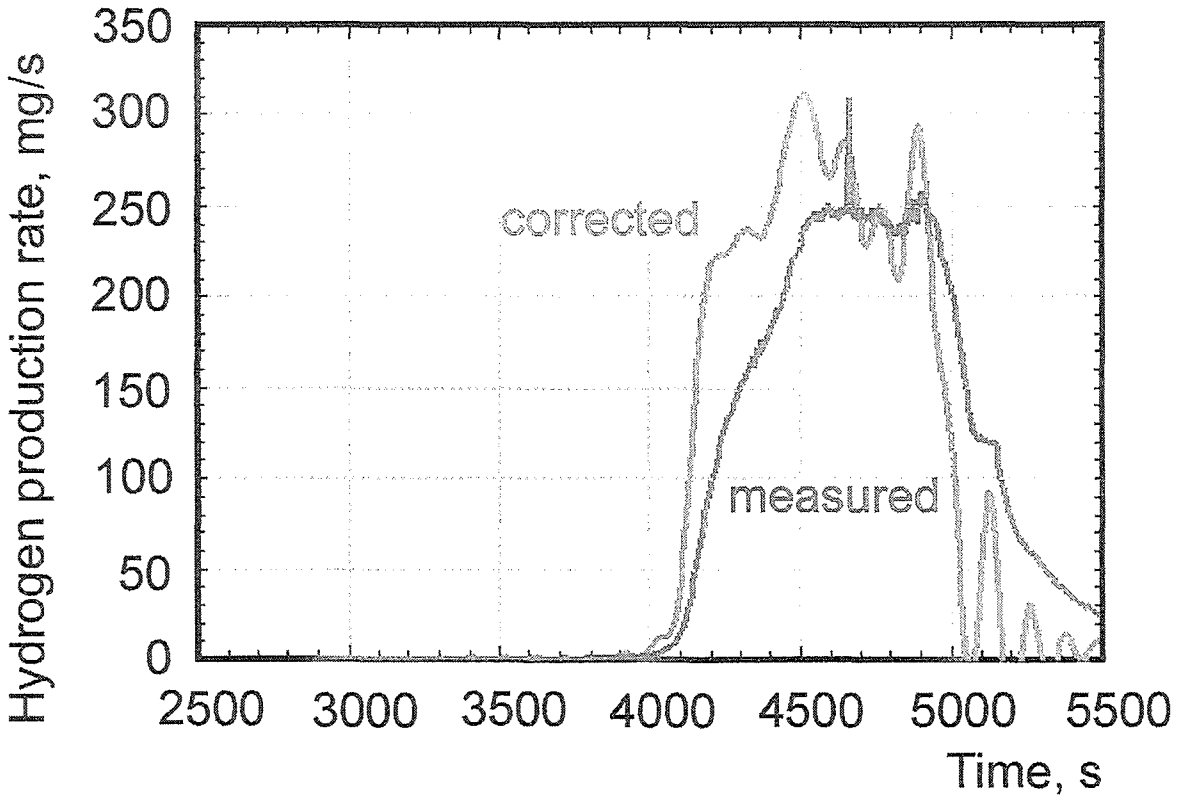

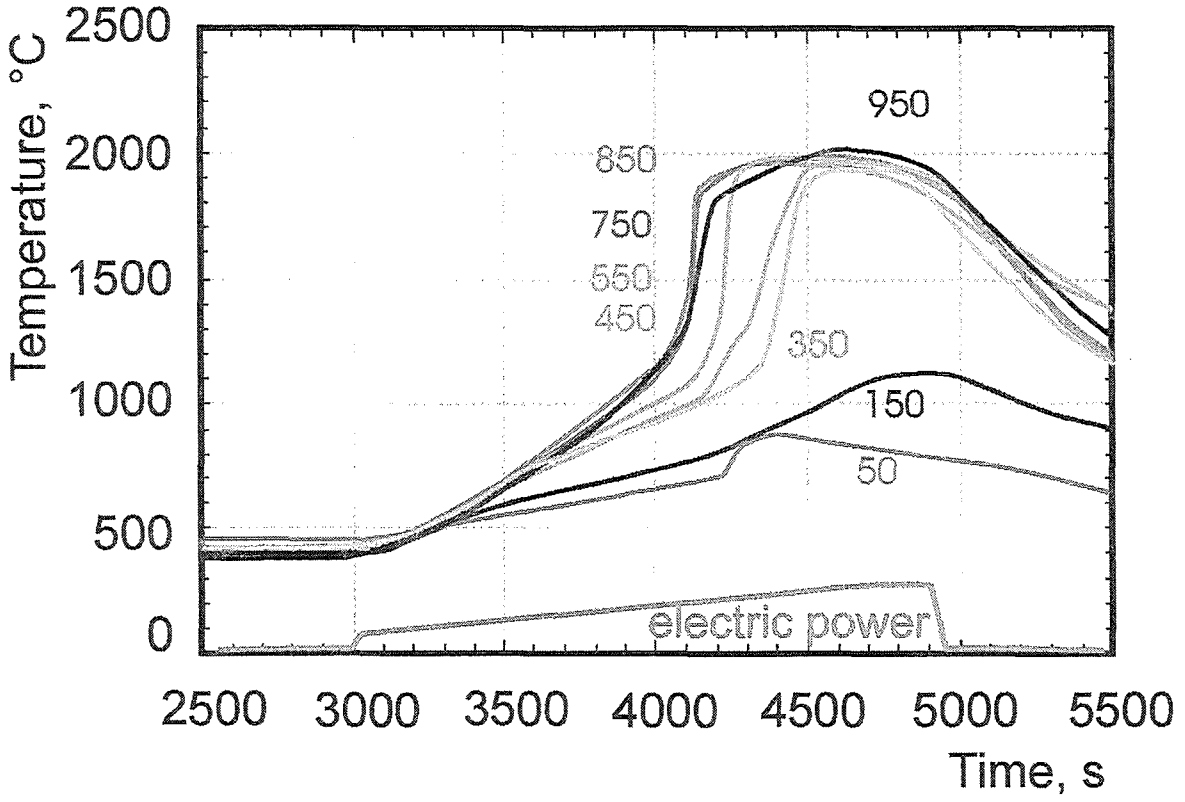

Fig. 46a: CORA-29: Comparison of hydrogen production rate and best estimate temperatures

c28_050b.cdr

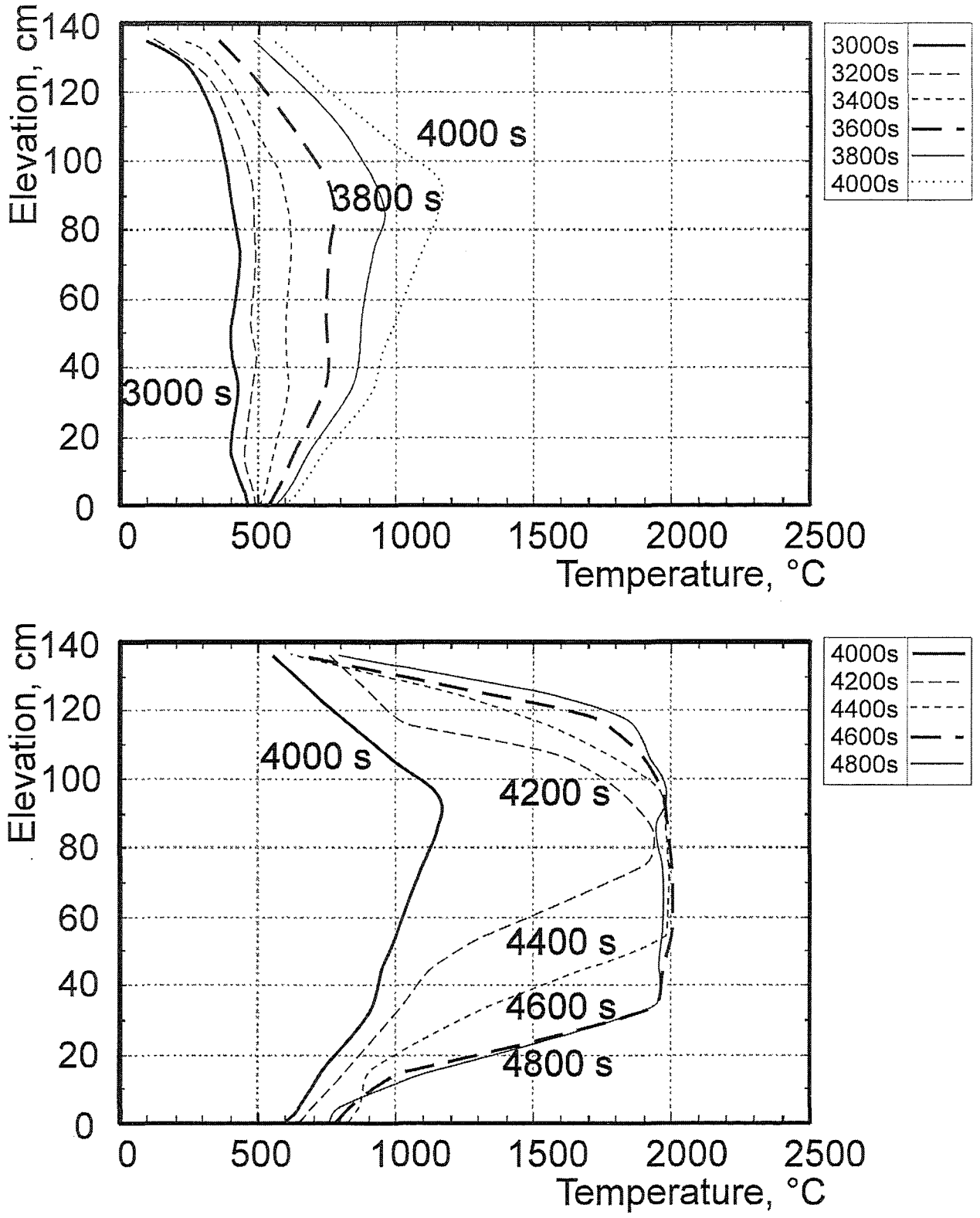

Fig. 47: Axial temperature profiles during the transient of test CORA-29

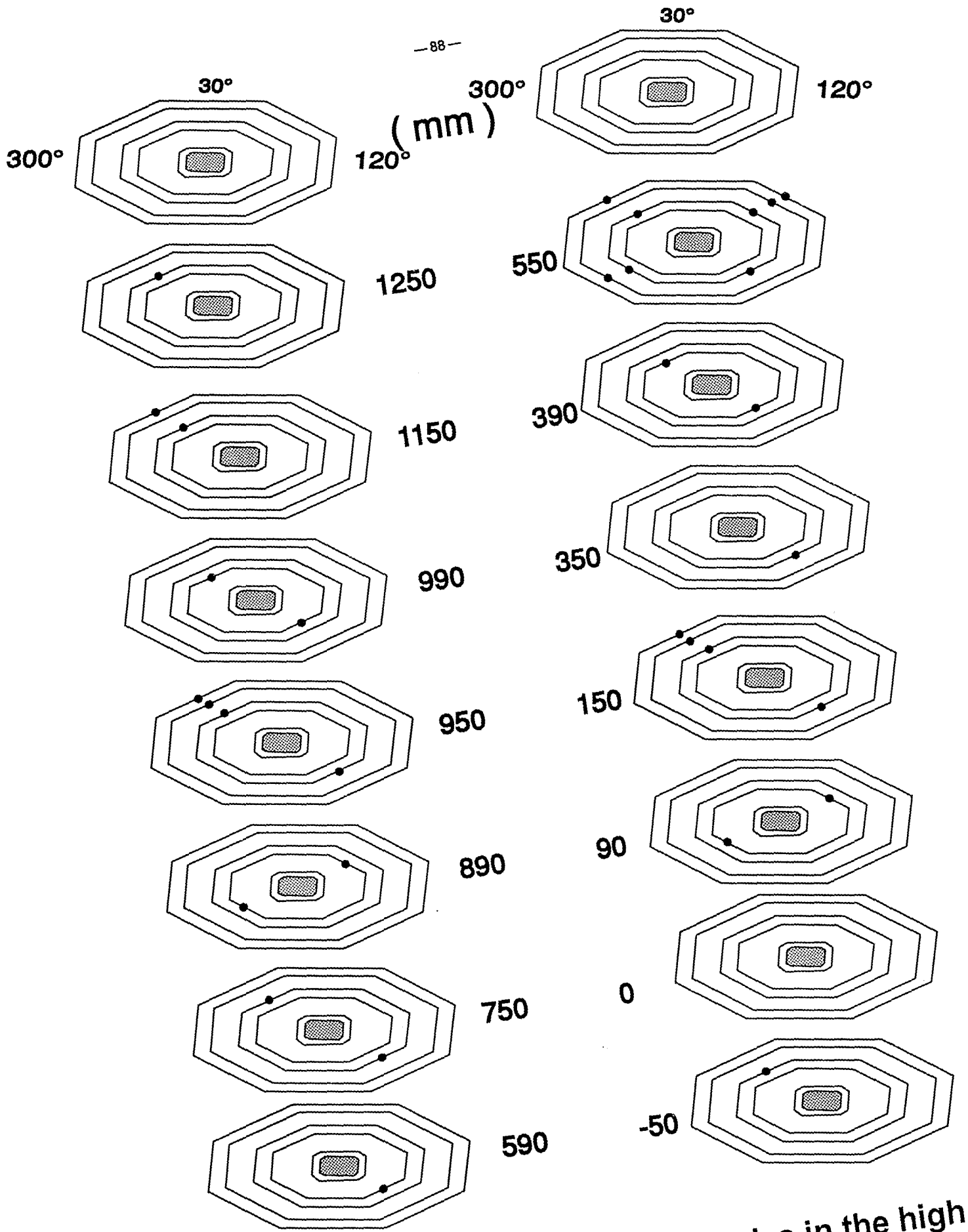

Fig. 48: Locations of thermocouples in the high temperature shield (CORA-29)

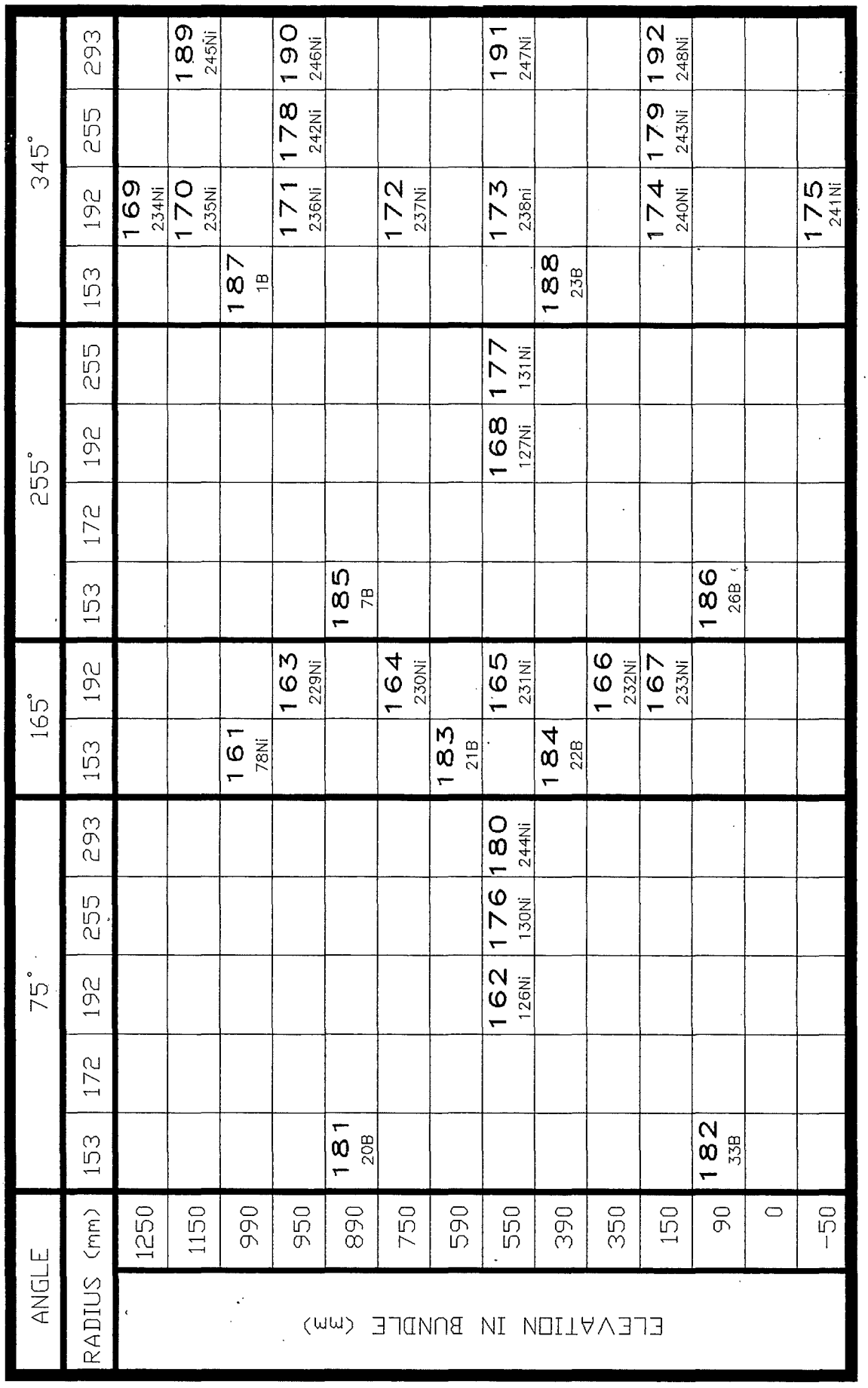

Fig. 49: Position of thermocouples in the high temperature shield for test CORA-29

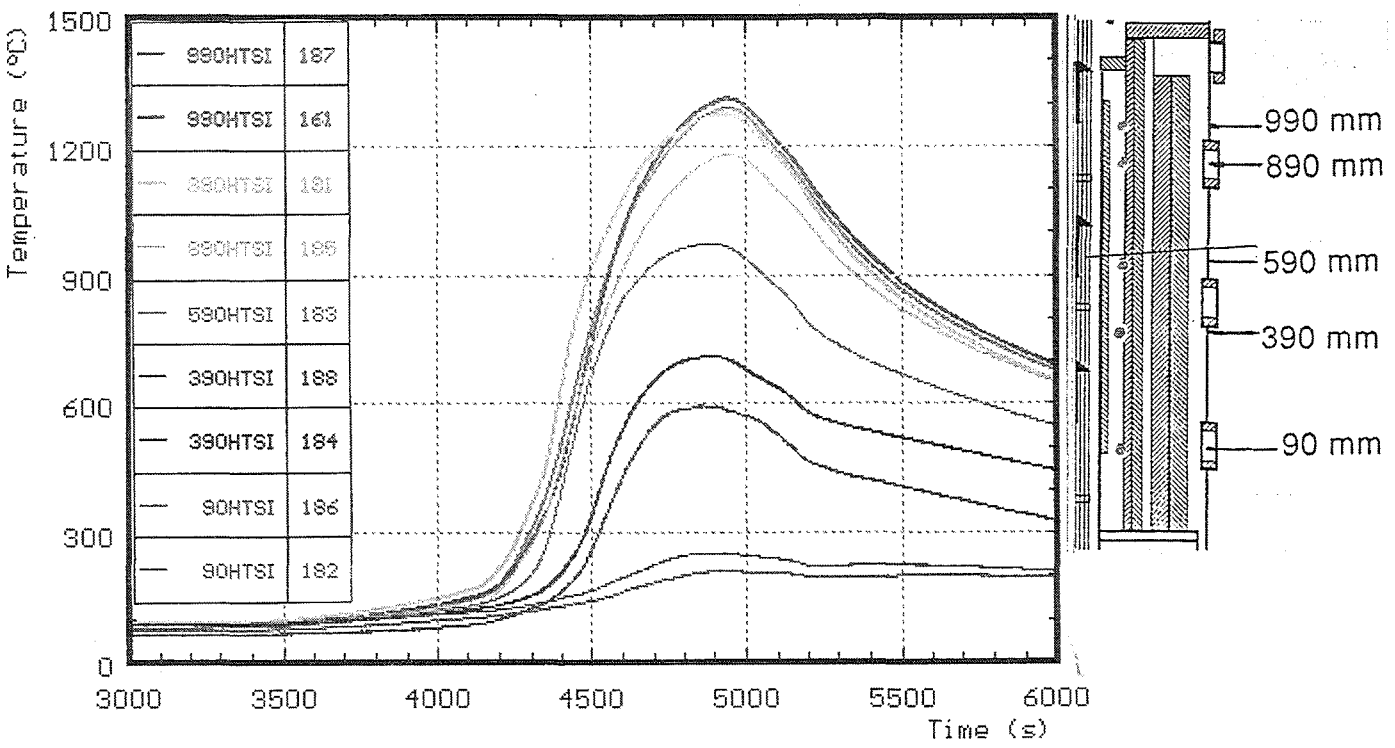

Fig. 50: CORA-29; Temperatures of HTS, Inner surface at 153 mm radius

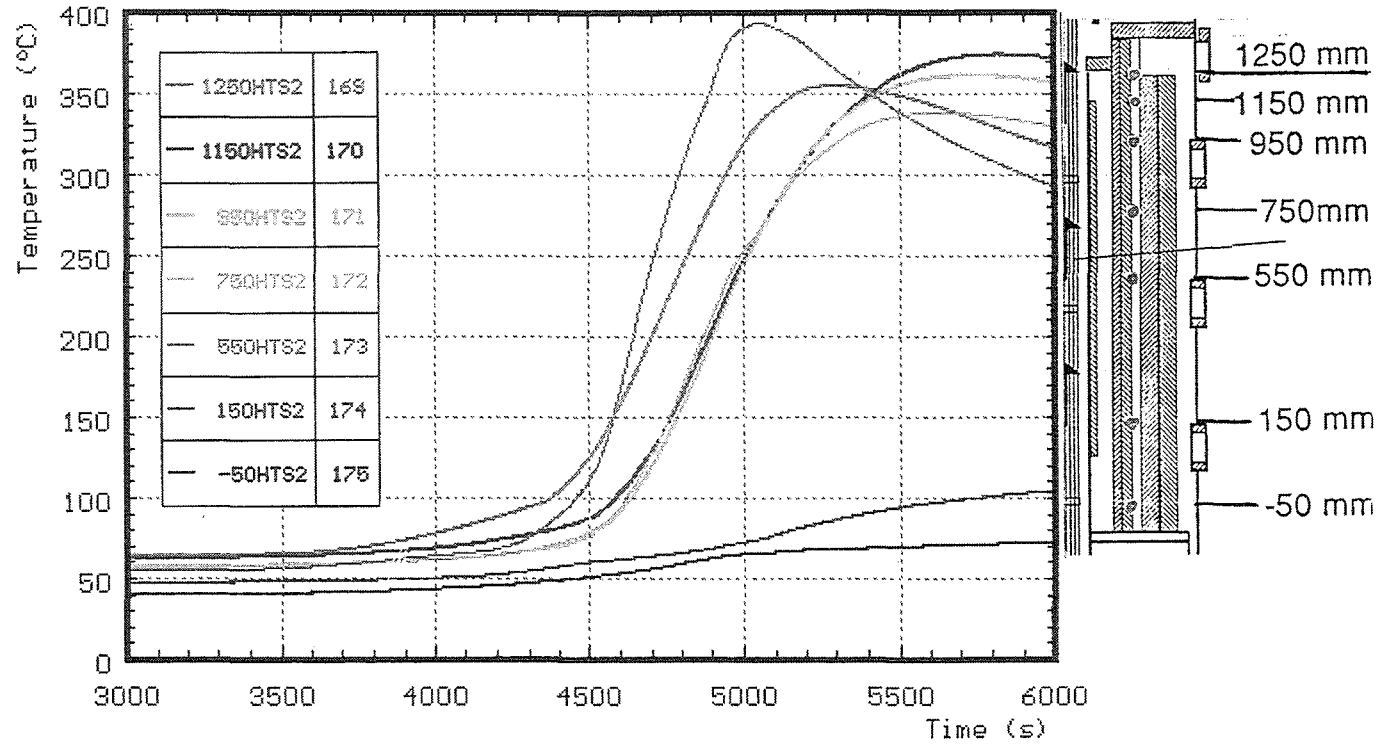

Fig. 51: CORA-29; Temperatures of HTS, Temperatures in HT shield at 192 mm radius, 345°

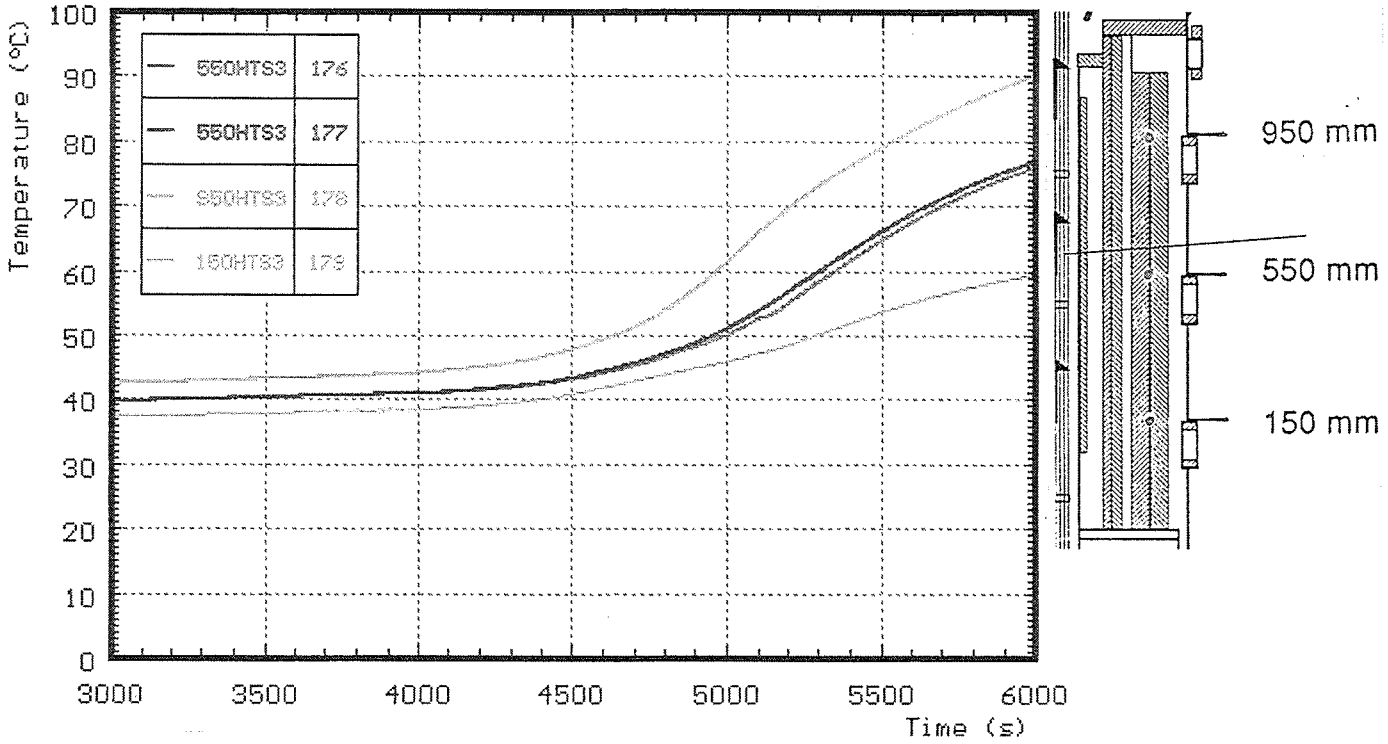

Fig. 52: CORA-29; Temperatures of HTS, Temperatures in HT shield at 255 mm radius

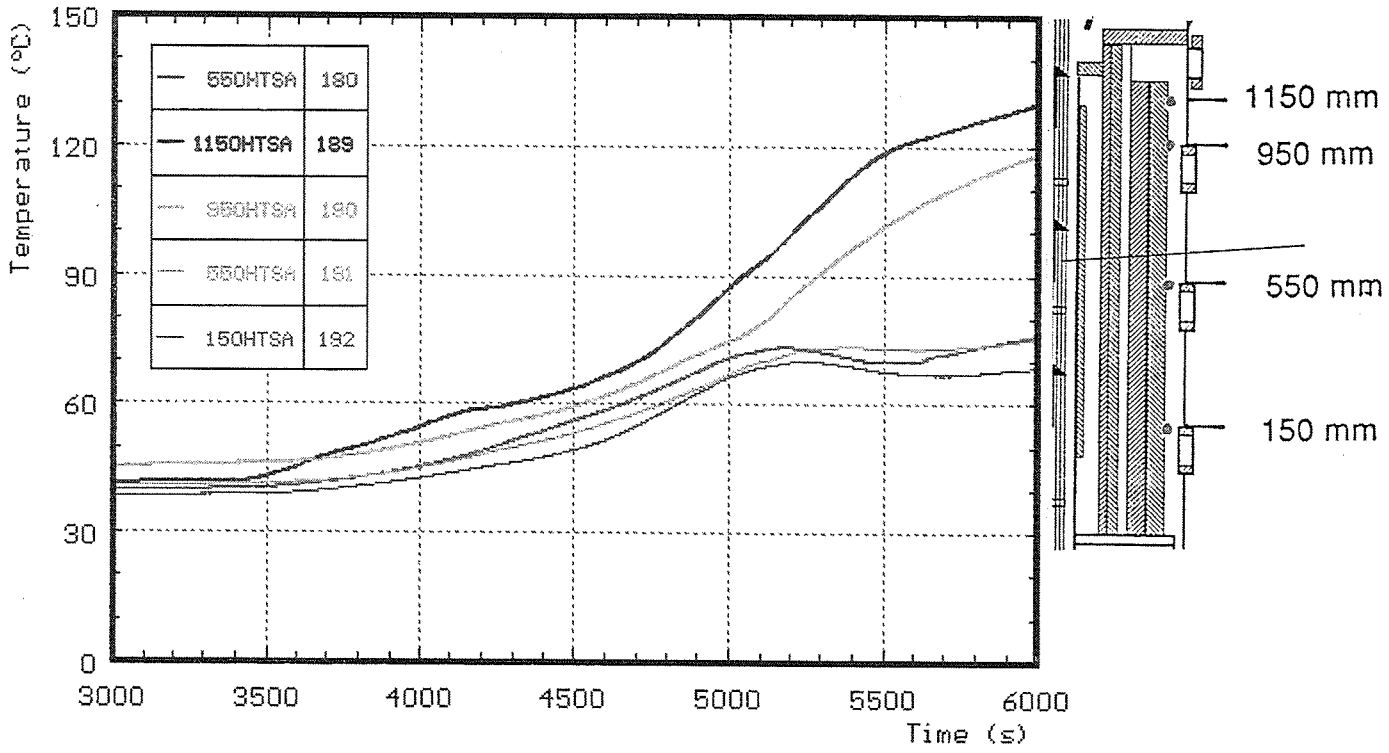

Fig. 53: CORA-29; Temperatures of HTS, Temperatures in HT shield at 293 mm radius

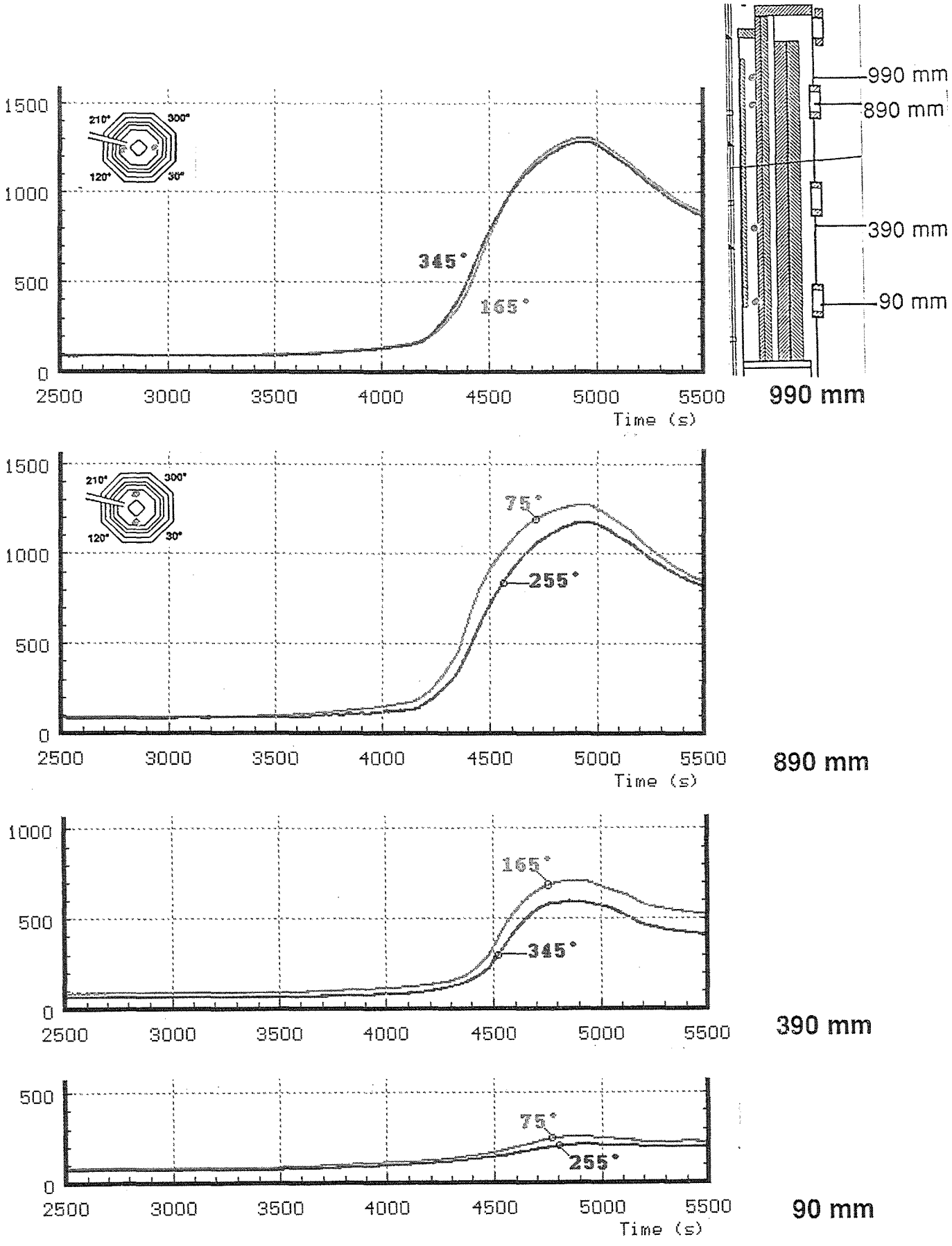

Fig. 54: CORA-29; Temperatures of HTS, Comparison on inner surface at 153 mm radius

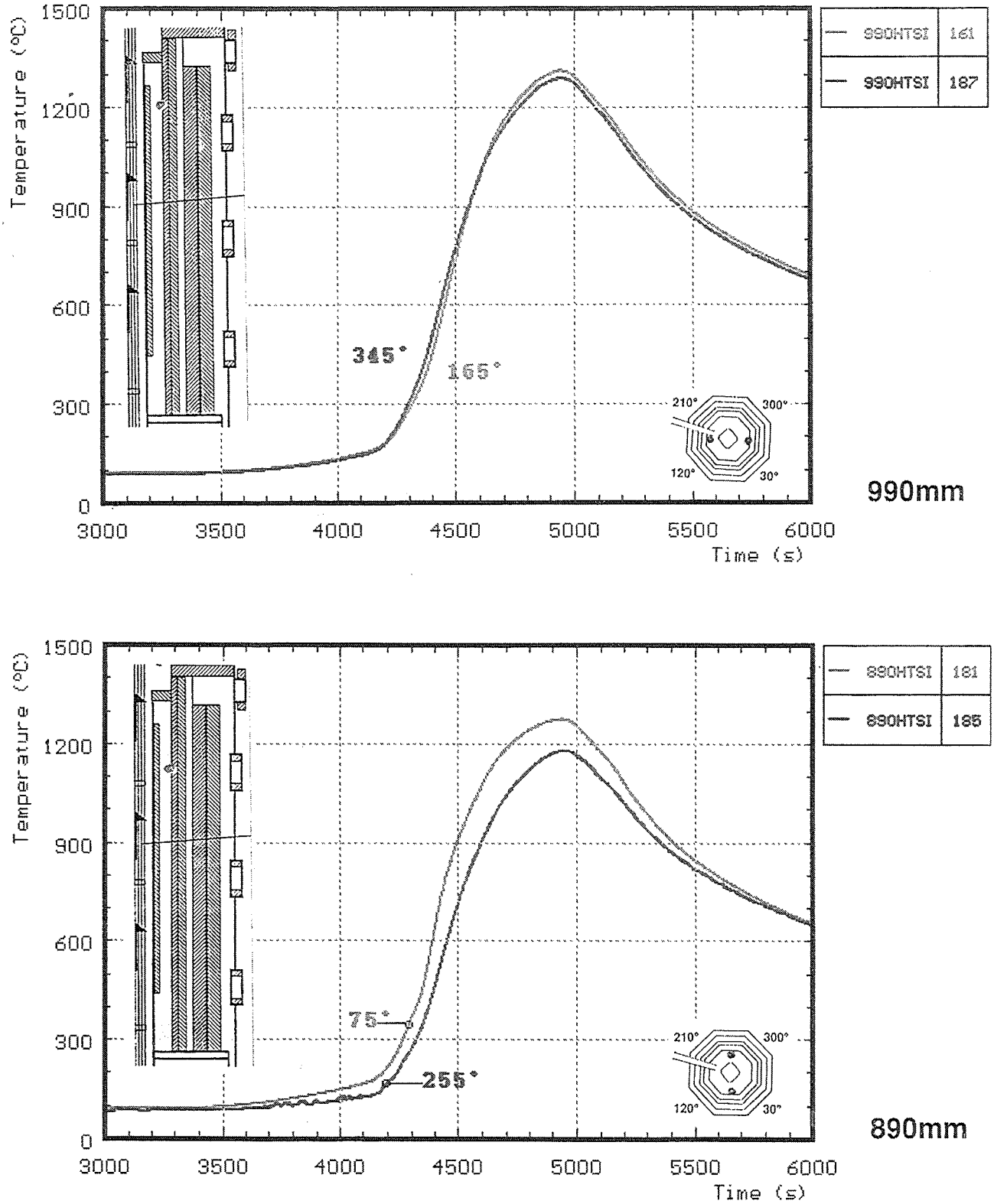

Fig. 55: CORA-29; Temperatures of HTS, Comparison on inner surface at 153 mm radius, 990 mm and 890 mm elevation

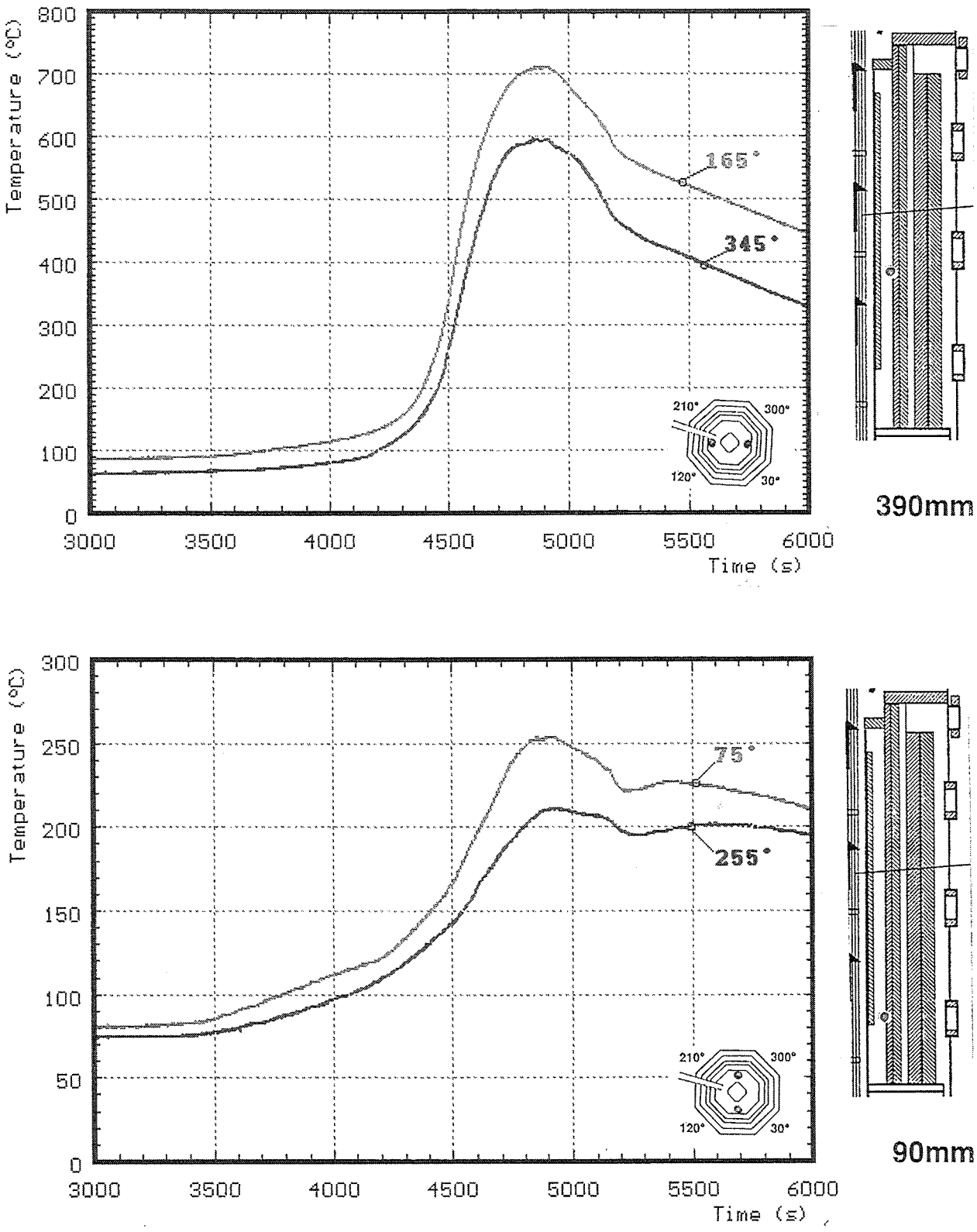

Fig. 56: CORA-29; Temperatures of HTS, Comparison on inner surface at 153 mm radius, 390 mm and 90 mm elevation

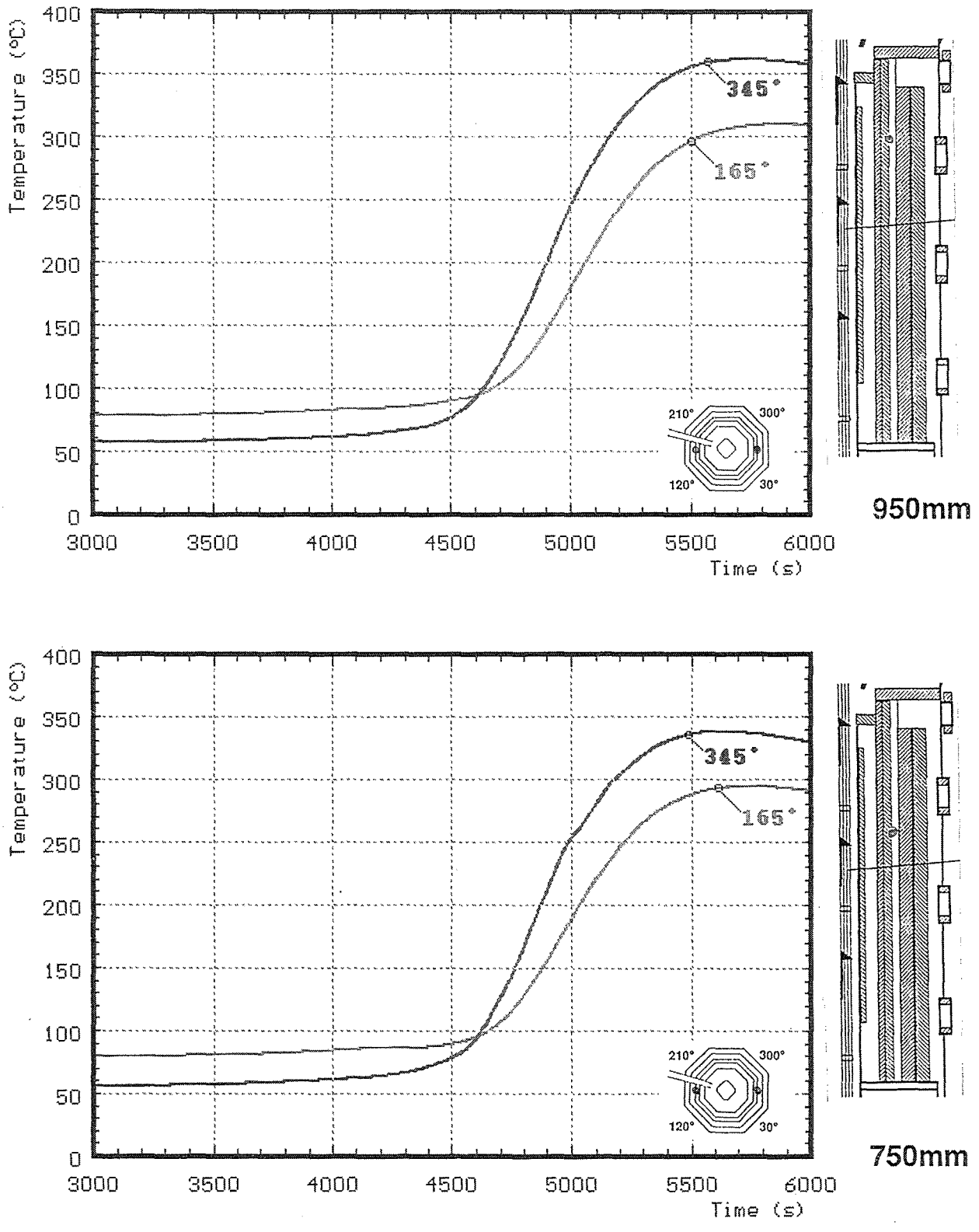

Fig. 57: CORA-29; Temperatures of HTS, Comparison in HT-shield at 192 mm radius, 950 mm and 750 mm elevation

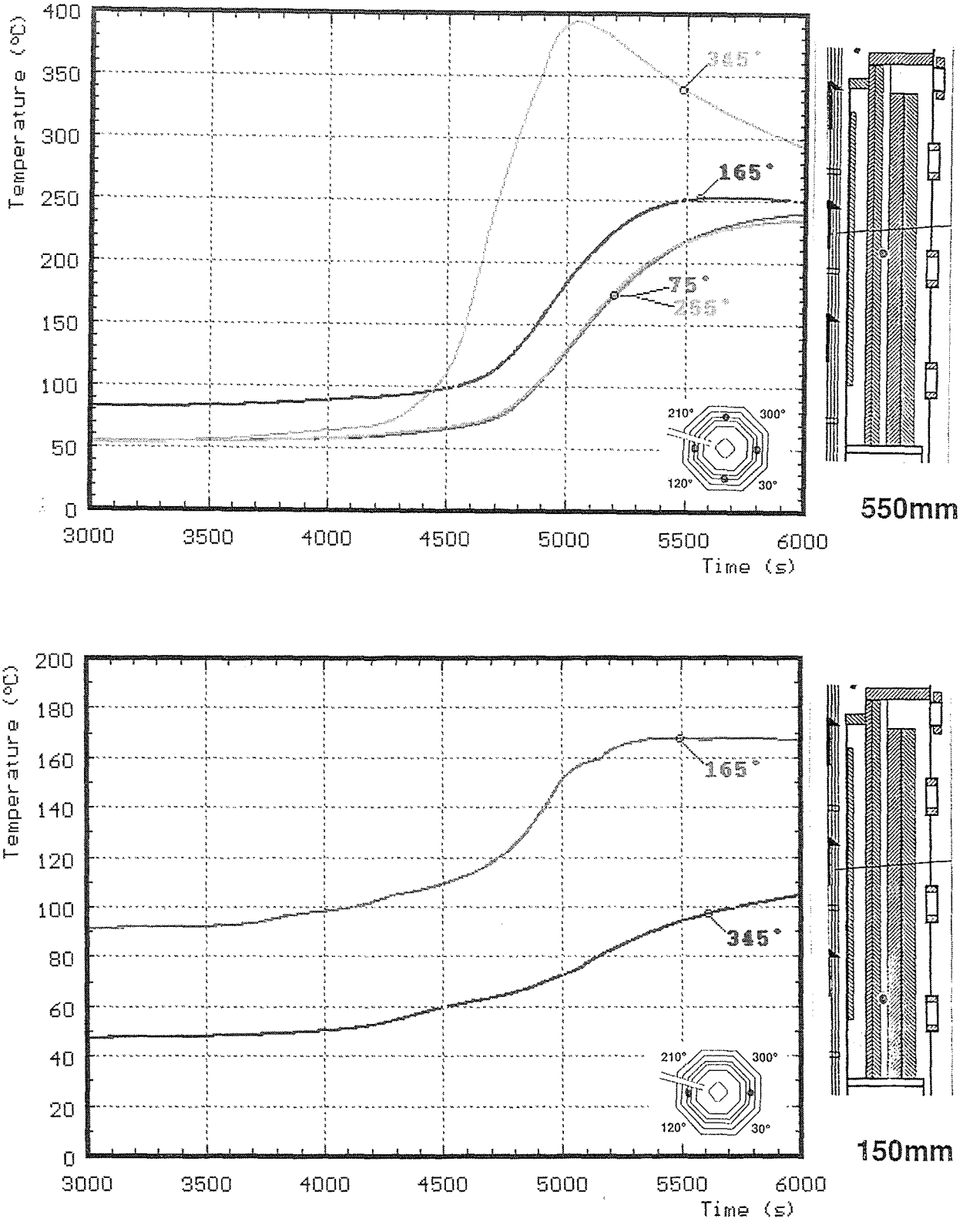

Fig. 58: CORA-29; Temperatures of HTS, Comparison in HT-shield at 192 mm radius, 550 mm and 150 mm elevation

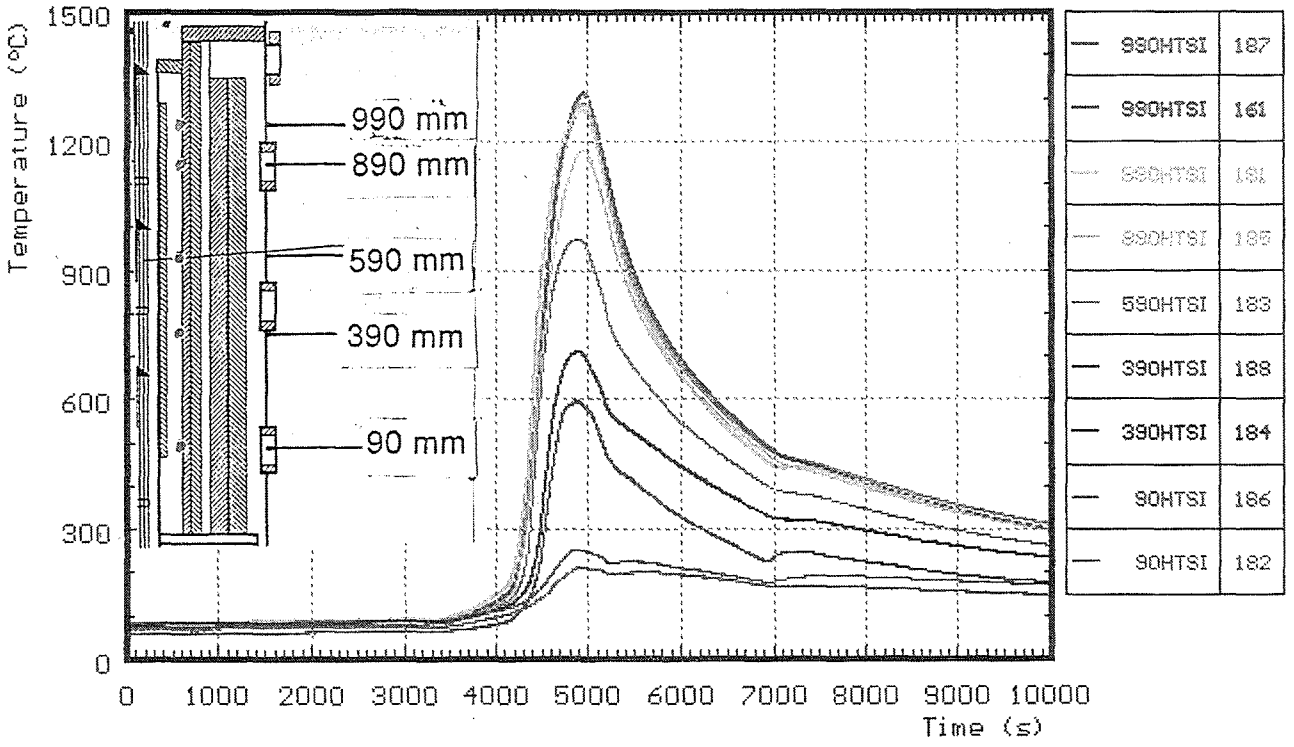

Fig. 59: CORA-29; Temperatures of HTS, Inner surface at 153 mm radius, 0 - 10000 s

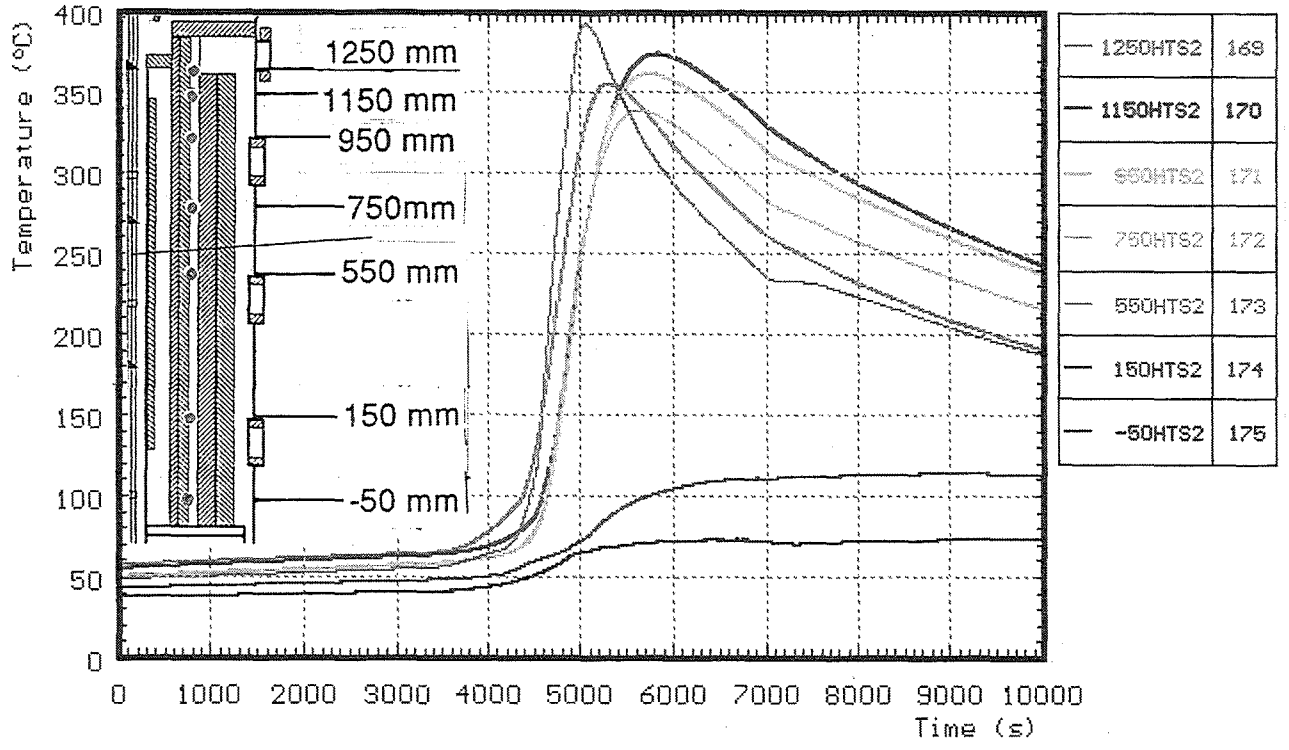

Fig. 60: CORA-29; Temperatures of HTS, Temperatures in HT shield at 192 mm radius, 345°, 0 - 10000 s

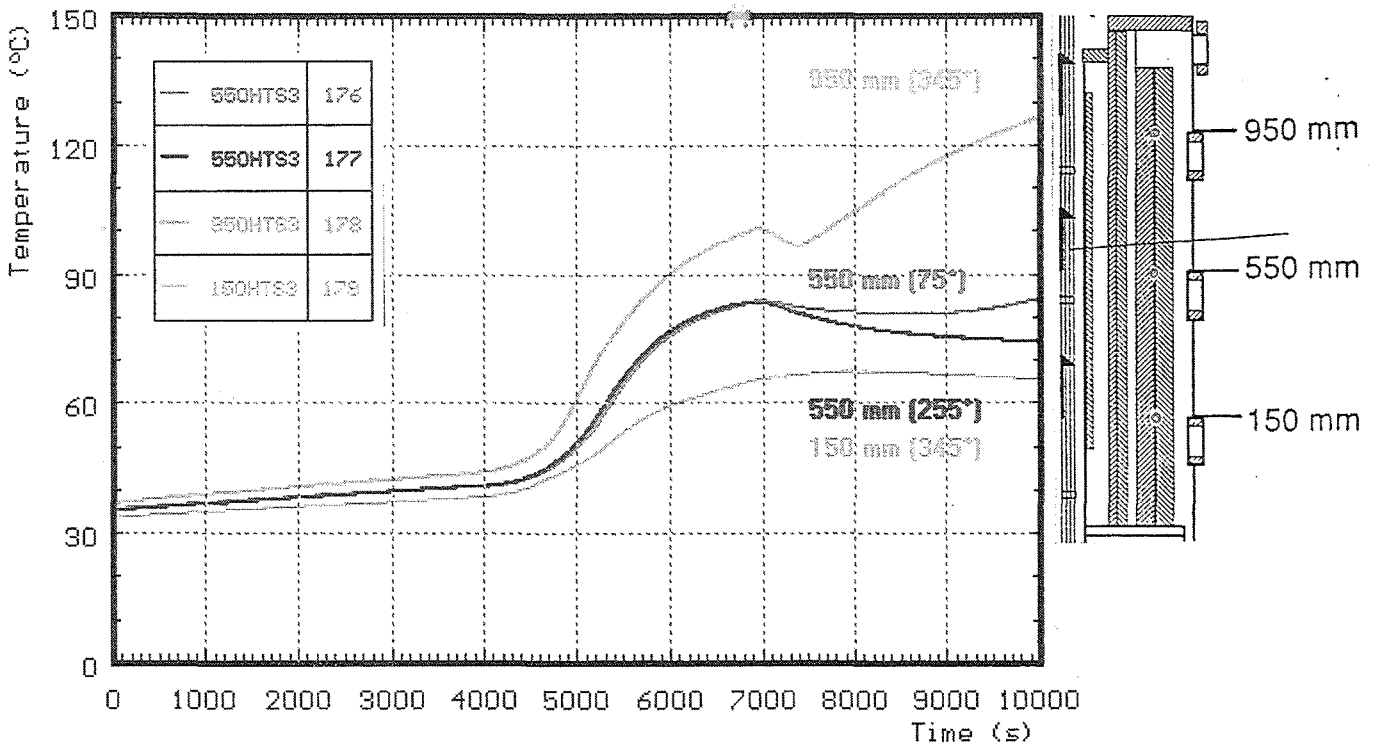

Fig. 61: CORA-29; Temperatures of HTS, Temperatures in HT shield at 255 mm radius, 0 - 10000 s

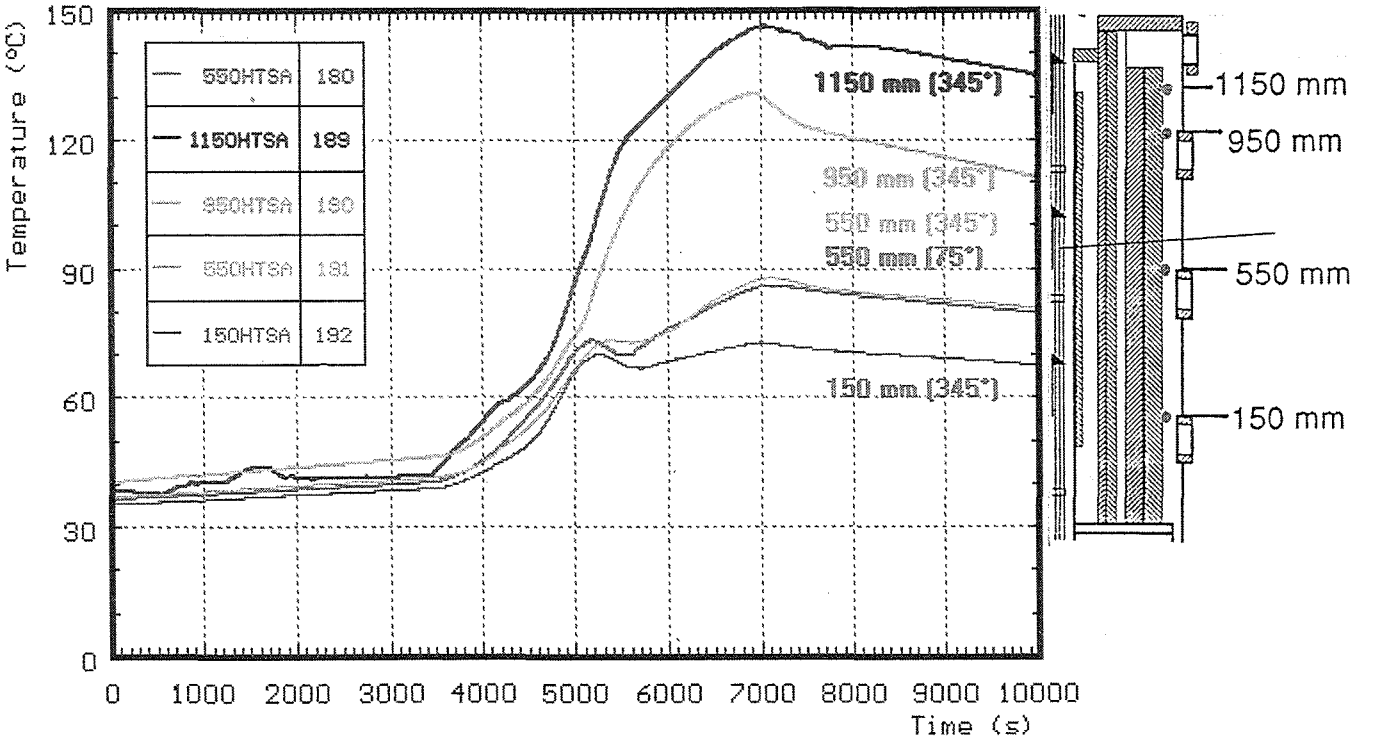

Fig. 62: CORA-29; Temperatures of HTS, Temperatures in HT shield at 293 mm radius, 0 - 10000 s

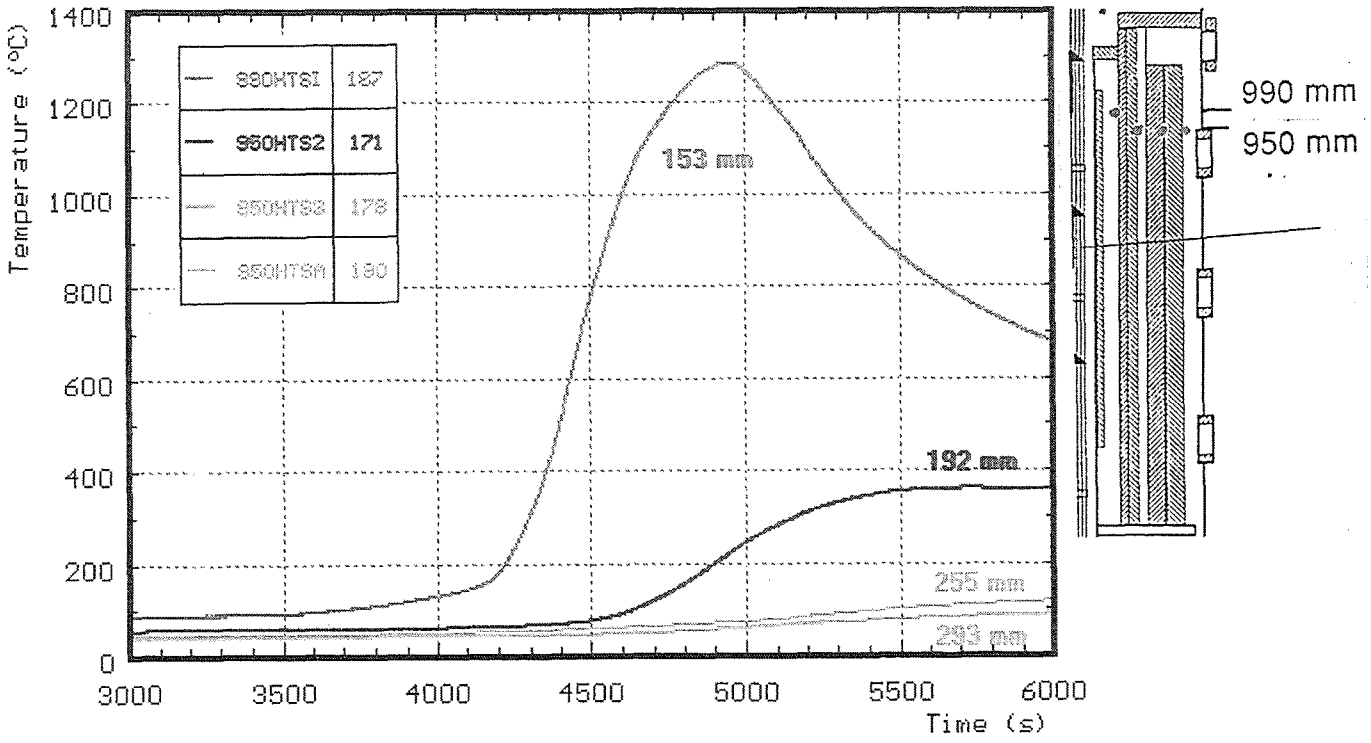

Fig. 63: CORA-29; Temperatures of HTS, Radial dependence at about 950 mm elevation

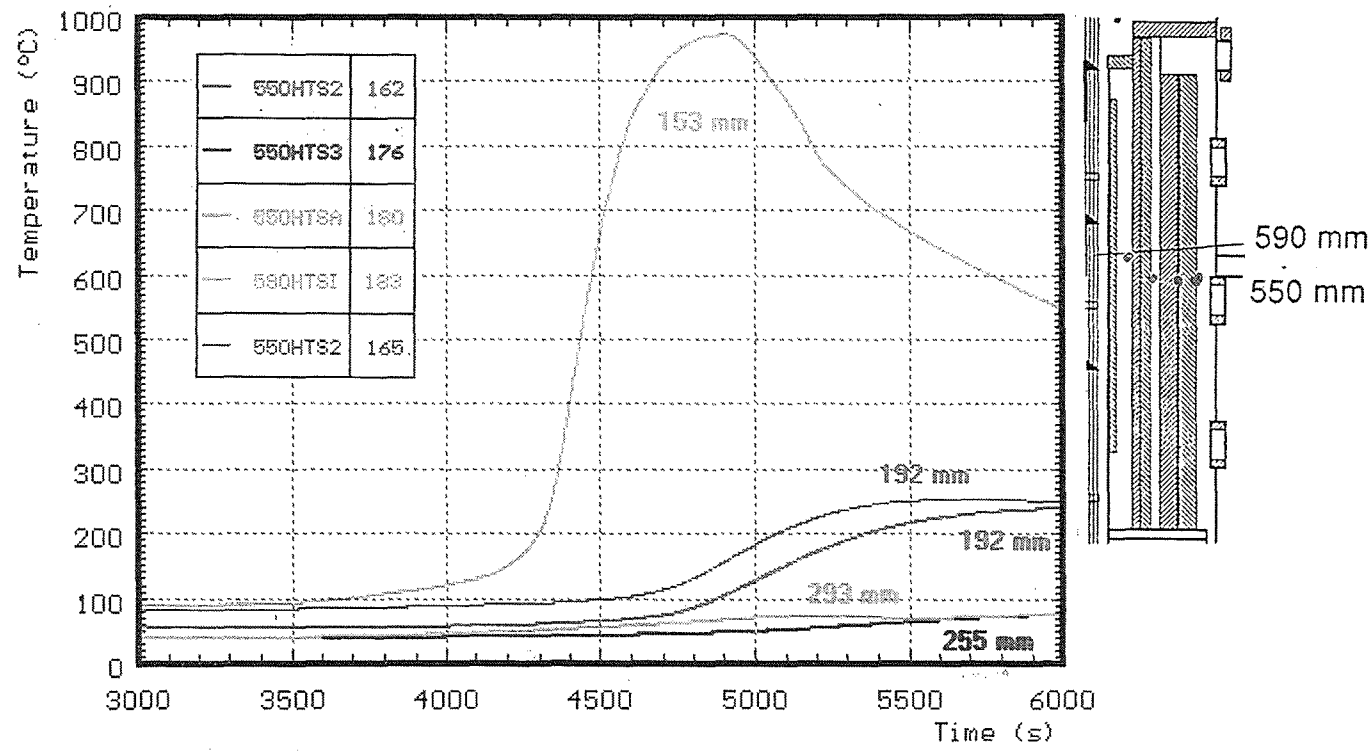

Fig. 64: CORA-29; Temperatures of HTS, Radial dependence at about 550 mm elevation

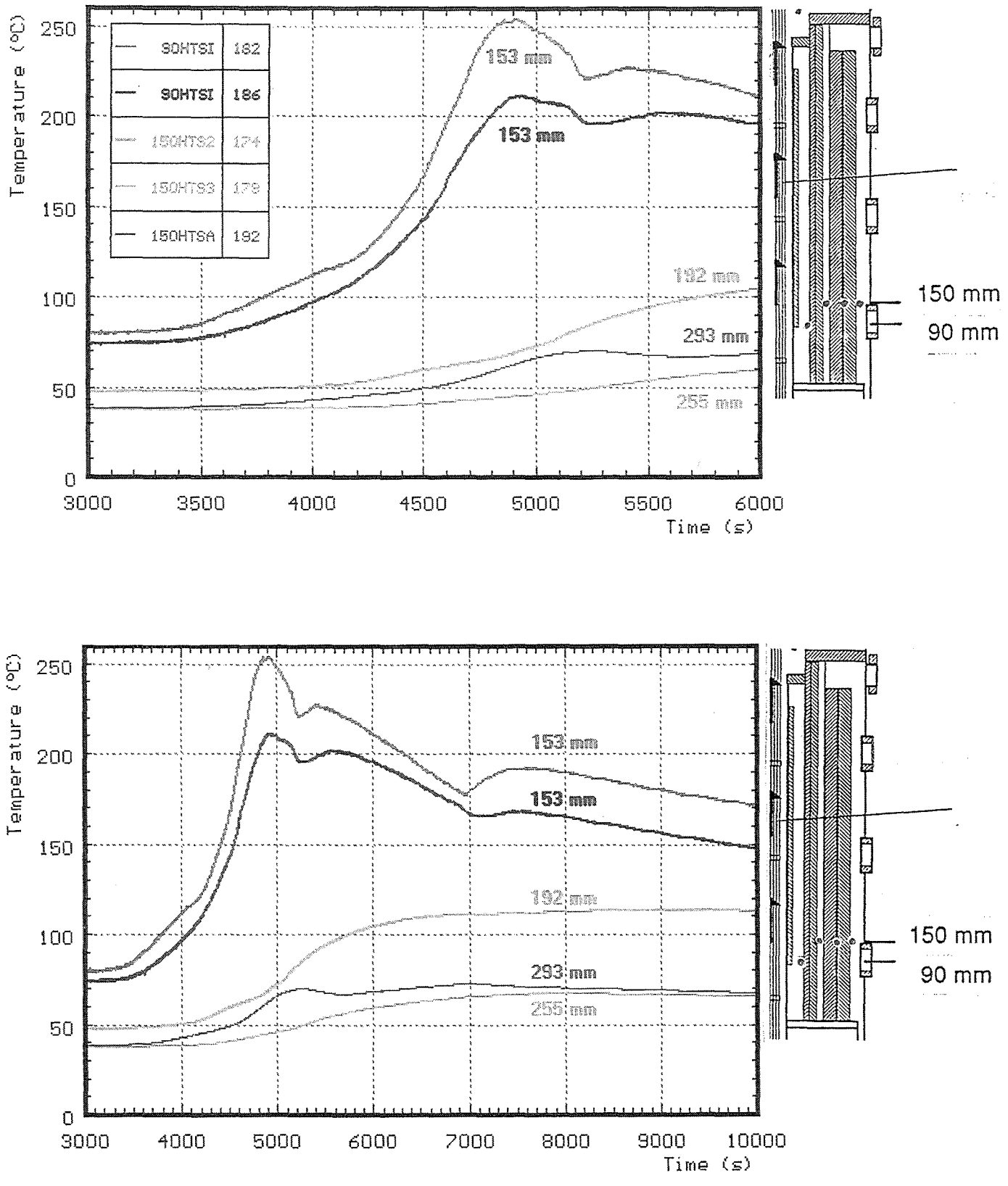

Fig. 65: CORA-29; Temperatures of HTS, Radial dependence at about 100 mm elevation

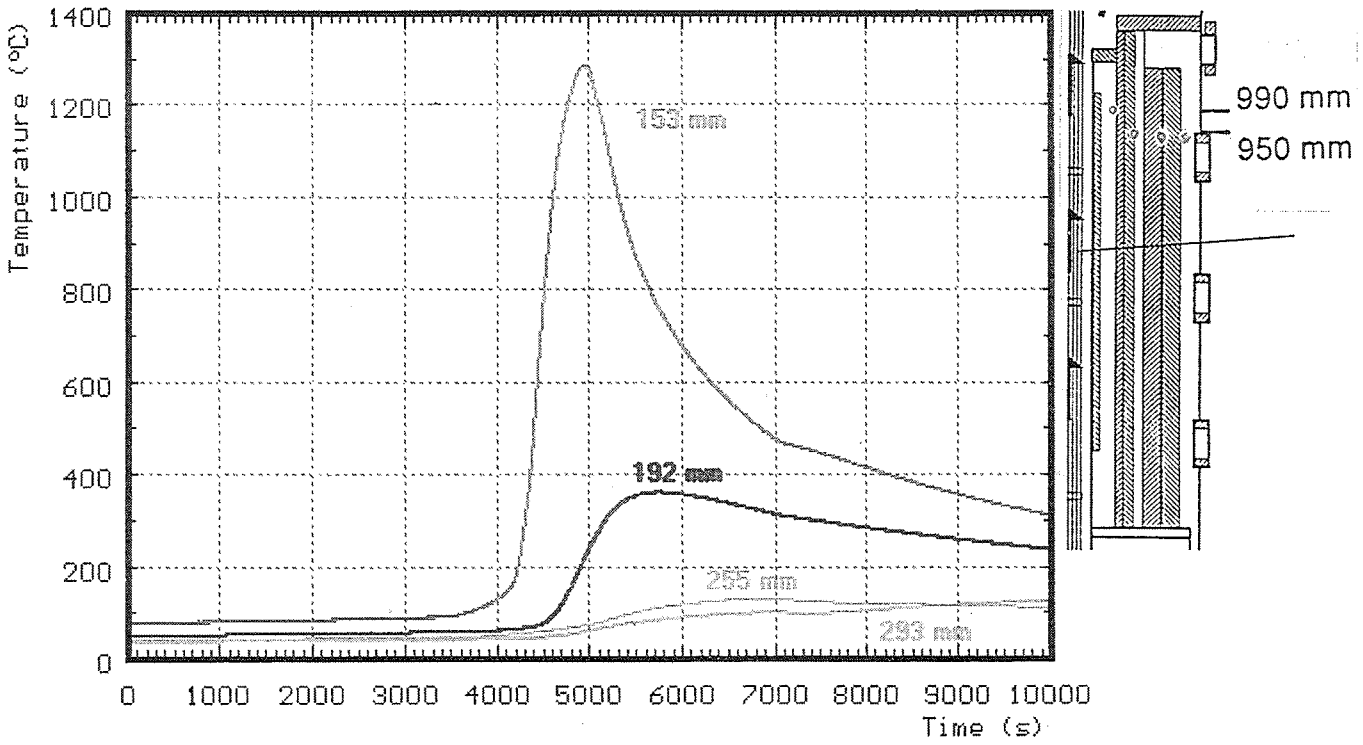

Fig. 66: CORA-29; Temperatures of HTS, Radial dependence at about 950 mm elevation, 0 - 10000 s

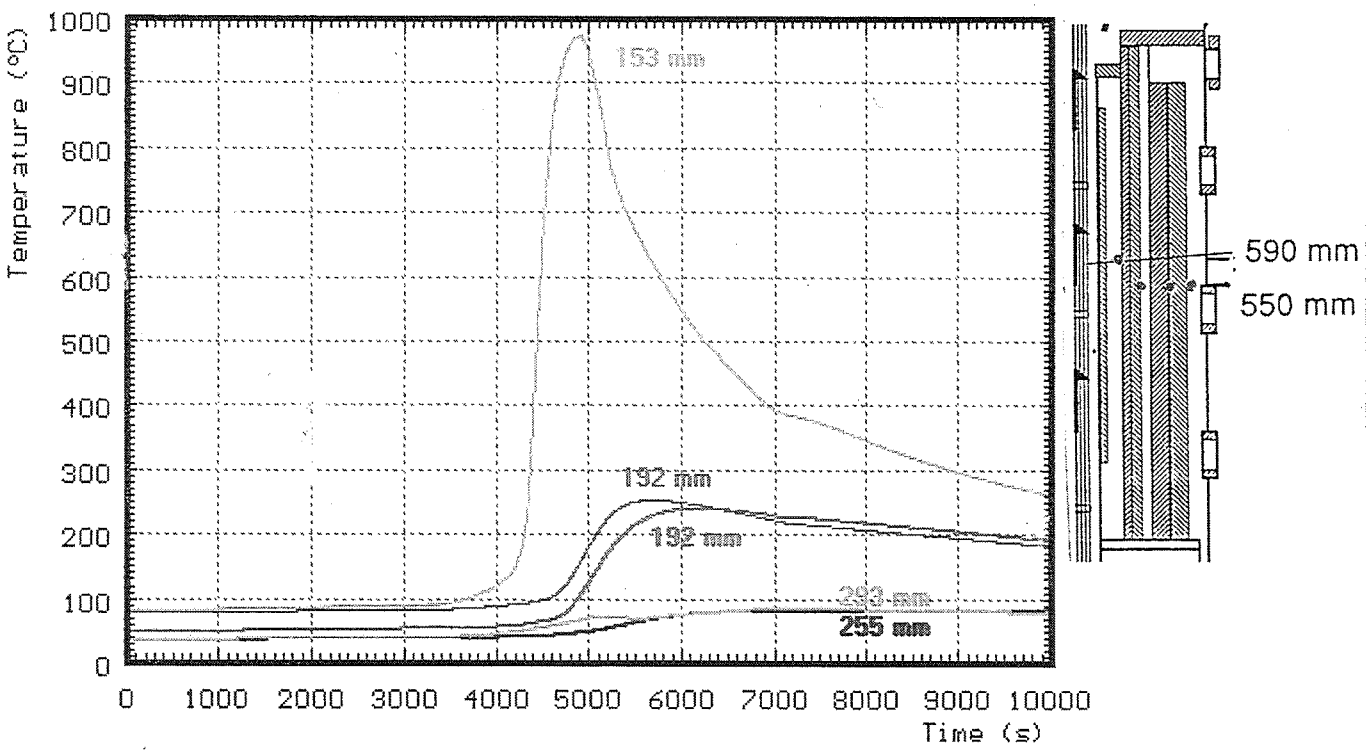

Fig. 67: CORA-29; Temperatures of HTS, Radial dependence at about 550 mm elevation, 0 - 10000 s

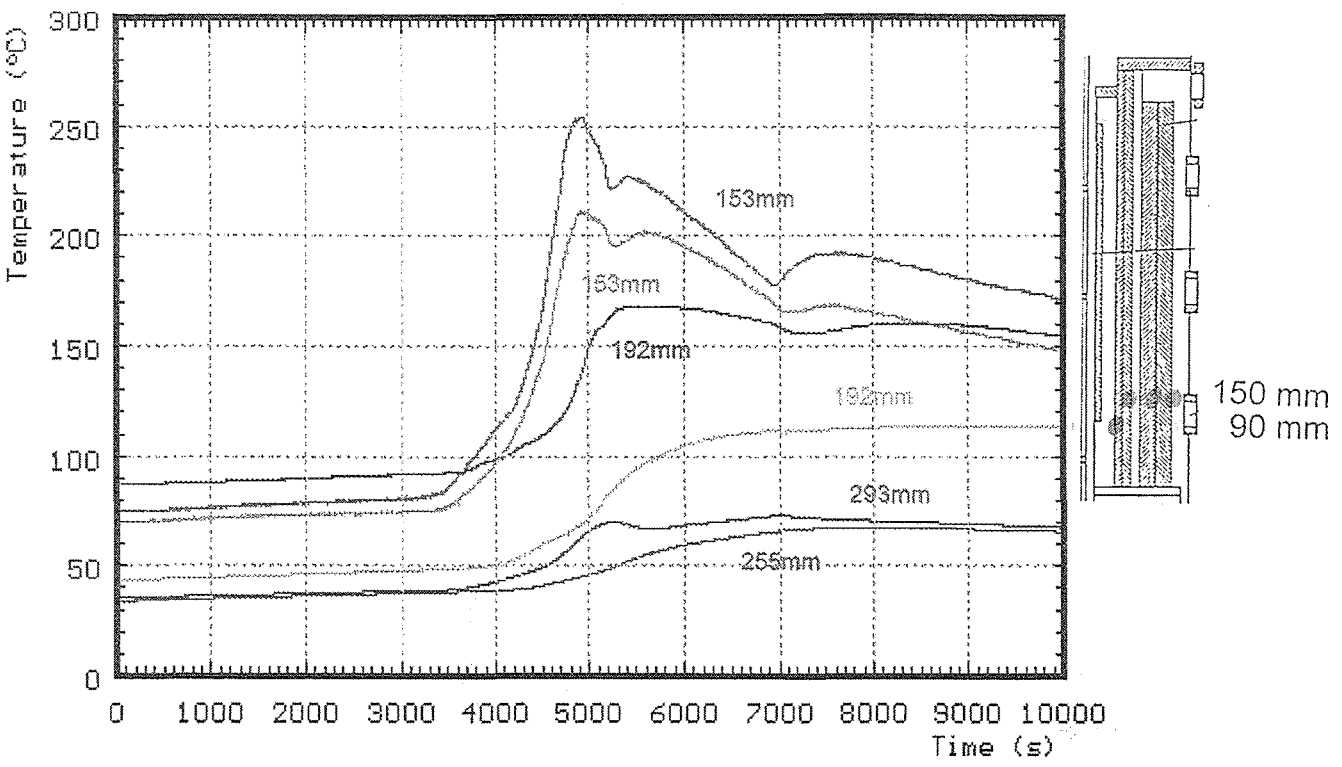

Fig. 68: CORA-29; Temperatures of HTS, Radial dependence at about 100mm elevations, 0 - 10000 s

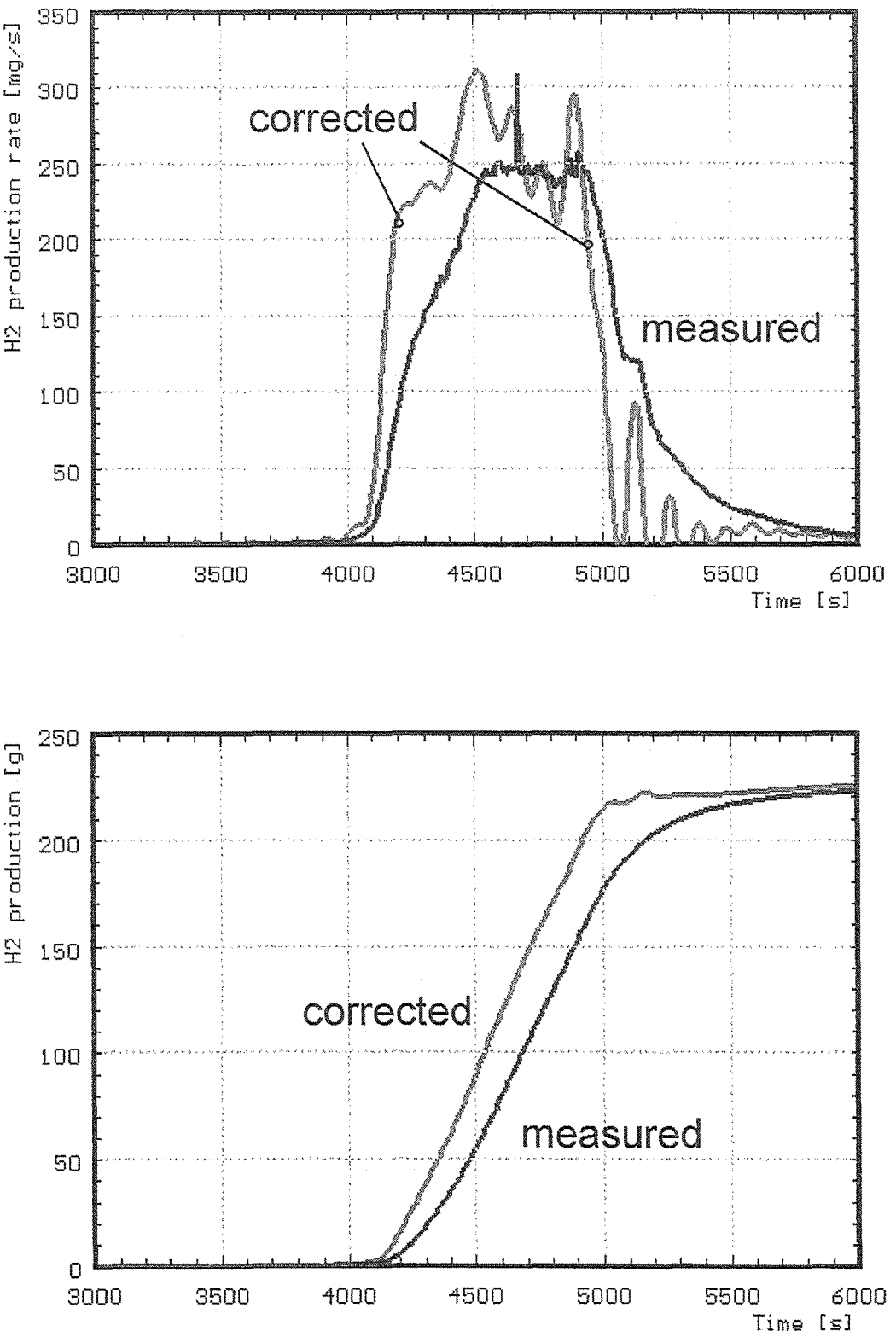

Fig. 69: Hydrogen production in test CORA-29; production rate (top) and integral values (bottom)

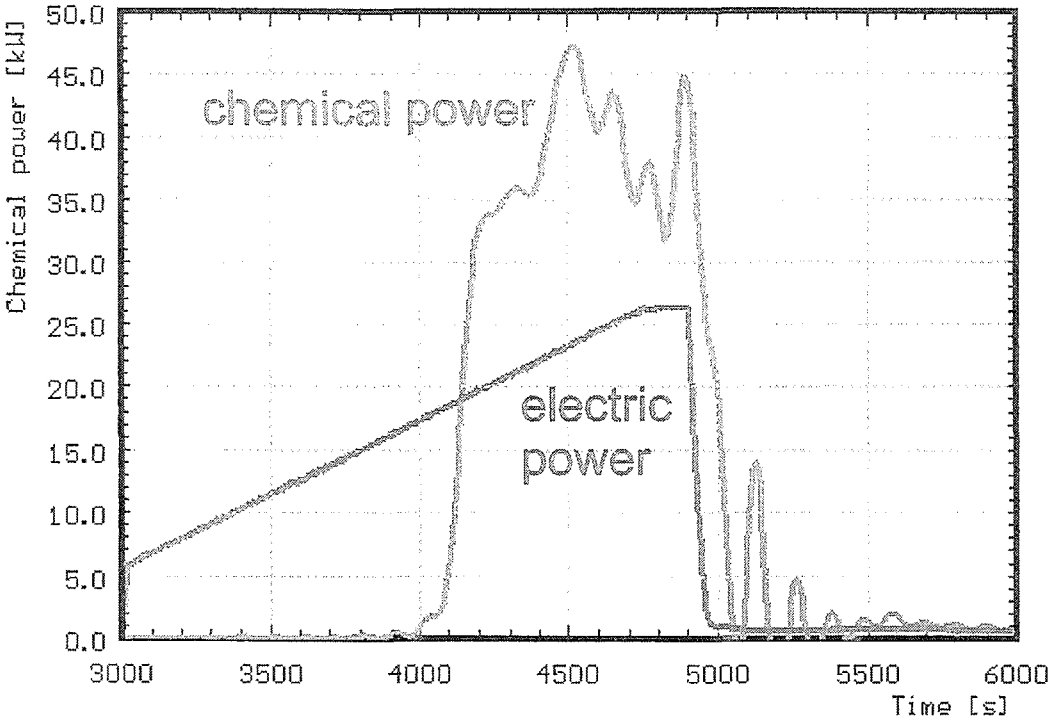

Fig. 70: CORA-29; Comparison of chemical and electric power

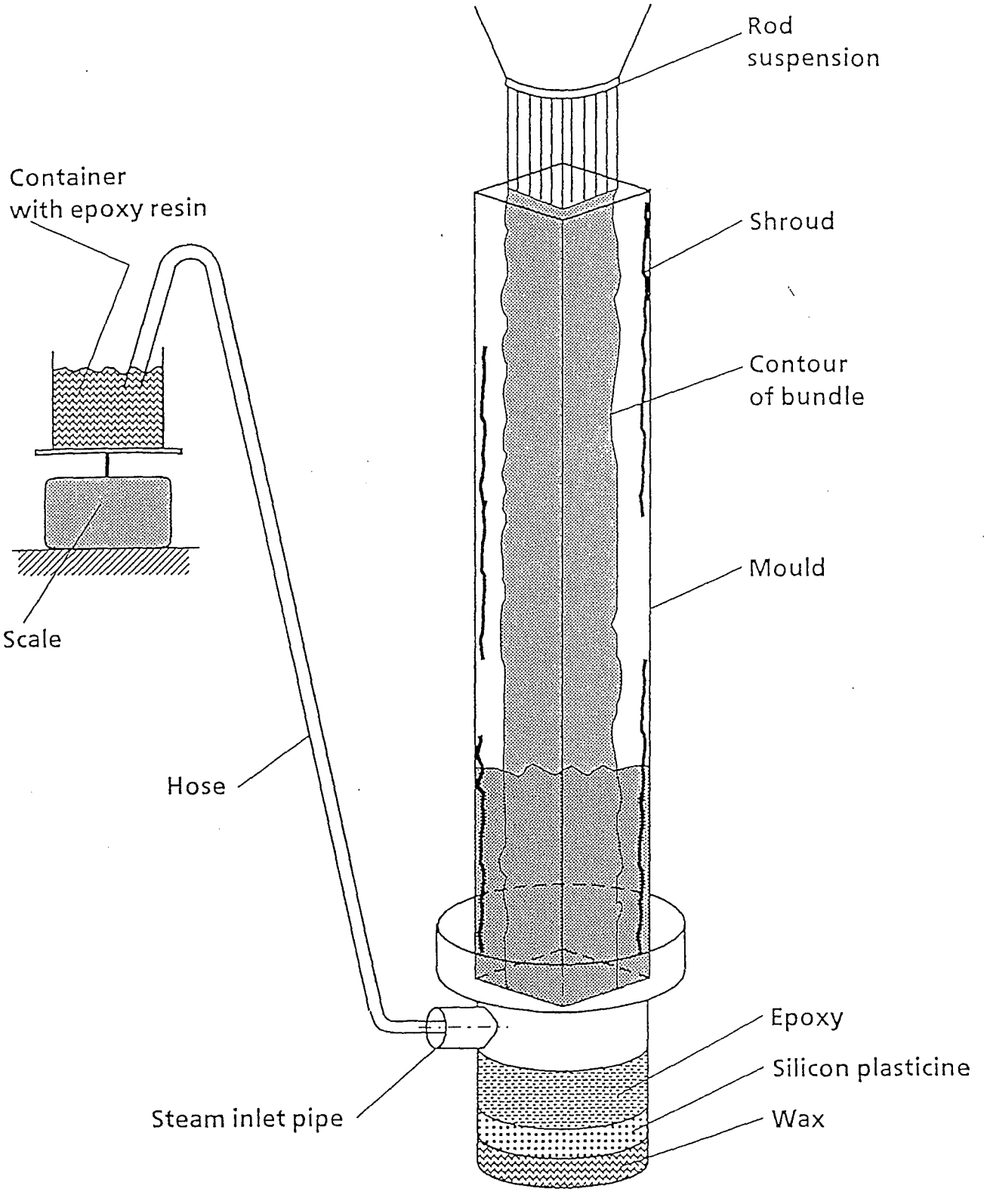

Fig. 79: CORA-29; Epoxing process of the tested bundle

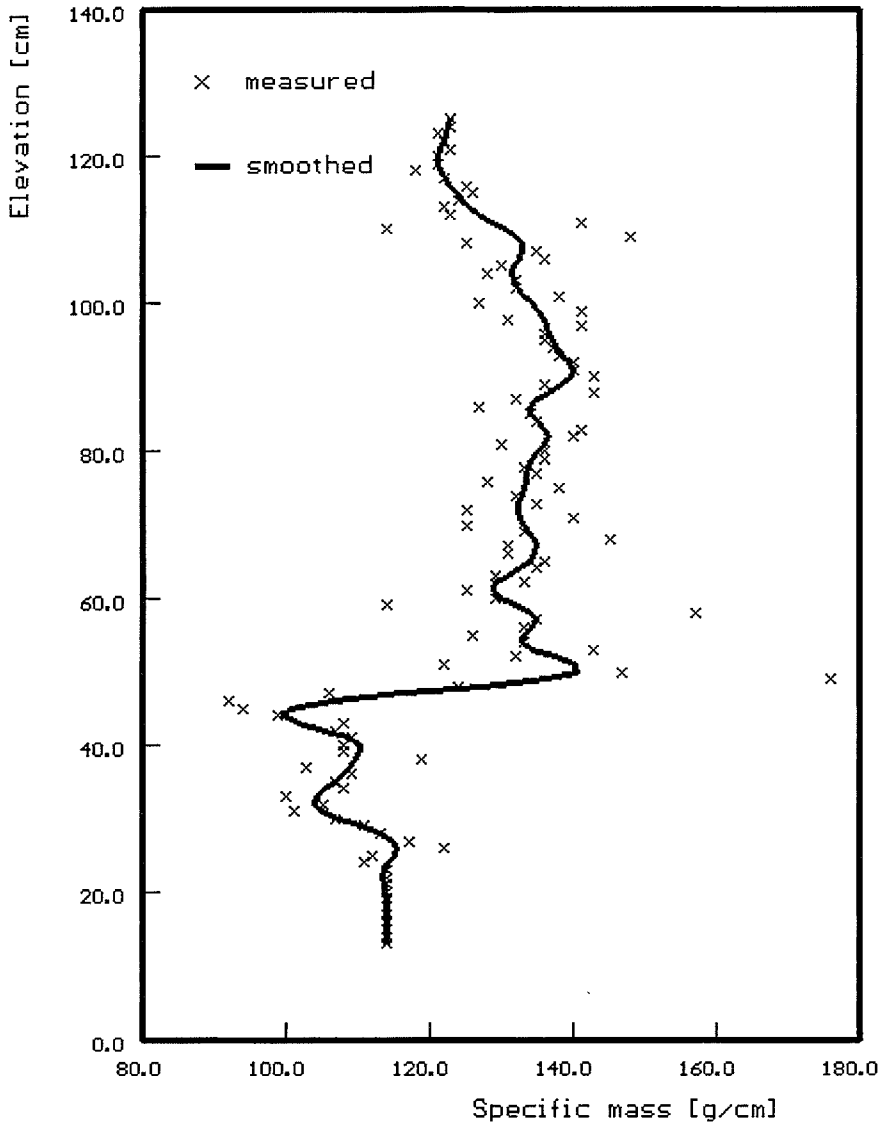

Fig. 80: CORA-29; Axial distribution of the bundle fill-up with epoxy resin

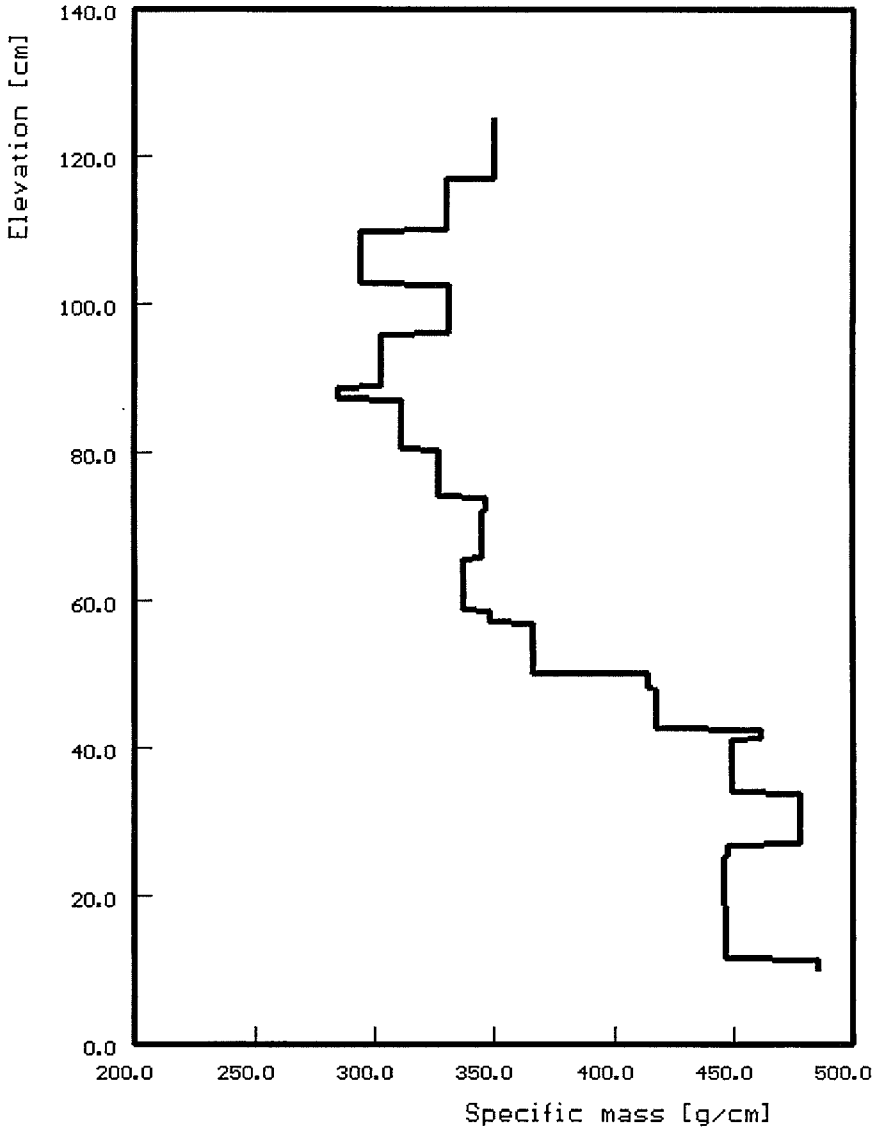

Fig. 81: CORA-29; Axial mass distribution of bundle segments filled with epoxy resin

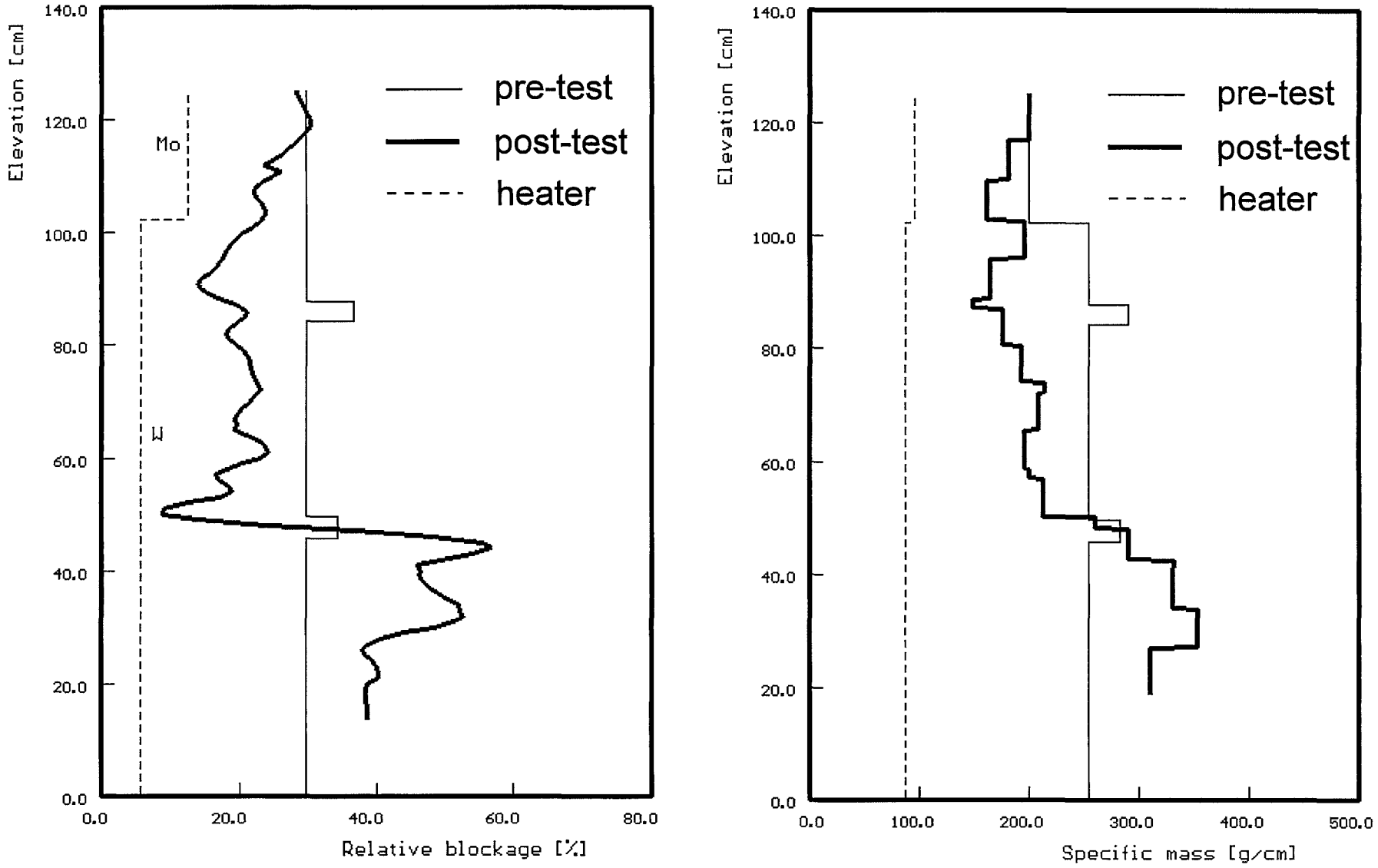

Fig. 82: CORA-29; Comparison of axial mass distribution and axial volume distribution after the test

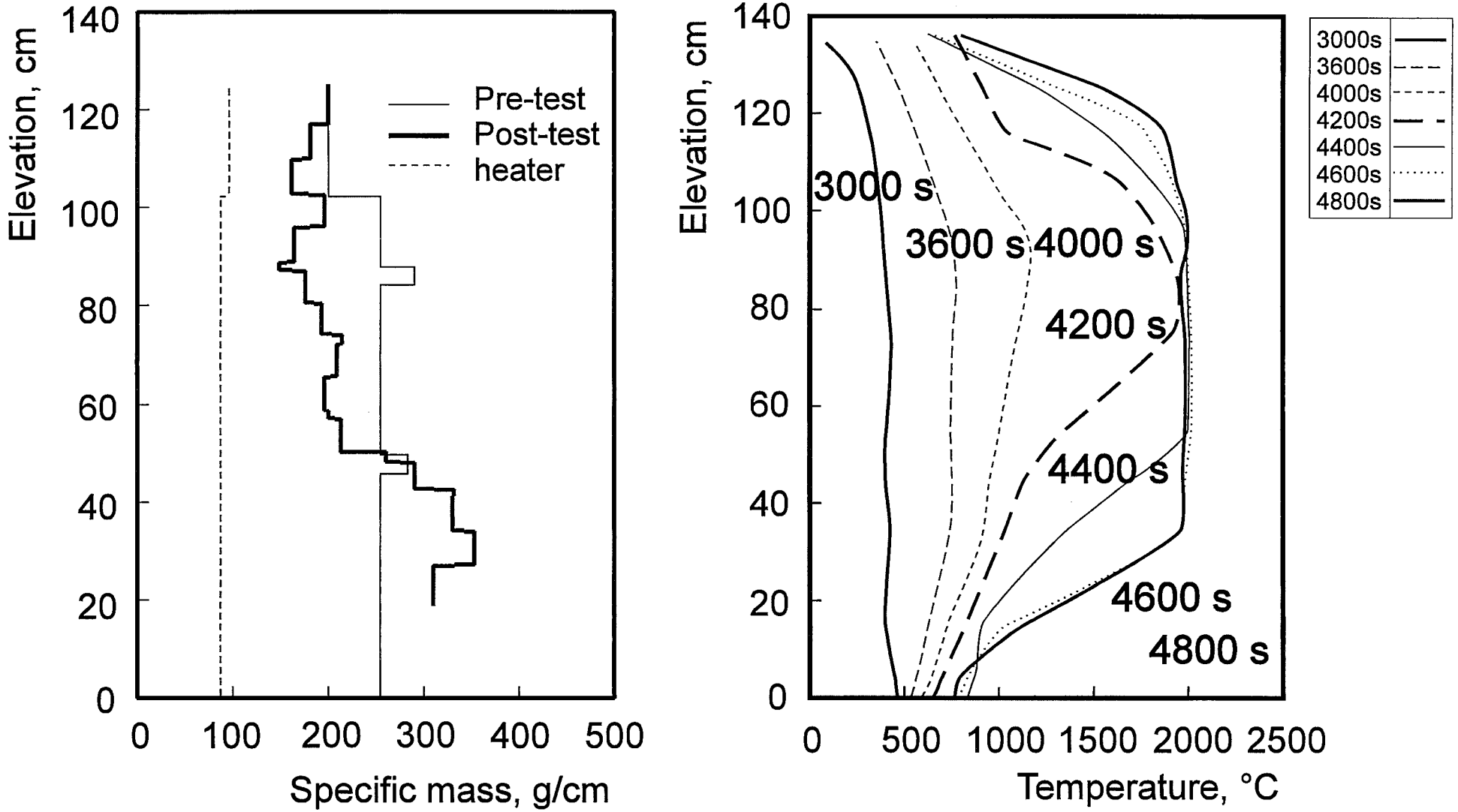

Fig. 83: CORA-29; Axial mass distribution after the test and axial temperature profiles during the test

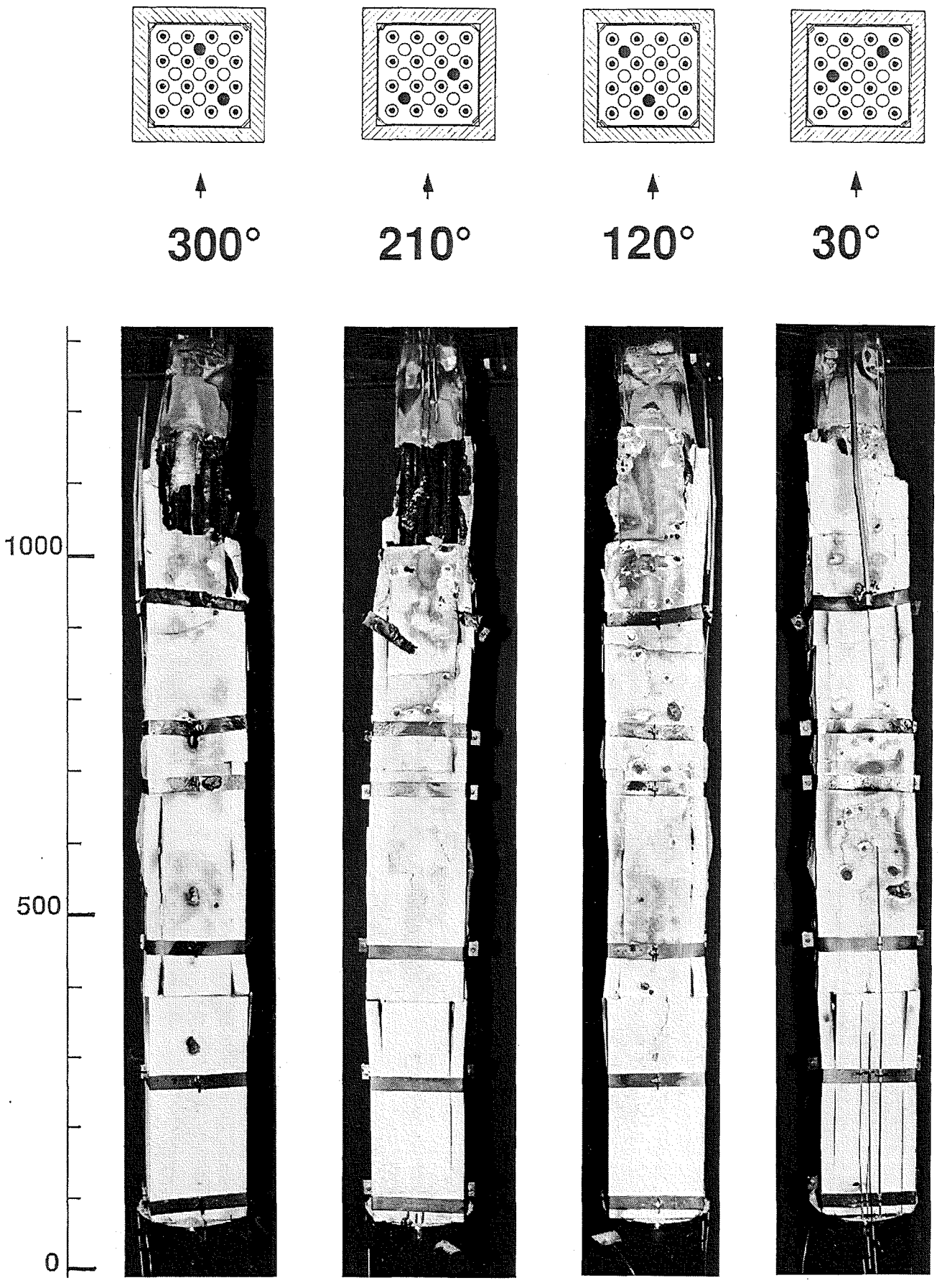

Fig. 84: CORA-29; Posttest appearance of bundle, shroud and shroud insulation; 300°, 210°, 120°, 30° orientation

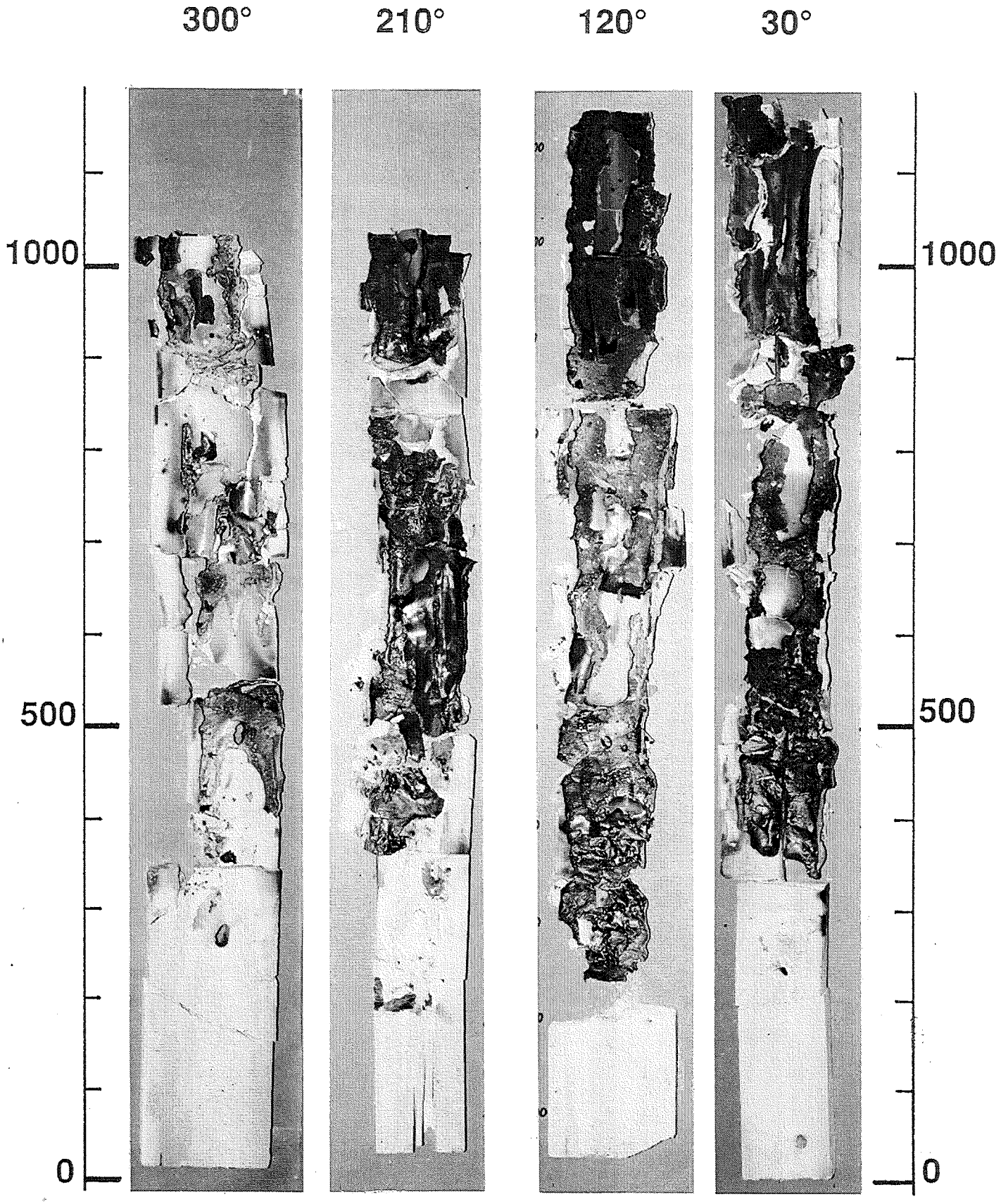

Fig. 85: CORA-29; Posttest view of the inner side of shroud insulation; 300°, 210°, 120°, 30° orientation

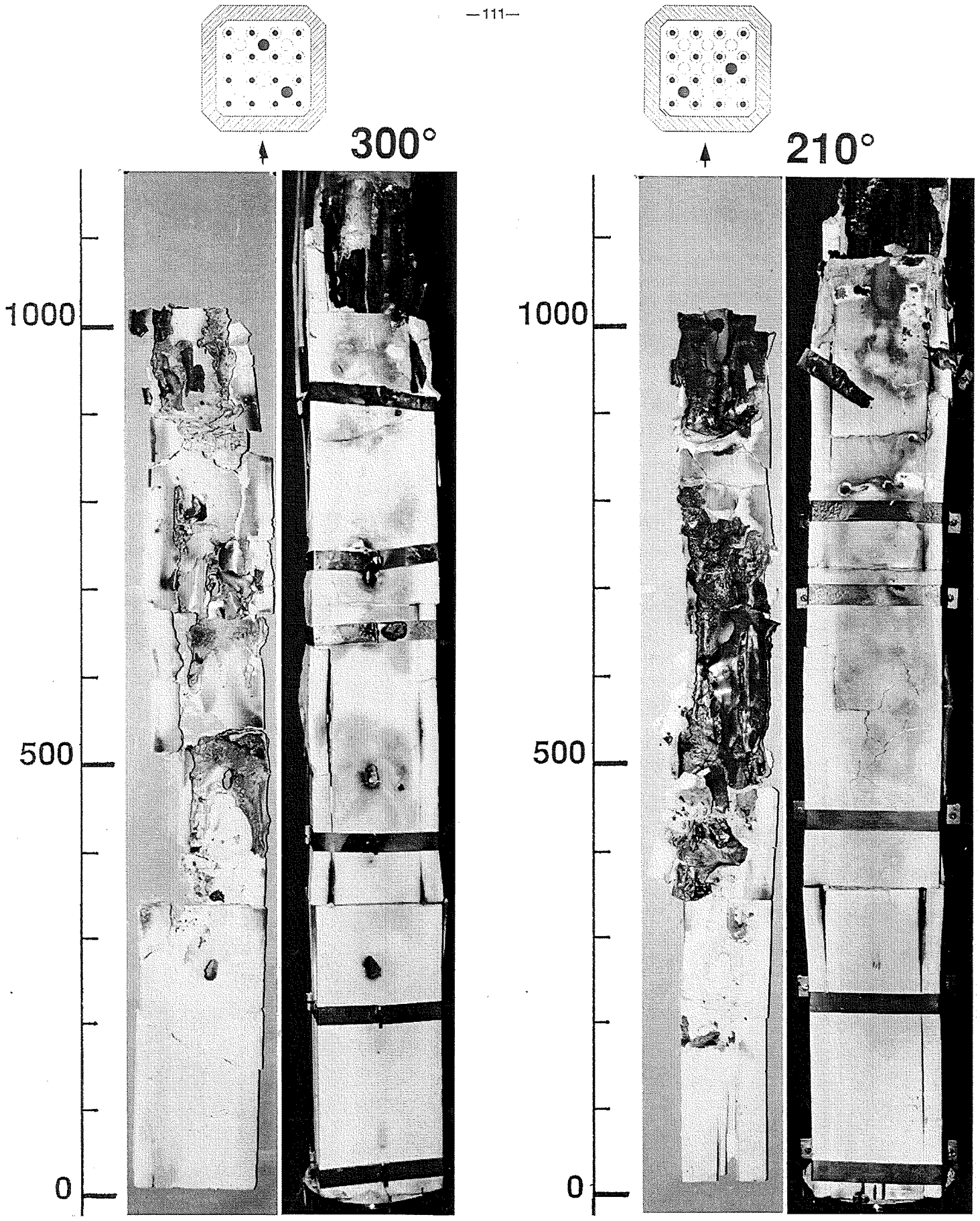

Fig. 86: CORA-29; Comparison of inner and outer side of shroud insulation; 300° and 210° orientation

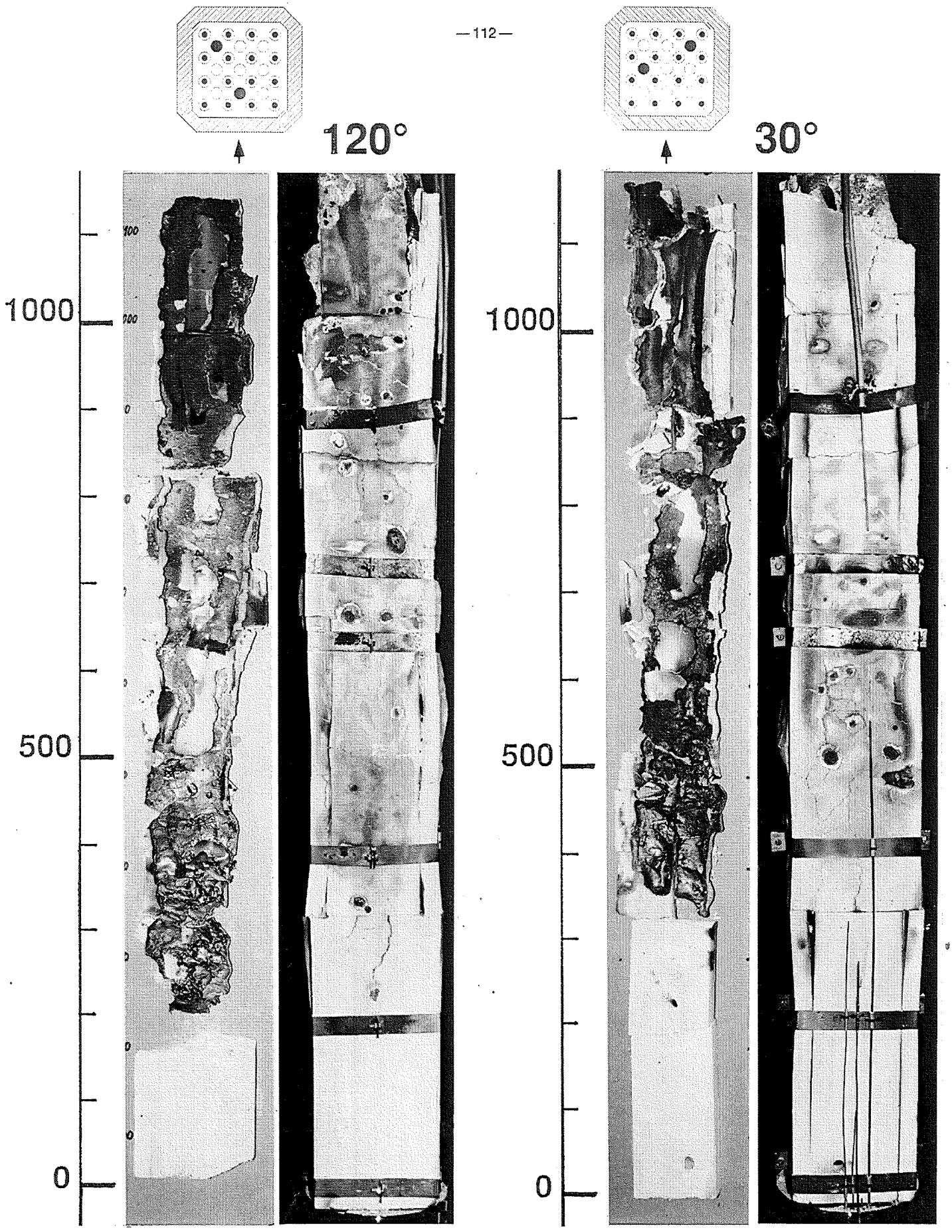

Fig. 87: CORA-29; Comparison of inner and outer side of shroud insulation; 120° and 30° orientation

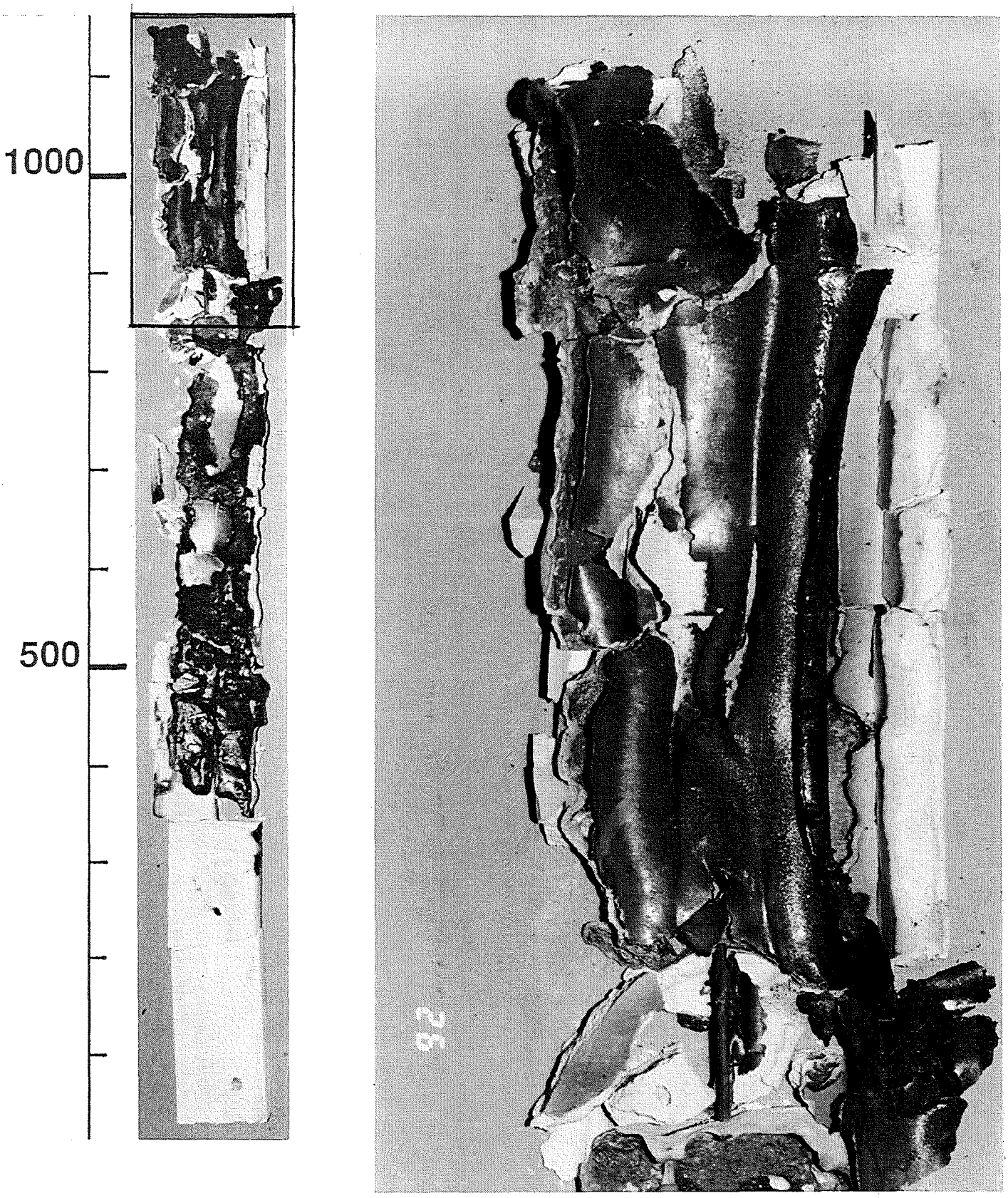

Fig. 88: CORA-29; Posttest view of the inner side of shroud insulation; 30° orientation, 850-1150 mm elevation

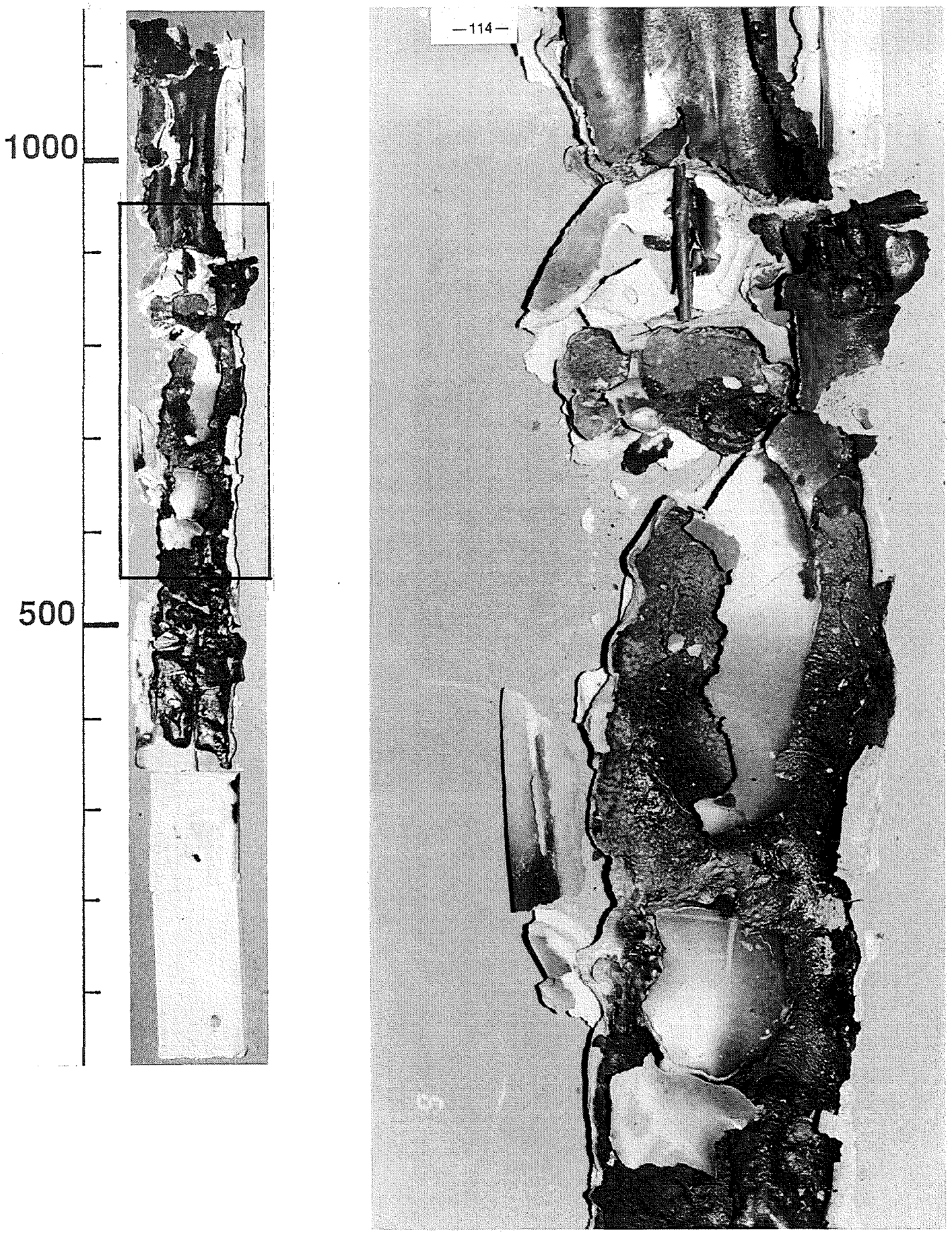

Fig. 89: CORA-29; Posttest view of the inner side of shroud insulation; 30° orientation, 550-950 mm elevation

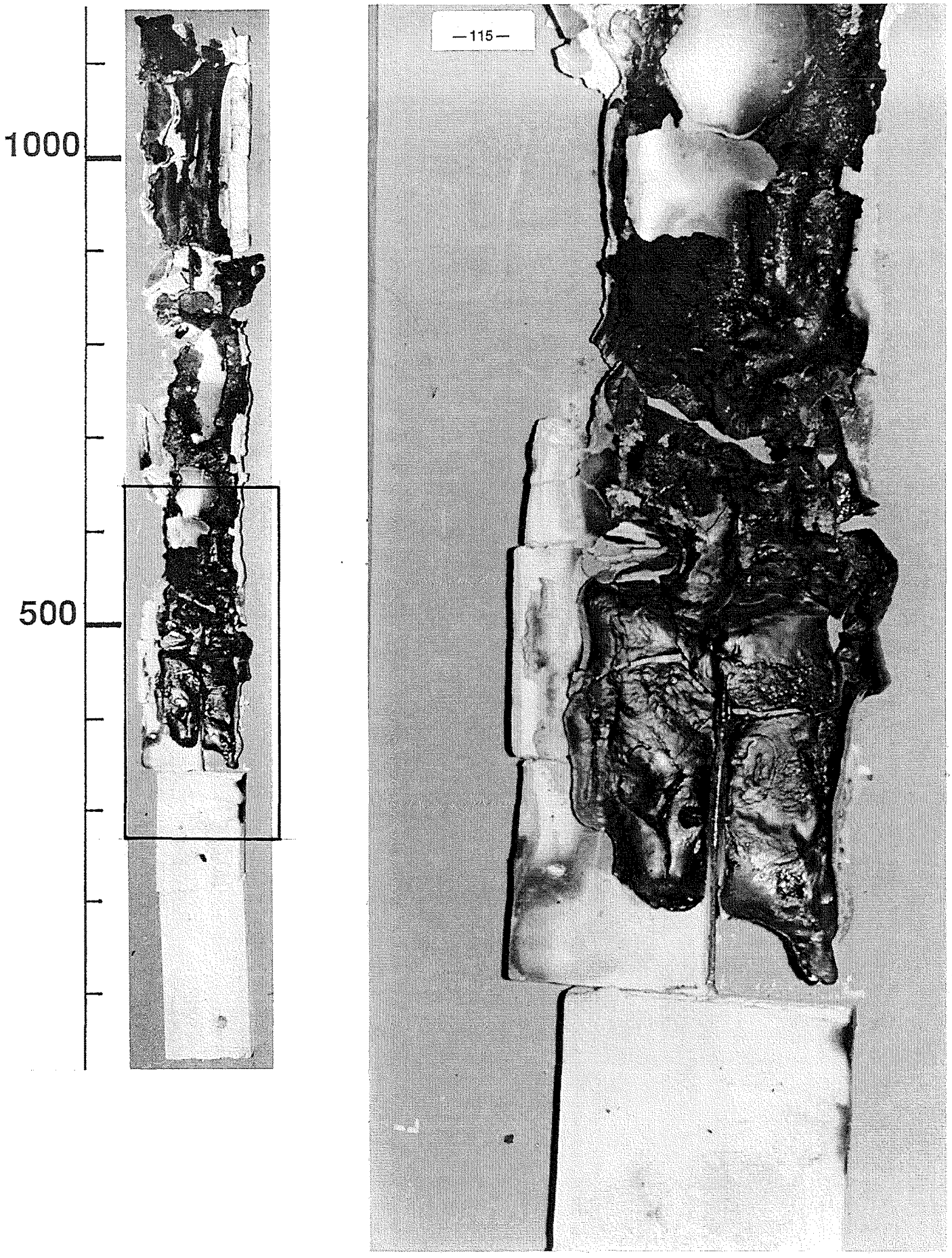

Fig. 90: CORA-29; Posttest view of the inner side of shroud insulation; 30° orientation, 350-650 mm elevation

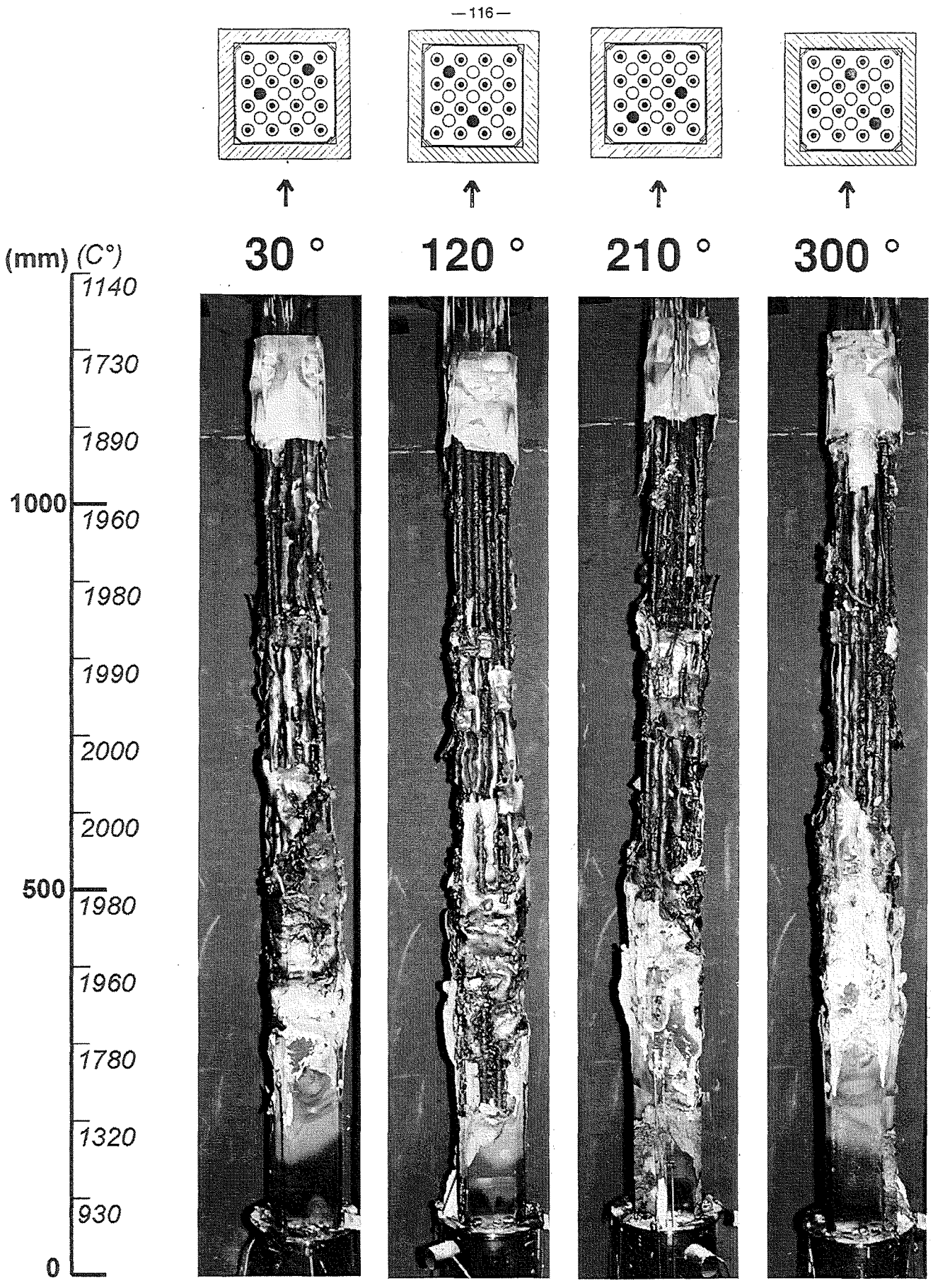

Fig. 91: Posttest view of bundle CORA-29 after partial removal of shroud;
300°, 210°, 120°, 30° orientation

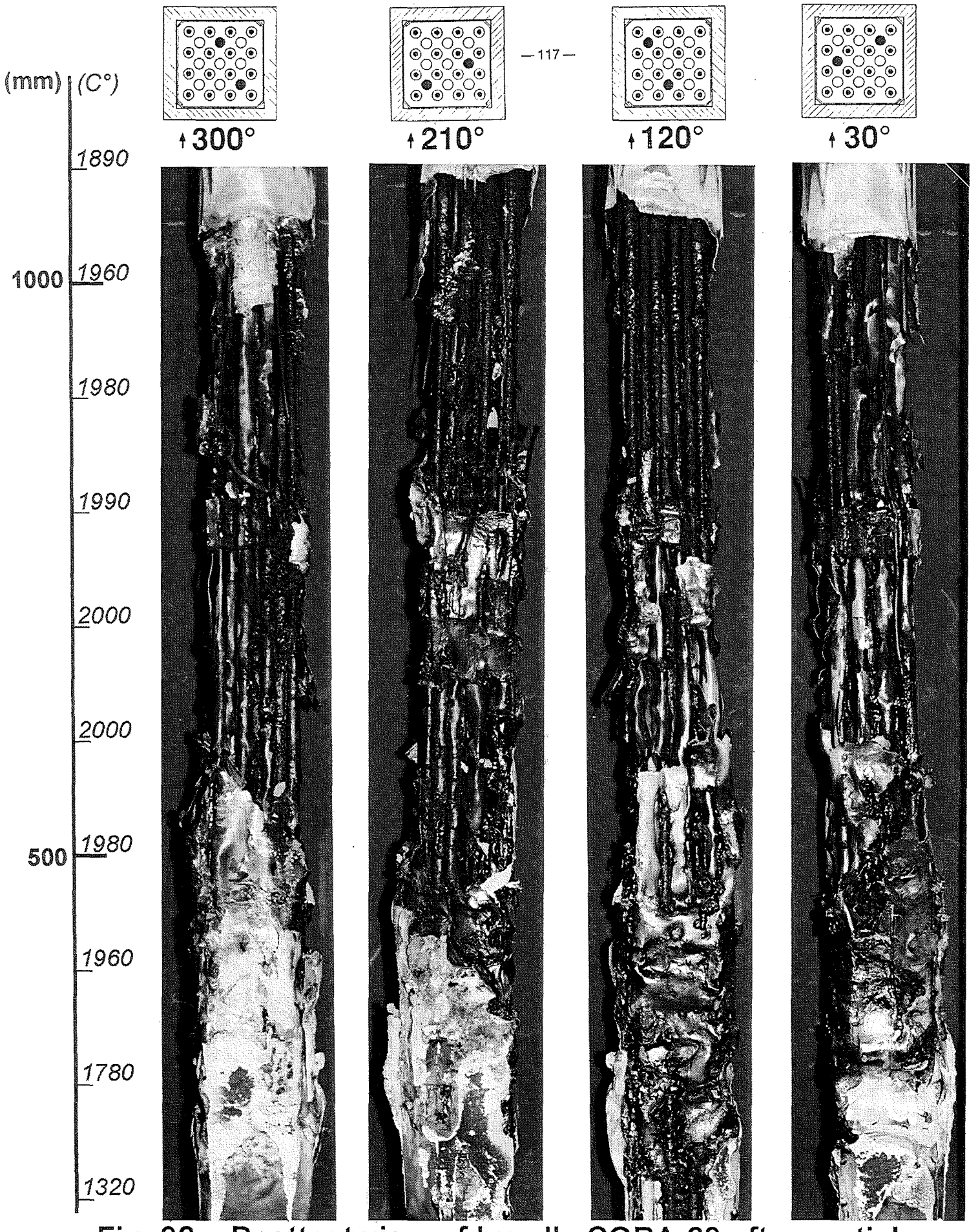

Fig. 92: Posttest view of bundle CORA-29 after partial removal of shroud; 300°, 210°, 120°, 30° orientation; 200 - 1100 mm elevation

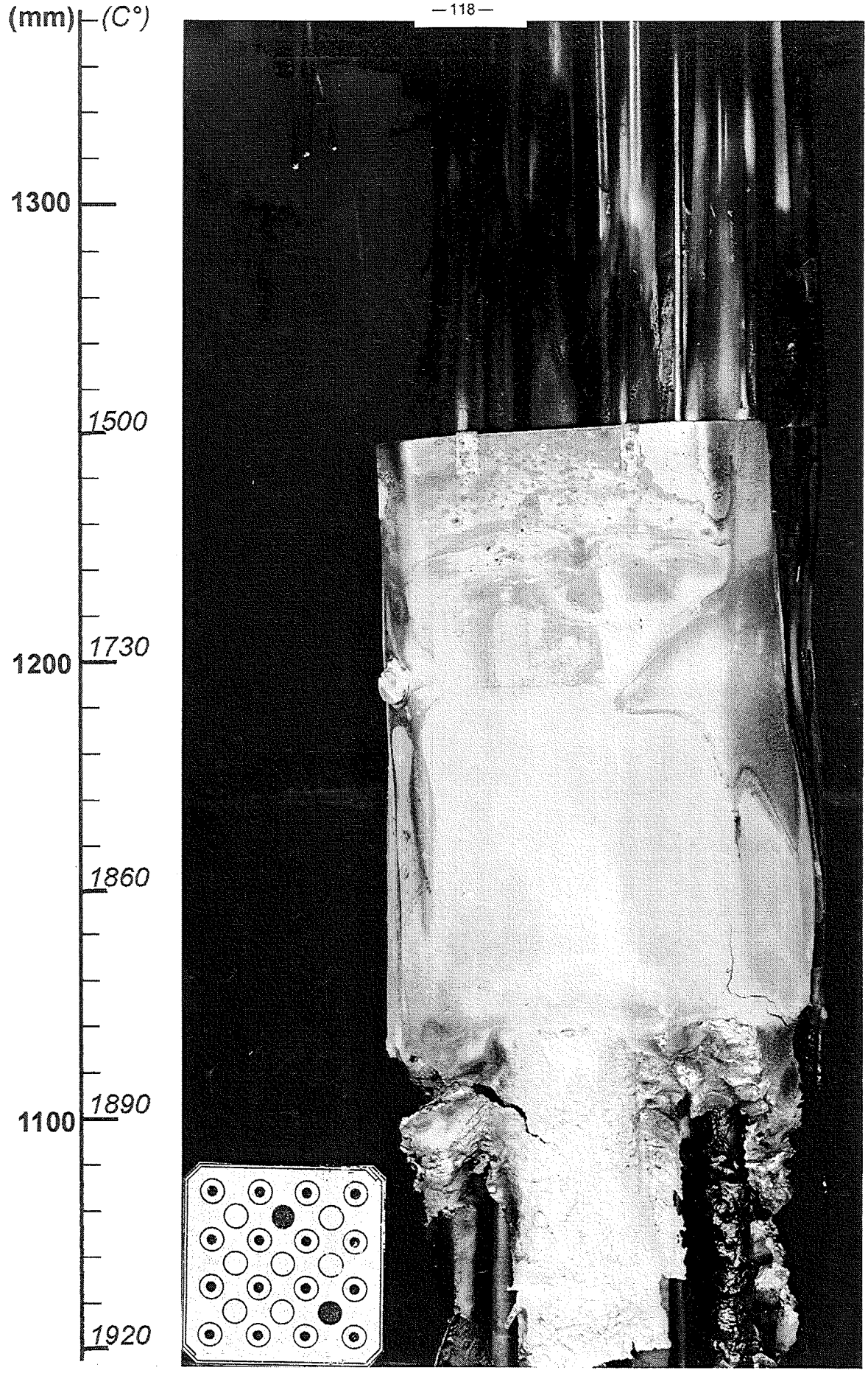

Fig. 93: CORA-29; Posttest view of bundle, 300° partial view, 1050-1350 mm

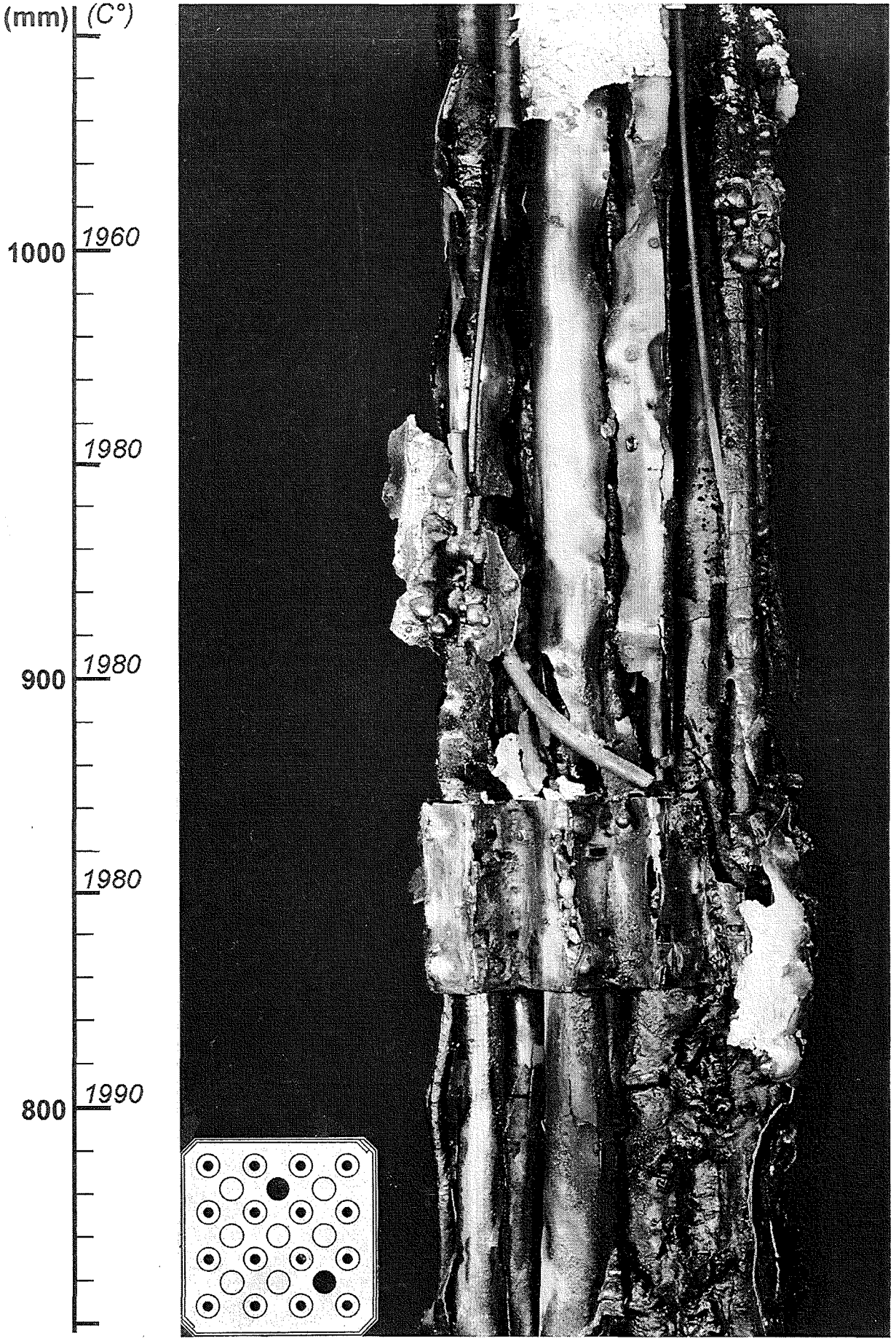

Fig. 94: CORA-29; Posttest view of bundle, 300° partial view, 750-1050 mm

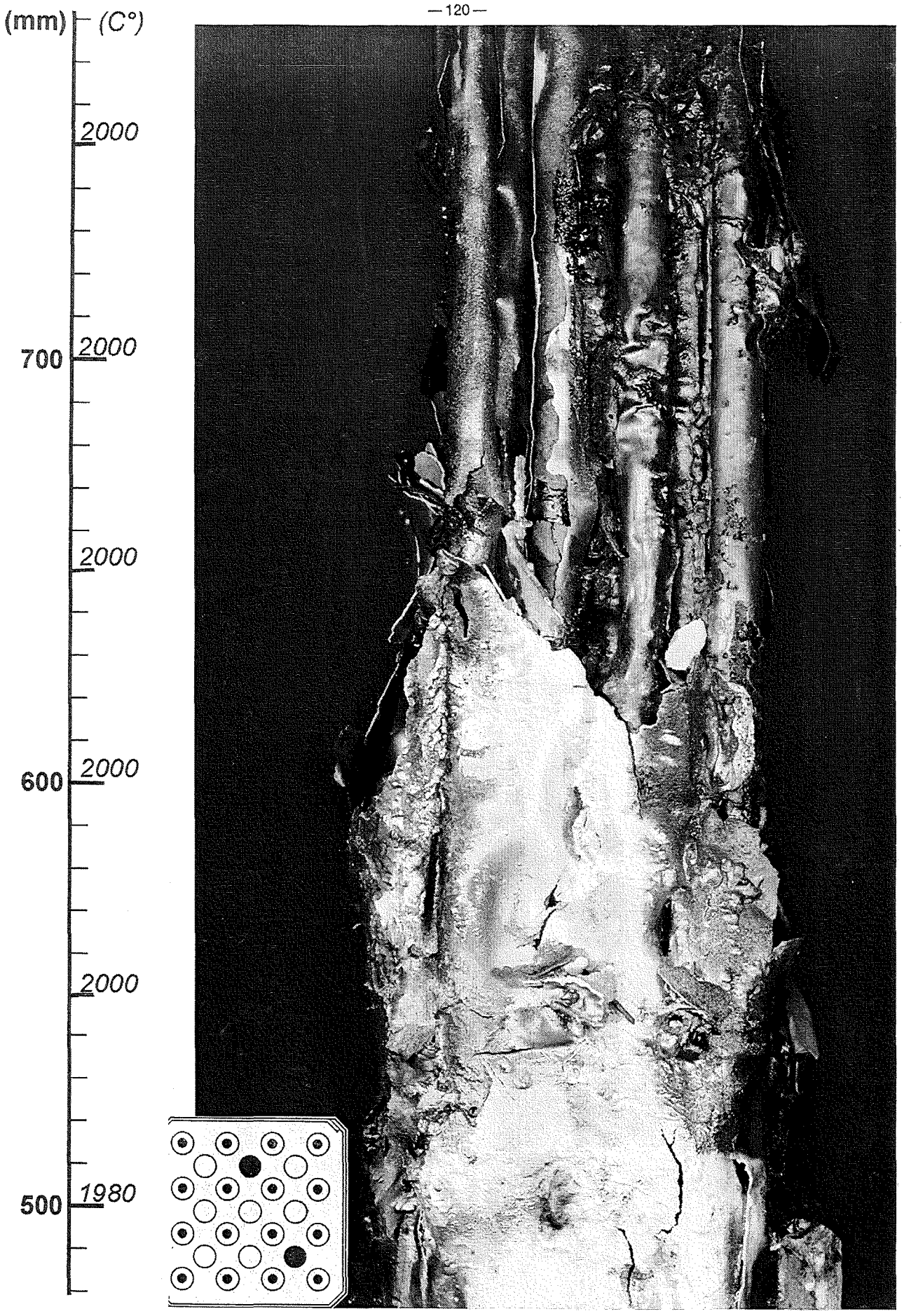

Fig. 95: CORA-29; Posttest view of bundle, 300° partial view, 500-750 mm

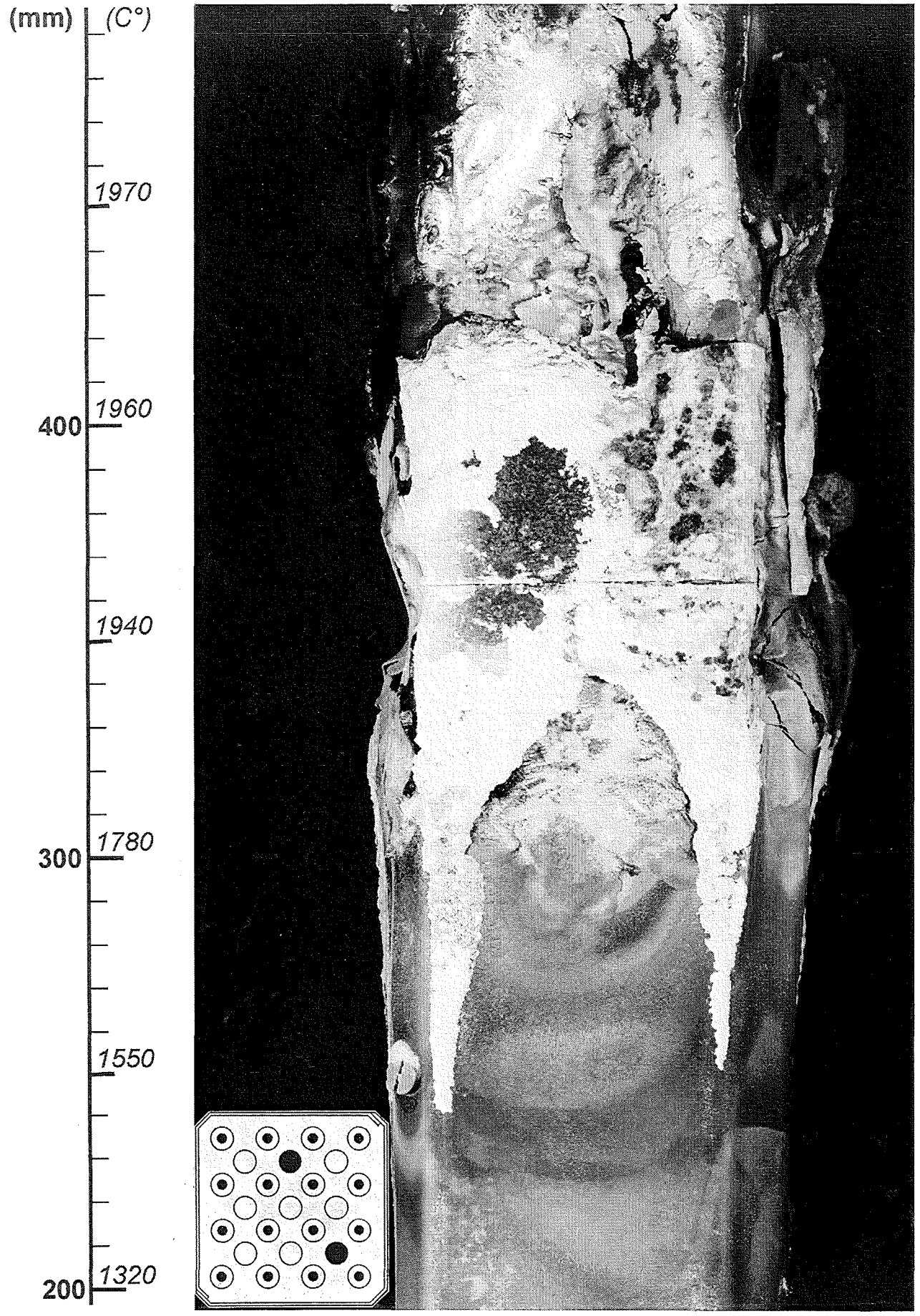

Fig. 96: CORA-29; Posttest view of bundle, 300° partial view, 200-500 mm

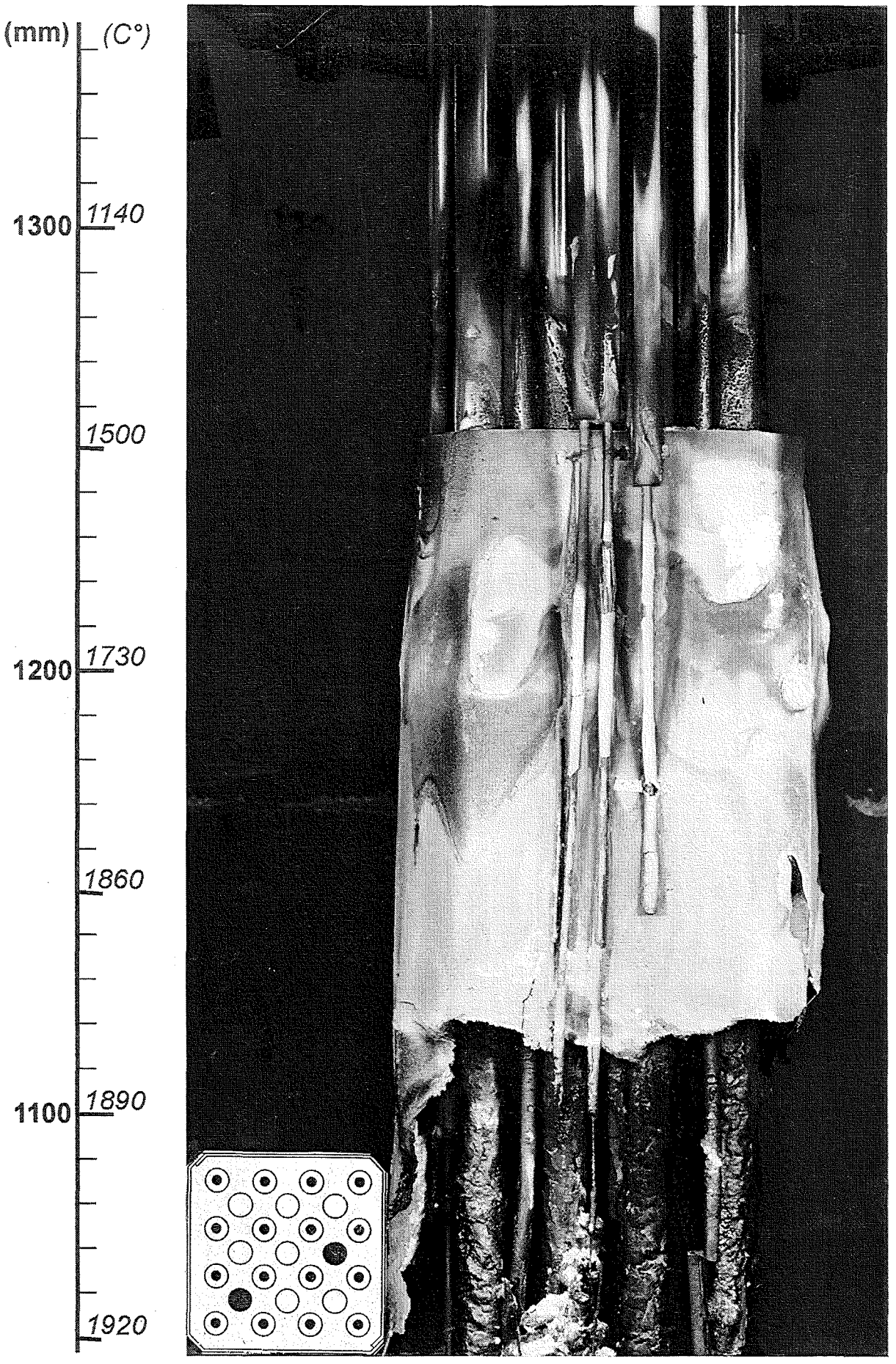

Fig. 97: CORA-29; Posttest view of bundle, 210° partial view, 1050-1350 mm

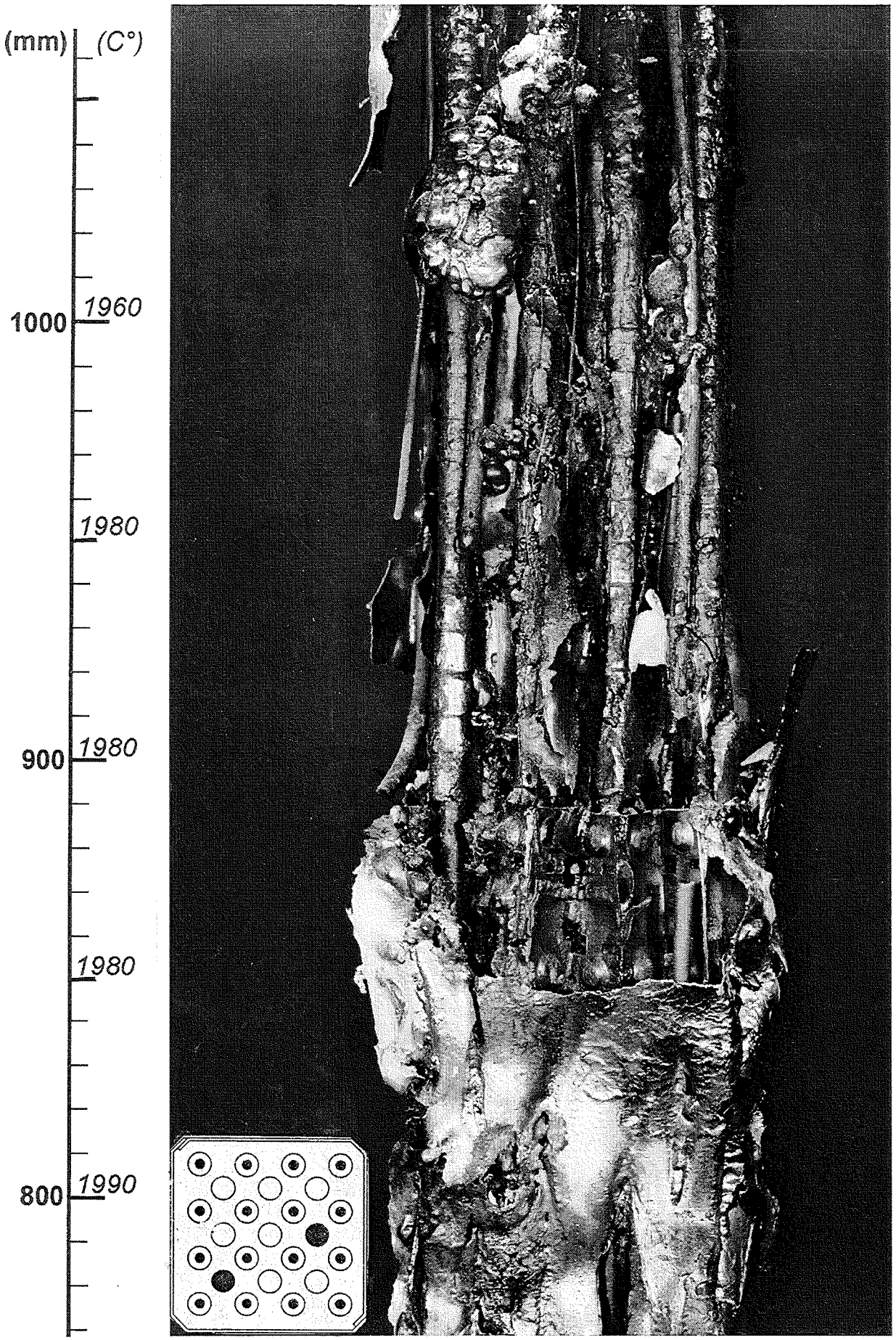

Fig. 98: CORA-29; Posttest view of bundle, 210° partial view, 750-1050 mm

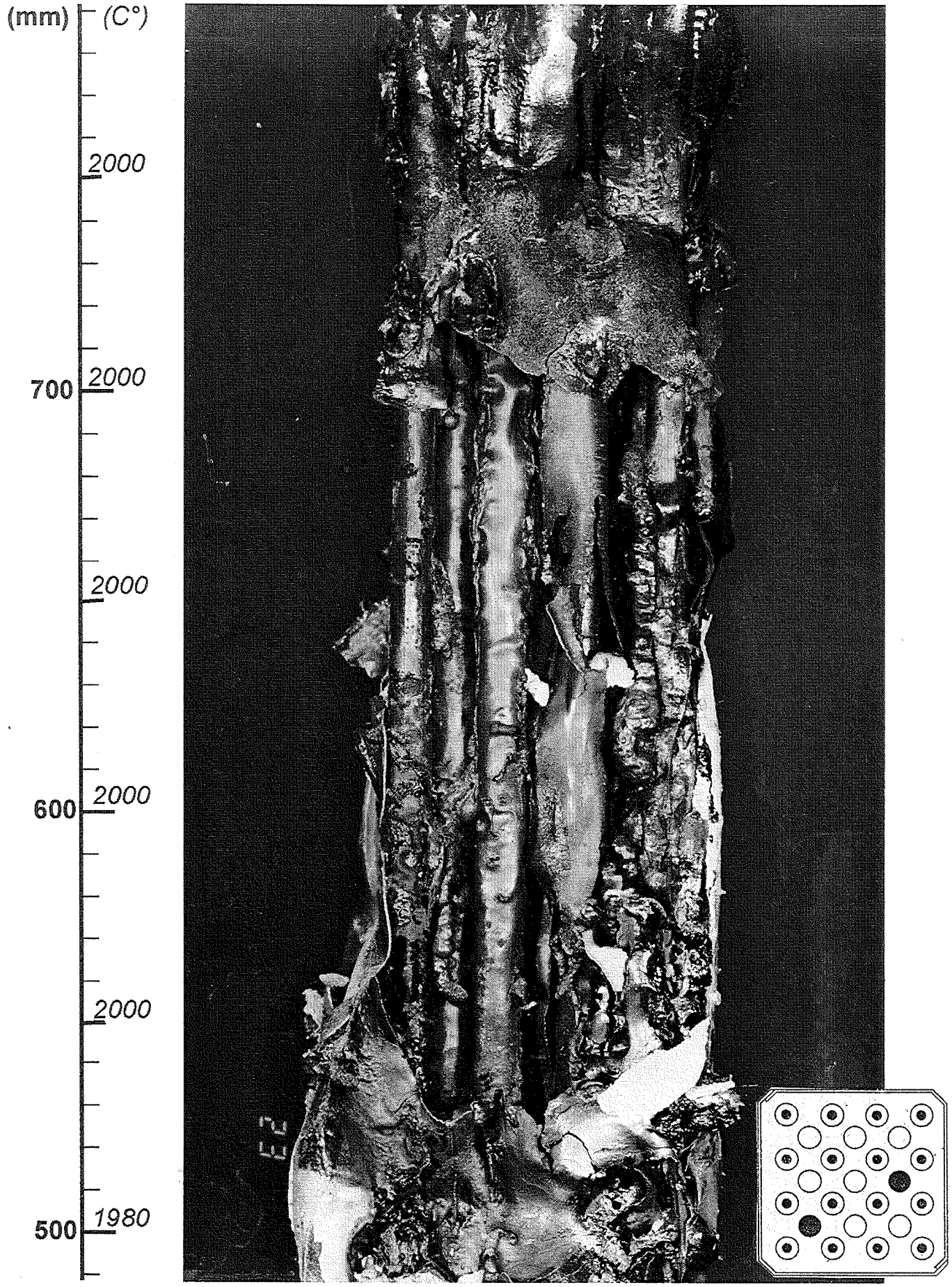

Fig. 99: CORA-29; Posttest view of bundle, 210° partial view, 500-800 mm

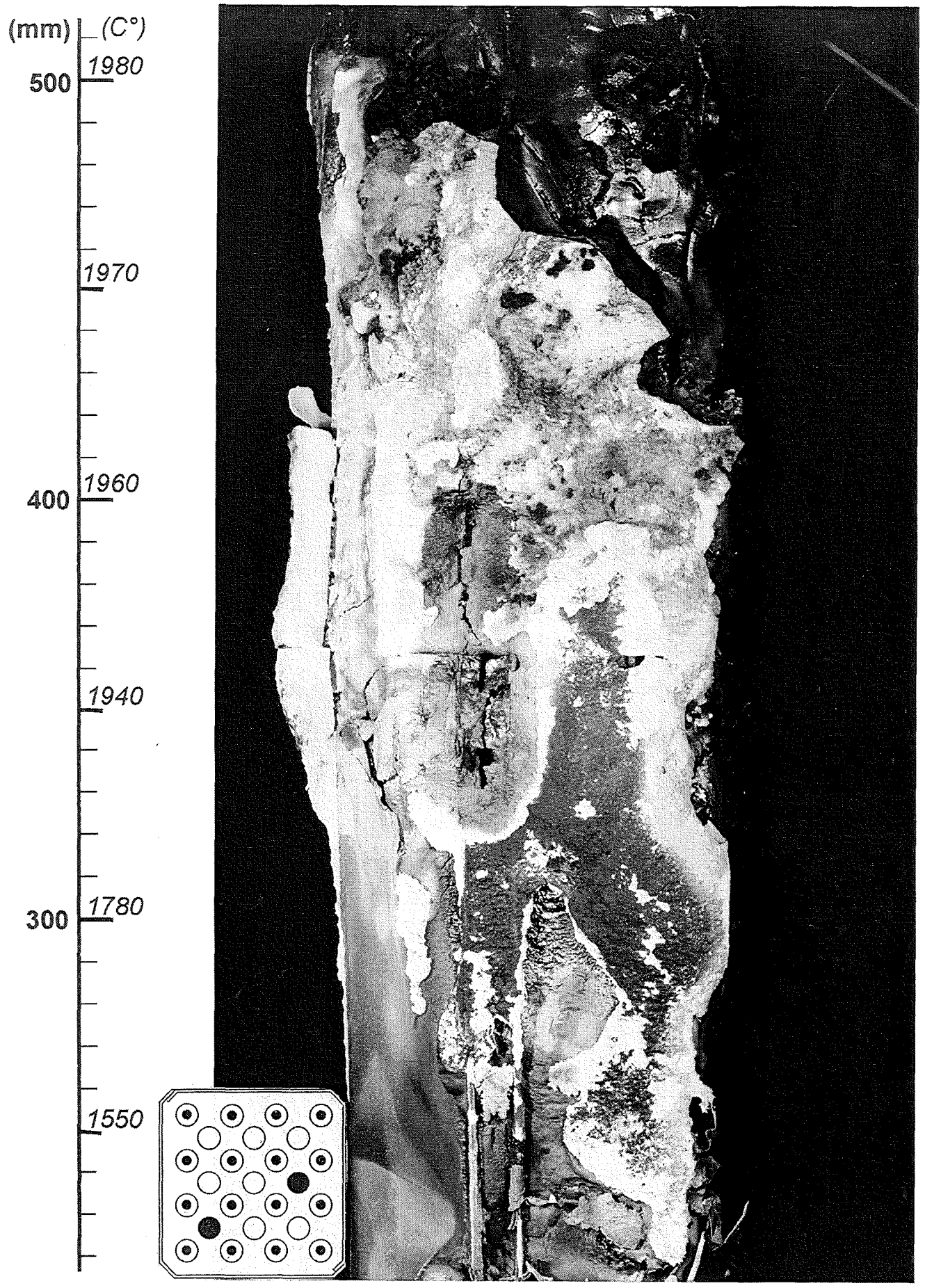

Fig. 100: CORA-29; Posttest view of bundle, 210° partial view, 200-500 mm

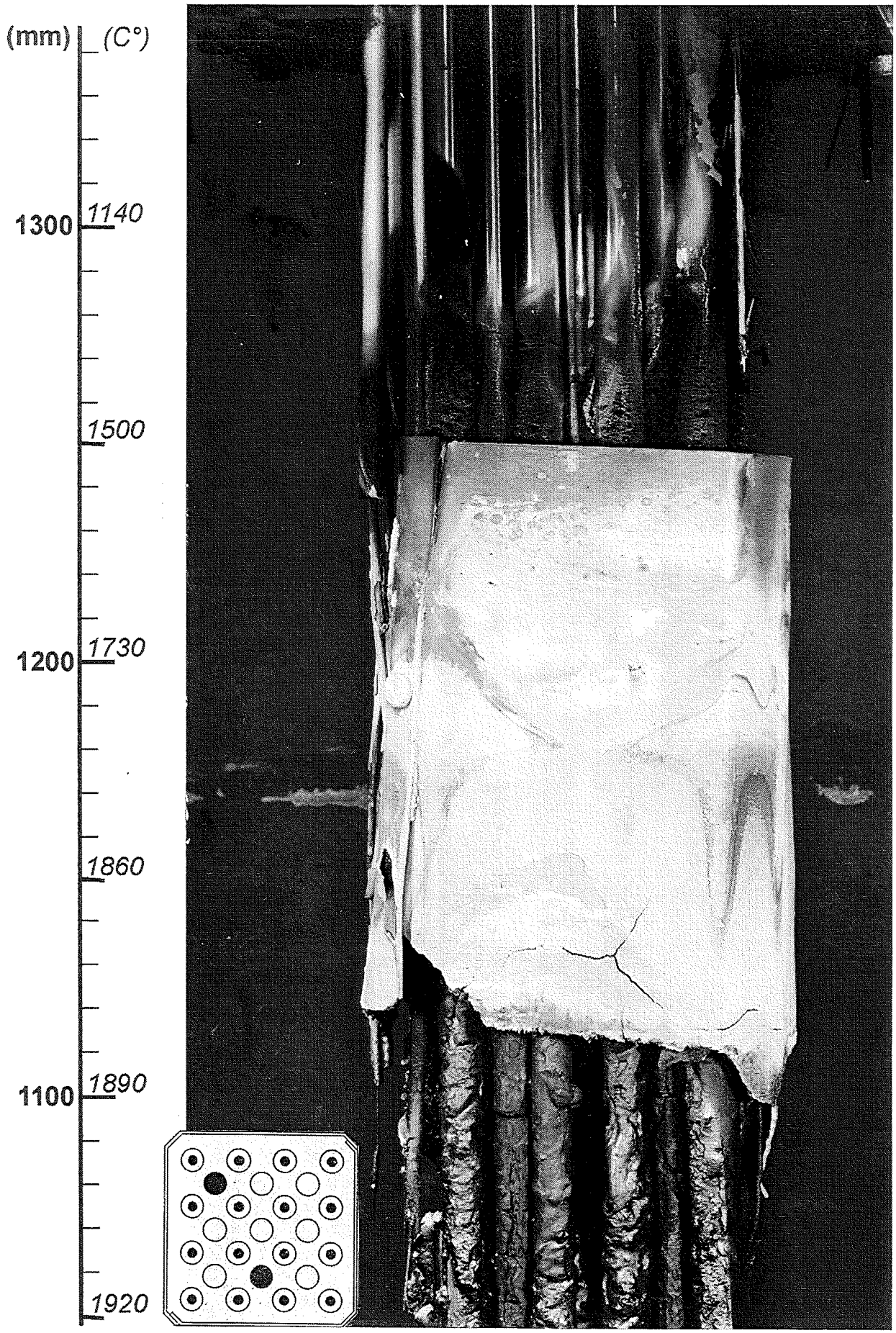

Fig. 101: CORA-29; Posttest view of bundle, 120° partial view, 1050-1350 mm

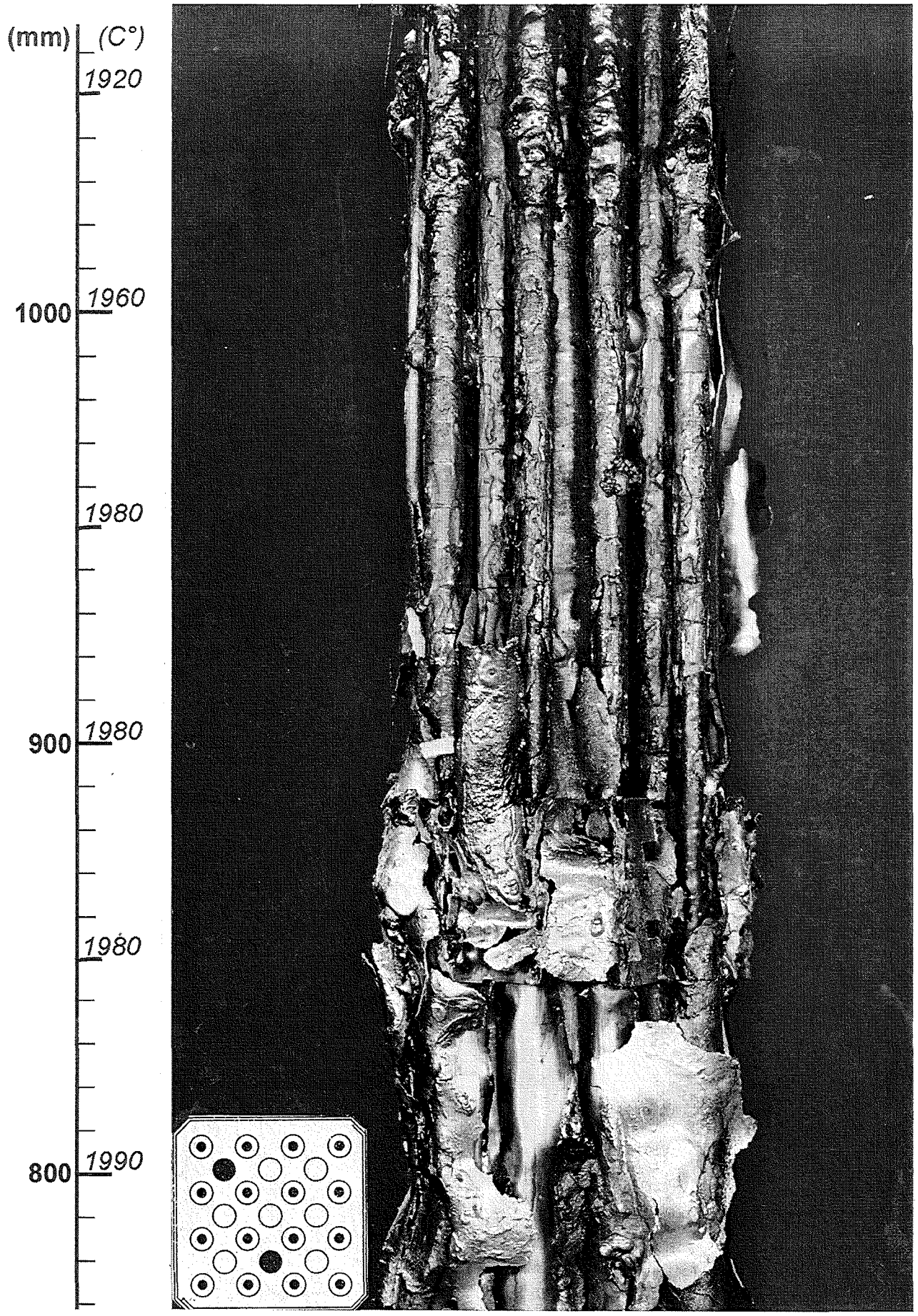

Fig. 102: CORA-29; Posttest view of bundle, 120° partial view, 750-1050 mm

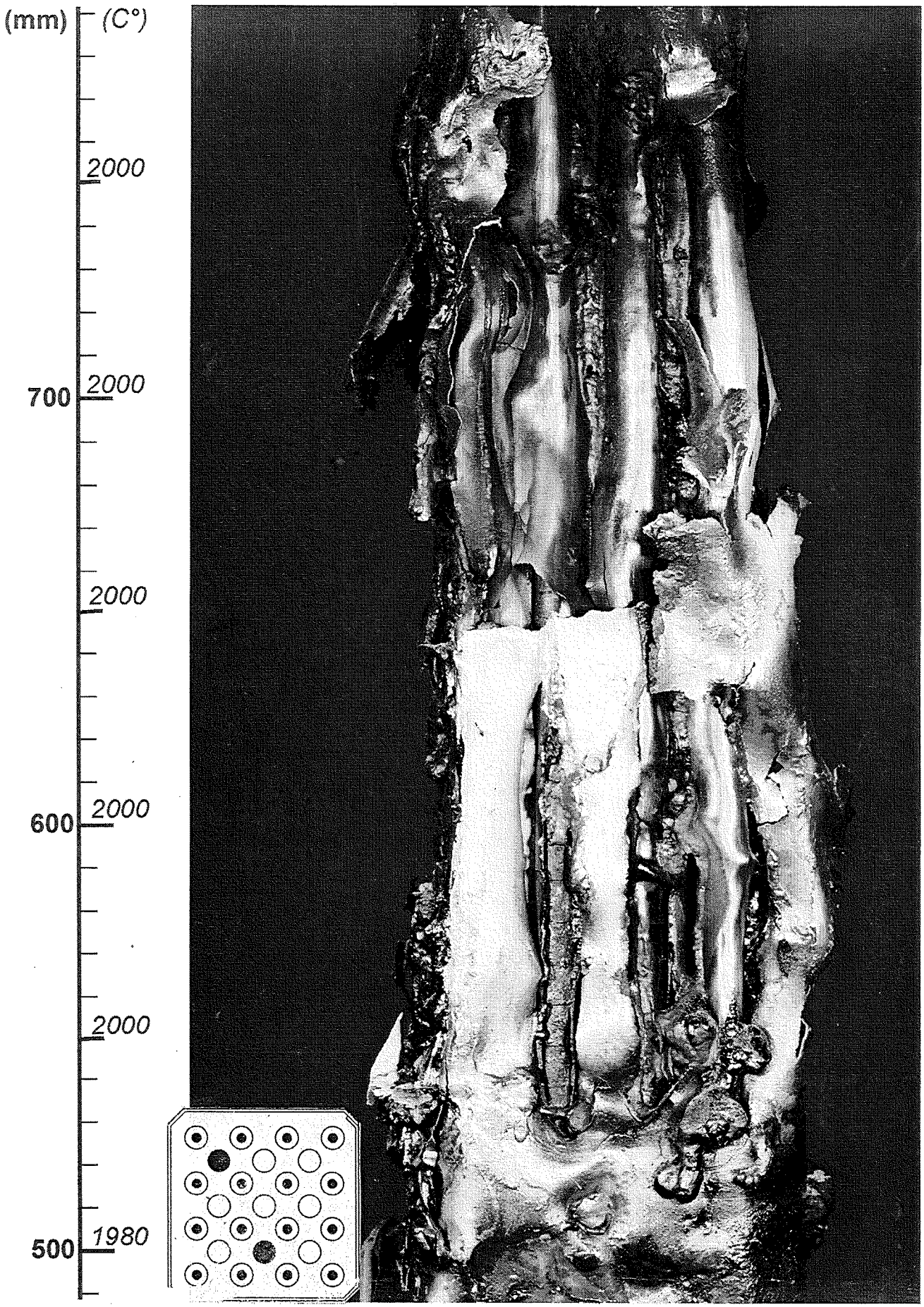

Fig. 103: CORA-29; Posttest view of bundle, 120° partial view, 500-800 mm

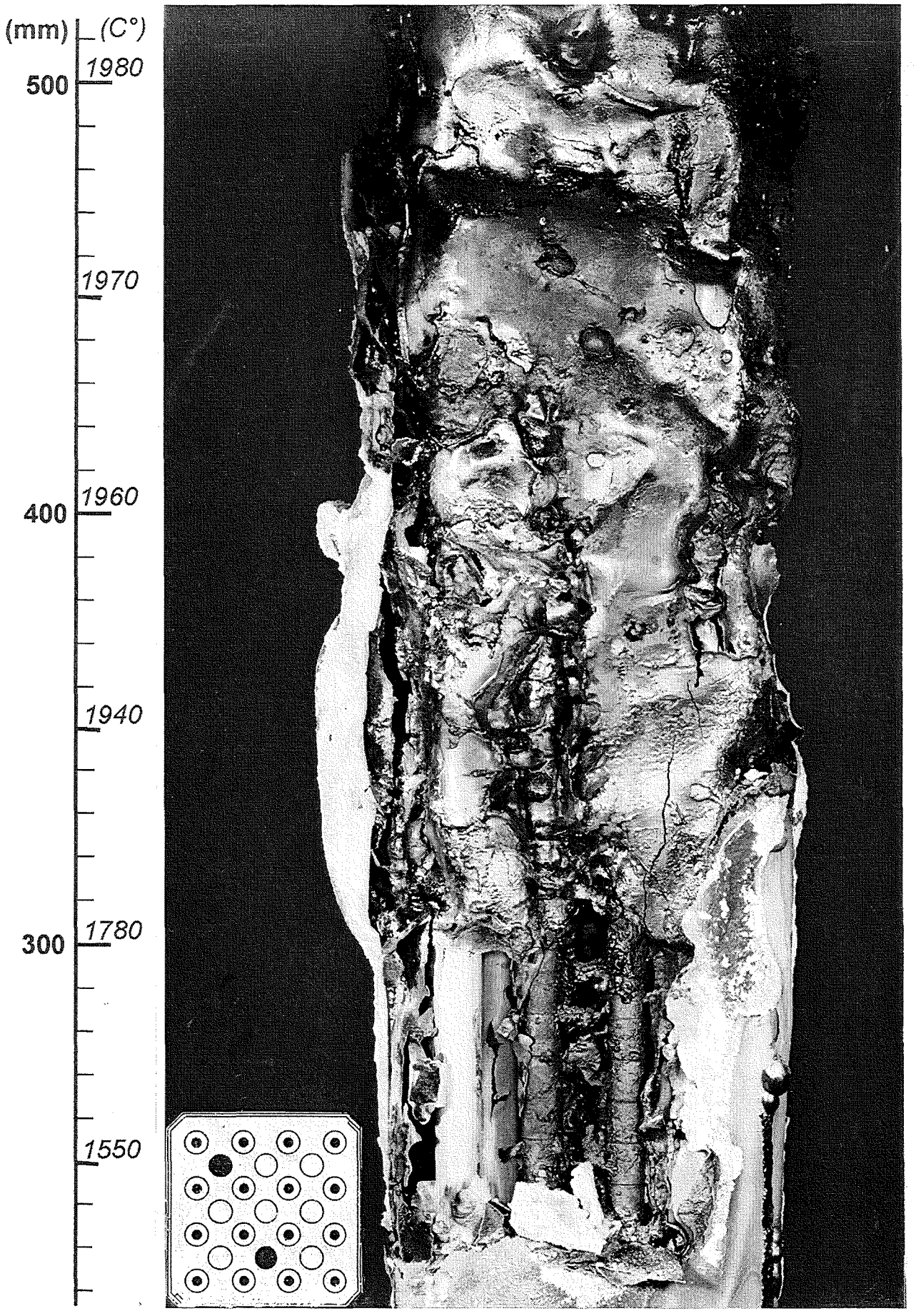

Fig. 104: CORA-29; Posttest view of bundle, 120° partial view, 200-500 mm

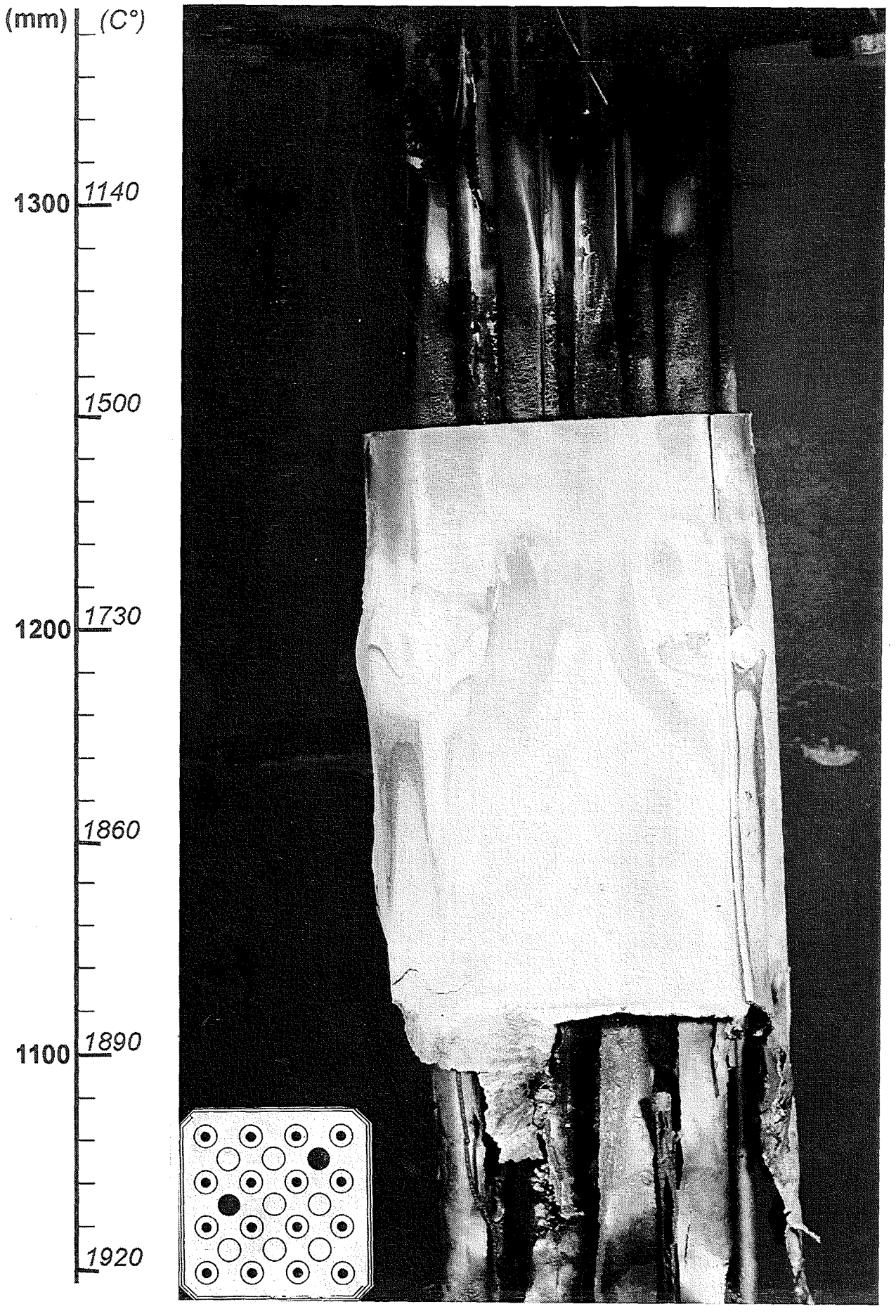

Fig. 105: CORA-29; Posttest view of bundle, 30° partial view, 1050-1350 mm

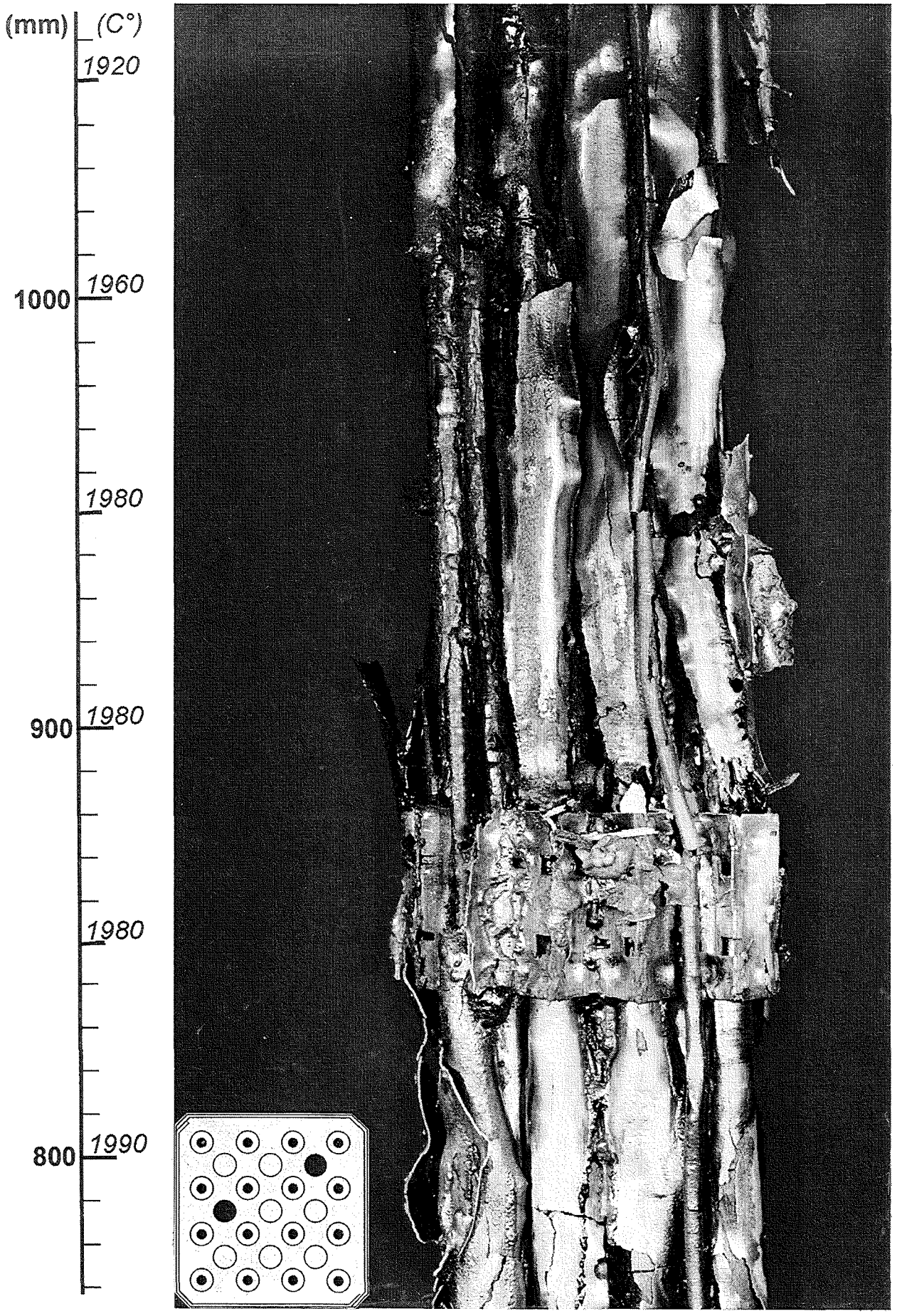

Fig. 106: CORA-29; Posttest view of bundle, 30° partial view, 750-1050 mm

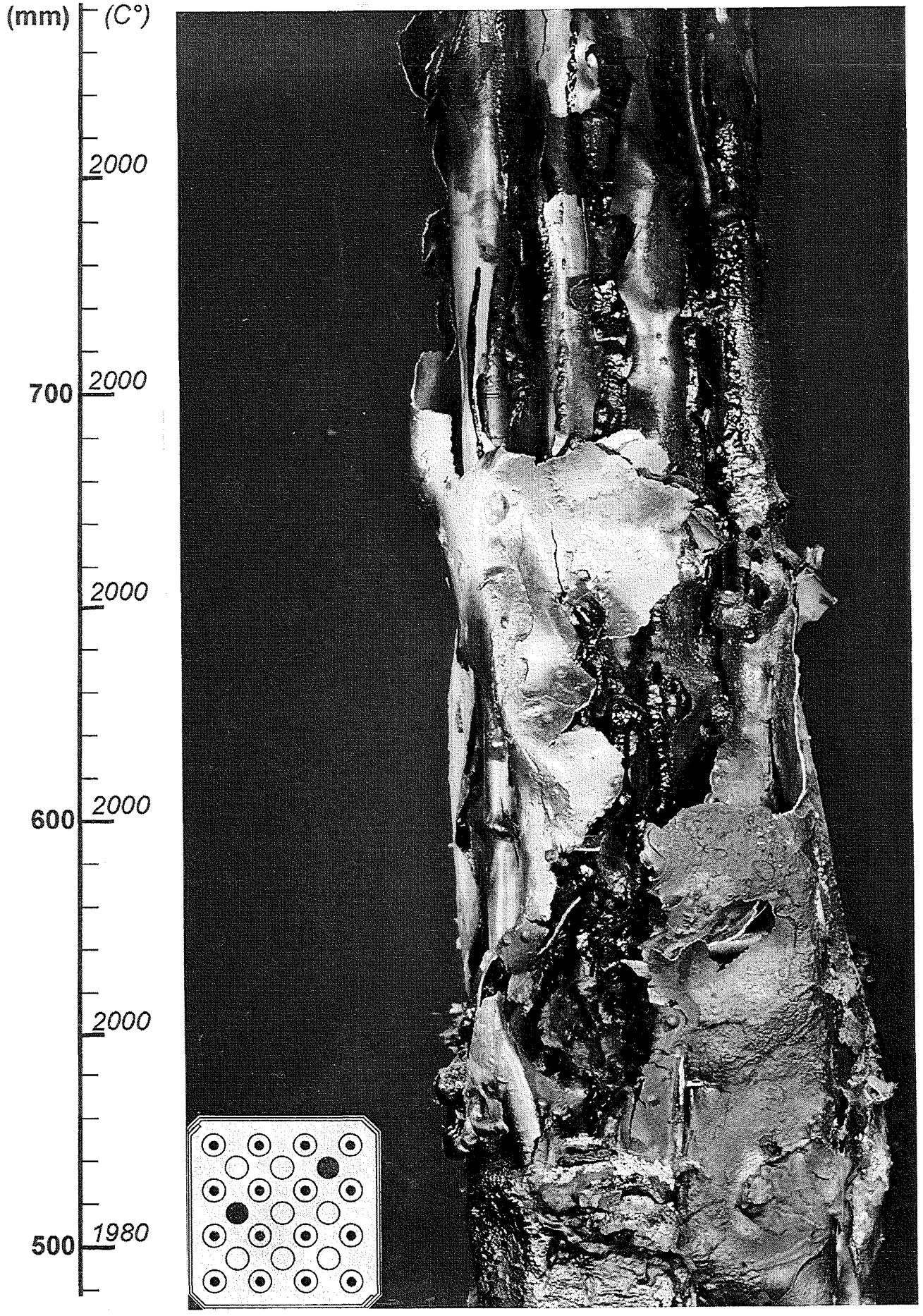

Fig. 107: CORA-29; Posttest view of bundle, 30° partial view, 500-800 mm

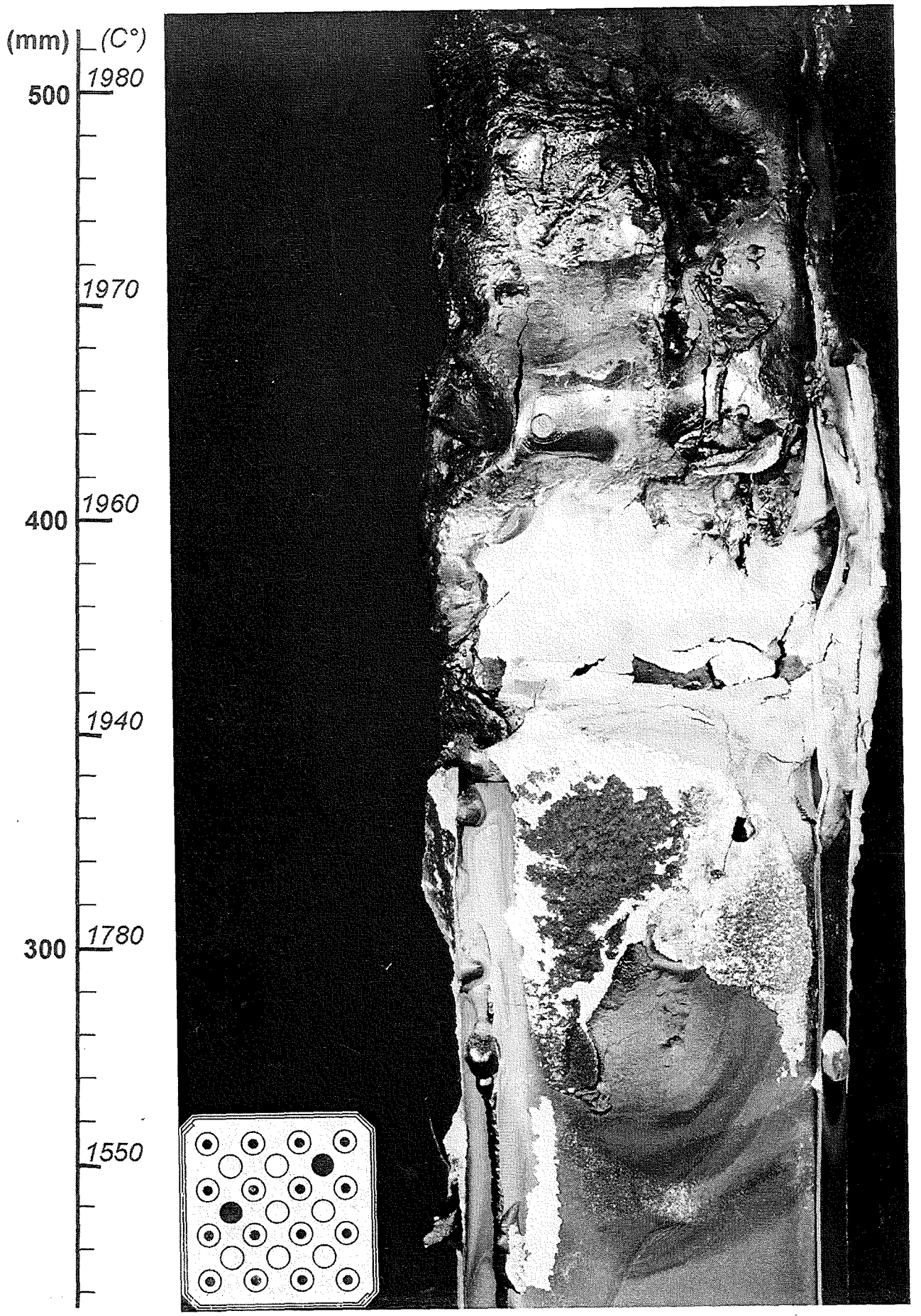

Fig. 108: CORA-29; Posttest view of bundle, 30° partial view, 200-500 mm

Fig. 108a: CORA-29: Refrozen melt at the lower end of the bundle seen in 120° direction

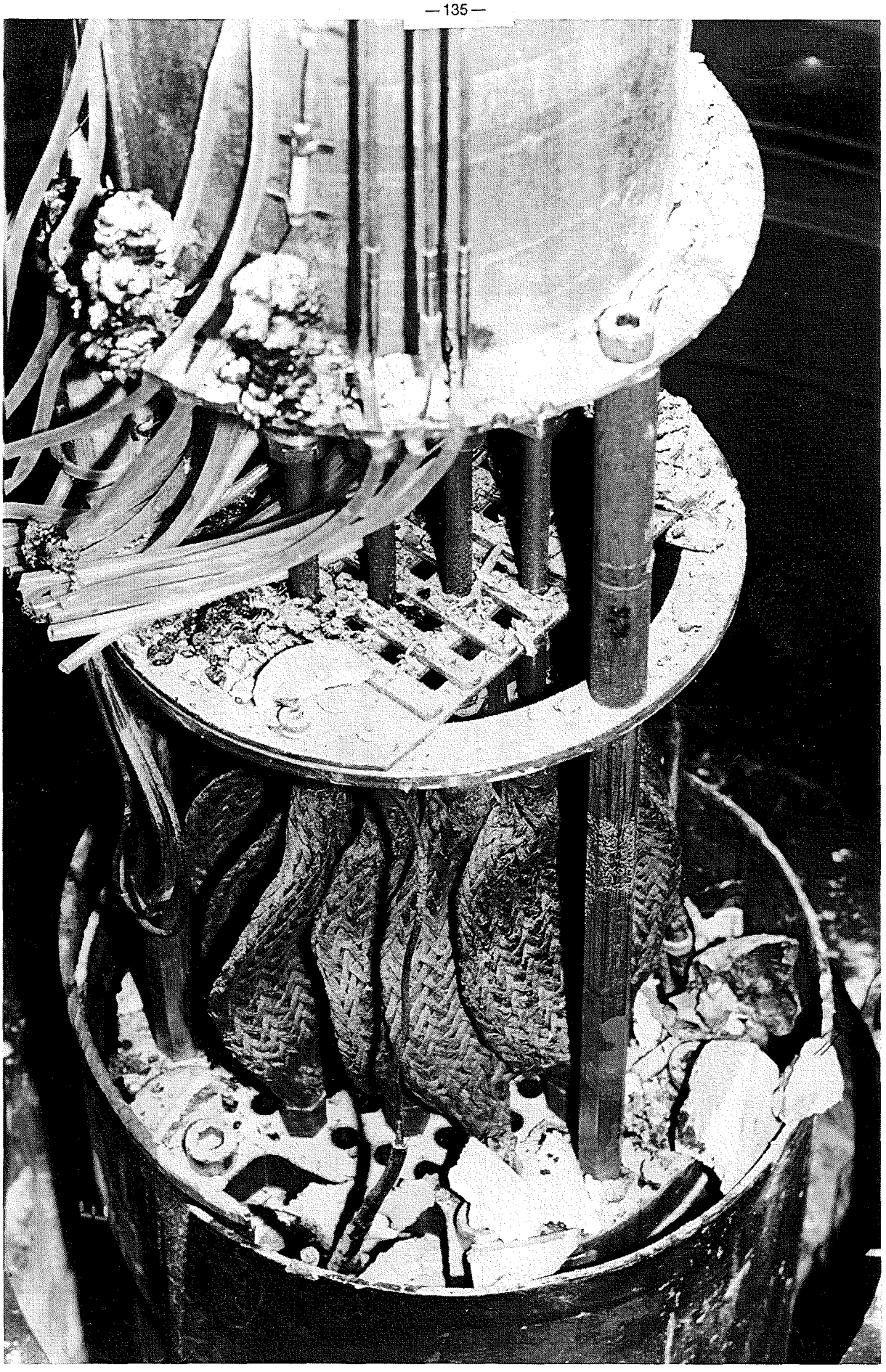

Fig. 108b: CORA-29: Refrozen melt at the lower end of the bundle seen in 210° direction

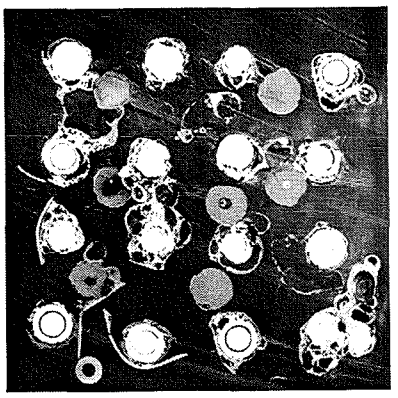

1029mm 1940°C

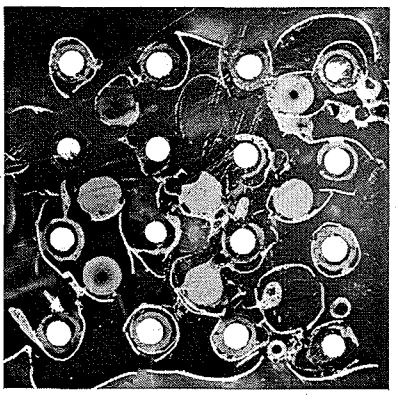

568 mm 2000°C

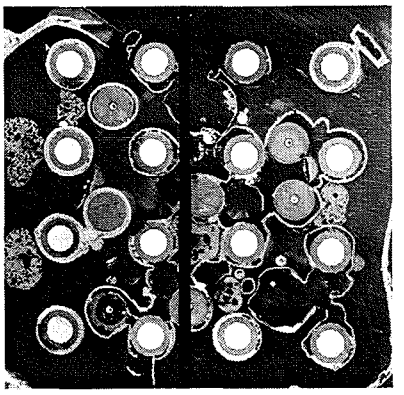

254mm 1540°C

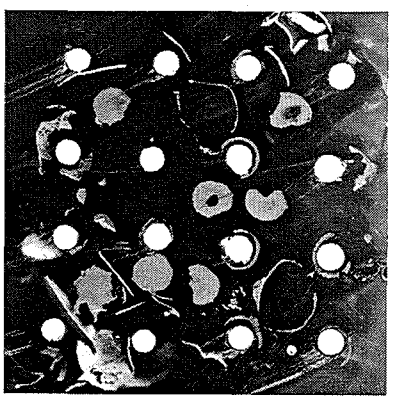

887mm 1995°C

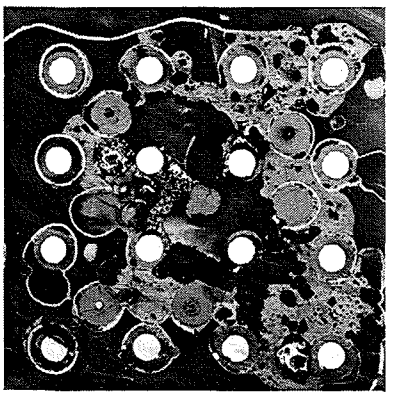

426mm 1965°C

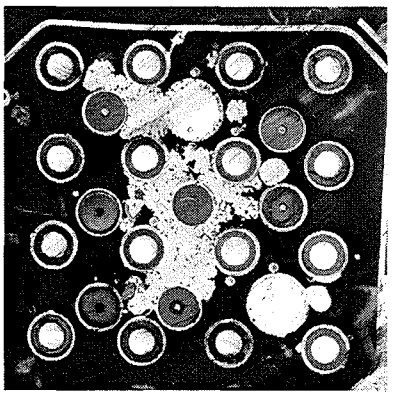

112mm 1005°C

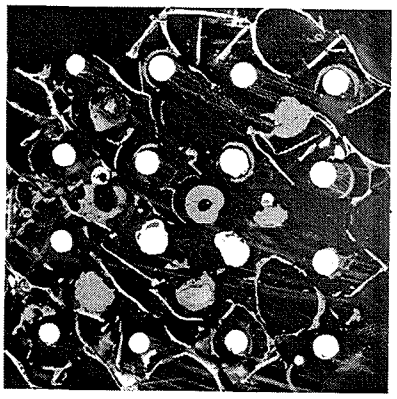

872mm 1975°C

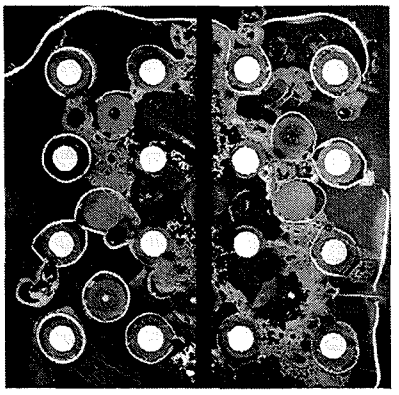

411mm 1965°C

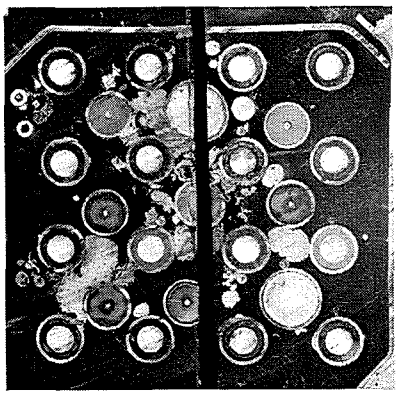

97mm 1005°C

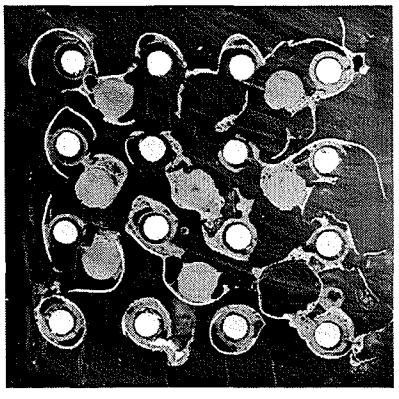

725mm 2000°C

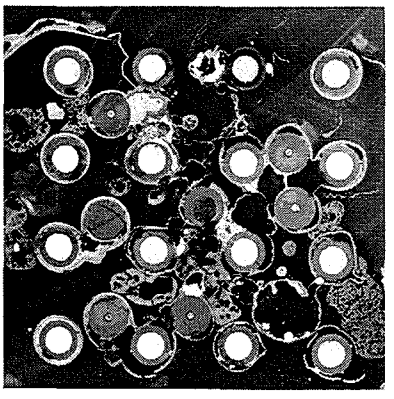

269mm 1620°C

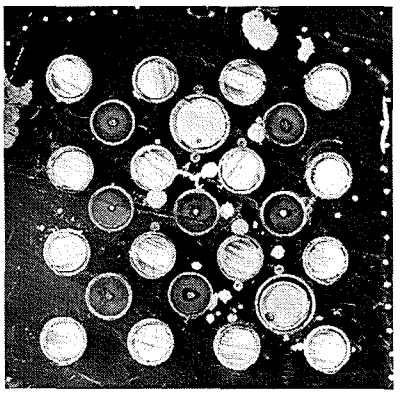

-45mm 670°C

Fig. 109: Horizontal cross sections of bundle CORA-29, top view

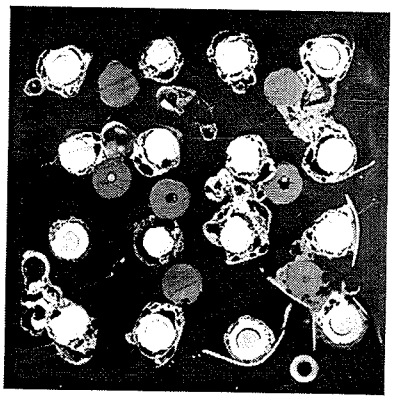

1031mm *1940C*

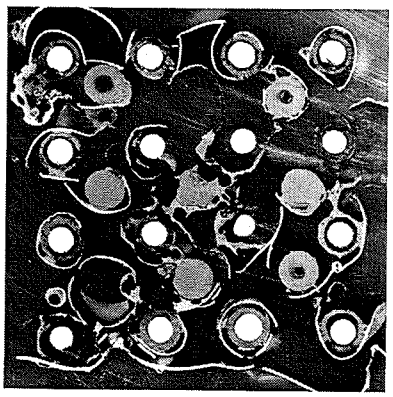

570 mm *2000°C*

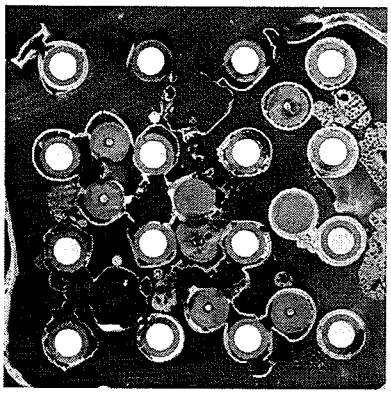

256mm *1540°C*

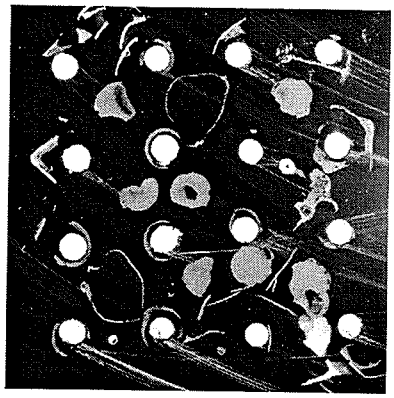

889mm *199511°C*

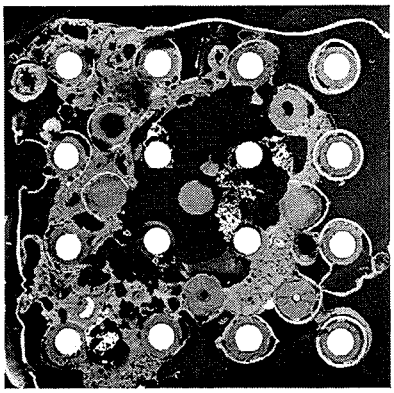

428mm *1965°C*

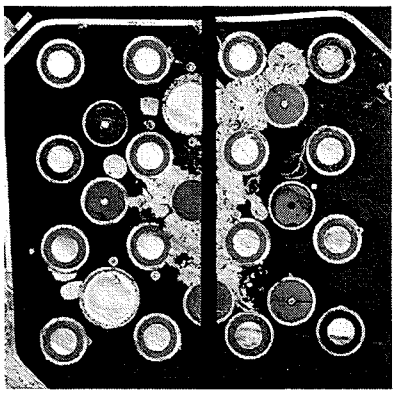

114mm *1005°C*

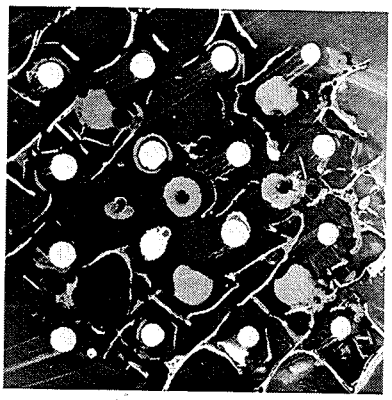

874mm *1975°C*

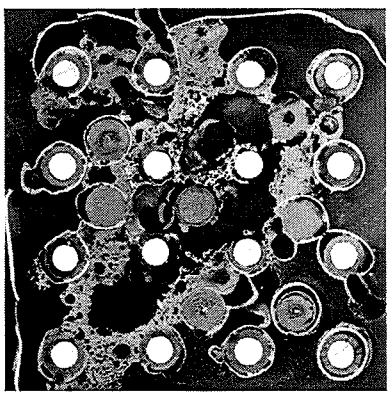

413mm *1965°C*

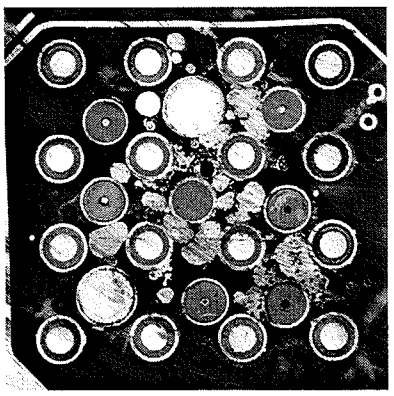

99mm *1005°C*

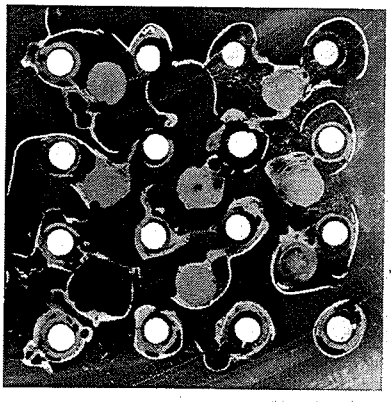

727mm *2000°C*

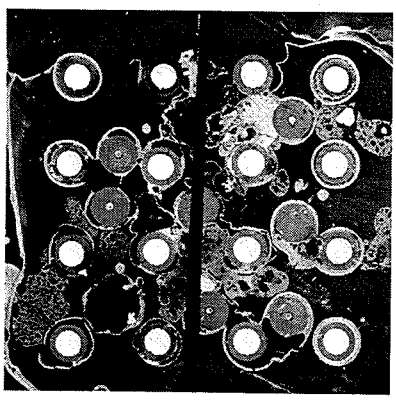

271mm *1620°C*

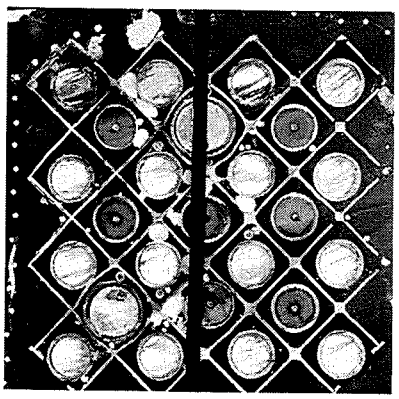

-43mm *670°C*

Fig 110: Horizontal cross sections of bundle CORA-29, bottom view

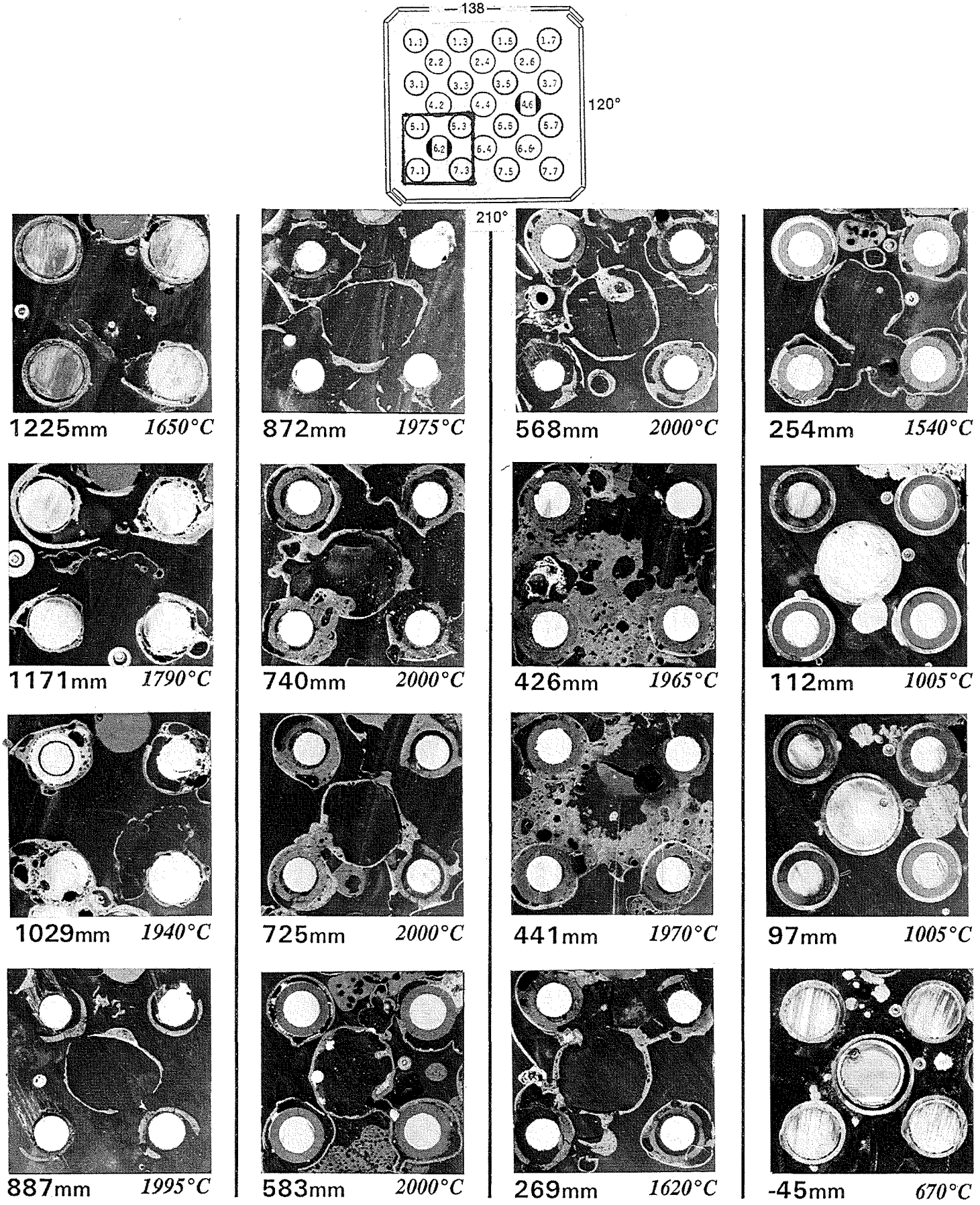

FIG. 111: CORA-29; Horizonteal cross sections of the region of absorber rod 6.2, top view (1225 to -45 mm)

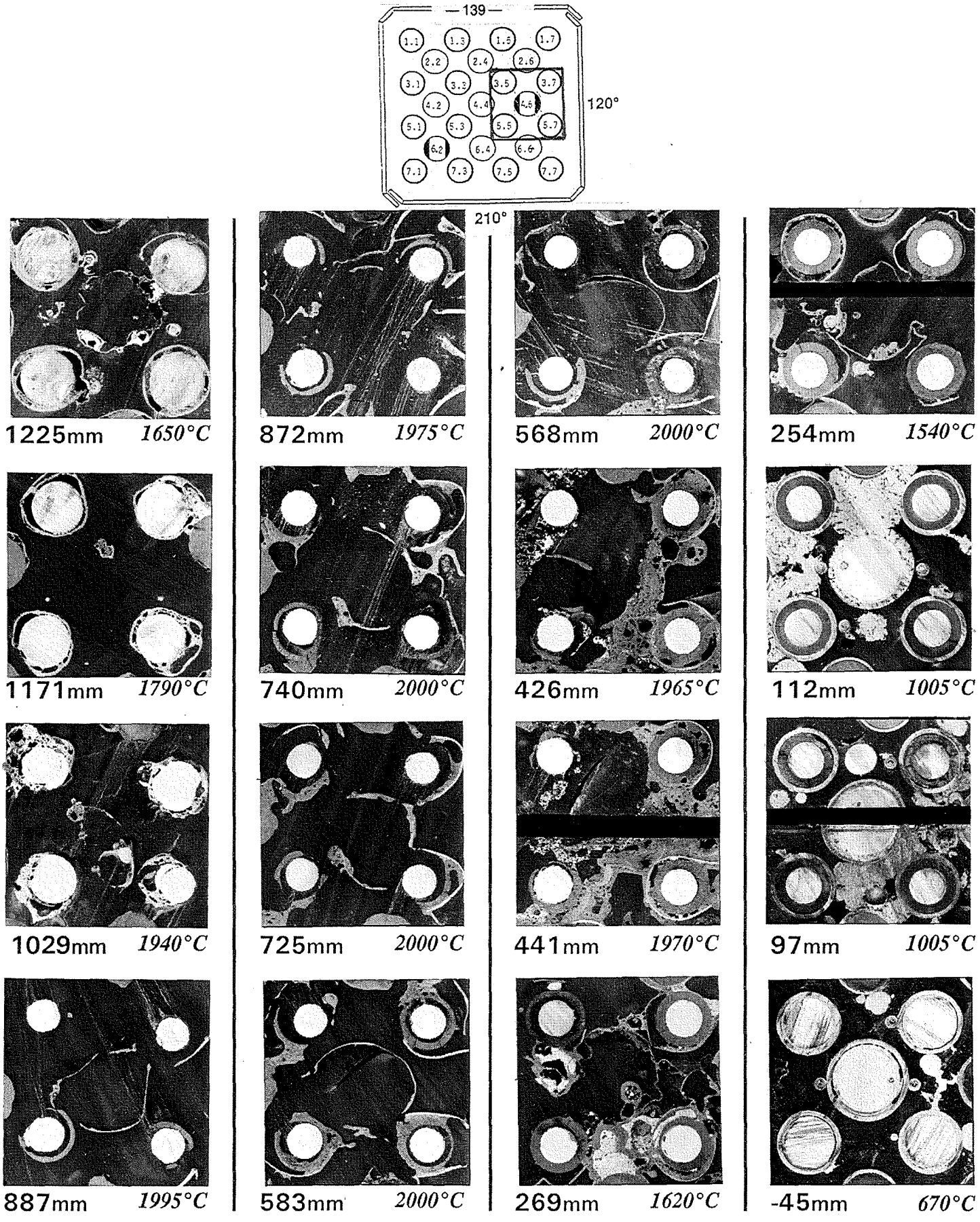

FIG. 112: CORA-29; Horizonteal cross sections of the region of absorber rod 4.6, top view (1225 to -45 mm)

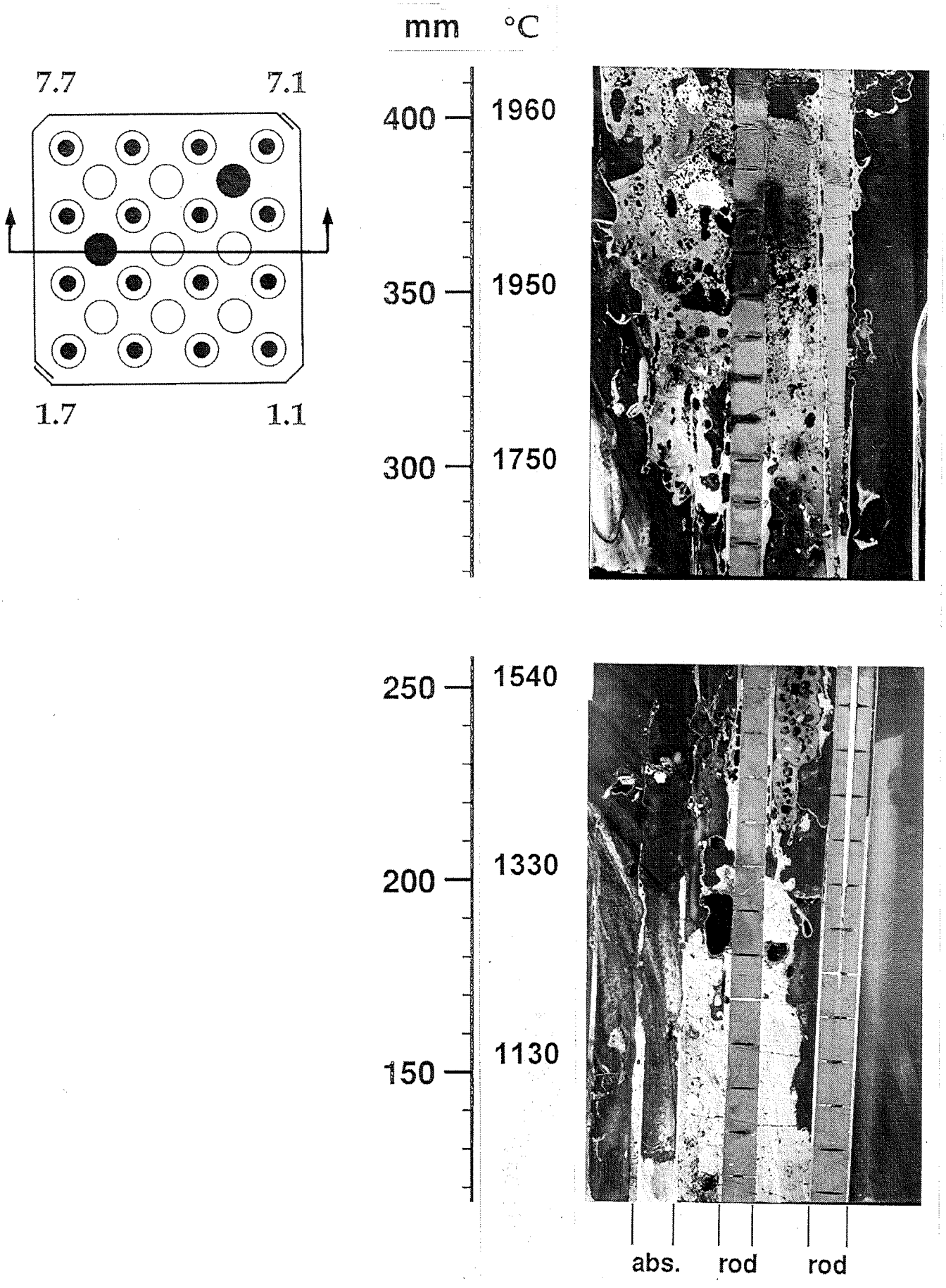

Fig. 113: CORA-29; Vertical cross sections through absorber rod 4.6, 120 - 410 mm

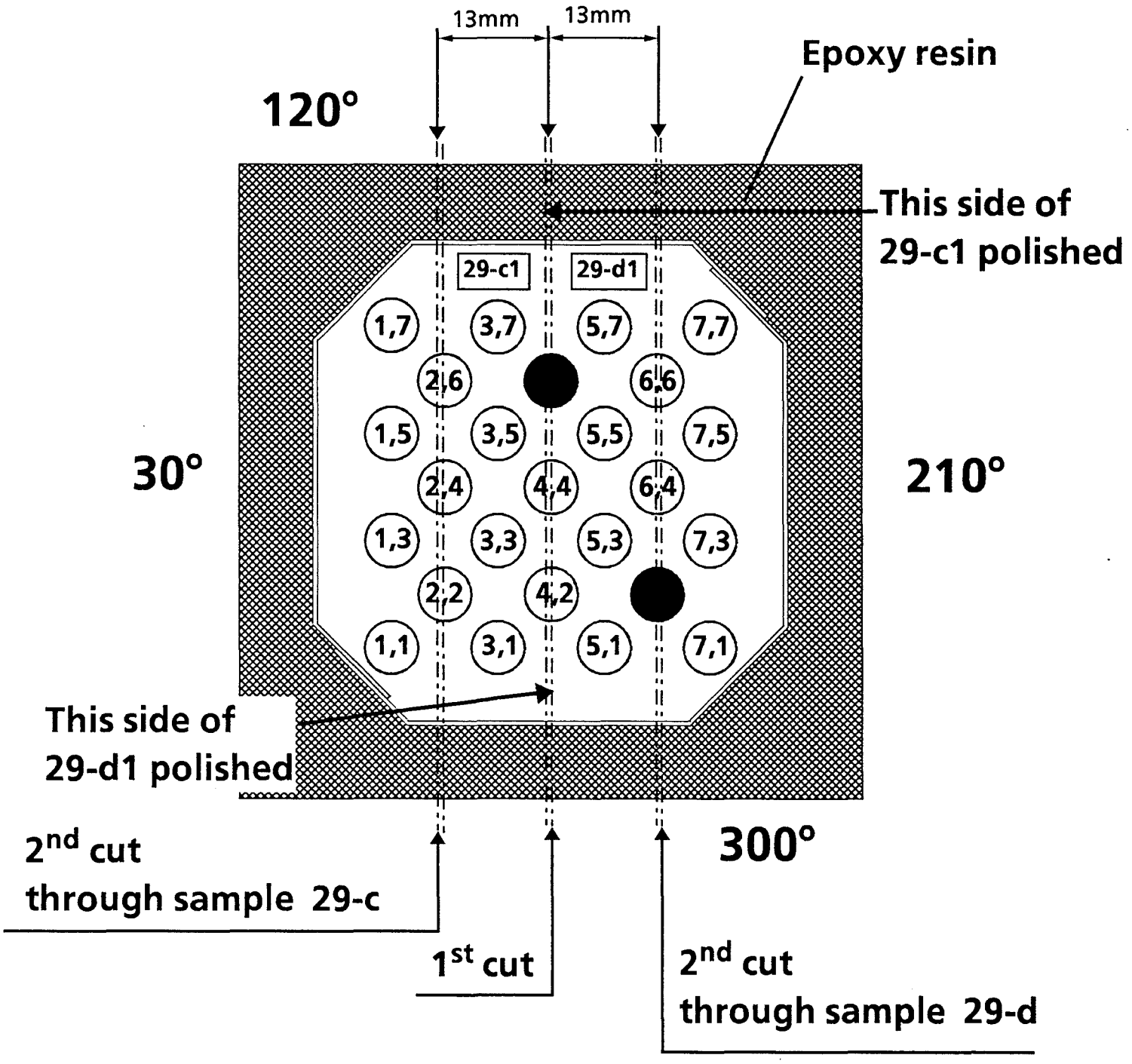

Fig. 113a: Locations of the vertical cuts through sections CORA - 29-b, 29-c, 29-d, 29-e

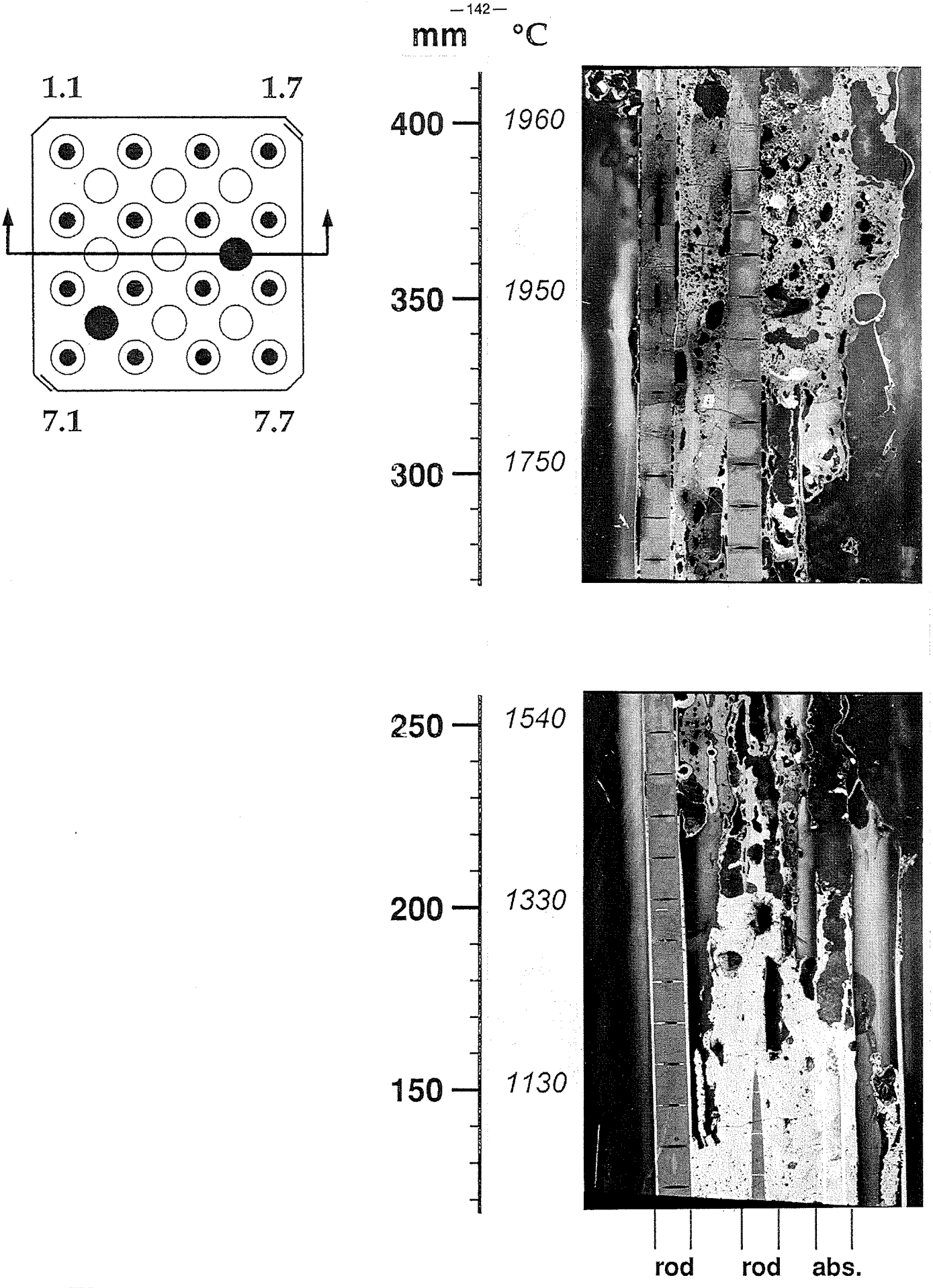

Fig. 114: CORA-29; Vertical cross sections through absorber rod 4.6, 120 - 410 mm

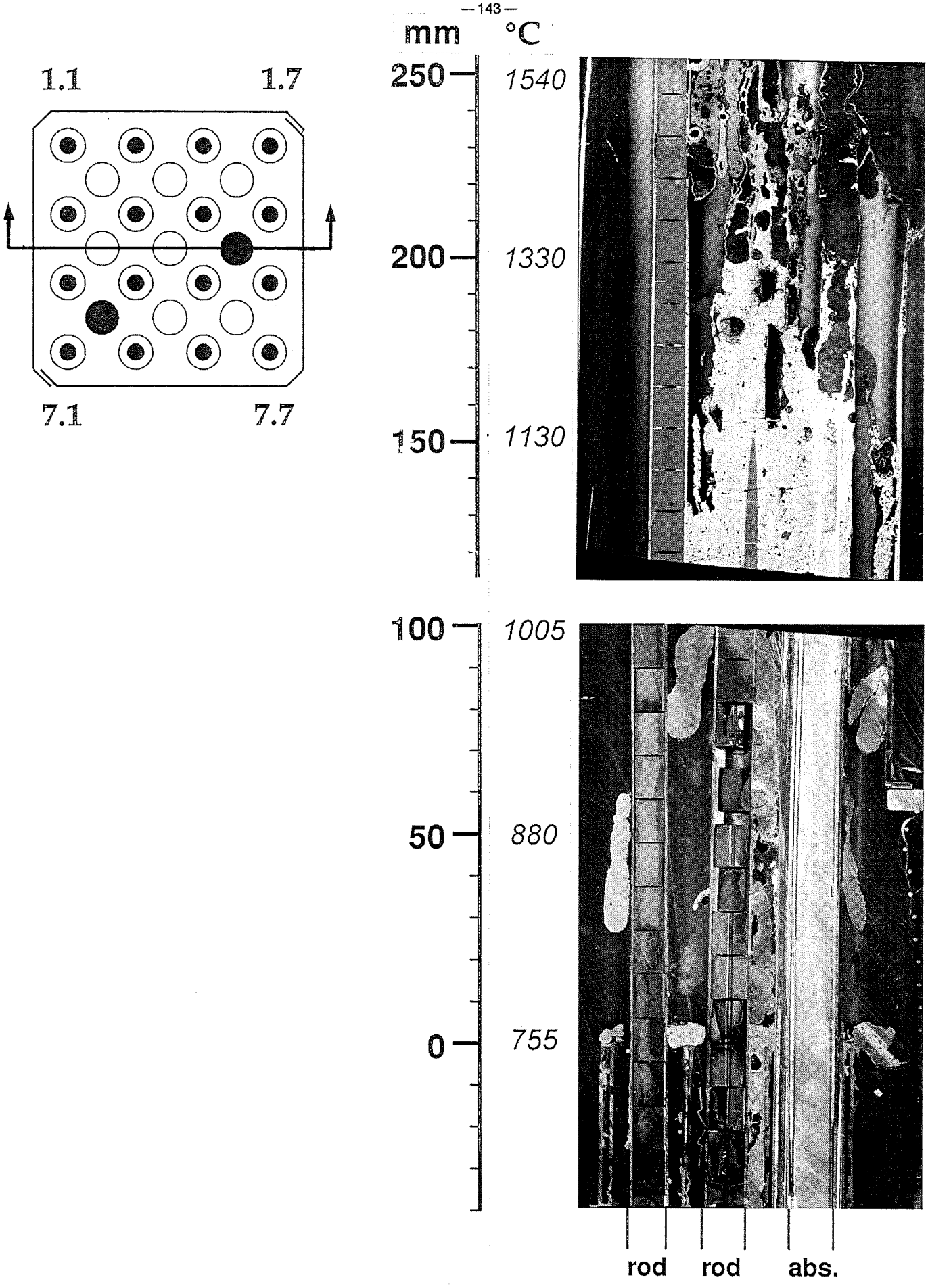

Fig. 115: CORA-29; Vertical cross sections through absorber rod 4.6, -40 - 250 mm

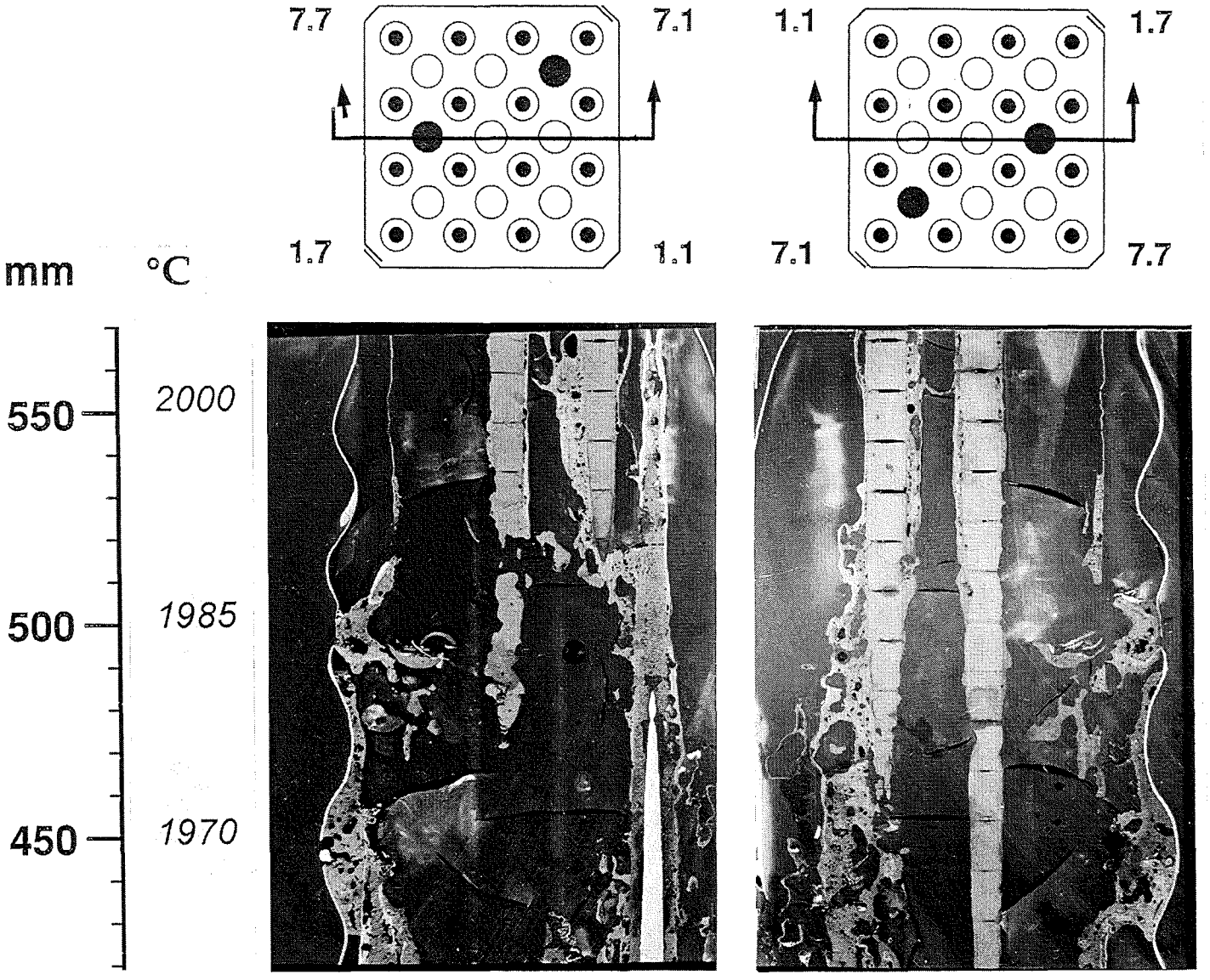

Fig. 116: CORA-29; Vertical cross sections through absorber rod 4.6, both sides of the cut (420 - 570 mm)

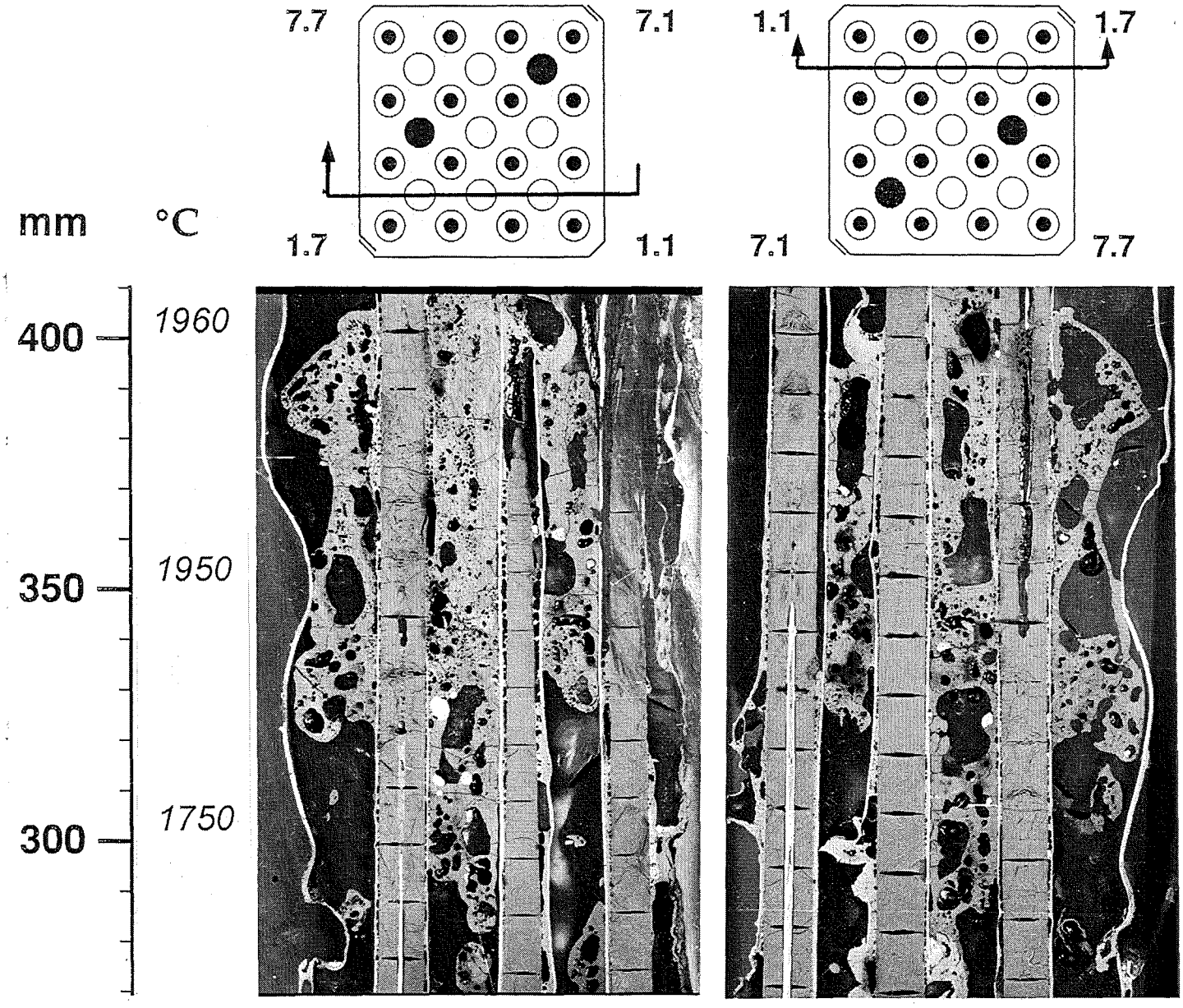

Fig. 117: CORA-29; Vertical cross sections through unheated rods 2.2, 2.4 and 2.6; both sides of the cut (270 - 410 mm)

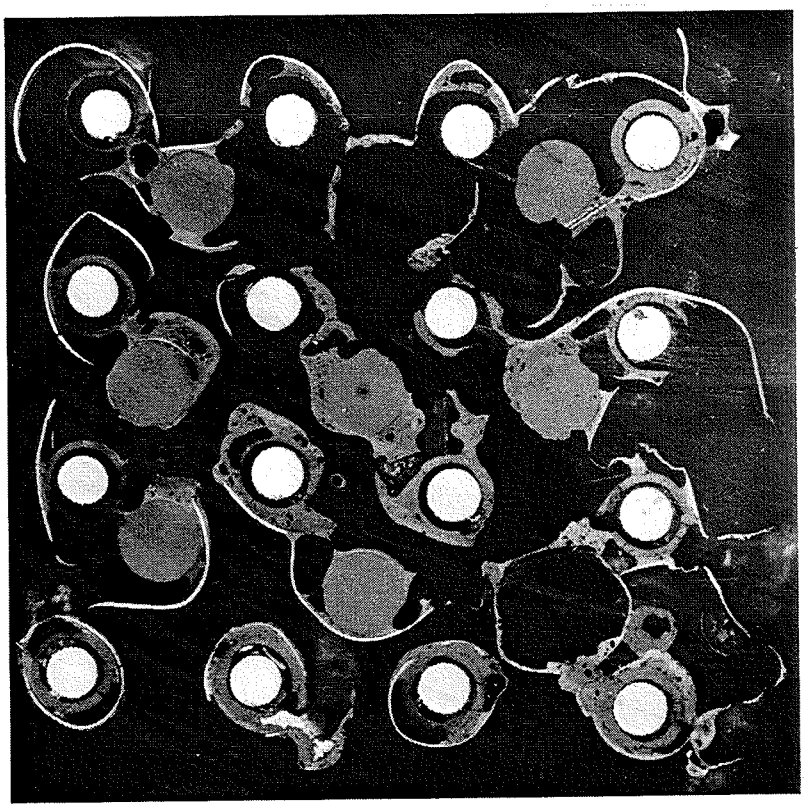

CORA-29

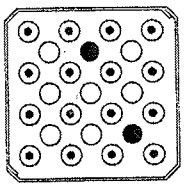

725mm

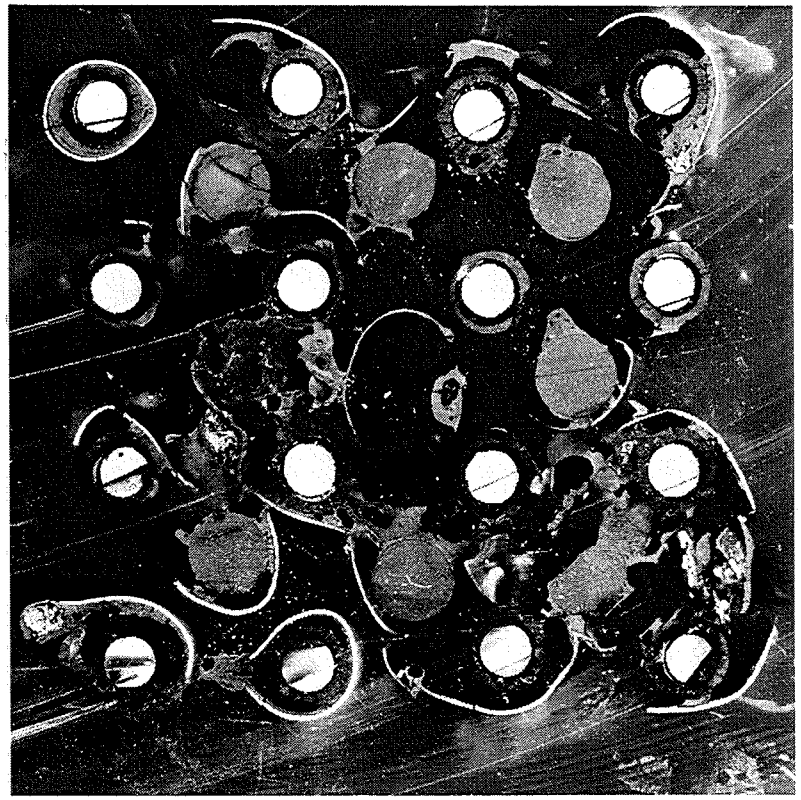

CORA-5

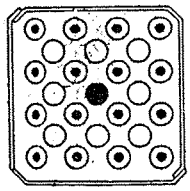

663mm

Fig. 118: Comparison of horizontal cross sections CORA-29/ CORA-5 (725, 663 mm)

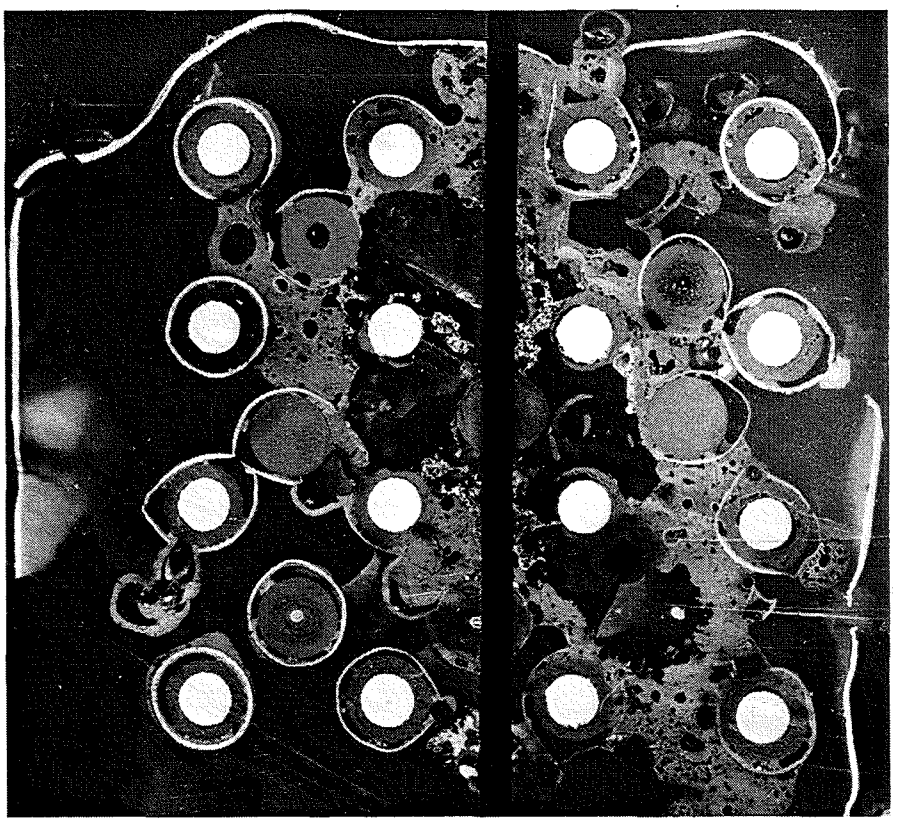

CORA-29

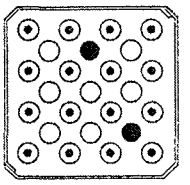

411mm

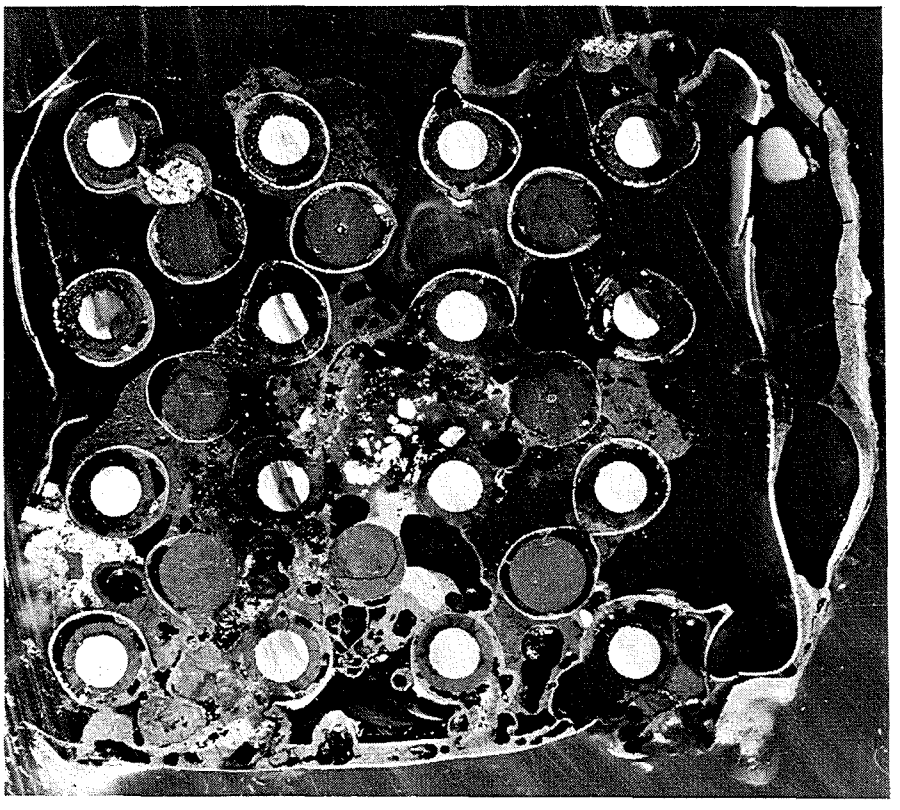

CORA-5

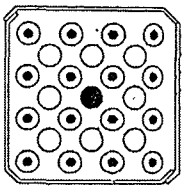

408mm

Fig. 119: Comparison of horizontal cross sections CORA-29/ CORA-5 (411, 408 mm)

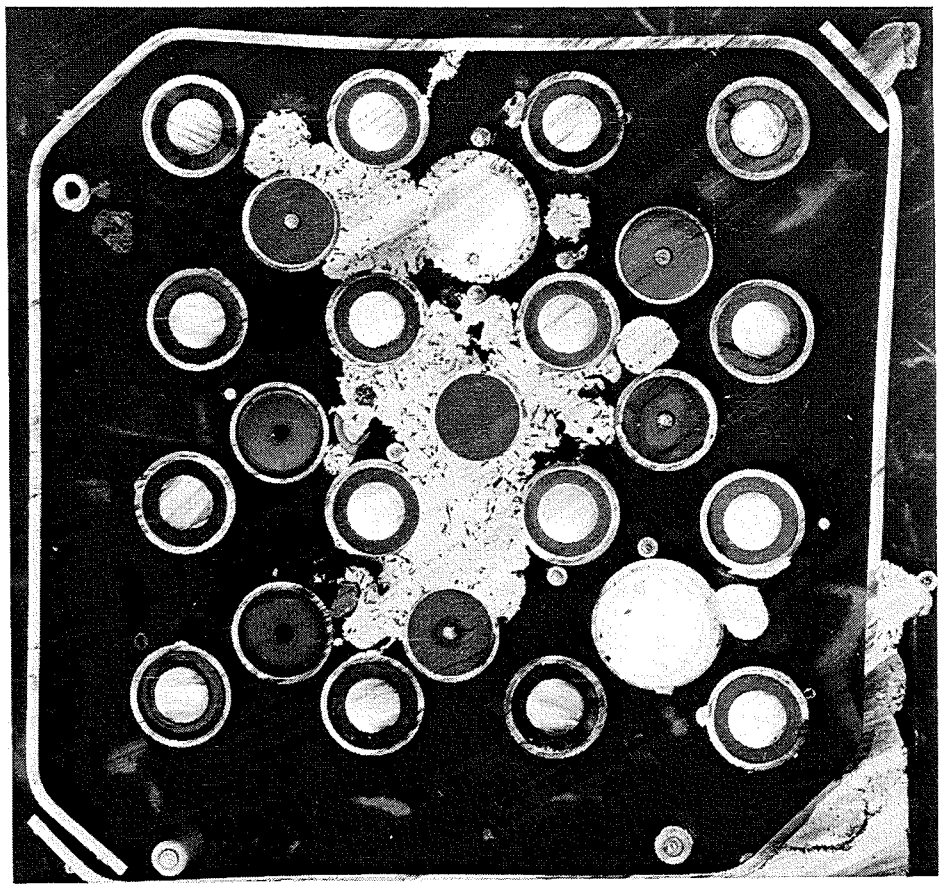

112mm

CORA-29

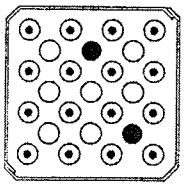

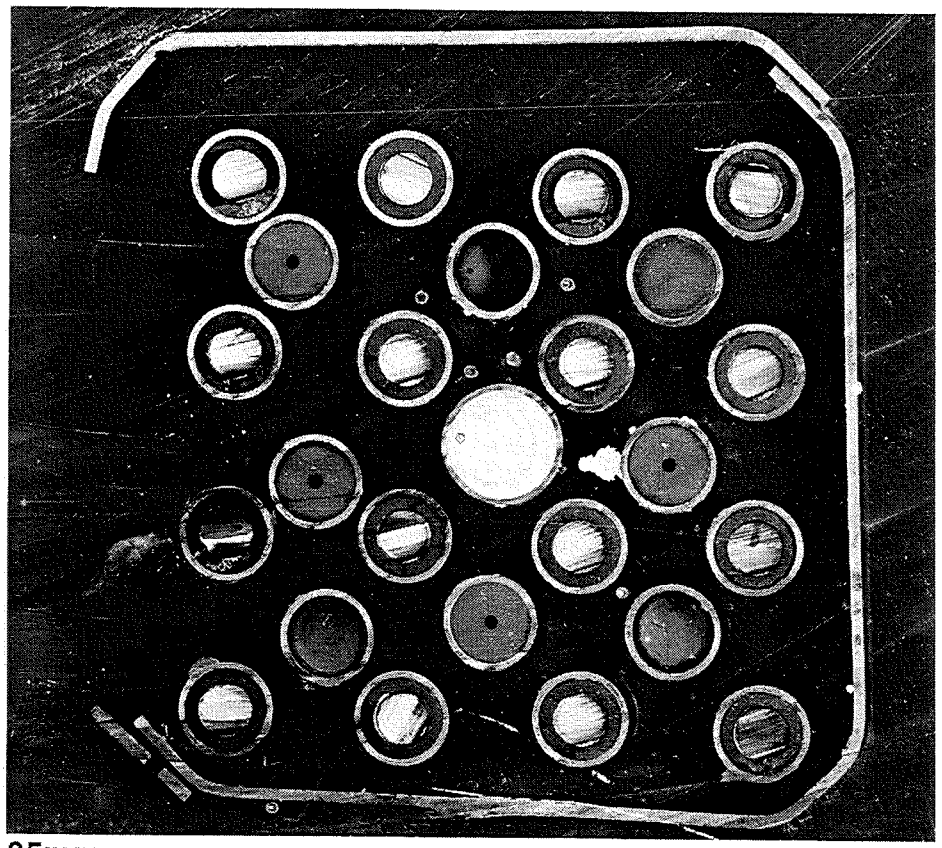

95mm

CORA-5

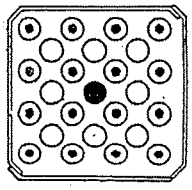

Fig. 120: Comparison of horizontal cross sections CORA-29/ CORA-5 (112, 95 mm)

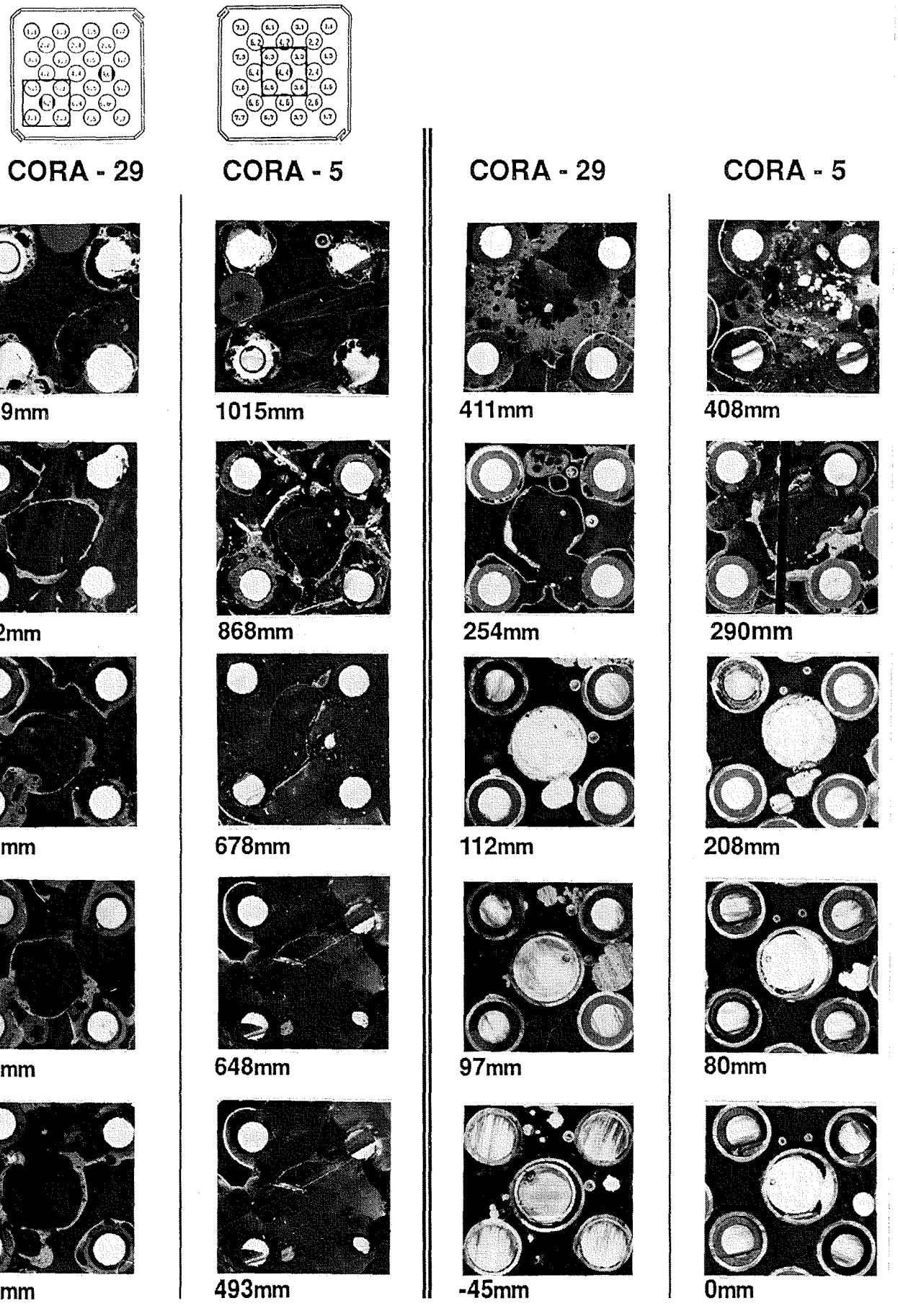

Fig. 121: Comparison of cross sections of region of one absorber rod in CORA-29/ CORA-5

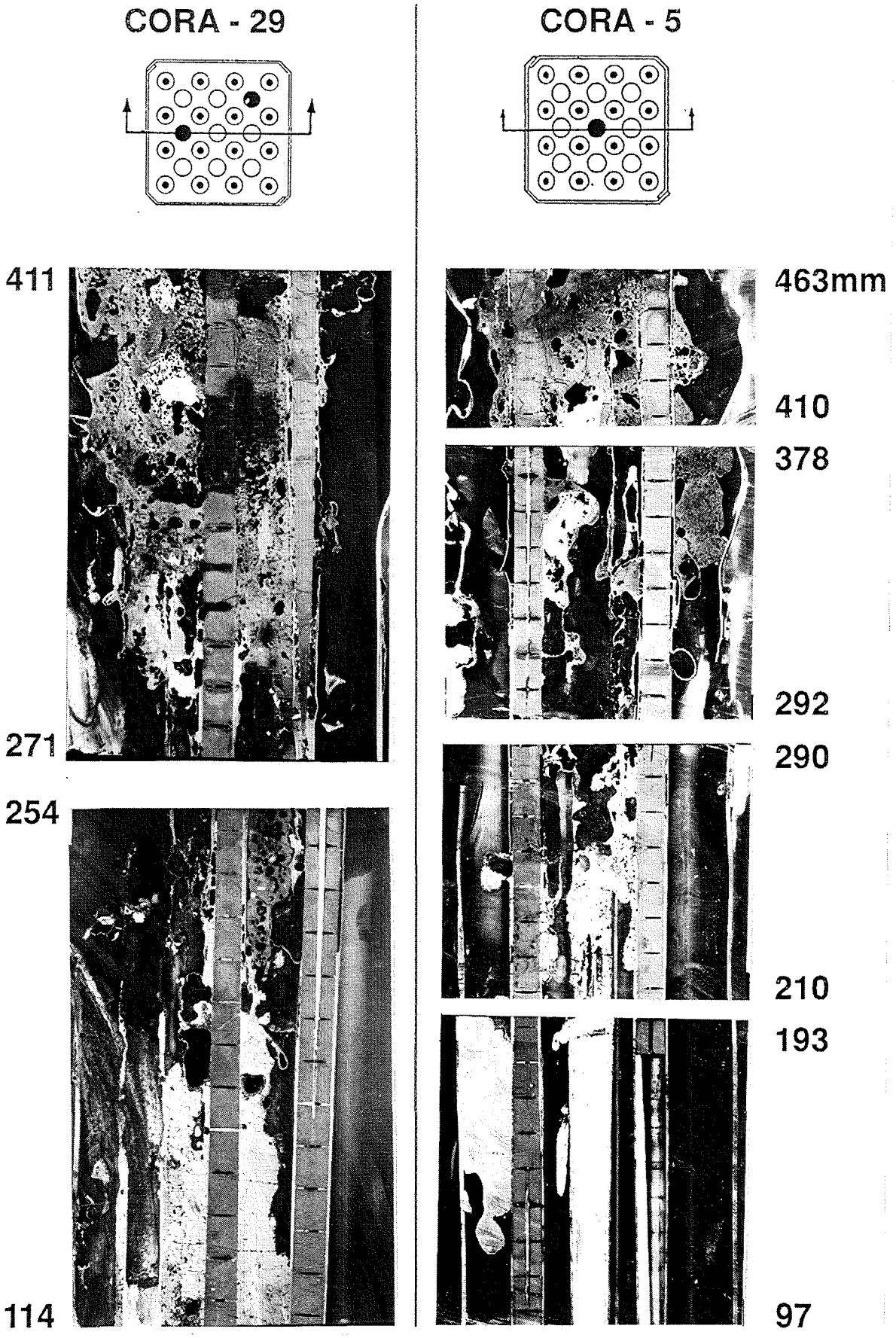

Fig. 122: Comparison of vertical cross sections CORA-29/CORA-5

APPENDIX A

Test Data of the pre-heating phase

Figures: A1 - A32

Complete set of cross sections

Figures: A33 - A41

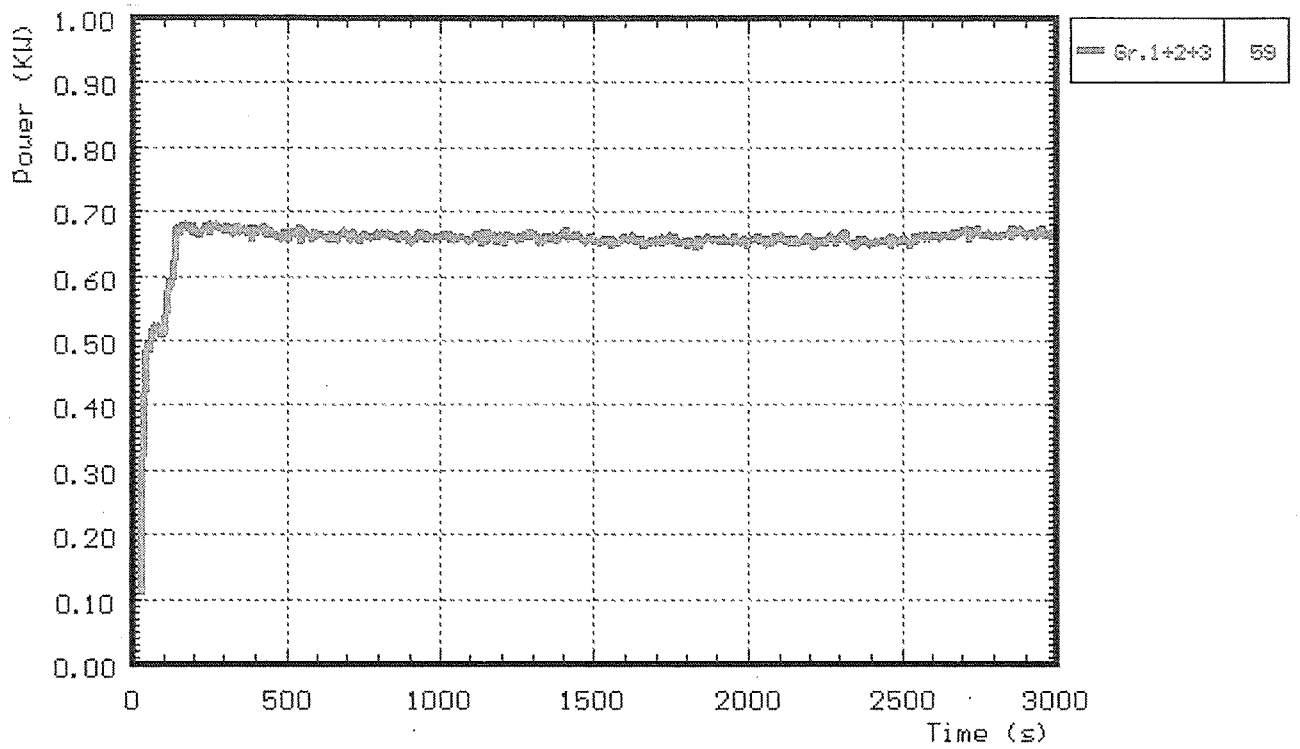

Fig. A1: CORA-29; Power input during pre-heat phase

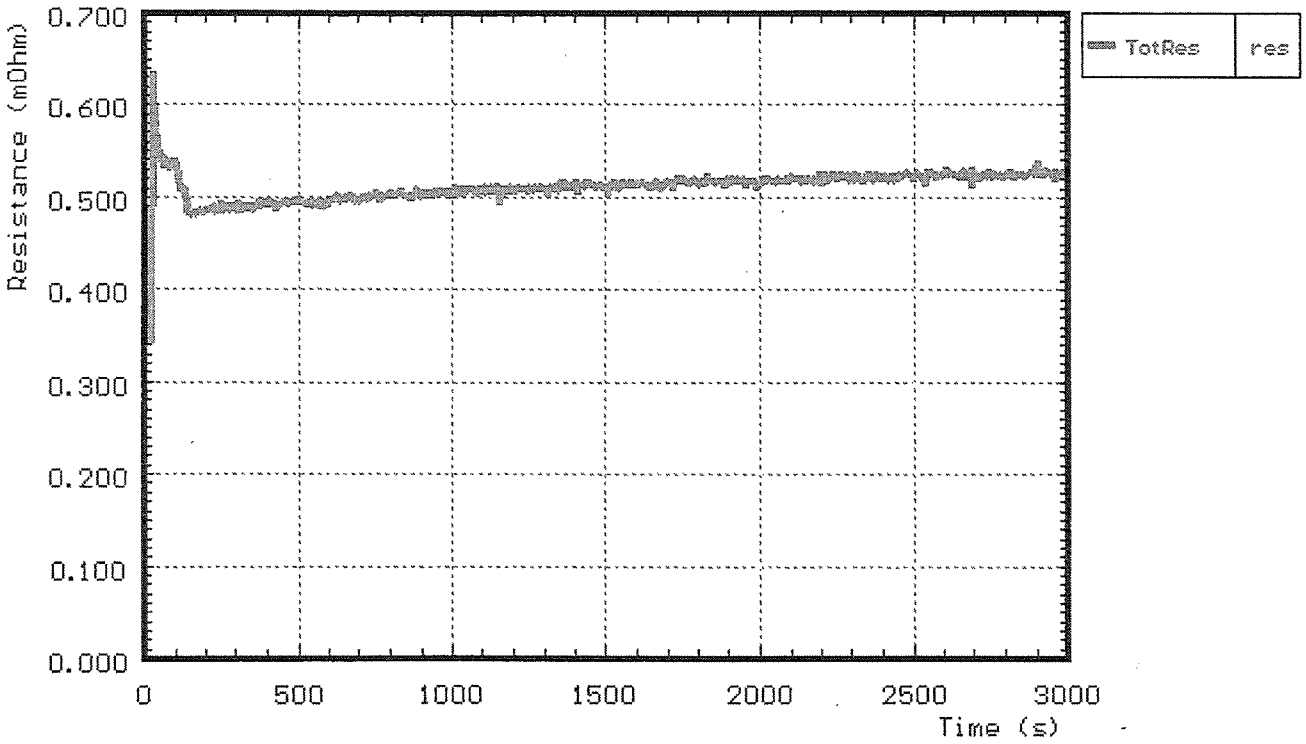

Fig. A2: CORA-29; Resistance of bundle during pre-heat phase

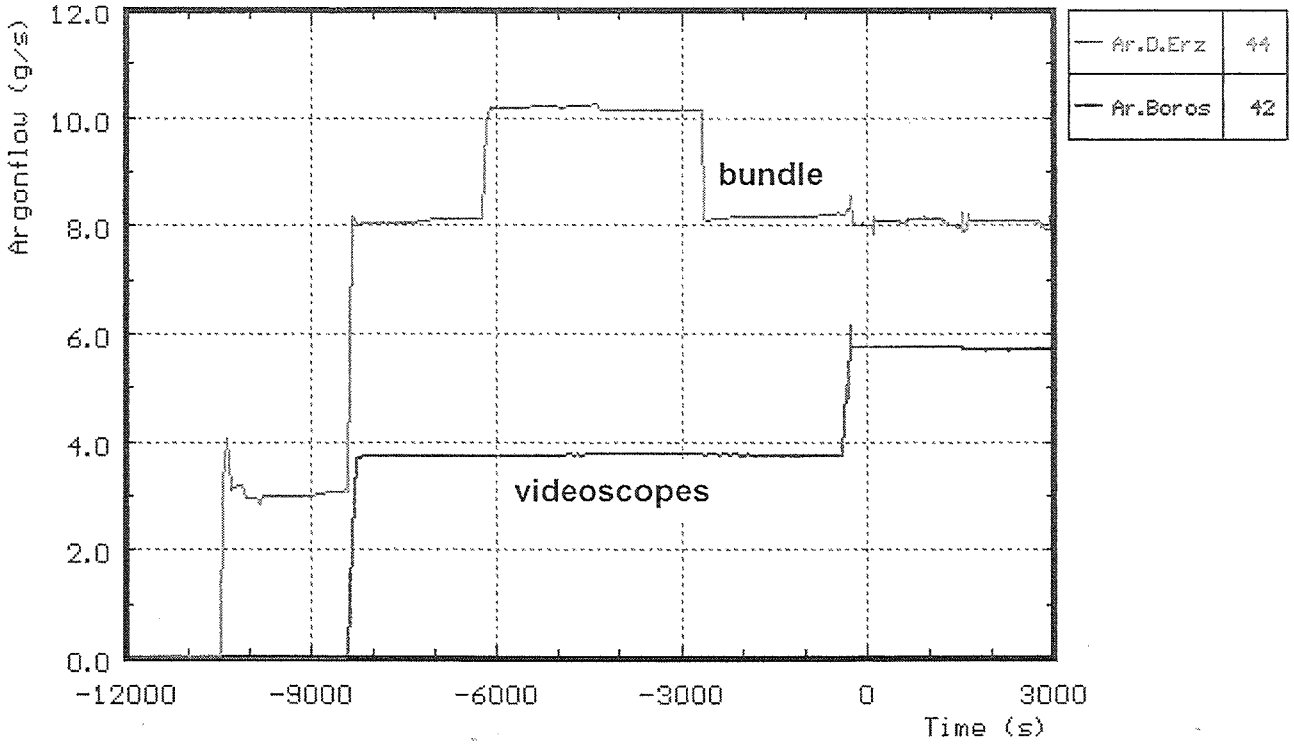

Fig. A3: CORA-29; Argon input prior to test

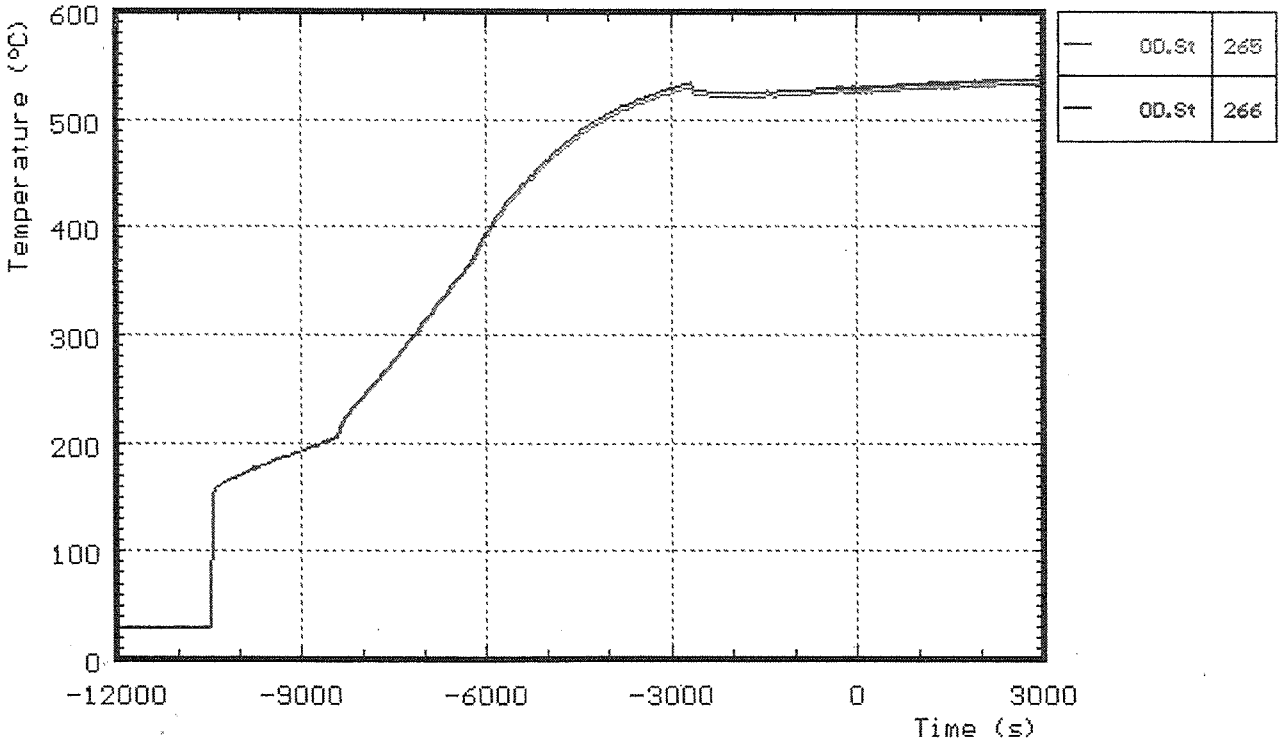

Fig. A4: CORA-29; Temperatures at steam inlet; pre-heat phase

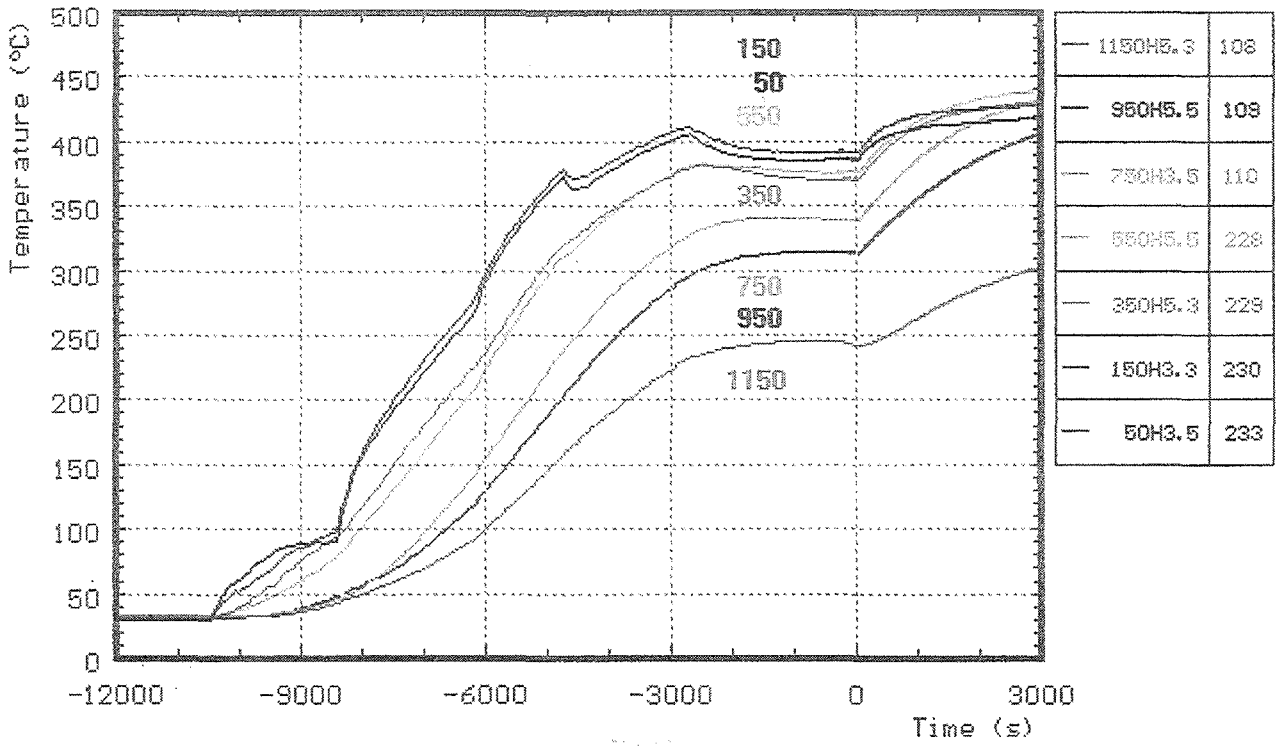

Fig. A5: CORA-29; Temperatures of heated rods; pre-heat phase

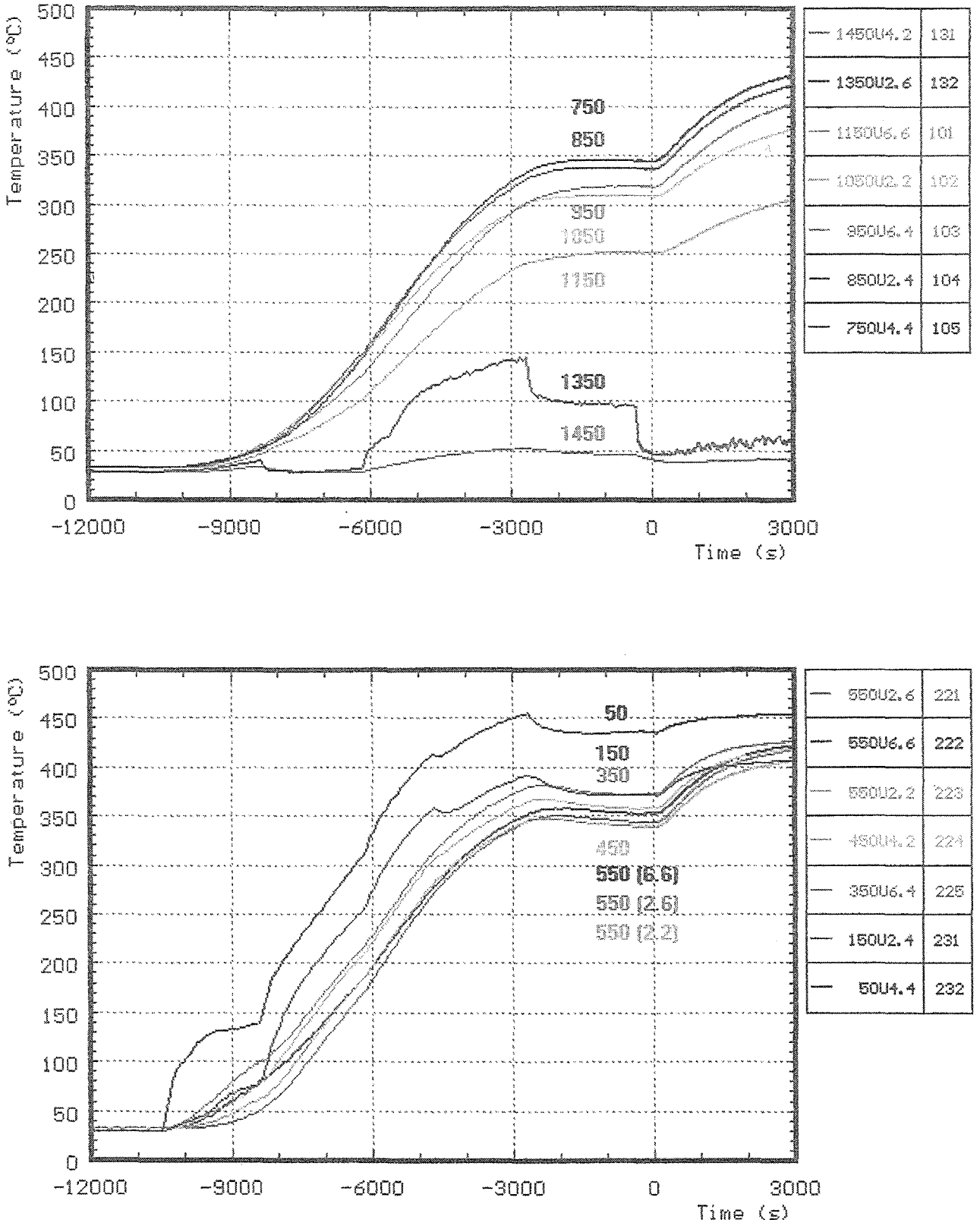

Fig. A6: CORA-29; Temperatures of unheated rods; pre-heat phase

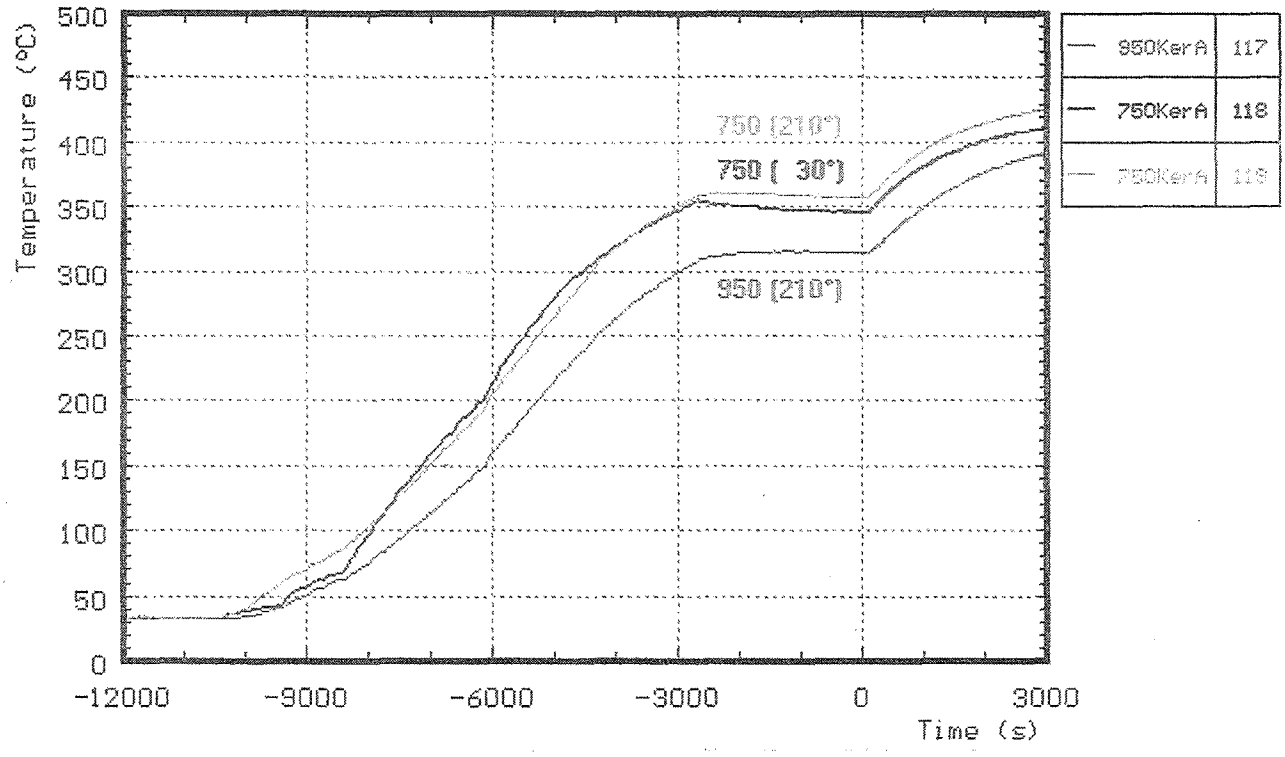

Fig. A7: CORA-29; Temperatures between bundle and shroud measured with ceramic protected TCs; pre-heat phase

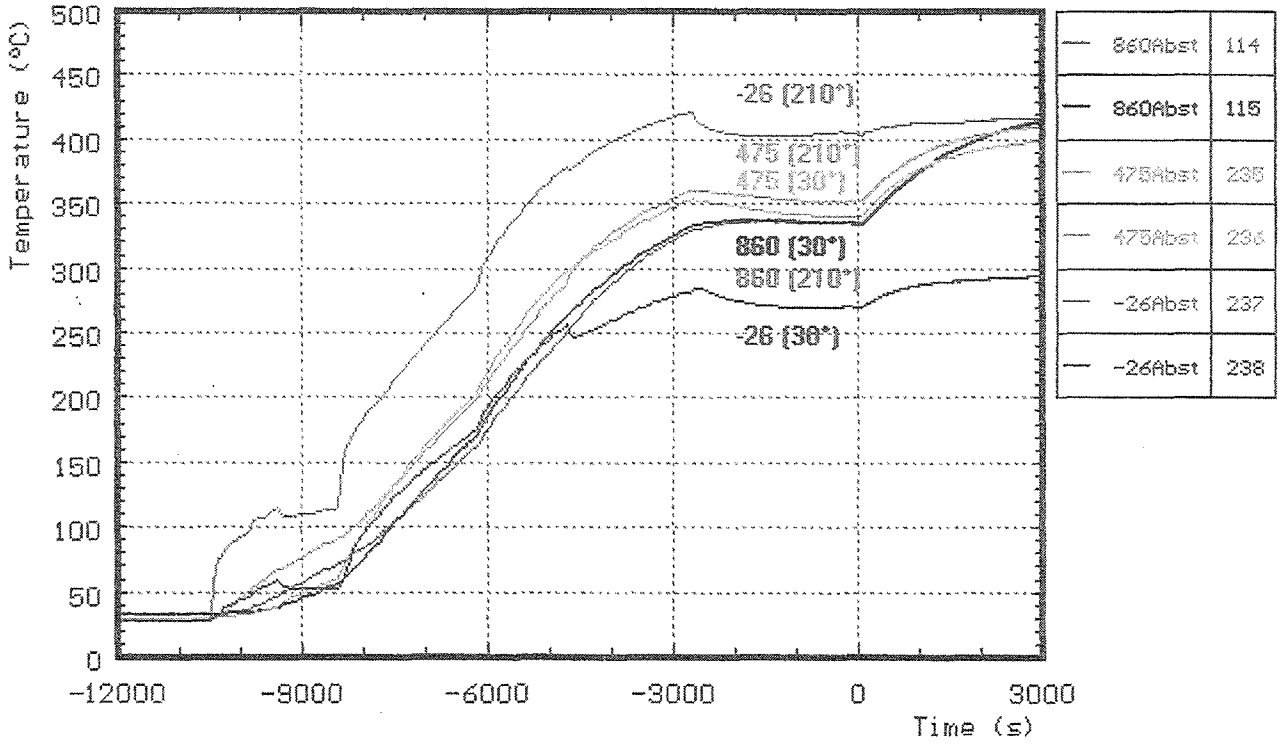

Fig. A7a: CORA-29; Temperatures of the spacers; pre-heat phase

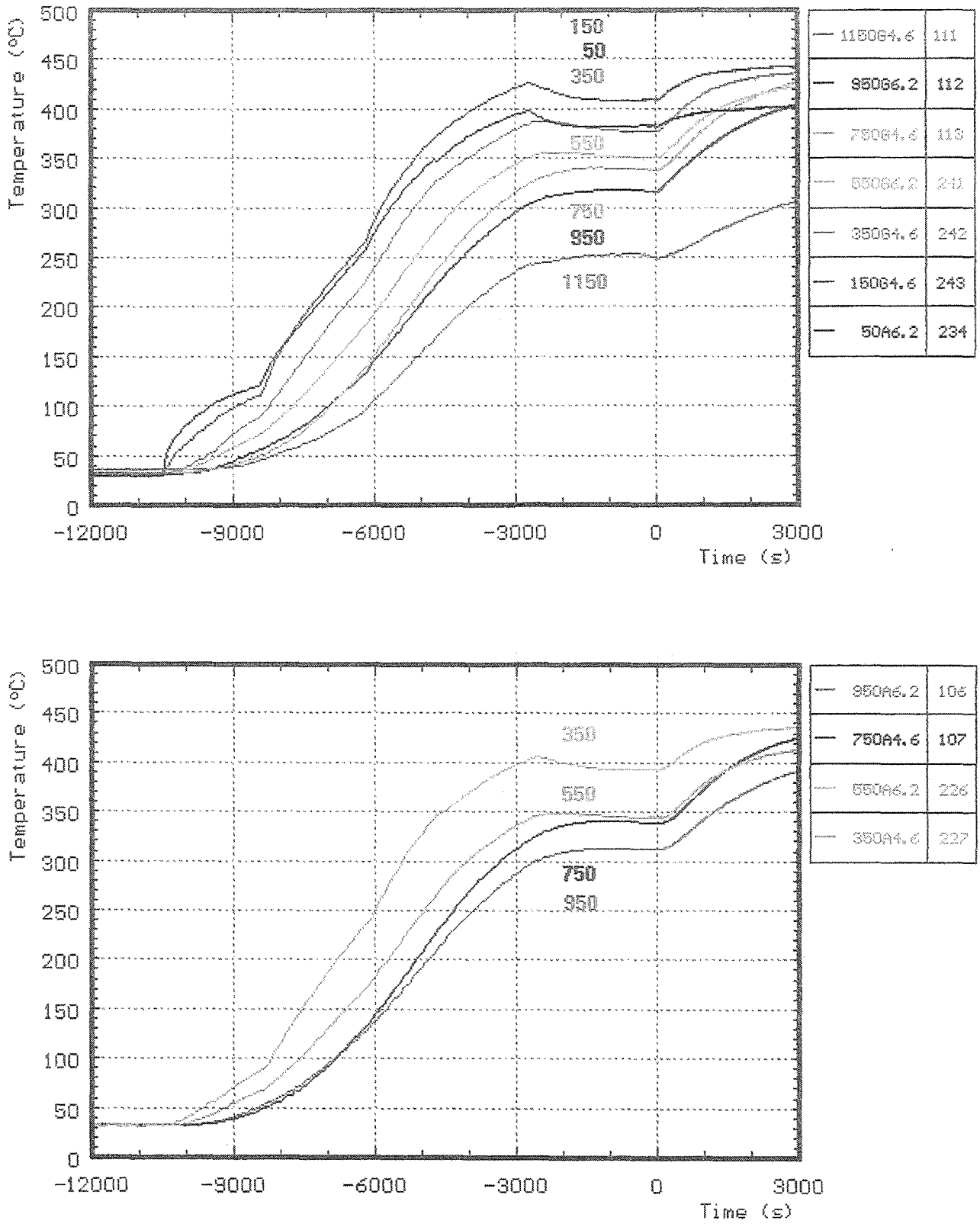

Fig. A8: CORA-29; Temperatures of the absorber rods and of the pertinent guide tubes; pre-heat phase

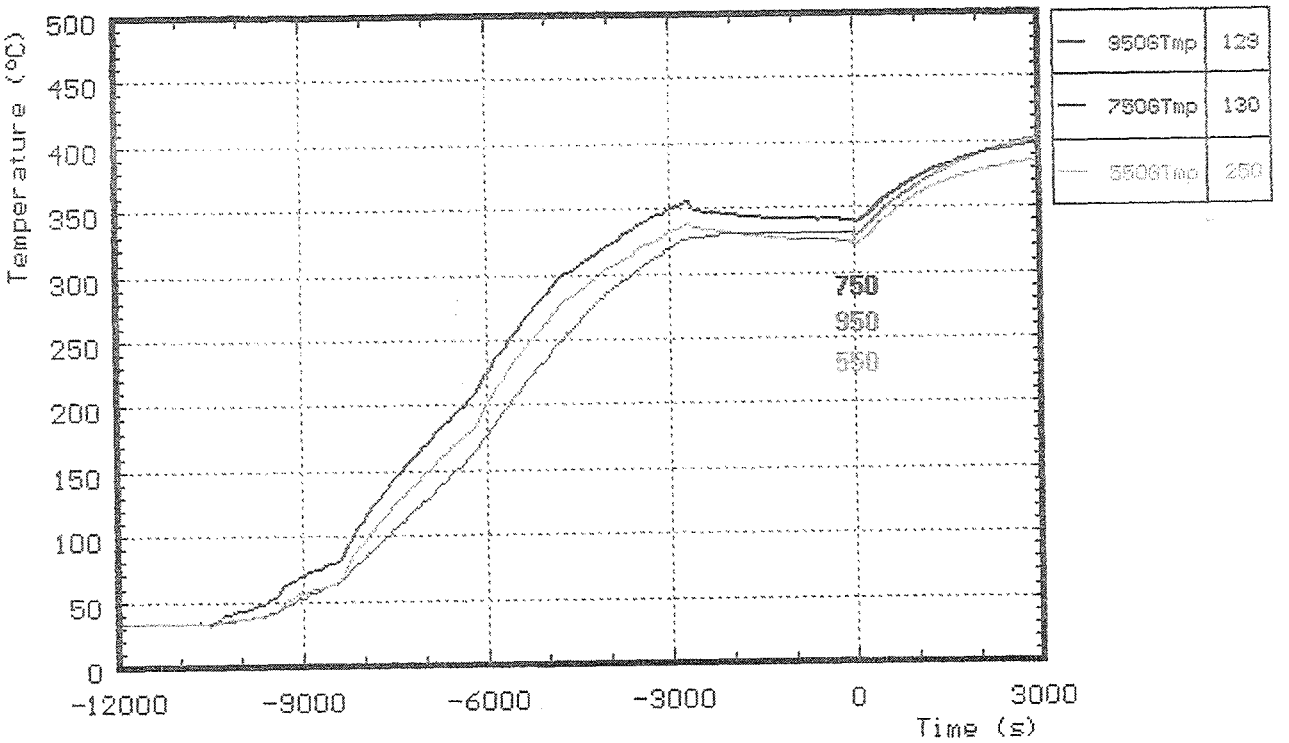

Fig. A9: CORA-29; Temperatures between bundle and shroud; pre-heat phase

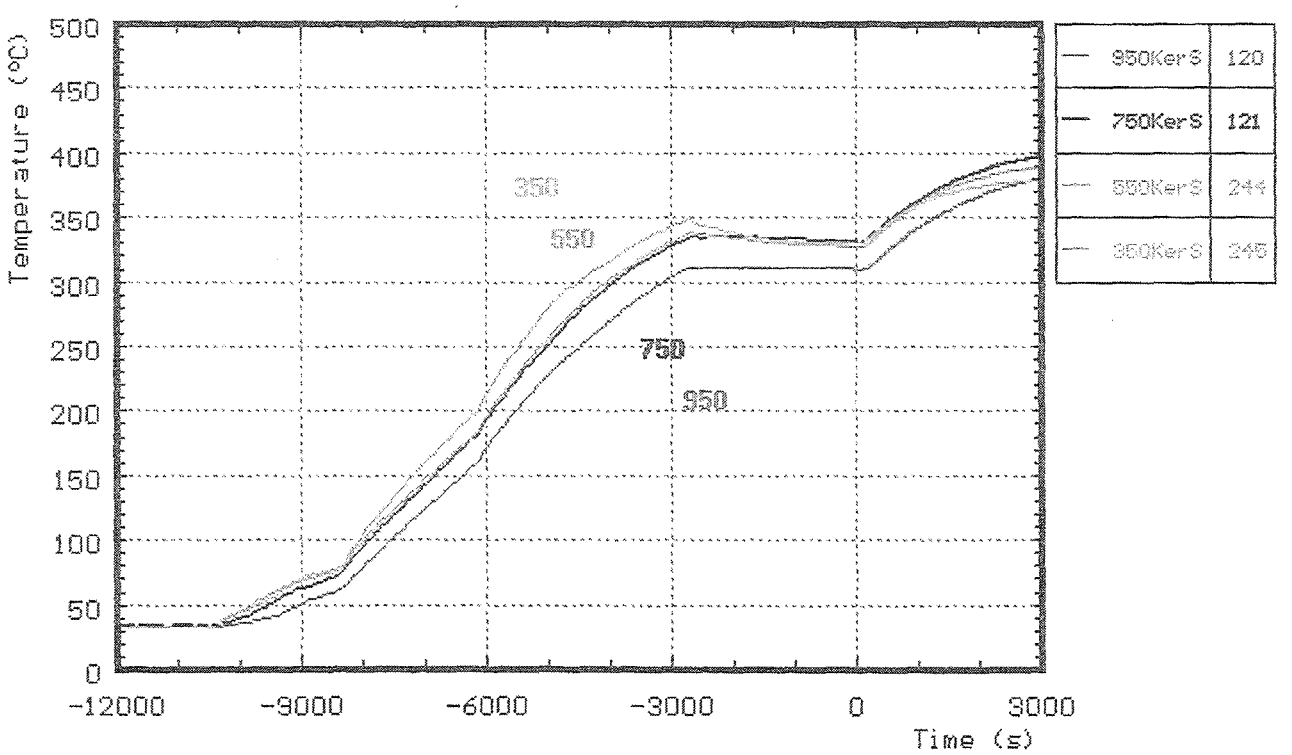

Fig. A10: CORA-29; Temperatures of inner side of shroud measured with ceramic protected TCs; pre-heat phase

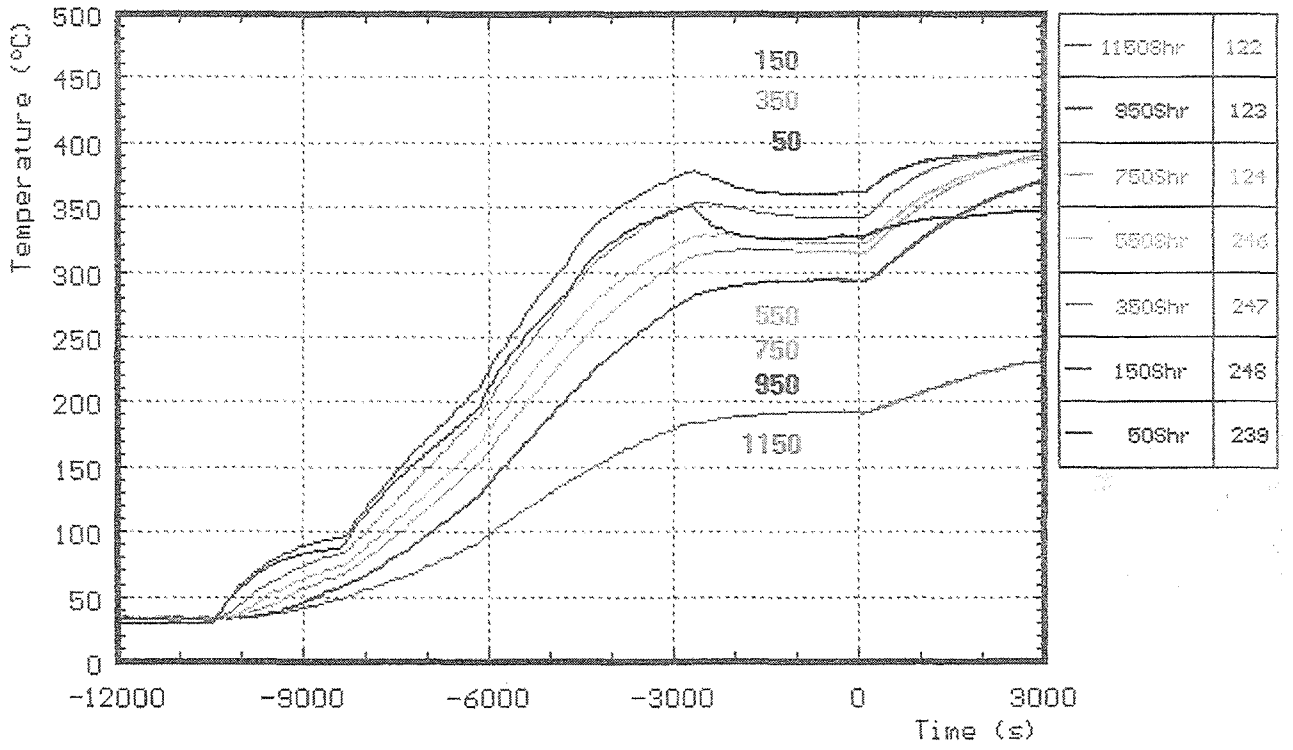

Fig. A11: CORA-29; Temperatures of outer side of shroud; pre-heat phase

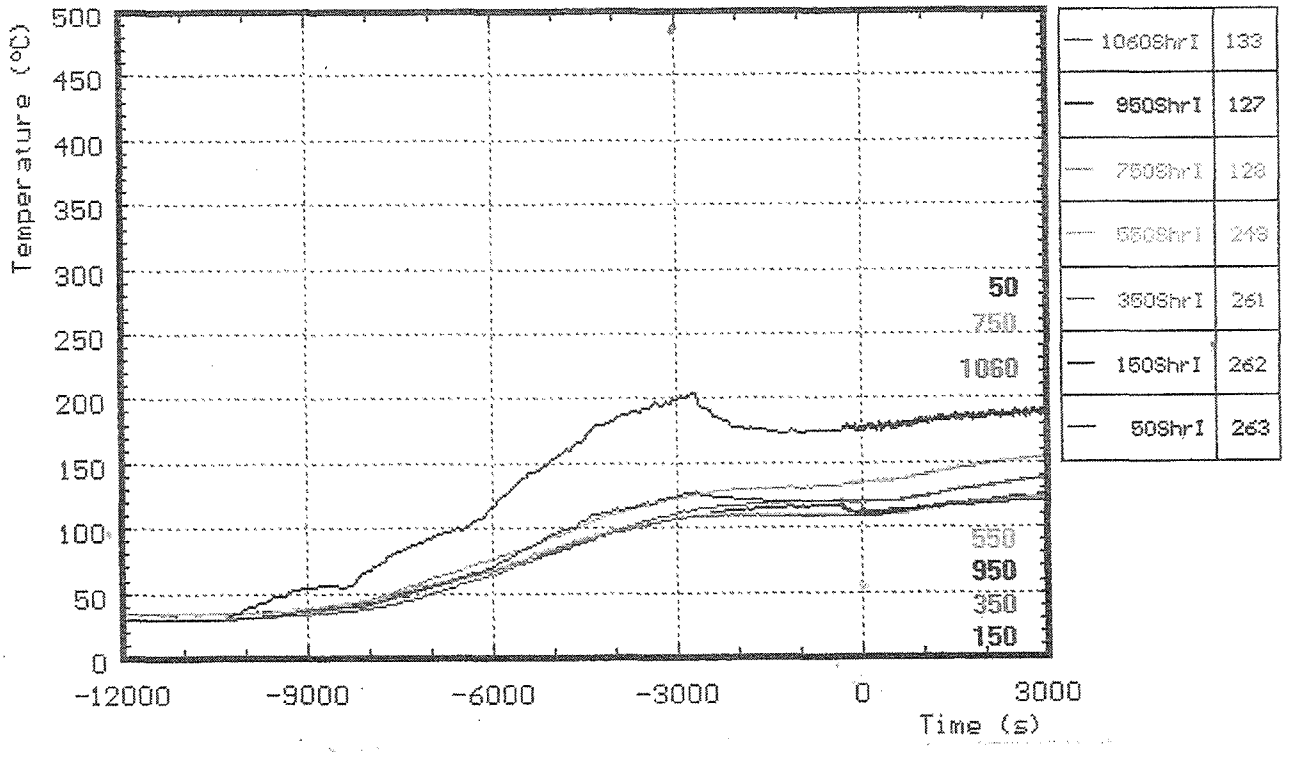

Fig. A12: CORA-29; Temperatures of the shroud insulation; pre-heat phase

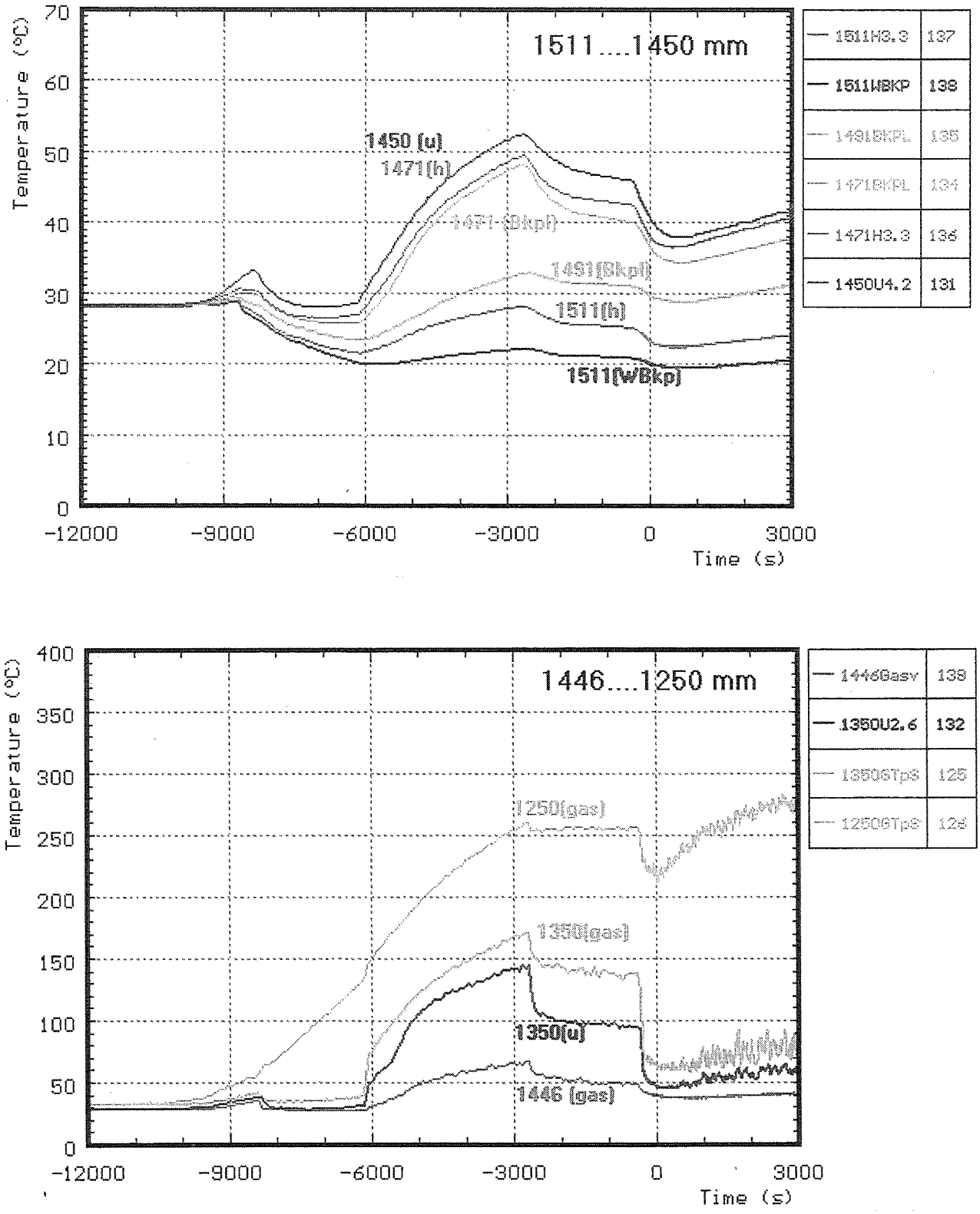

Fig. A13: CORA-29; Temperatures at elevations given (1511-1250 mm); pre-heat phase

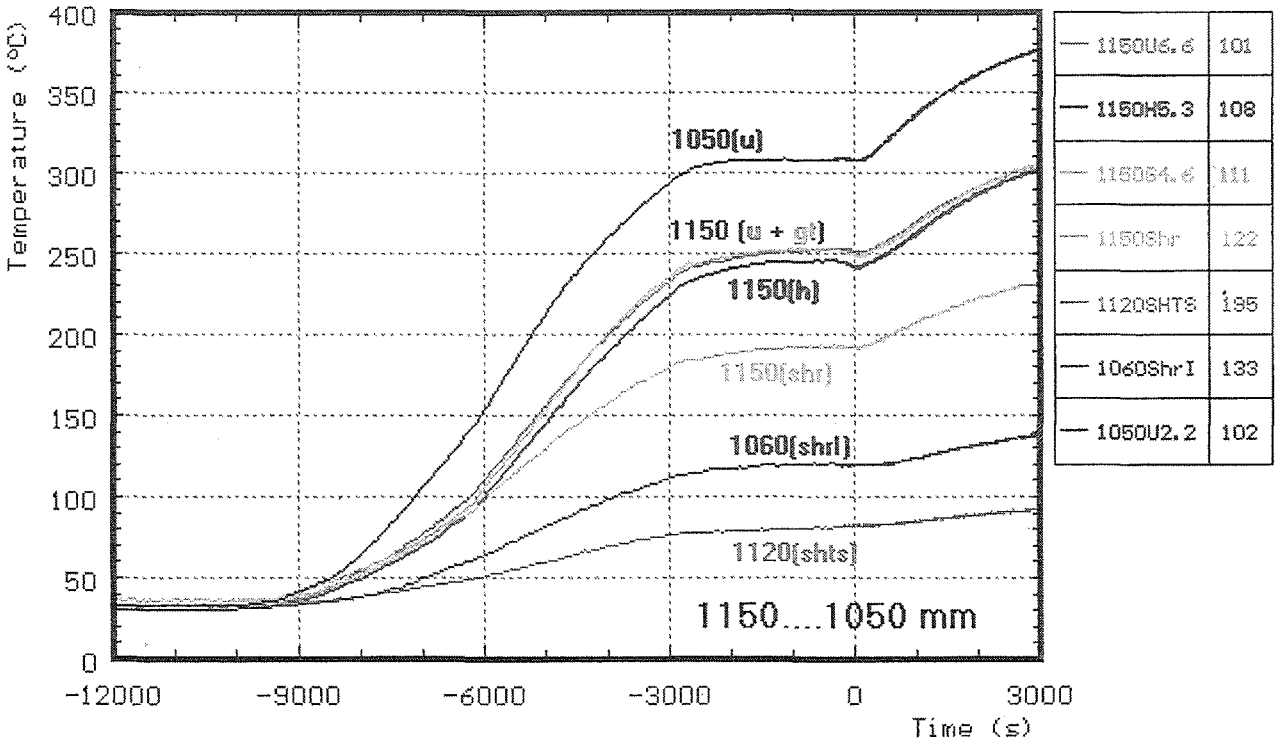

Fig. A14: CORA-29; Temperatures at elevations given (1150-1050 mm); pre-heat phase

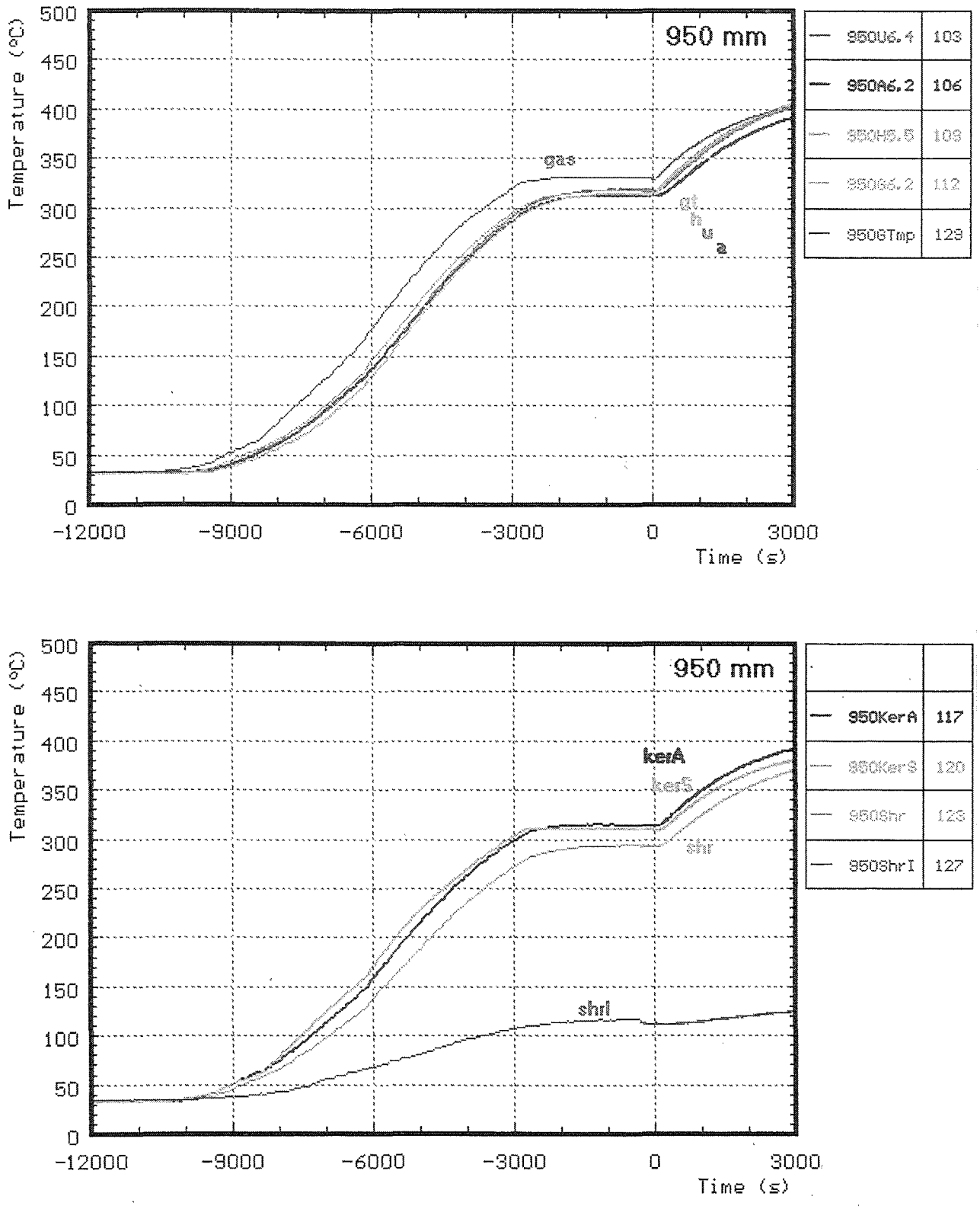

Fig. A15: CORA-29; Temperatures at elevations given (950 mm); pre-heat phase

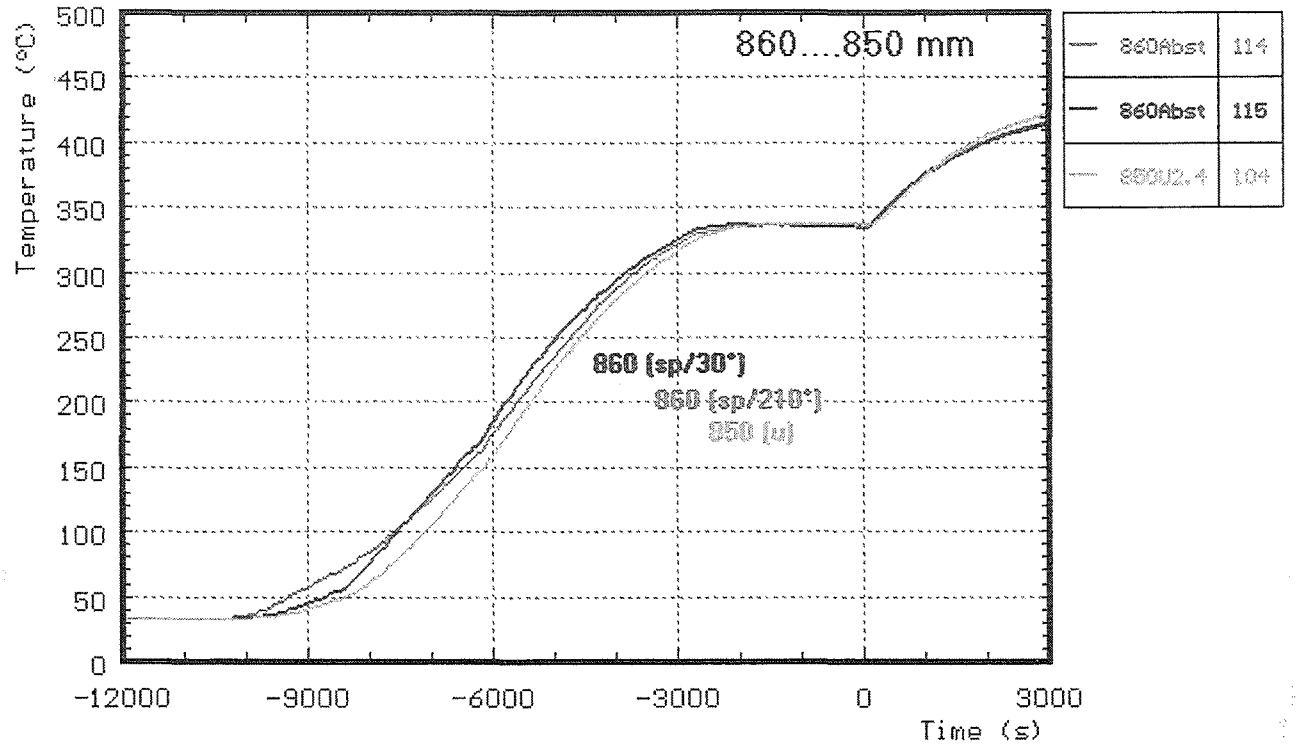

Fig. A16: CORA-29; Temperatures at elevations given (860-850 mm); pre-heat phase

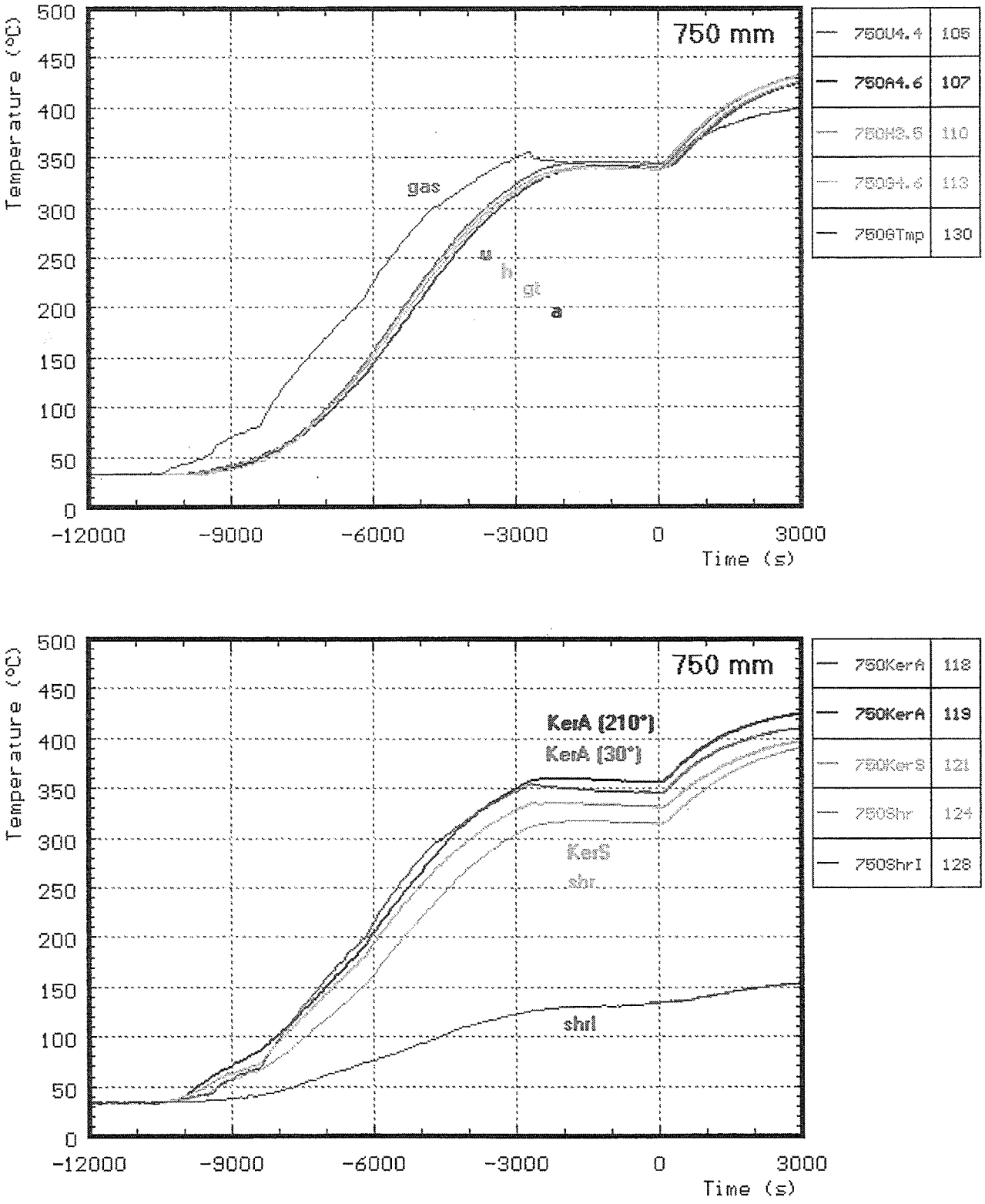

Fig. A17: CORA-29; Temperatures at elevations given (750 mm); pre-heat phase

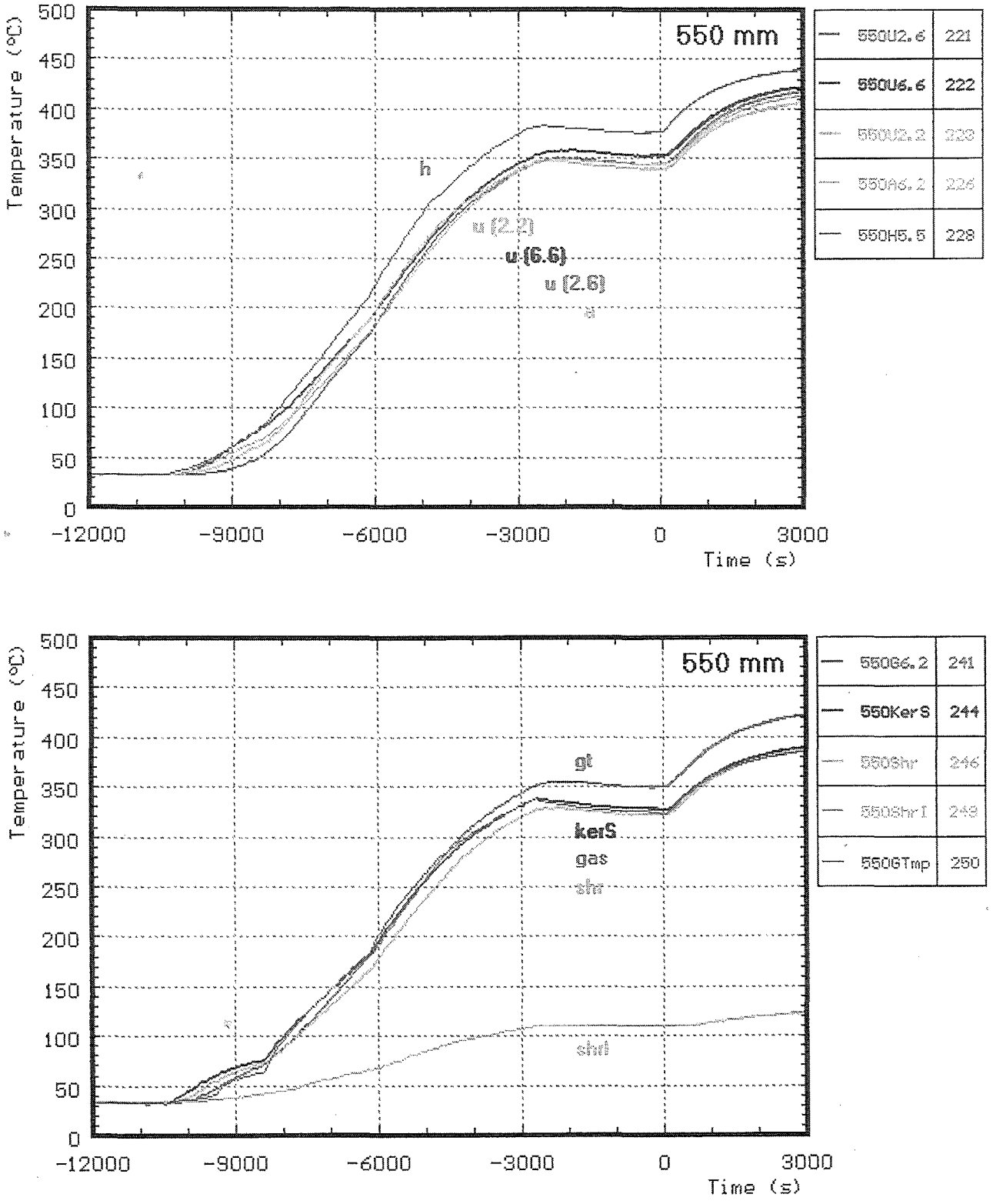

Fig. A18: CORA-29; Temperatures at elevations given (550 mm); pre-heat phase

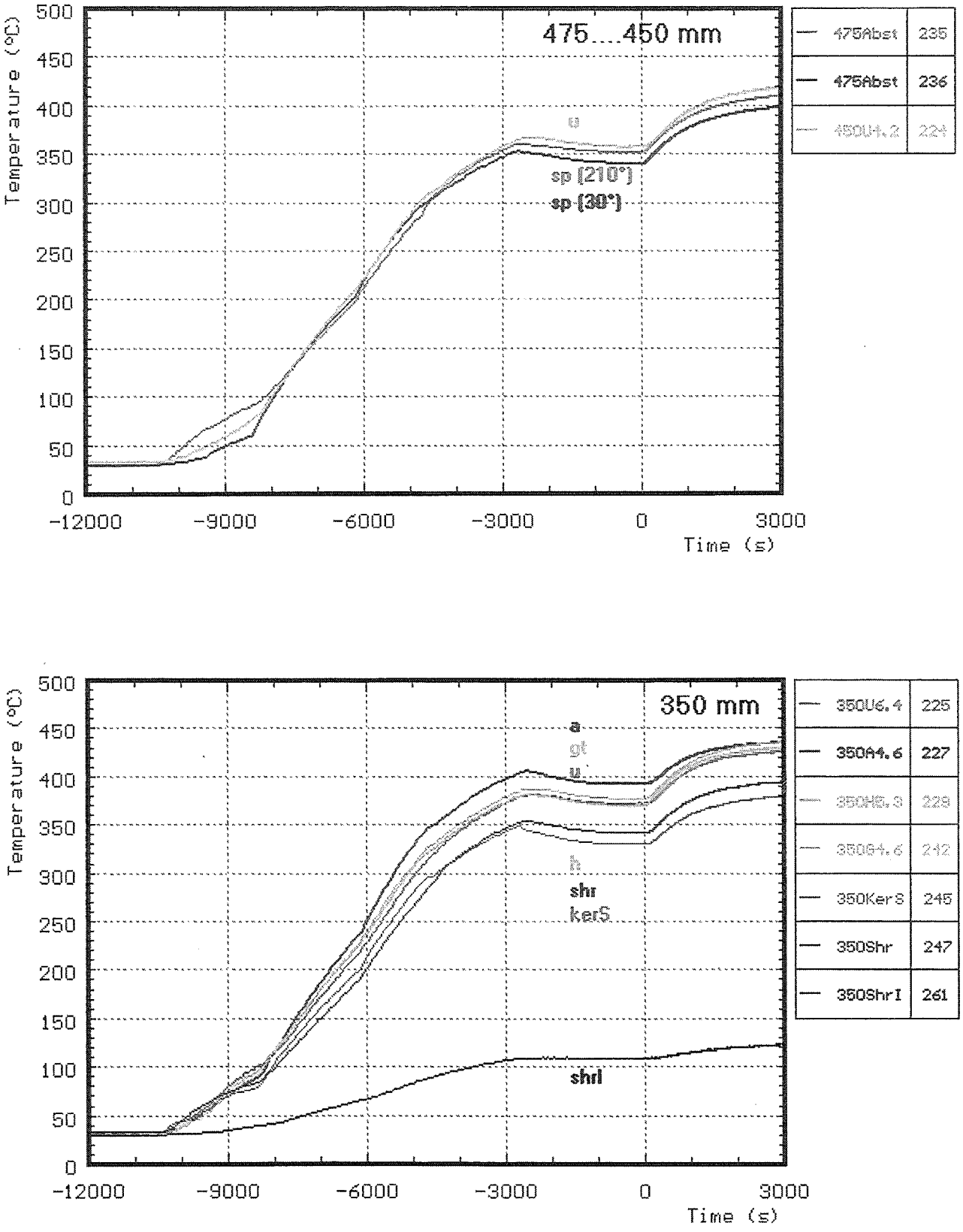

Fig. A19: CORA-29; Temperatures at elevations given (475-350 mm); pre-heat phase

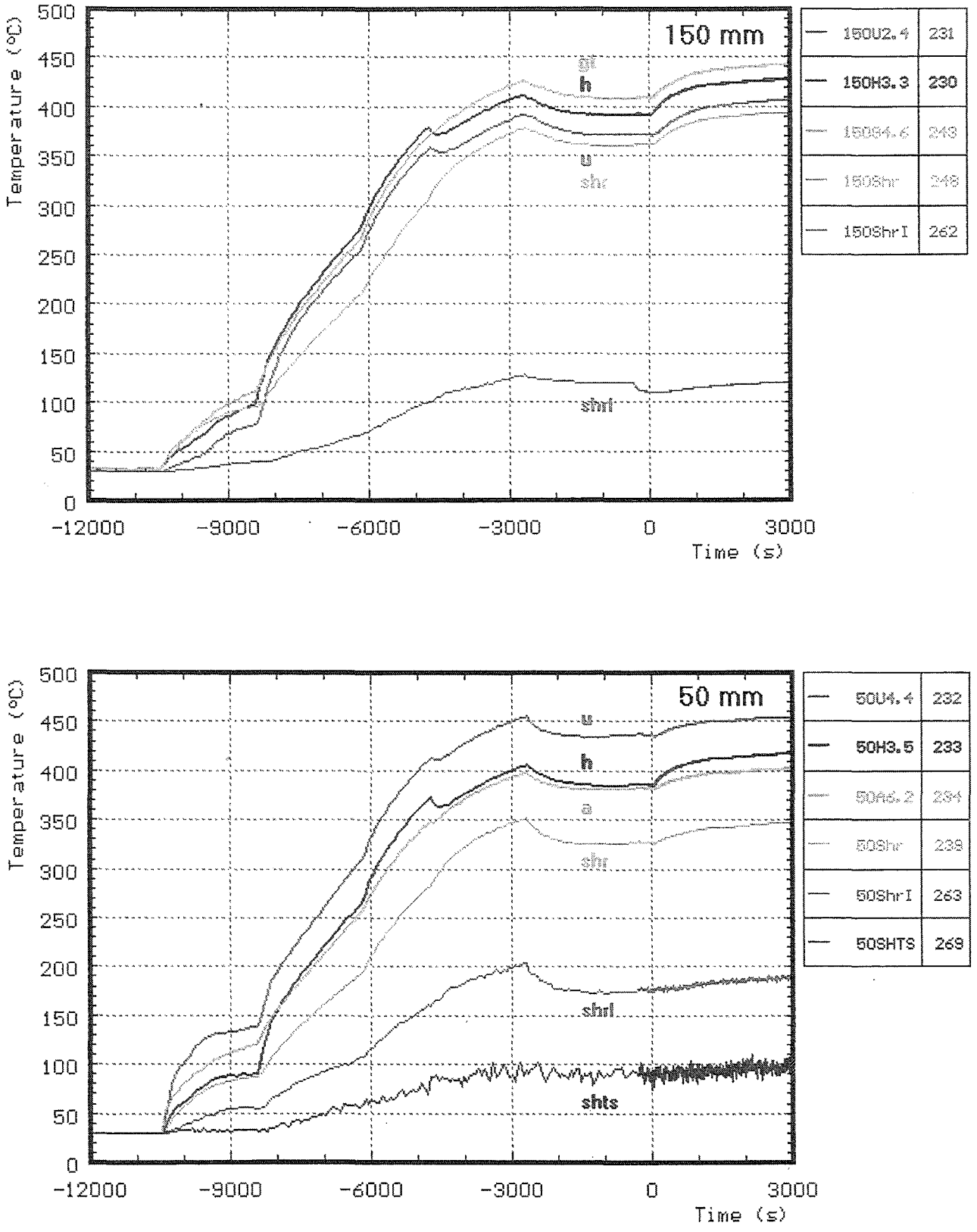

Fig. A20: CORA-29; Temperatures at elevations given (150-50 mm); pre-heat phase

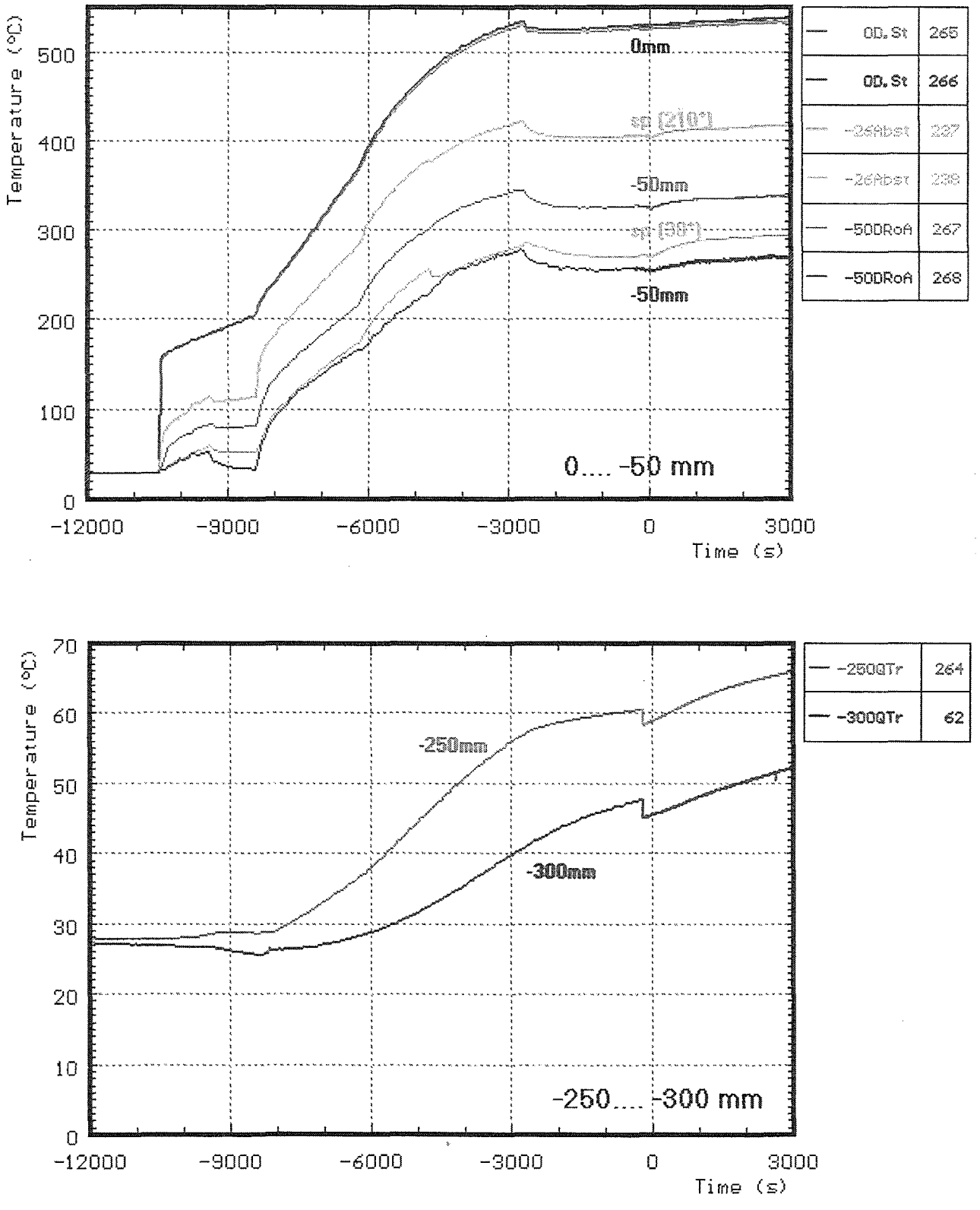

Fig. A21: CORA-29; Temperatures at elevations given (0 - -300 mm); pre-heat phase

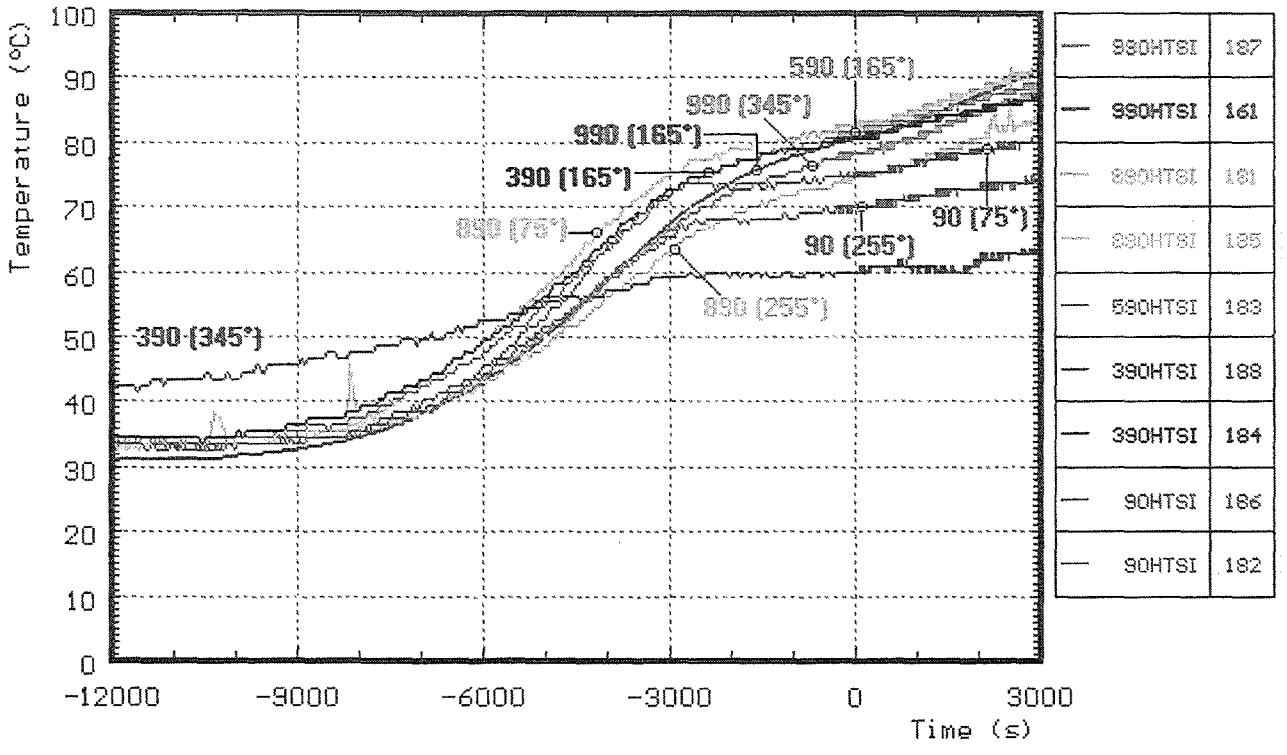

Fig. A22: CORA-29; Temperatures of HTS, Inner surface at 153 mm radius; pre-heat phase

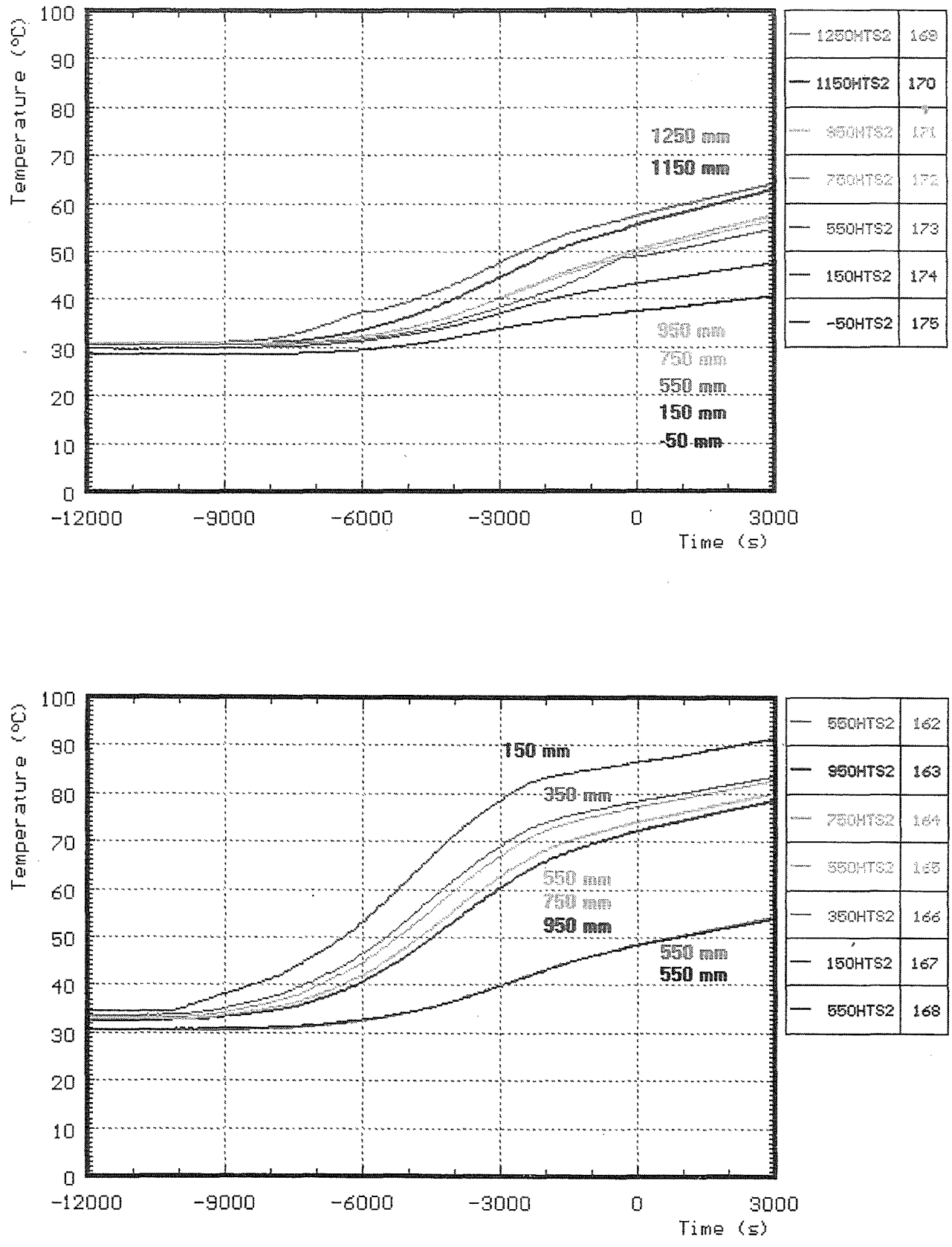

Fig. A23: CORA-29; Temperatures of HTS, Temperatures in HT shield at 192 mm radius; pre-heat phase

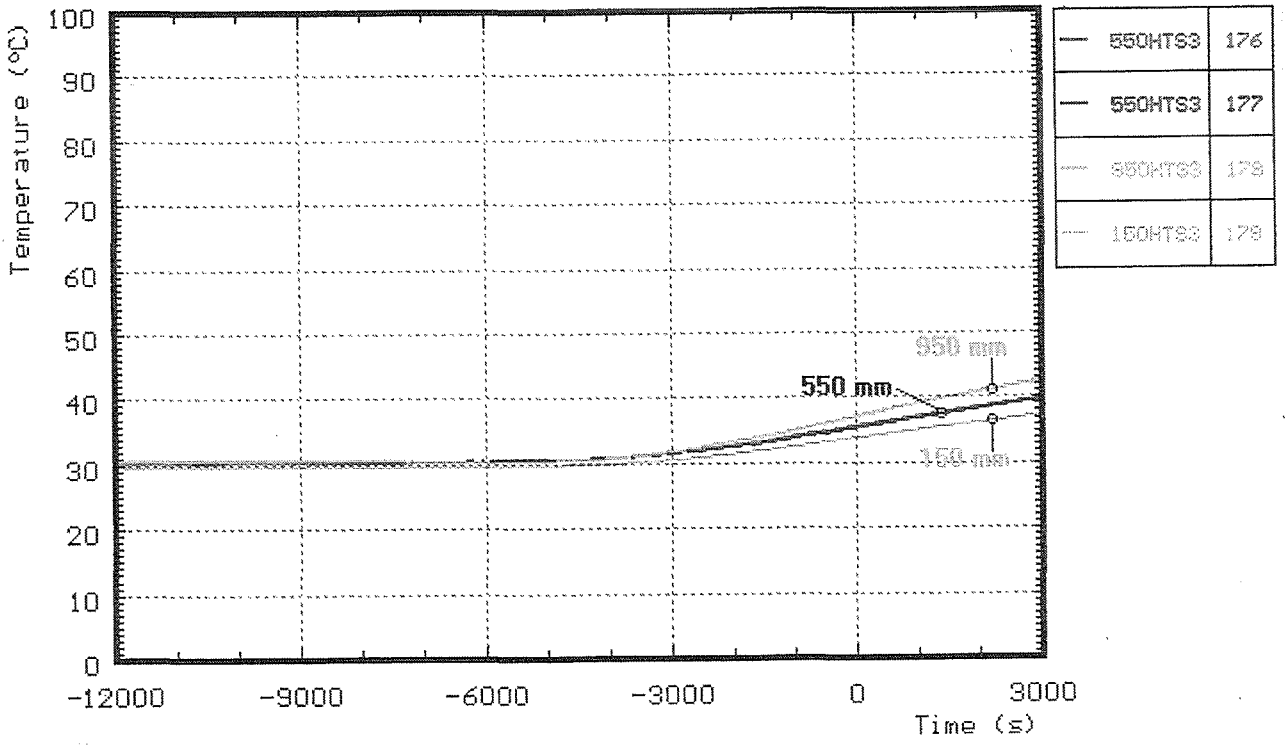

Fig. A24: CORA-29; Temperatures of HTS, Temperatures in HT shield at 255 mm radius; pre-heat phase

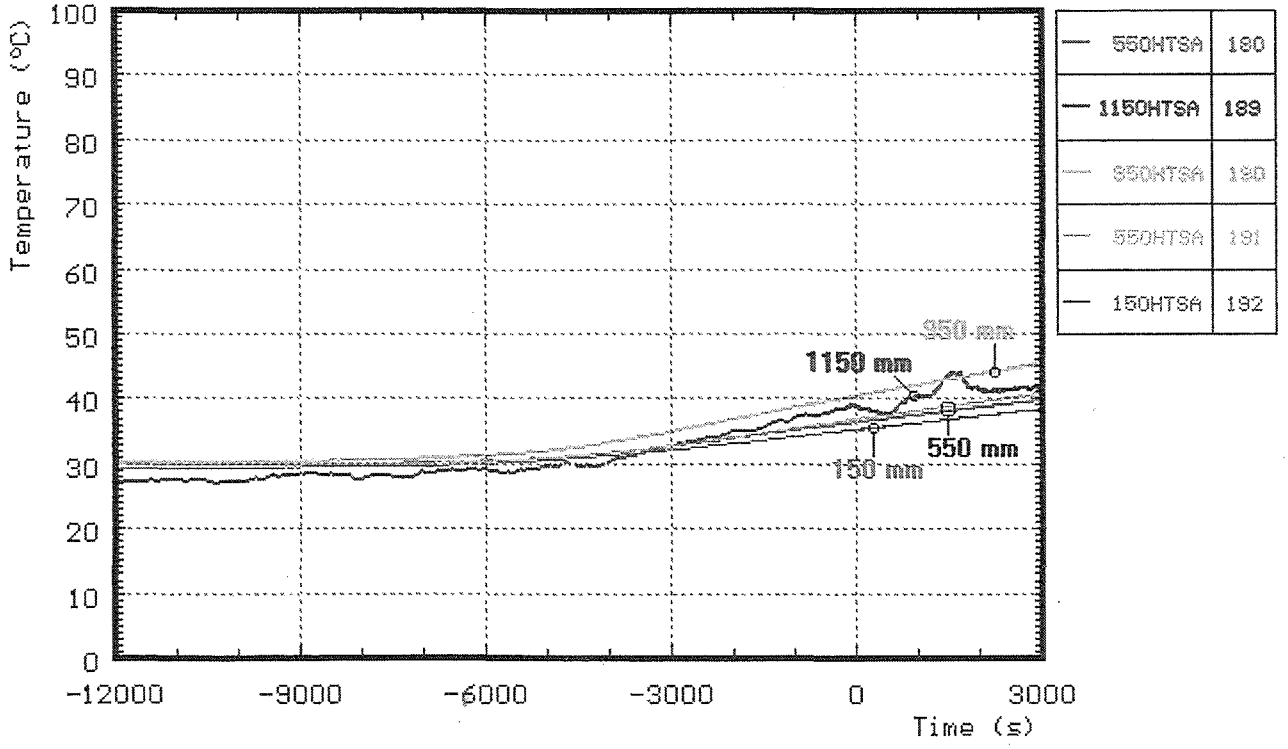

Fig. A25: CORA-29; Temperatures of HTS, Temperatures in HT shield at 293 mm radius; pre-heat phase

APPENDIX B

Test data of pre-oxidation

Figures: B1 - B18

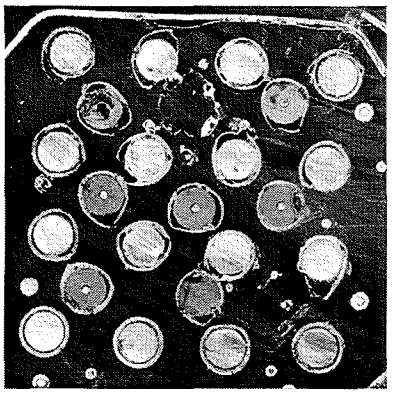

1650 °C
1225mm

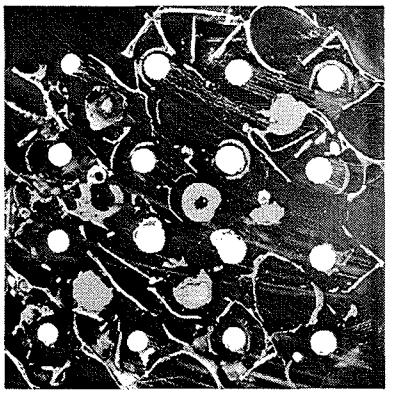

1983 °C
872mm

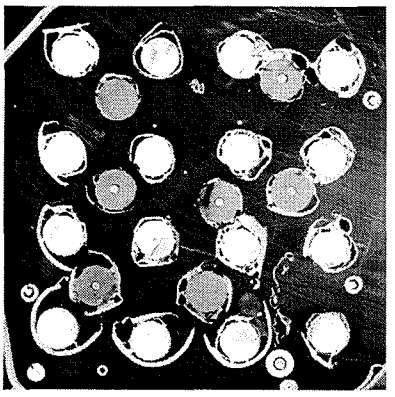

1800 °C
1171mm

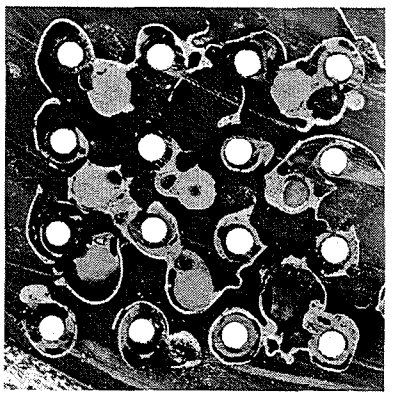

2000 °C
740mm

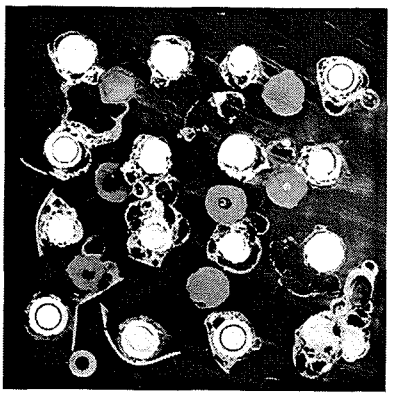

1940 °C
1029mm

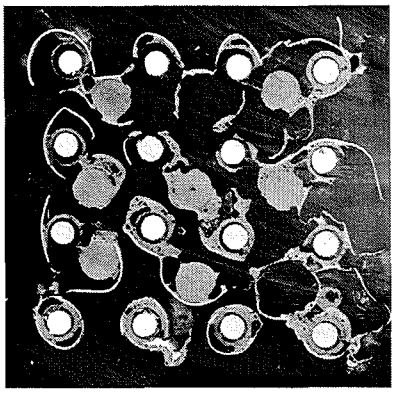

2000 °C
725mm

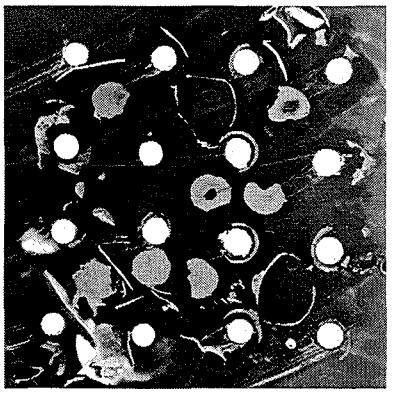

1989 °C
887mm

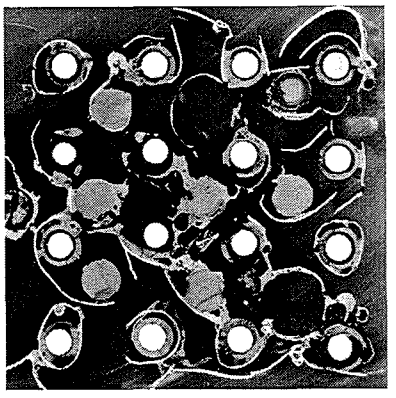

2000 °C
583mm

Fig. B1: Horizontal cross sections of bundle CORA-29; top view (1225 - 583 mm)

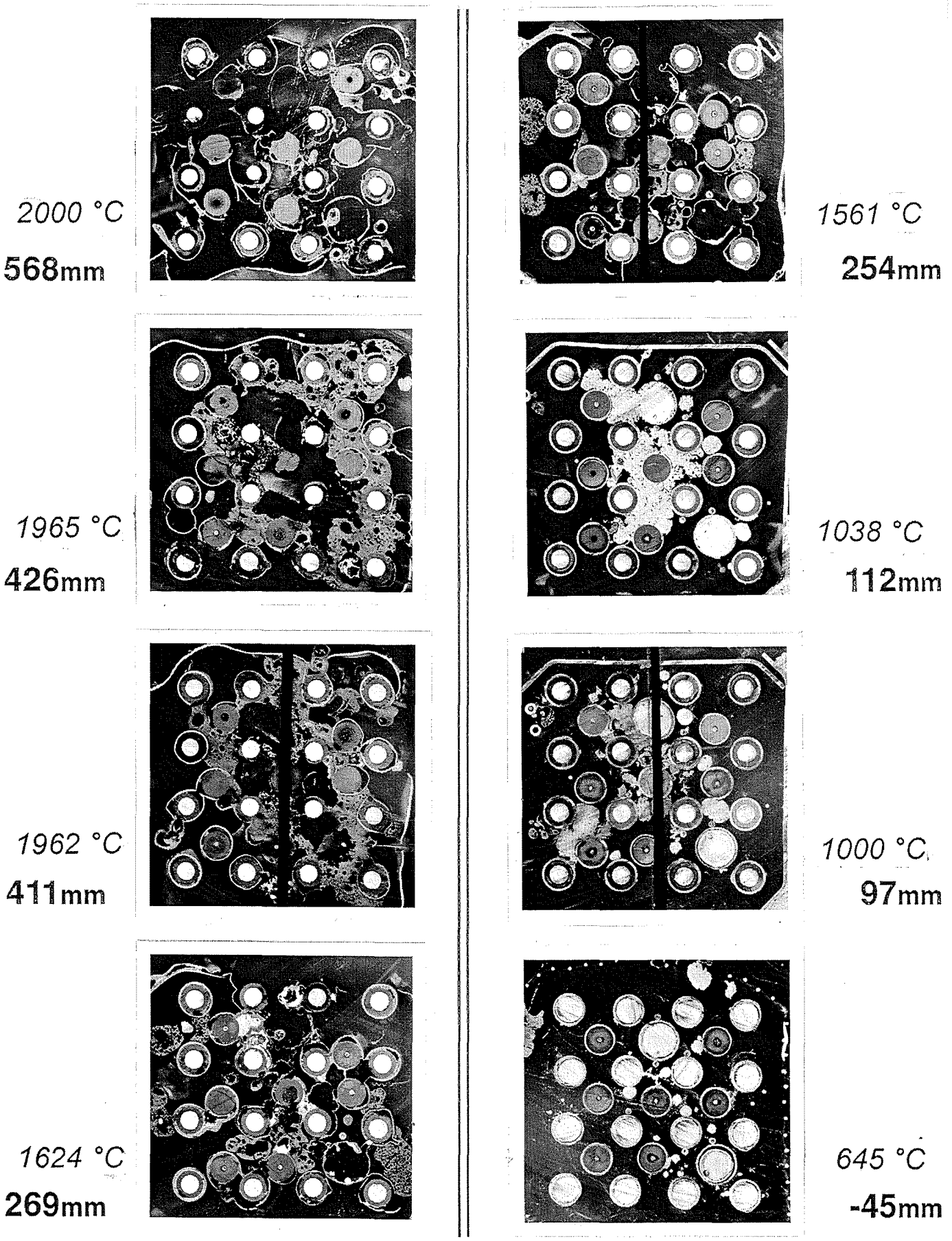

Fig. B2: Horizontal cross sections of bundle CORA-29; top view (568 - -45 mm)

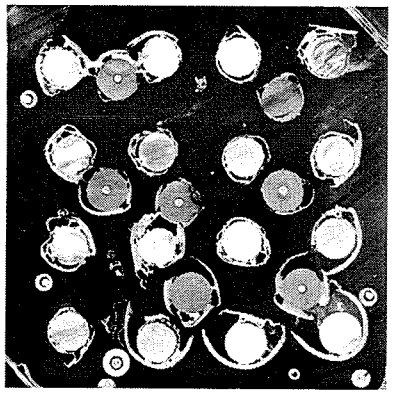

1800 °C
1173mm

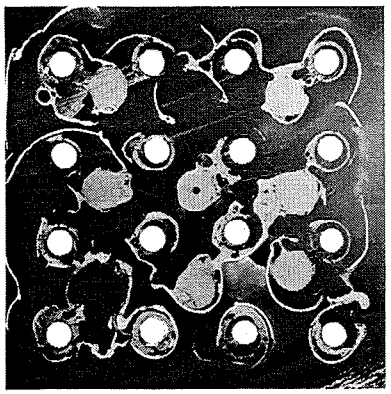

2000 °C
742mm

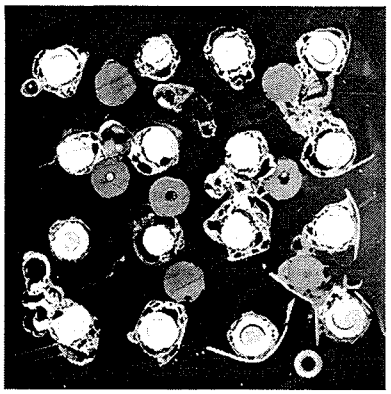

1940 °C
1031mm

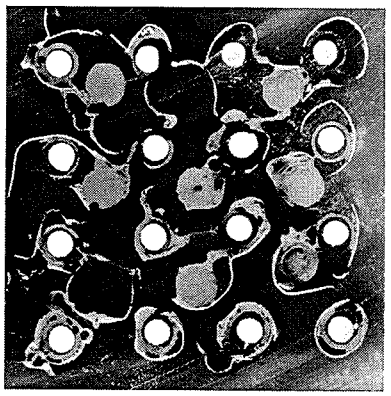

2000 °C
727mm

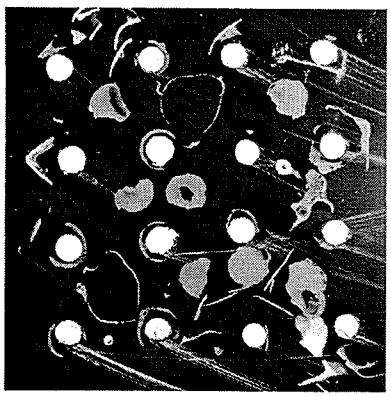

1989 °C
889mm

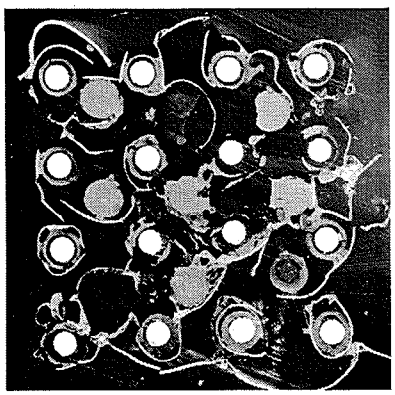

2000 °C
585mm

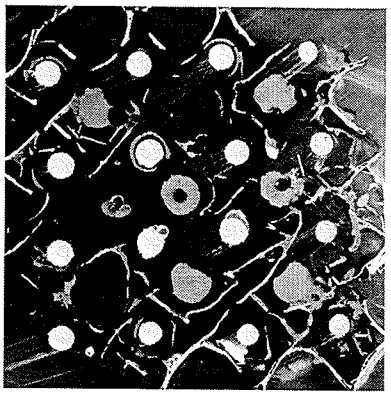

1983 °C
874mm

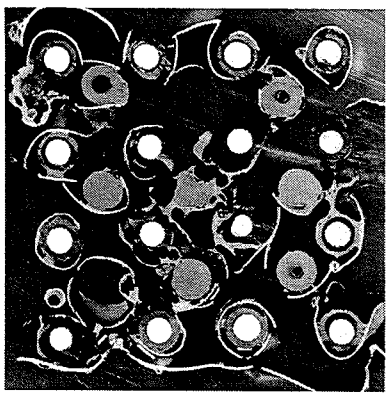

2000 °C
570mm

Fig. B3: Horizontal cross sections of bundle CORA-29; bottom view (1173 - 570 mm)

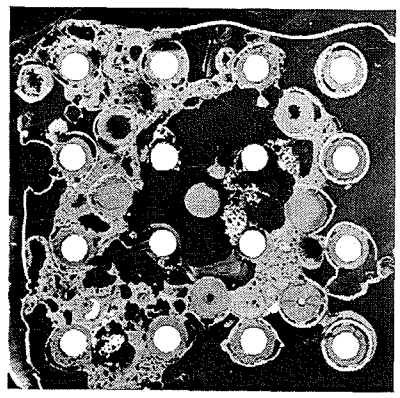

1965 °C
428mm

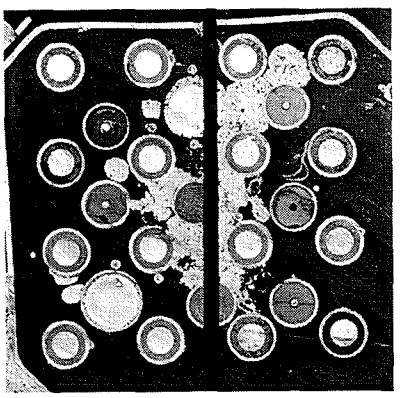

1038 °C
114mm

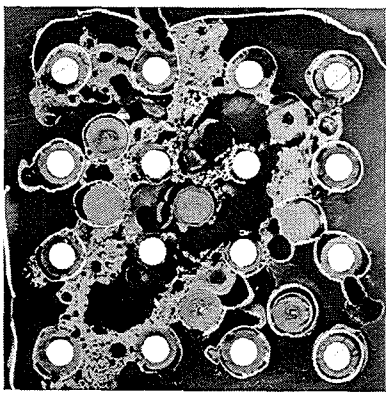

1962 °C
413mm

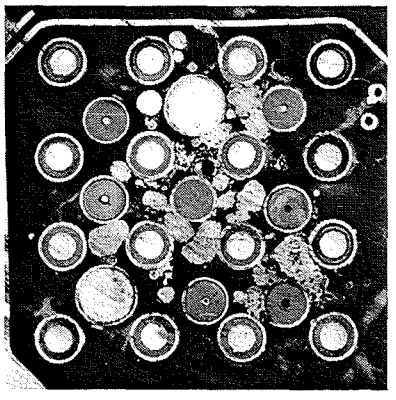

1000 °C
99mm

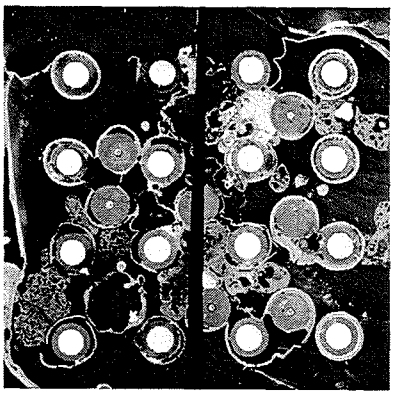

1624 °C
271mm

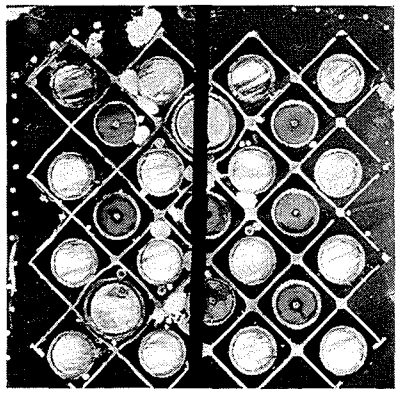

645 °C
-43mm

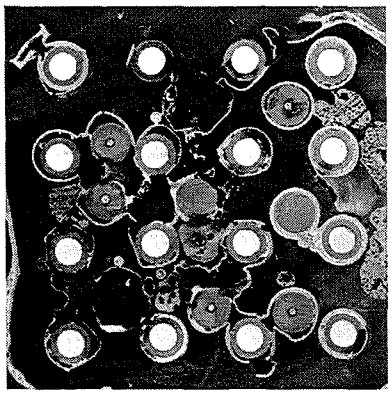

1561 °C
256mm

293 °C
-185mm

Fig. B4: Horizontal cross sections of bundle CORA-29; bottom view (428 - -185 mm)

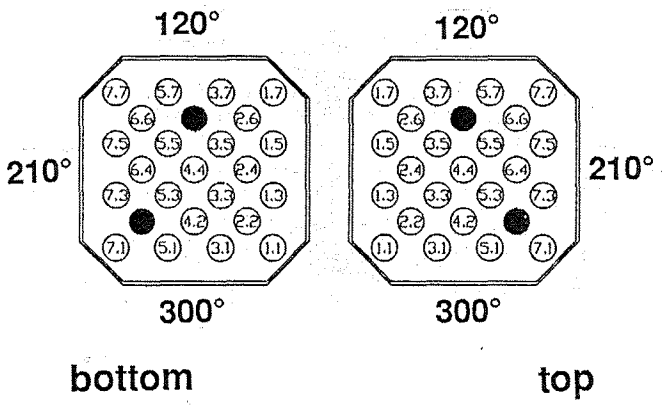

1650 °C **1225mm**

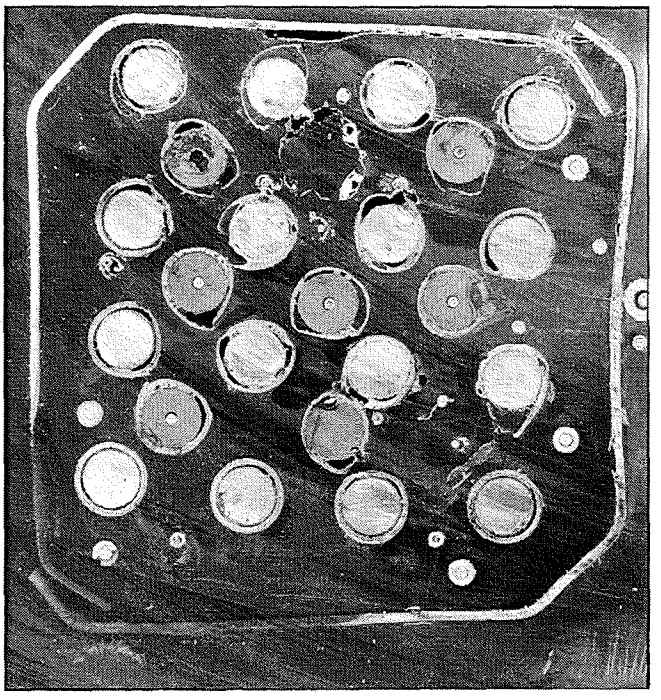

top 29-j

1173mm *1800 °C* **1171mm**

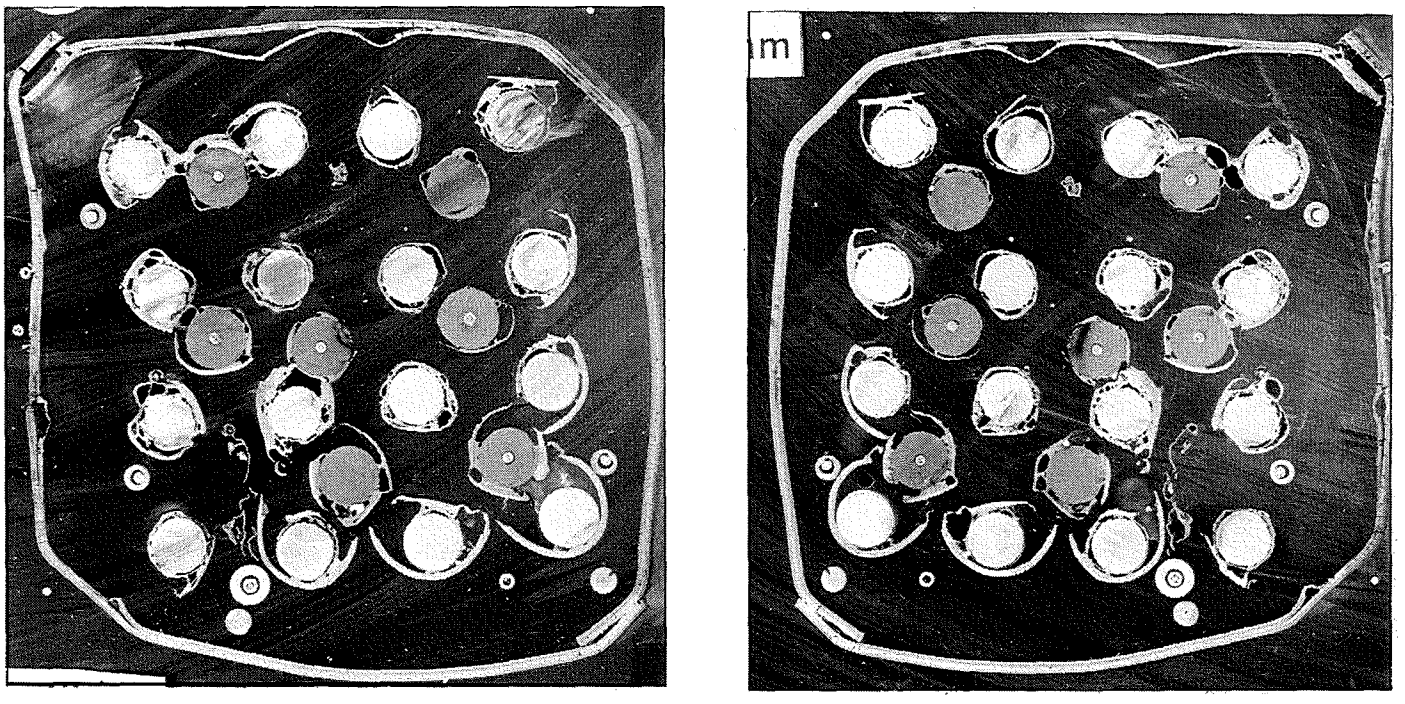

bottom 29-j top 29-i

0 5 10
(cm)

Fig. B5: Horizontal cross sections of bundle CORA-29 (1225 - 1171 mm)

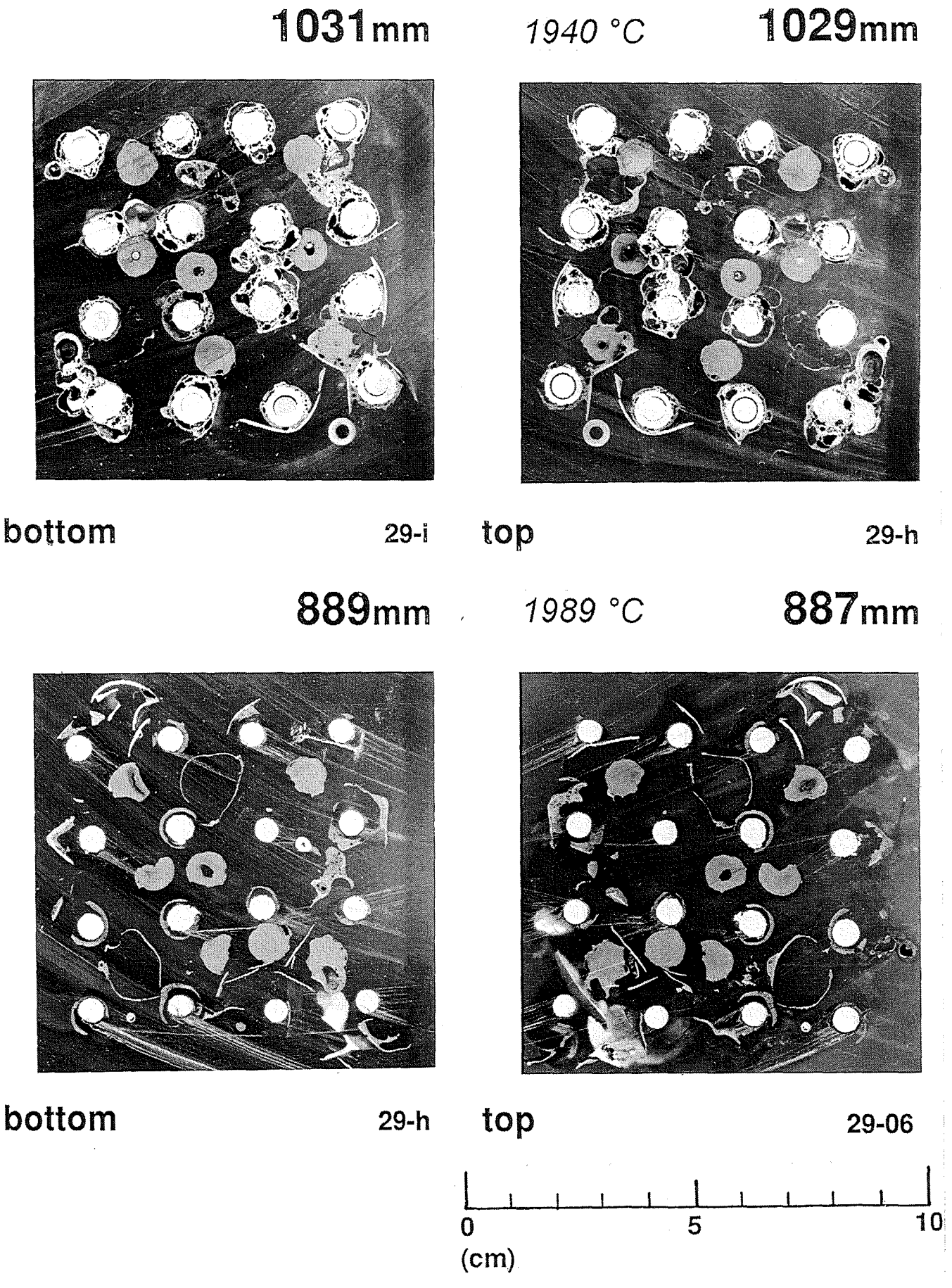

Fig. B6: Horizontal cross sections of bundle CORA-29 (1031 - 887 mm)

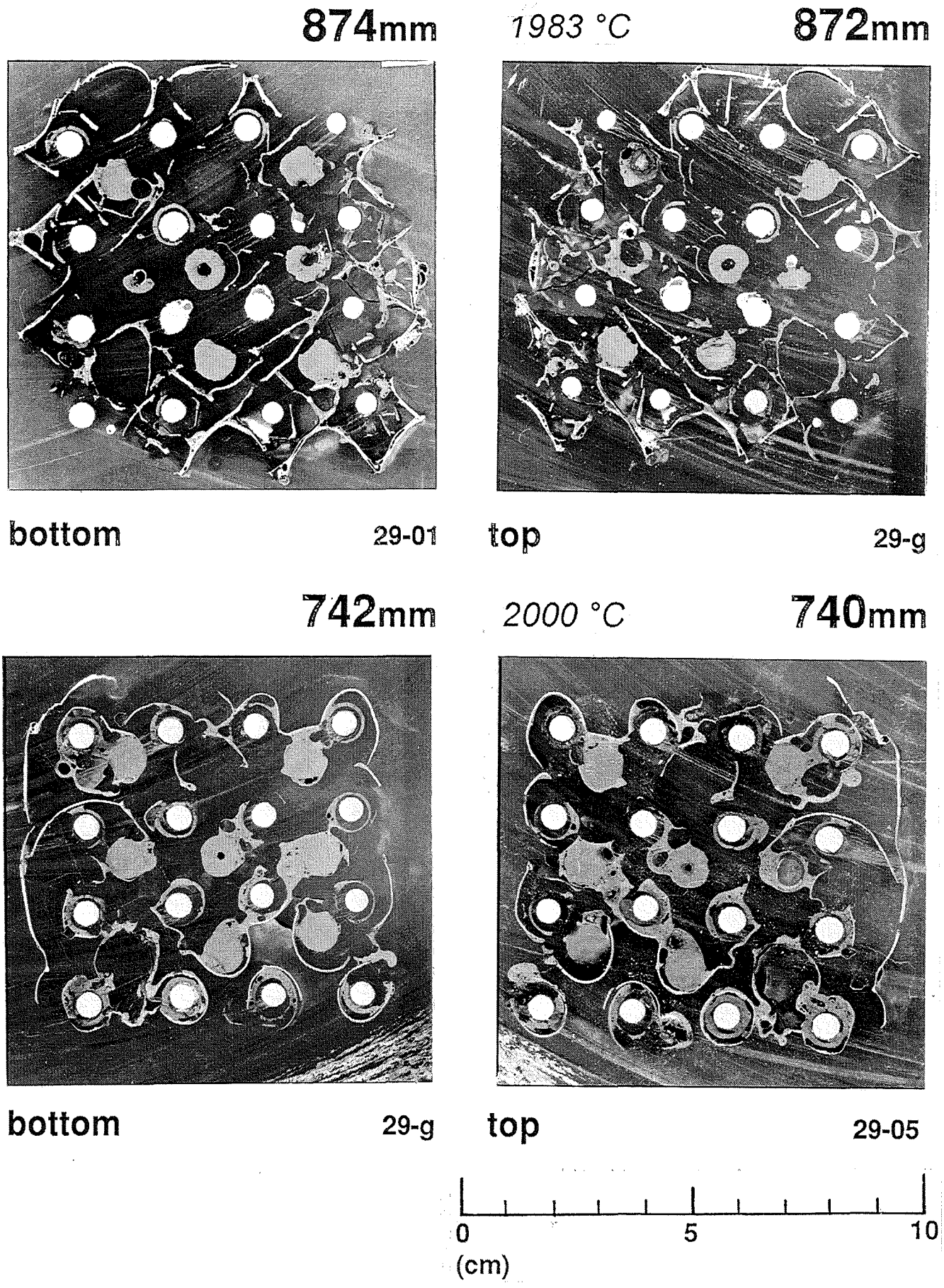

Fig. B7: Horizontal cross sections of bundle CORA-29 (874 - 740 mm)

727mm 2000 °C 725mm

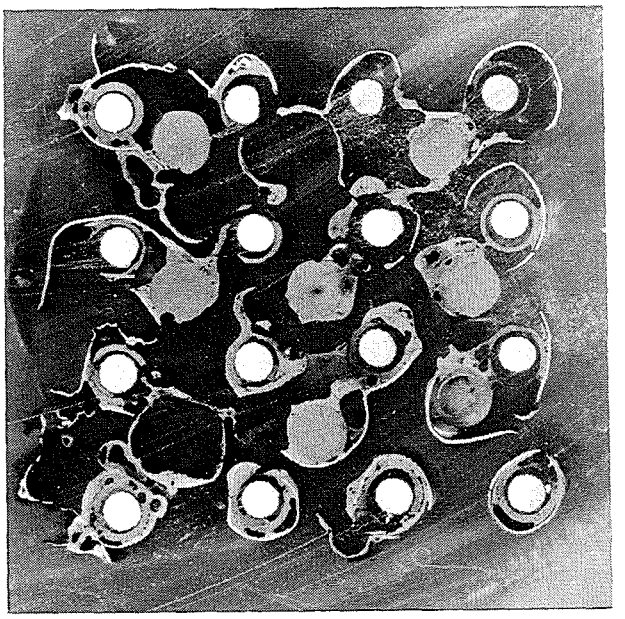

bottom 29-05

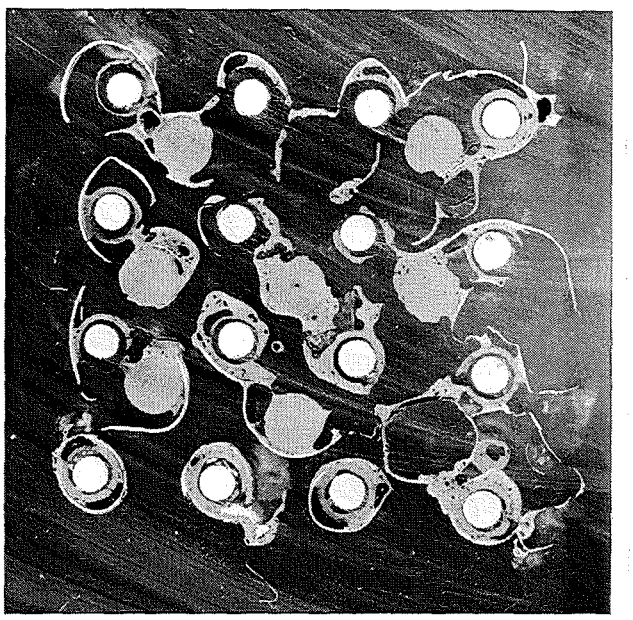

top 29-f

585mm 2000 °C 583mm

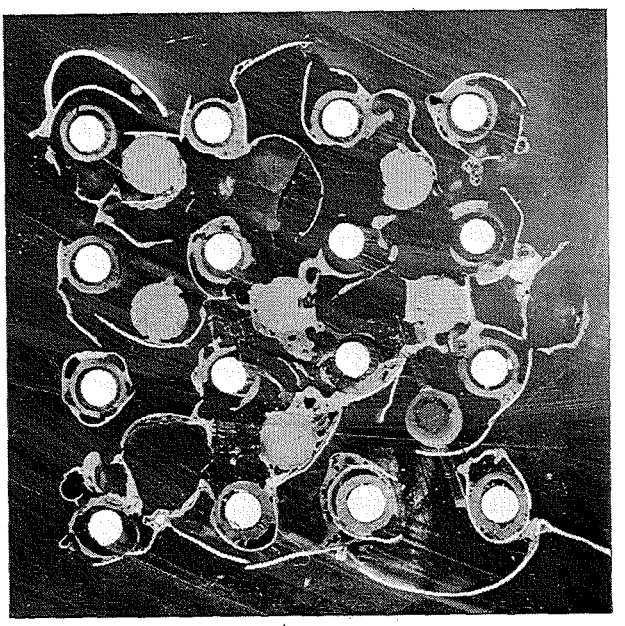

bottom 29-f

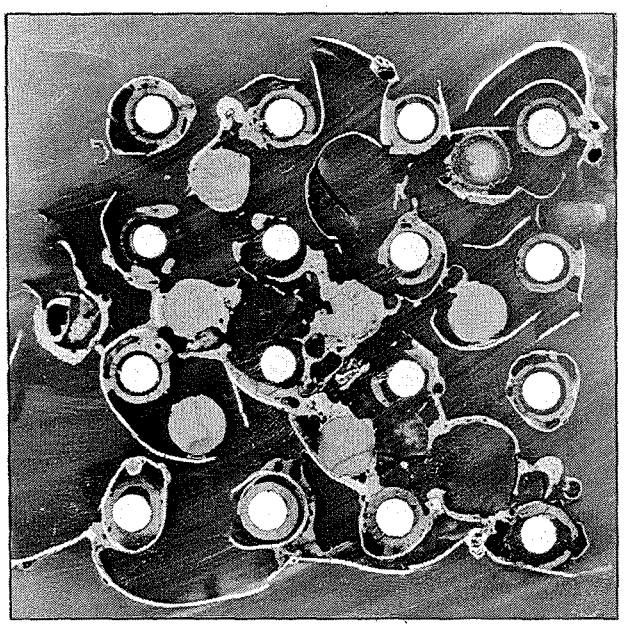

top 29-04

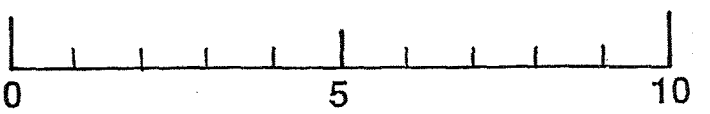

Fig. B8: Horizontal cross sections of bundle CORA-29 (727 - 583 mm)

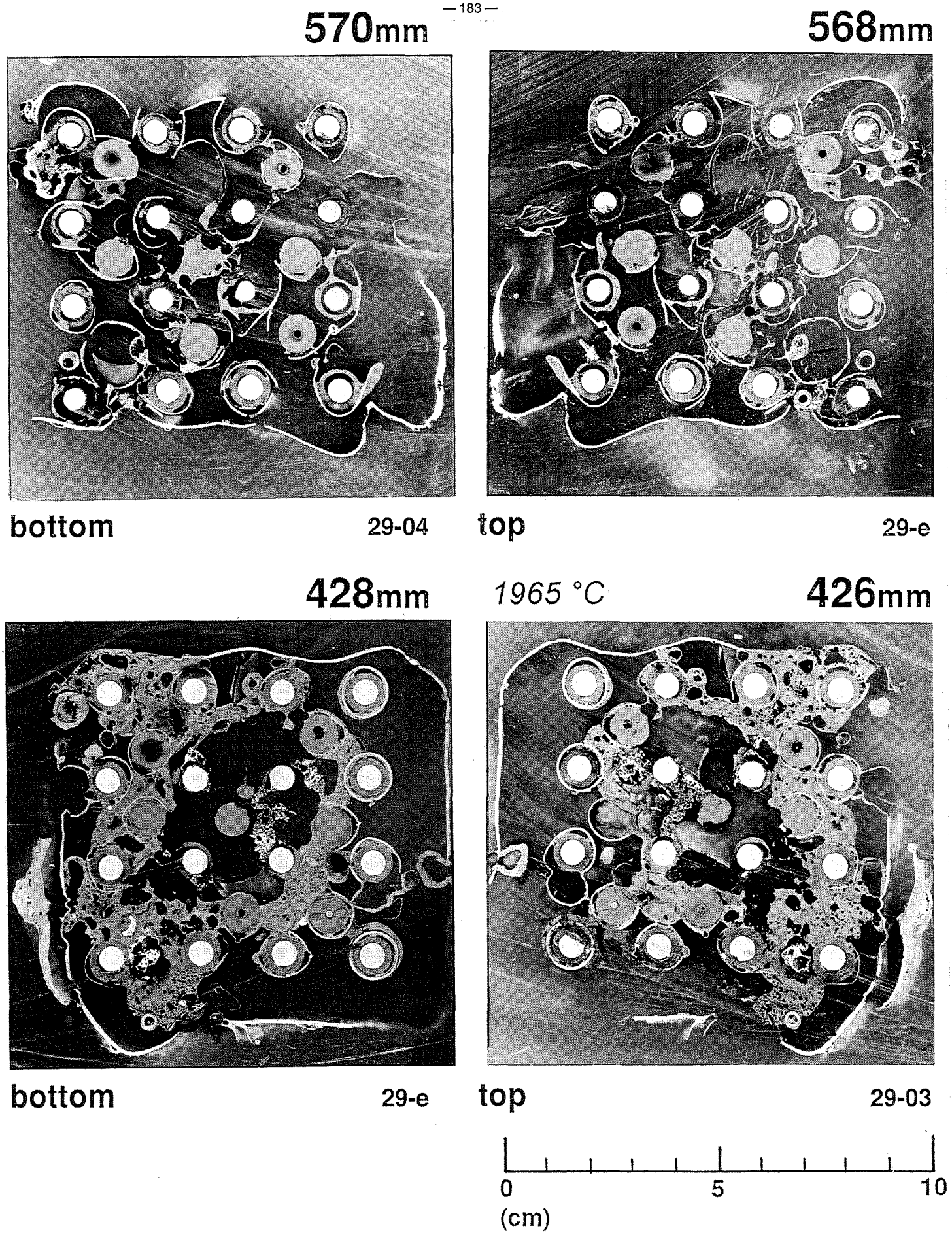

Fig. B9: Horizontal cross sections of bundle CORA-29 (570 - 426 mm)

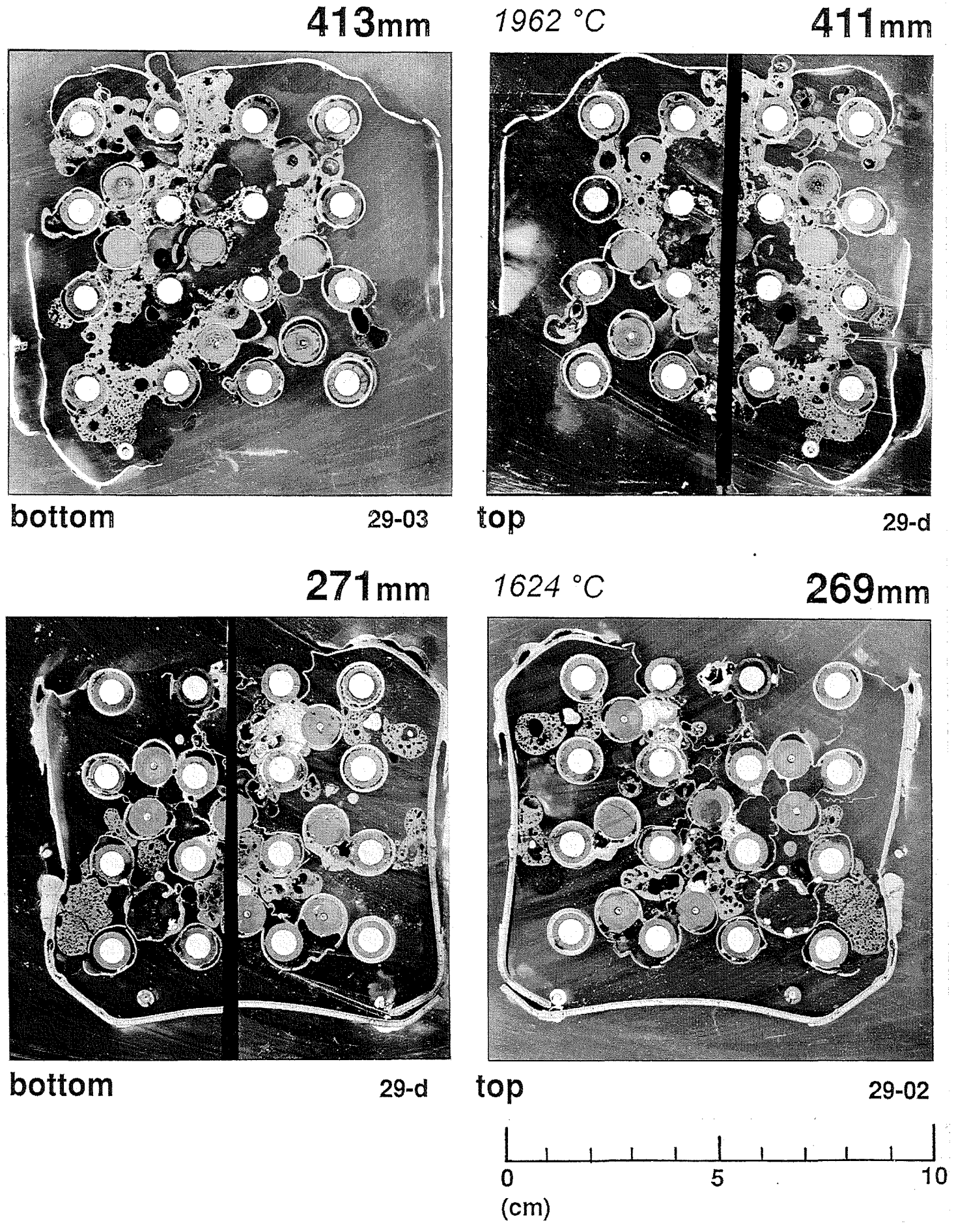

Fig. B10: Horizontal cross sections of bundle CORA-29 (413 - 269 mm)

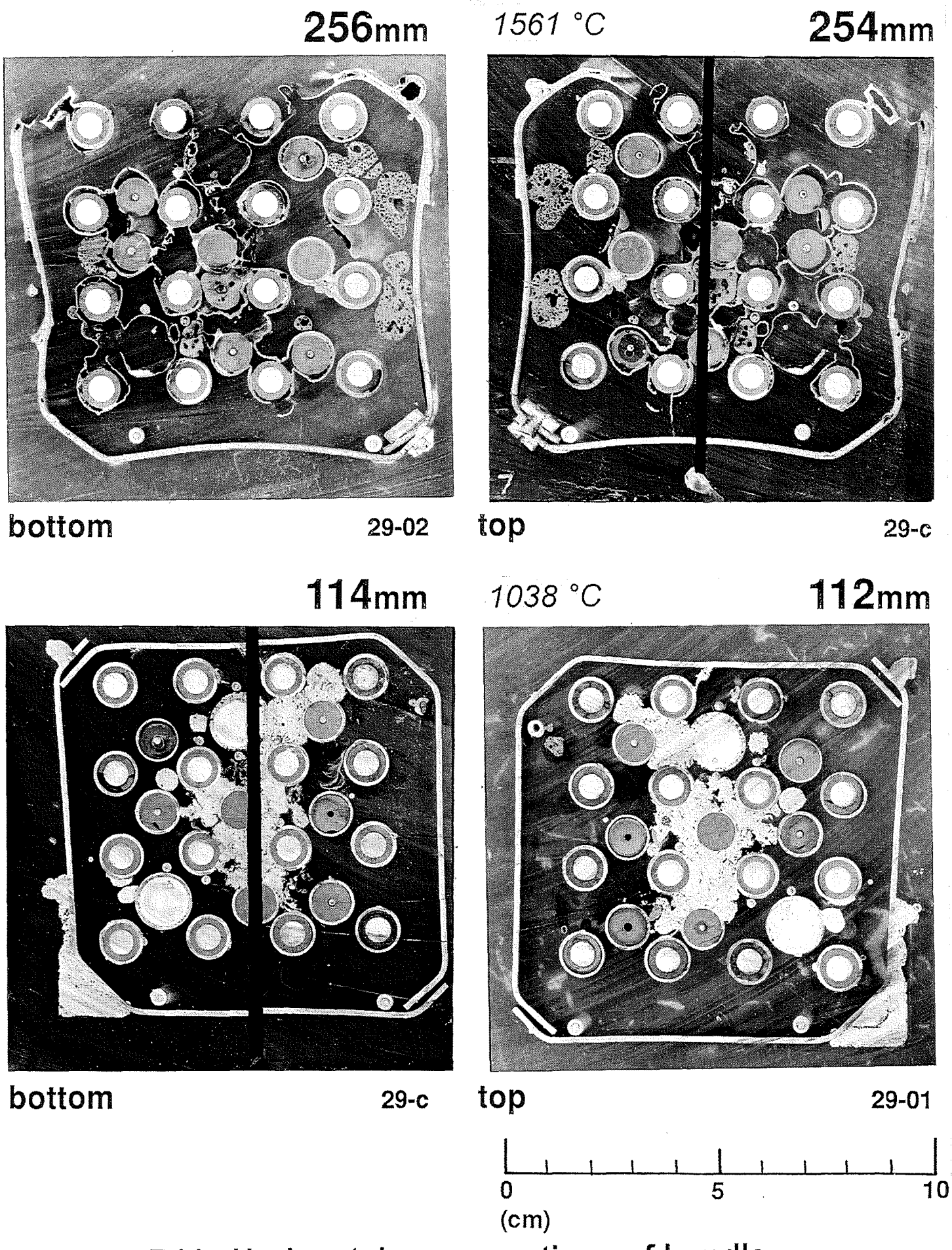

Fig. B11: Horizontal cross sections of bundle CORA-29 (256 - 112 mm)

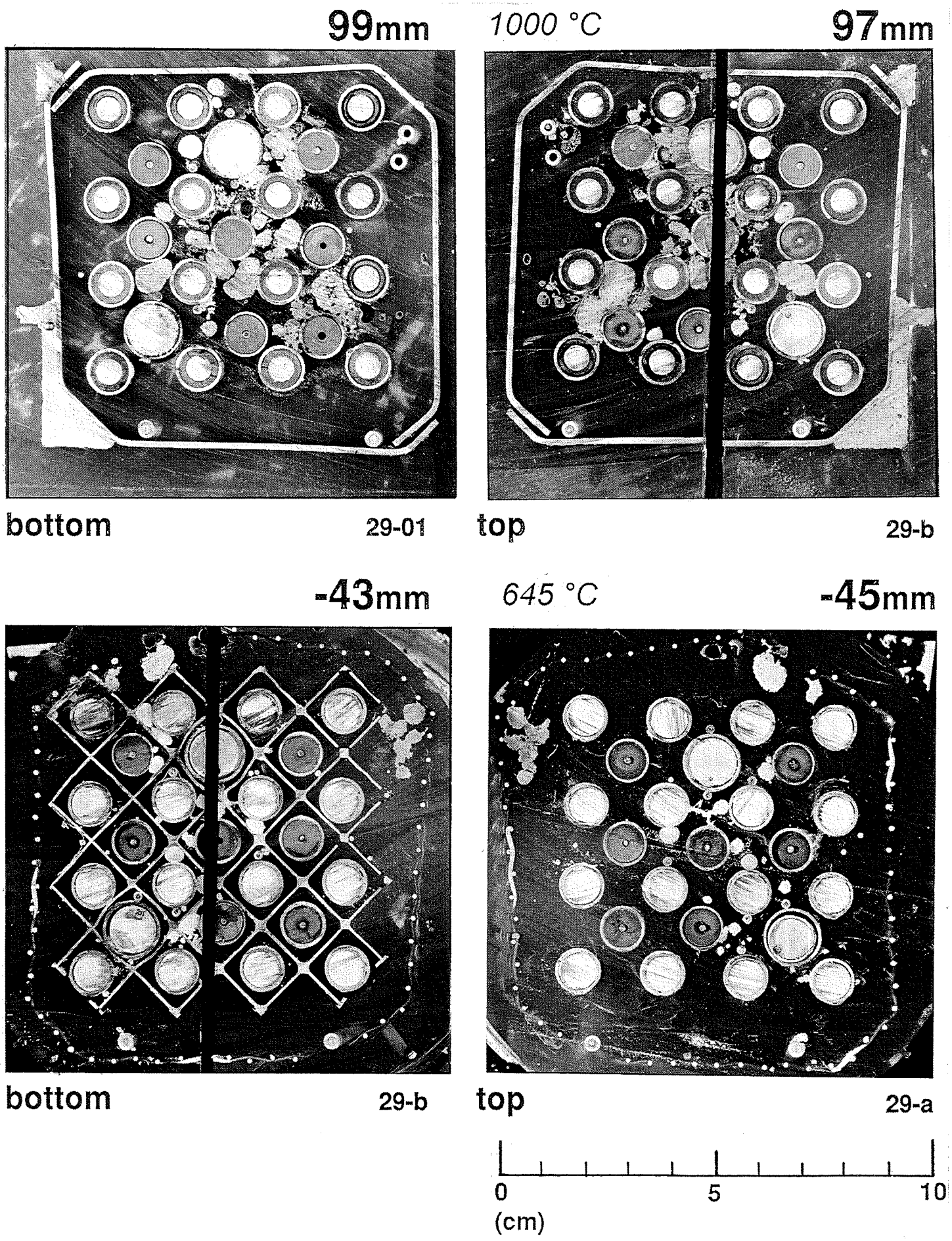

Fig. B12: Horizontal cross sections of bundle CORA-29 (99 - -45 mm)

Appendix C

Test data of the pre-oxidation phase

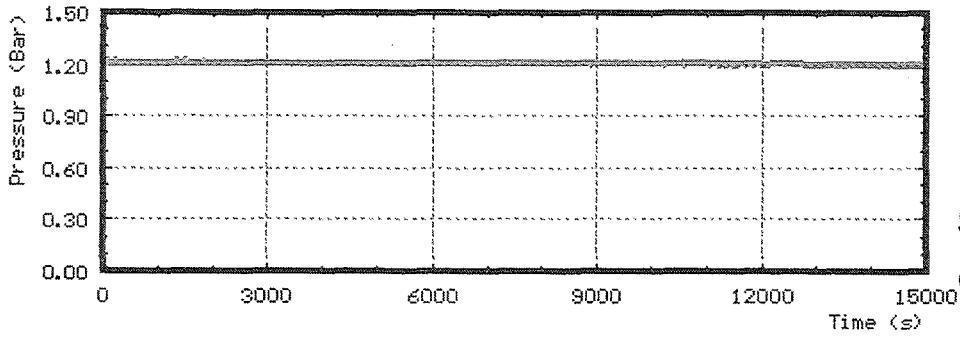

system overpressure

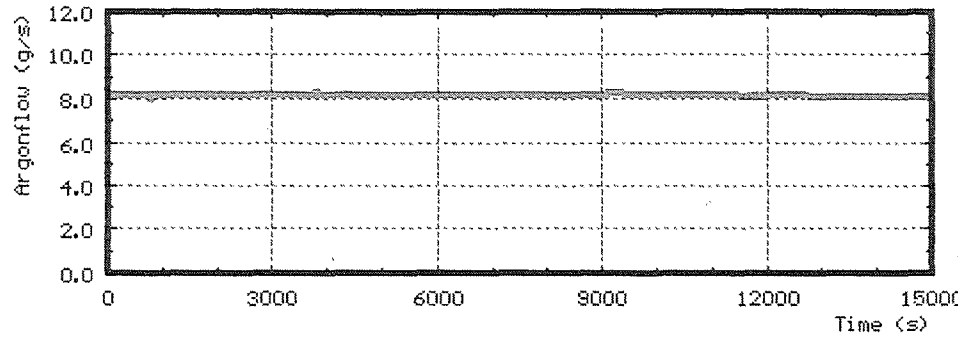

Argonflow

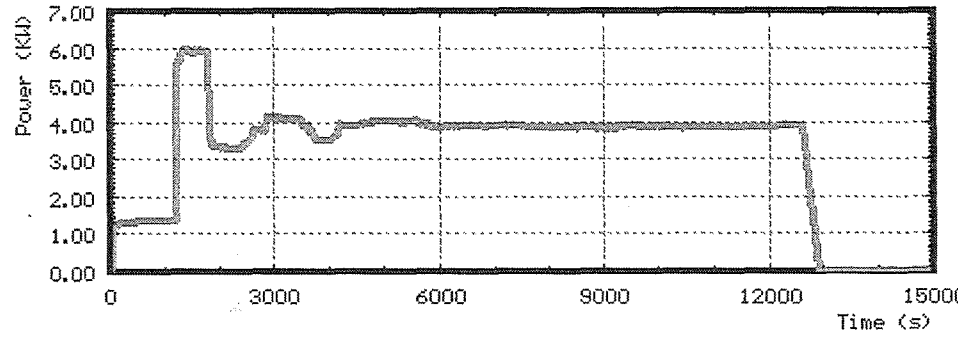

power

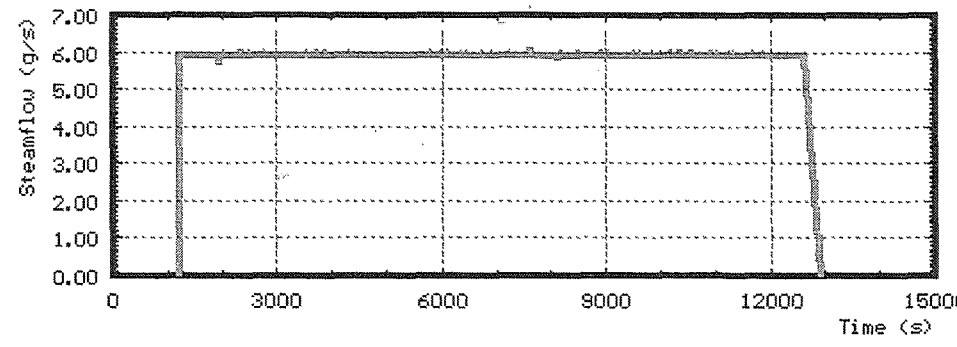

steam input

Fig. C1: System pressure, argon flow, steam input and power during pre-oxidation (CORA-29 P)

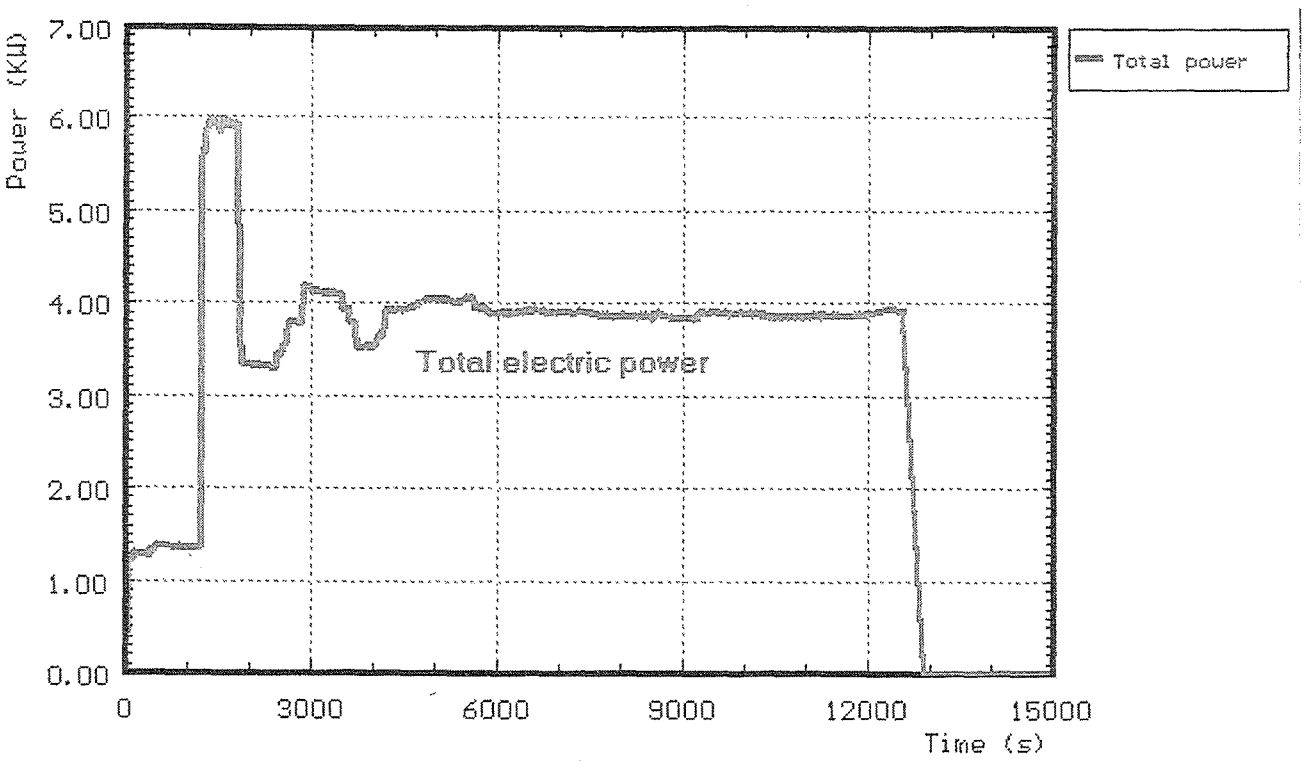

Fig. C2: Total electric power input during pre-oxidation (CORA-29 P)

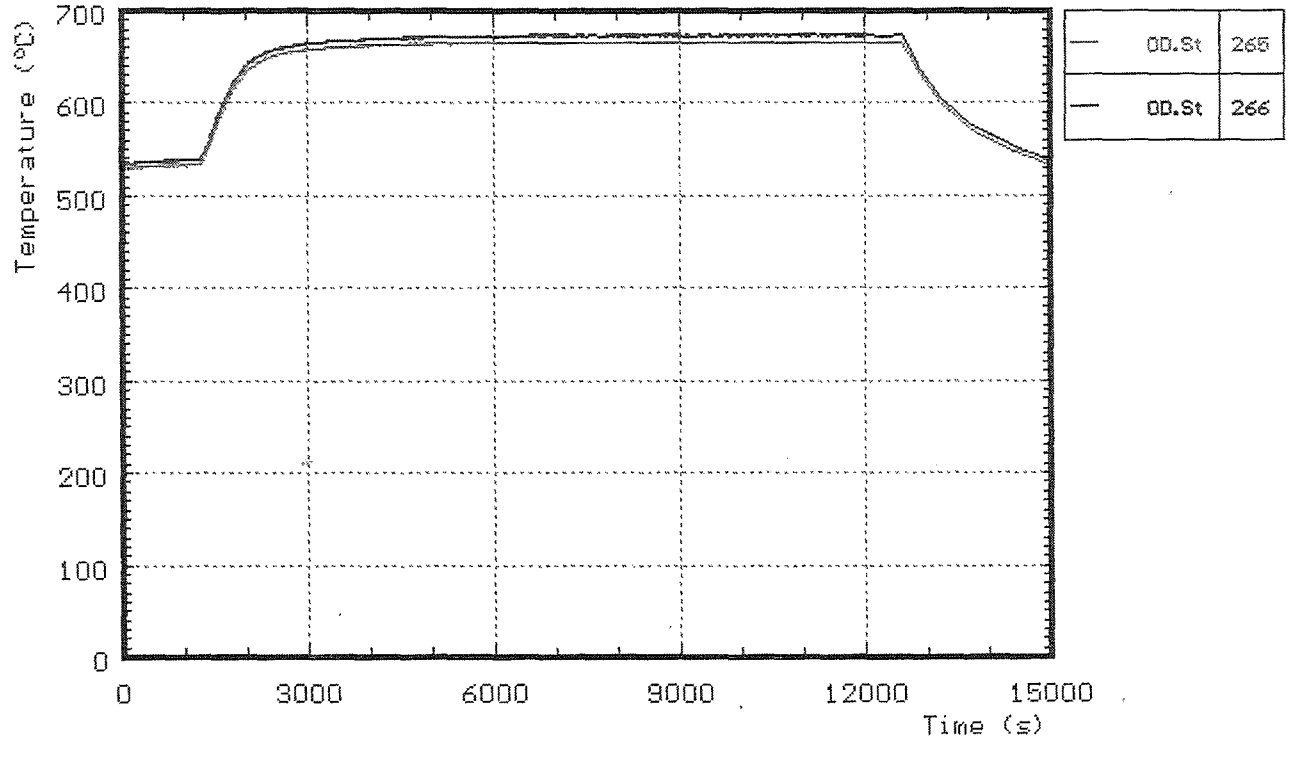

Fig. C3: Temperatures at steam inlet during pre-oxidation (CORA-29 P)

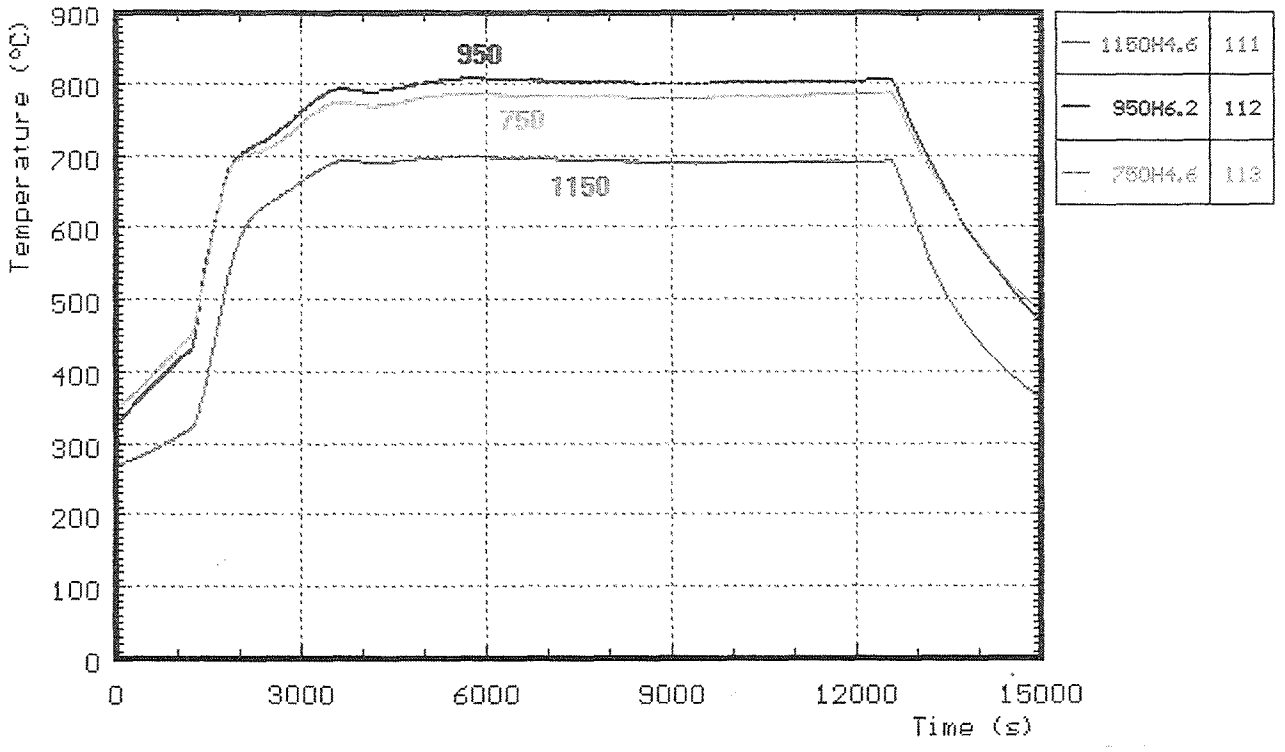

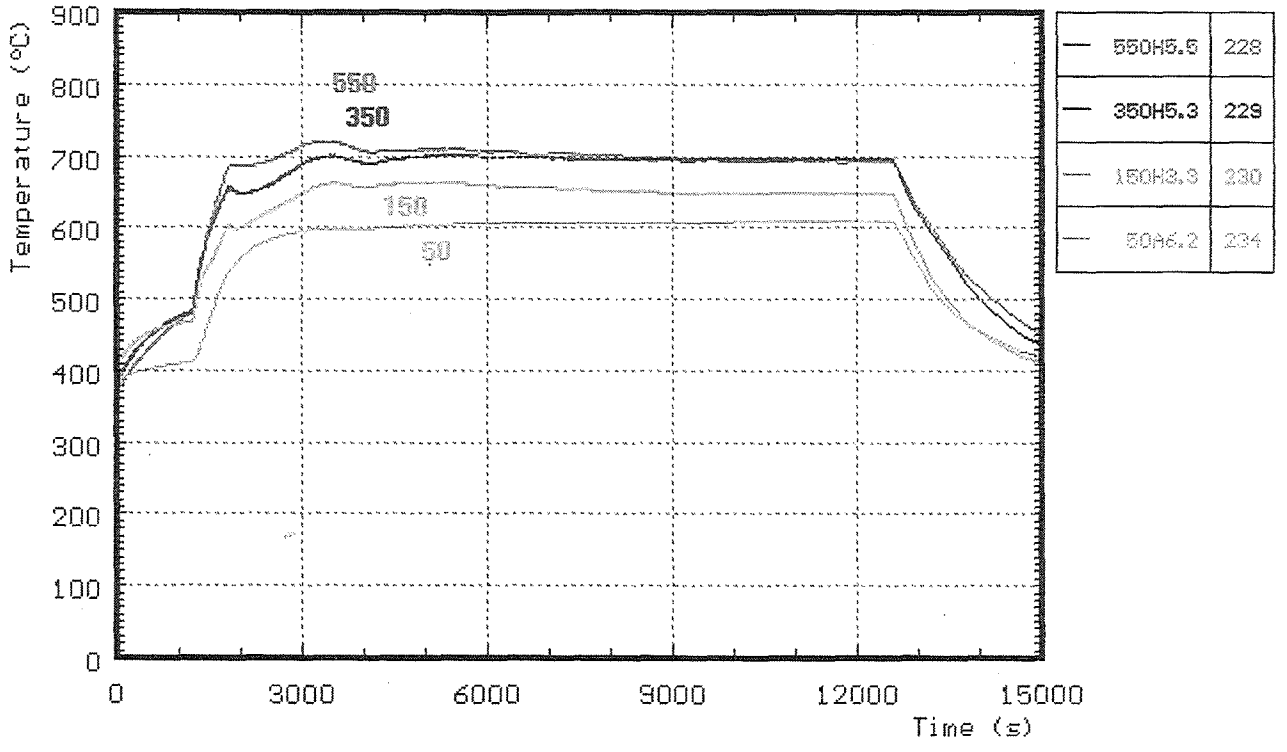

Fig. C4: Temperatures of heated rods during pre-oxidation (CORA-29 P)

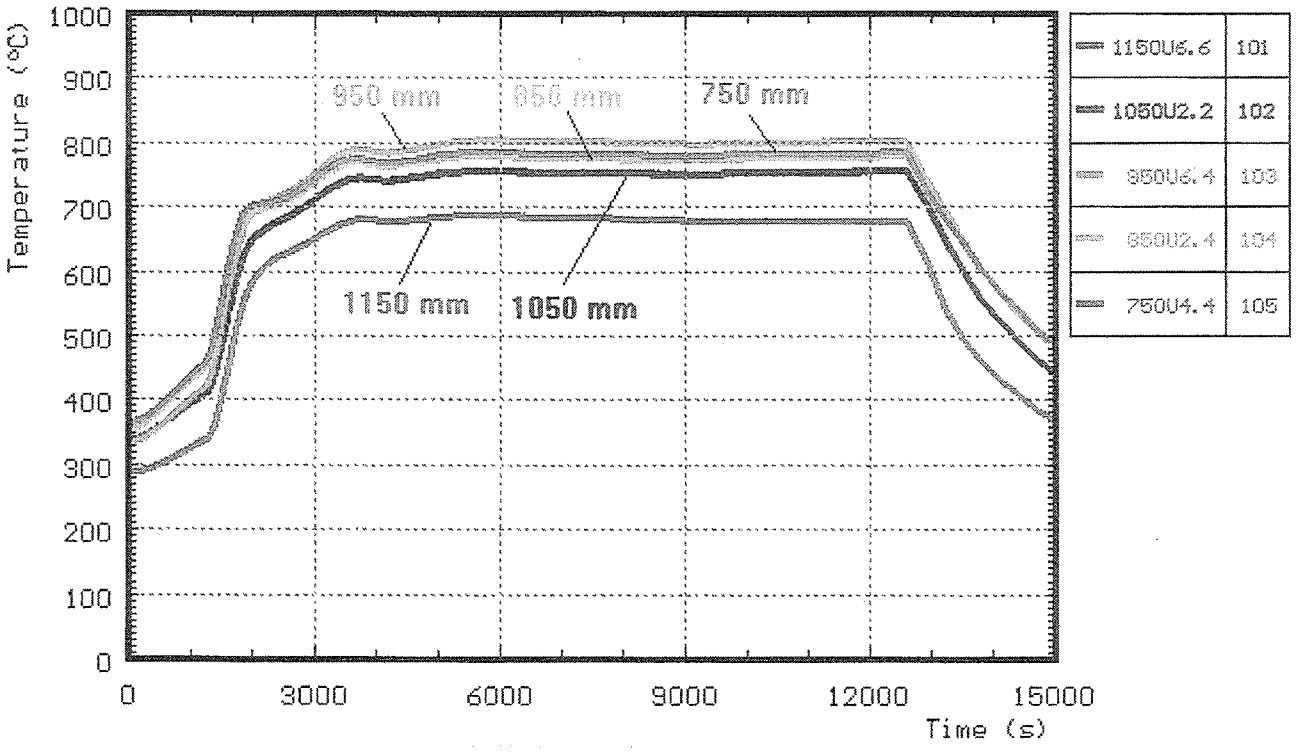

Fig. C5: Temperatures of unheated rods during pre-oxidation (CORA-29 P)

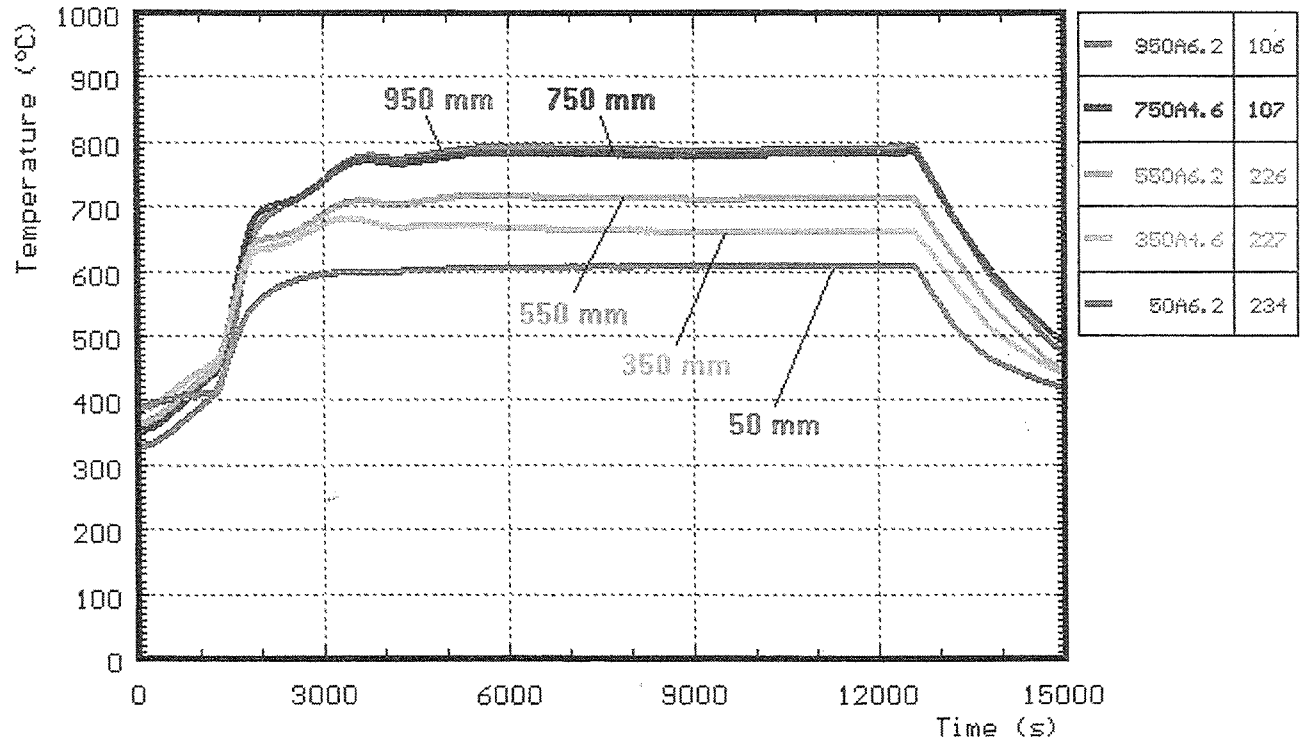

Fig. C6: Temperatures of the absorber rods during pre-oxidation (CORA-29 P)

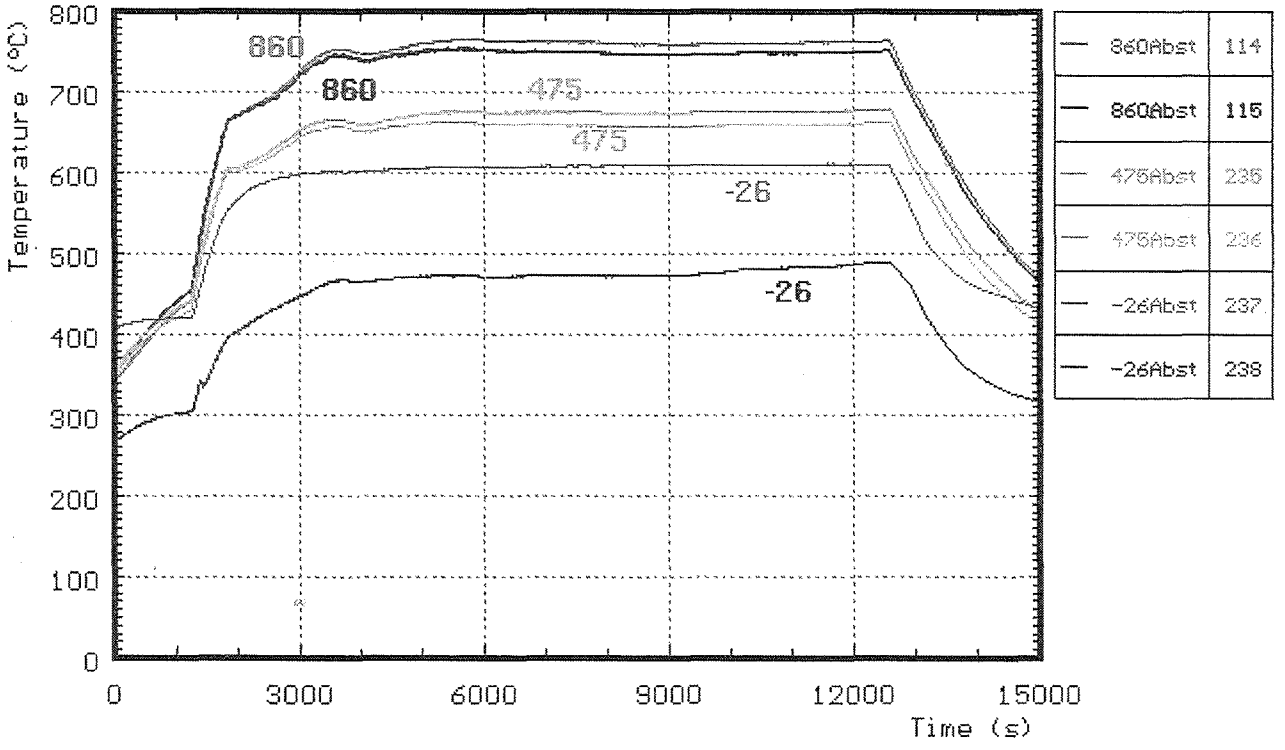

Fig. C7: Temperatures of the spacers during pre-oxidation (CORA-29 P)

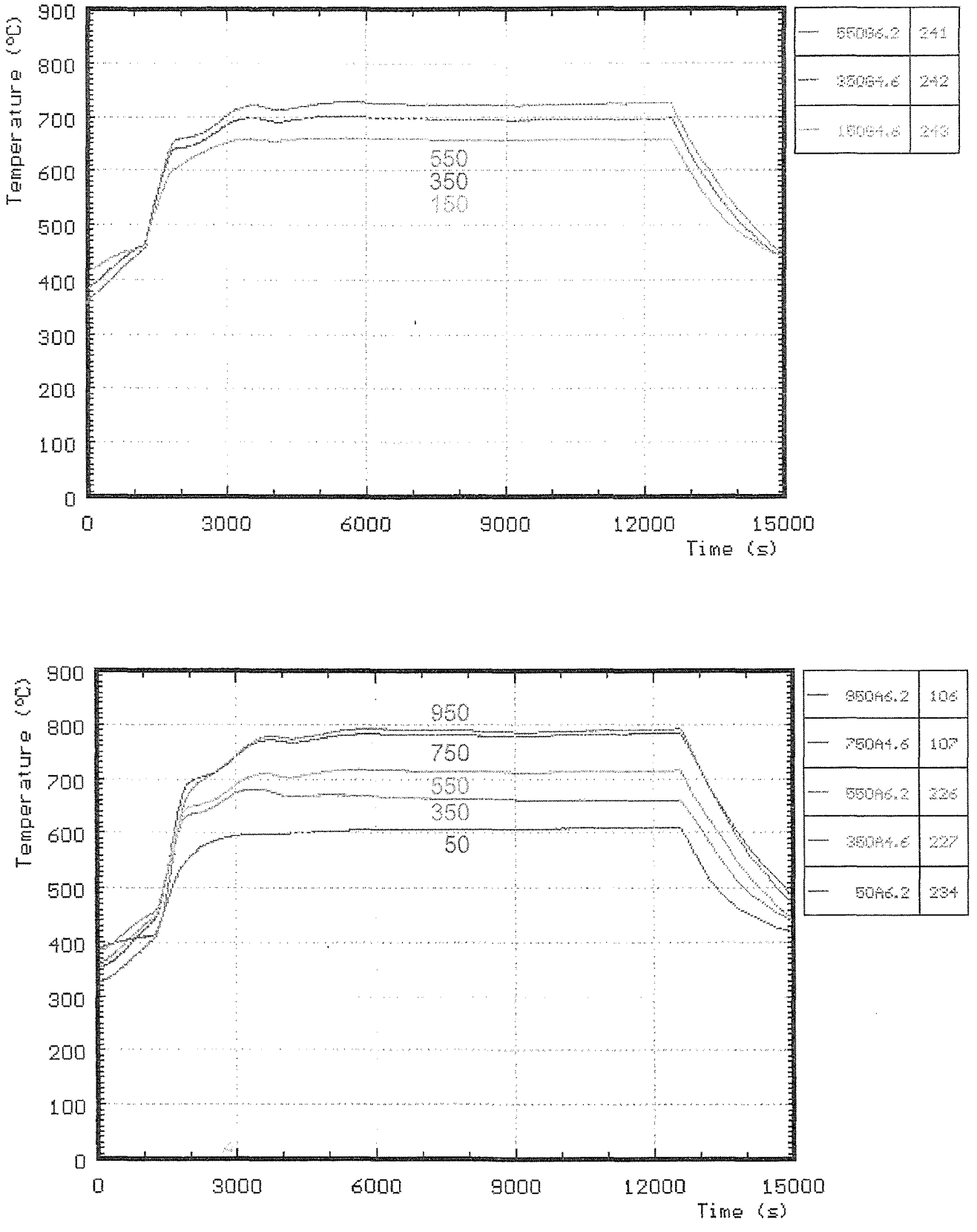

Fig. C8: Temperatures of the absorber rods and in the guide tubes during pre-oxidation (CORA-29 P) c29_c08.cdr

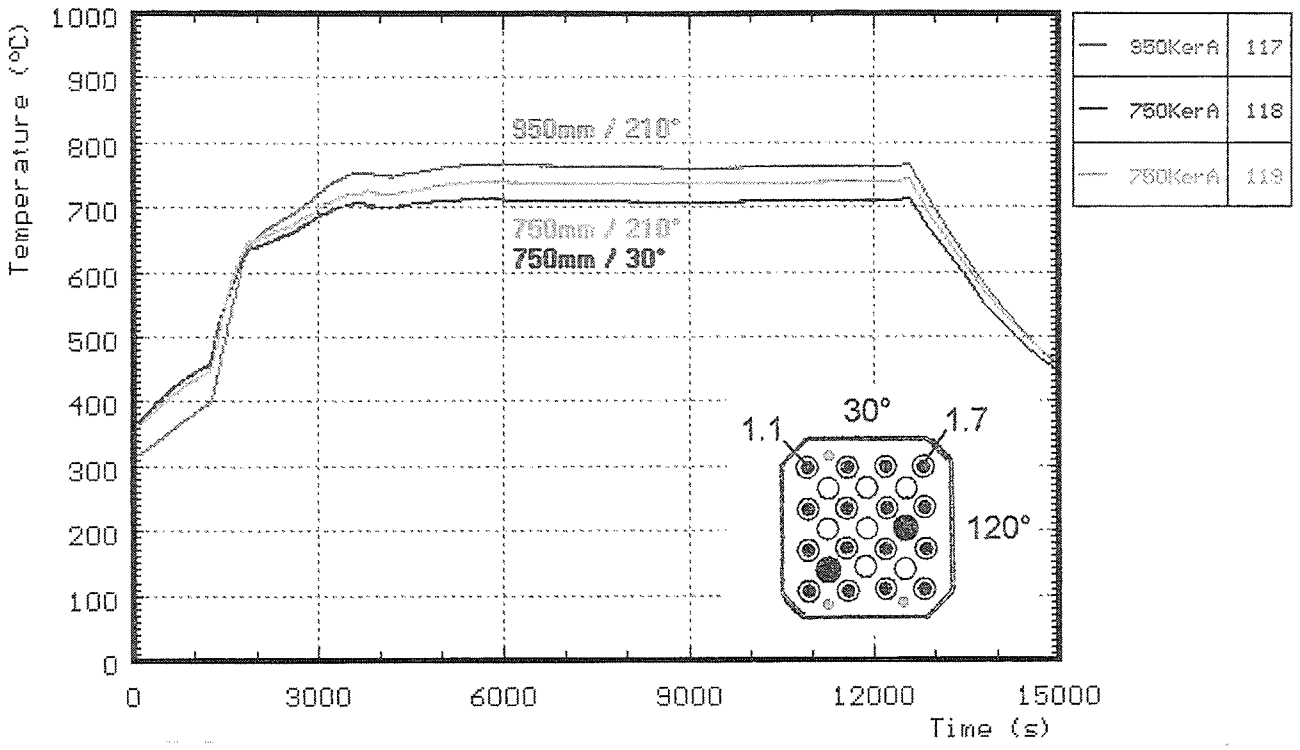

Fig. C9: Temperatures between bundle and shroud measured with ceramic protected TCs during pre-oxidation (CORA-29 P)

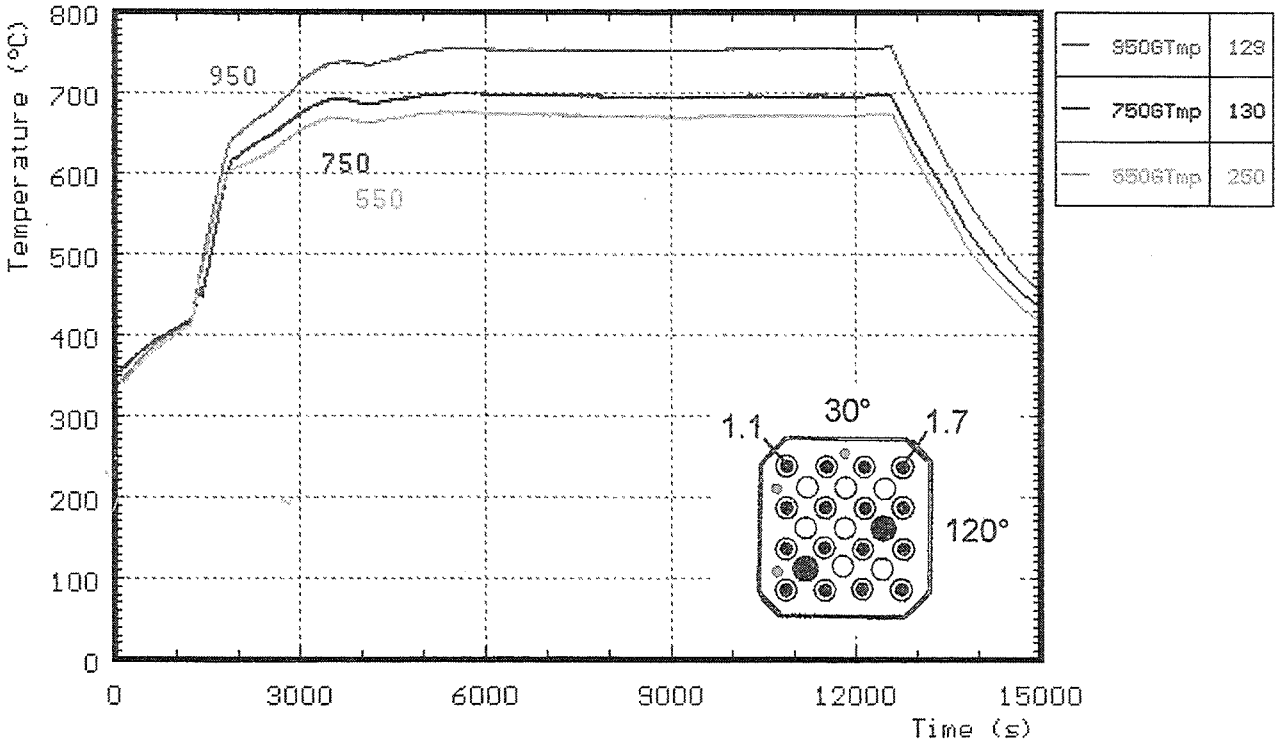

Fig. C10: Temperatures between bundle and shroud during pre-oxidation (CORA-29 P)

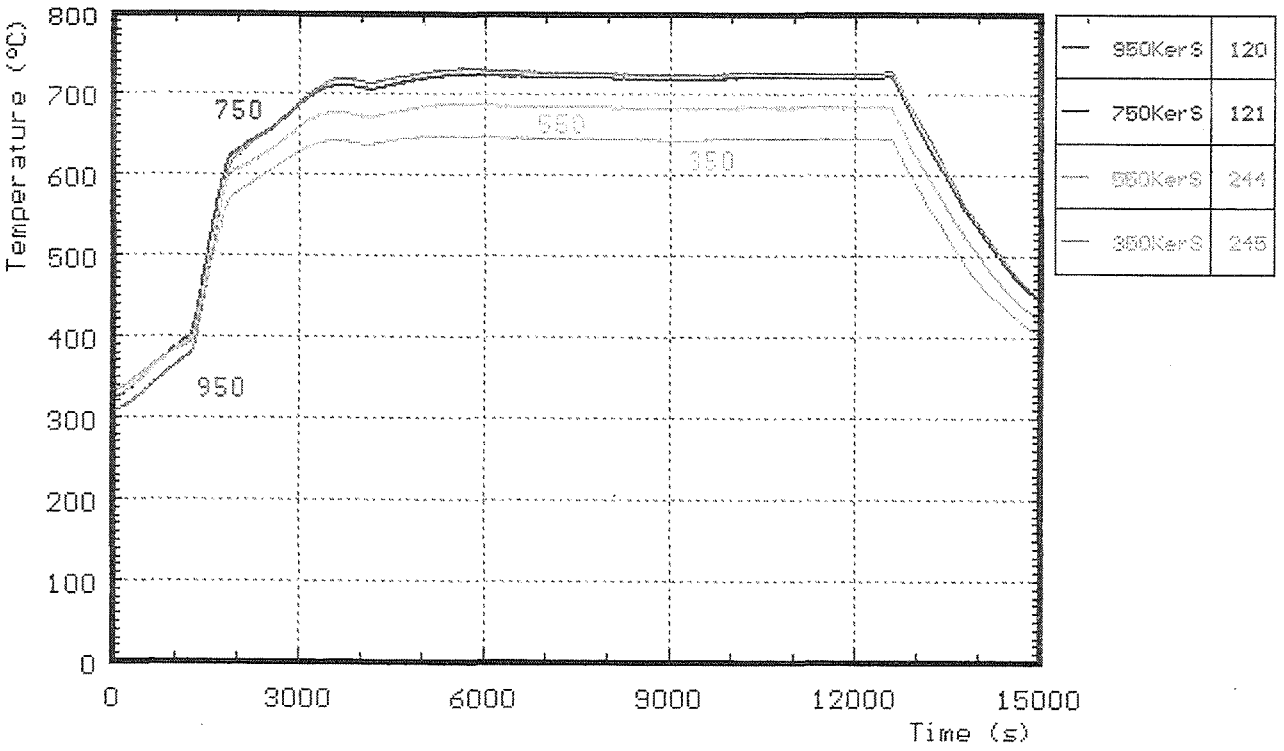

Fig. C11: Temperatures of inner side of shroud measured with ceramic protected TCs during pre-oxidation (CORA-29 P)

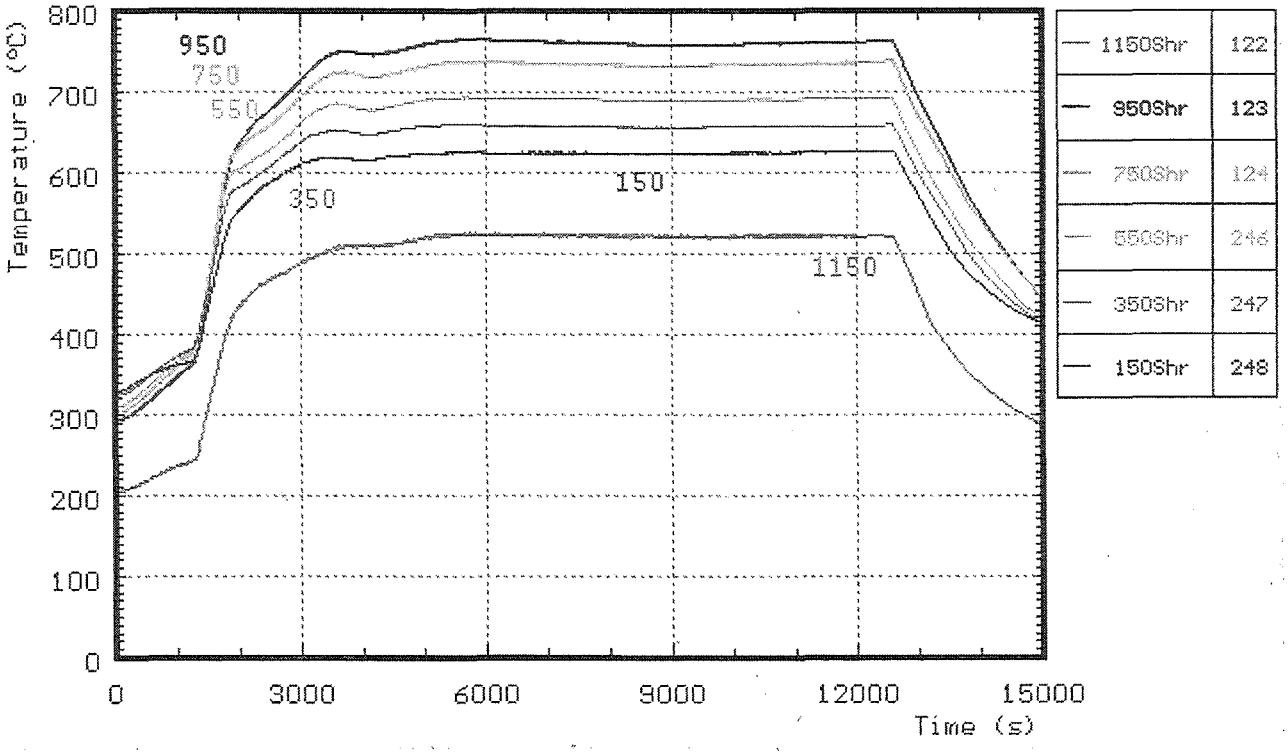

Fig. C12: Temperatures of outer side of shroud during pre-oxidation (CORA-29 P)

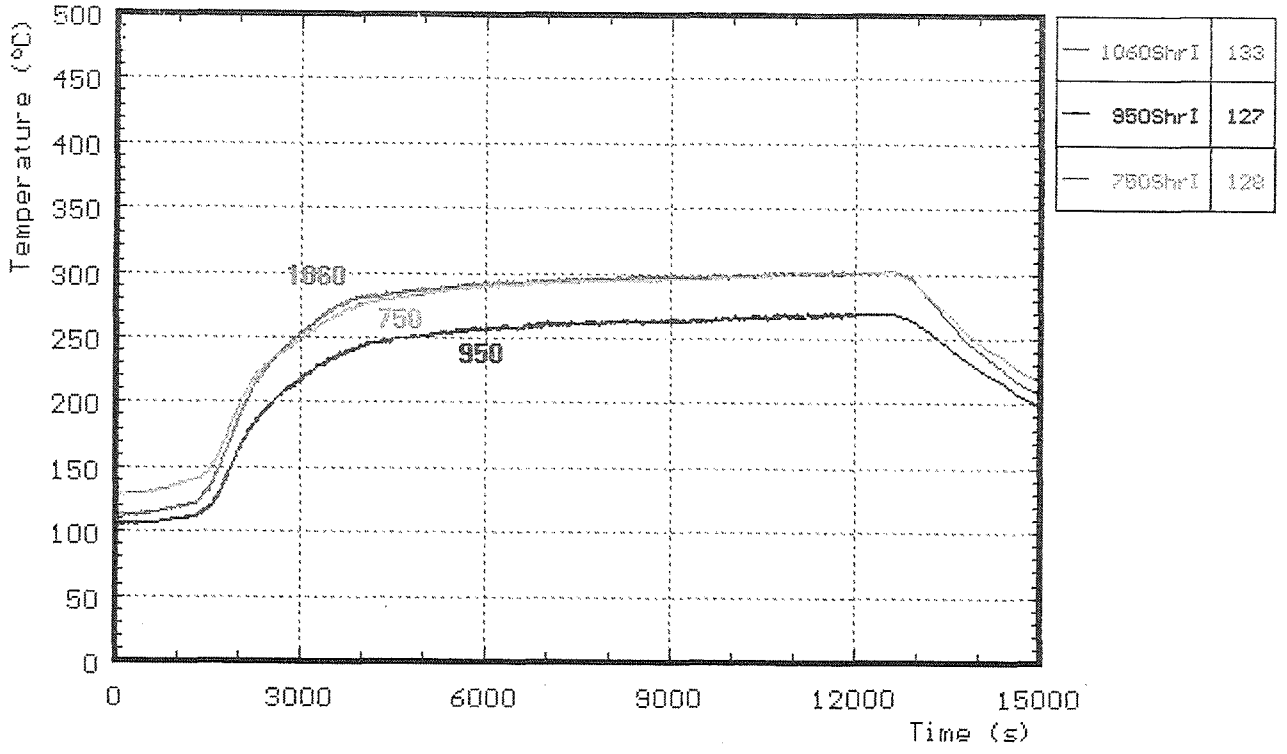

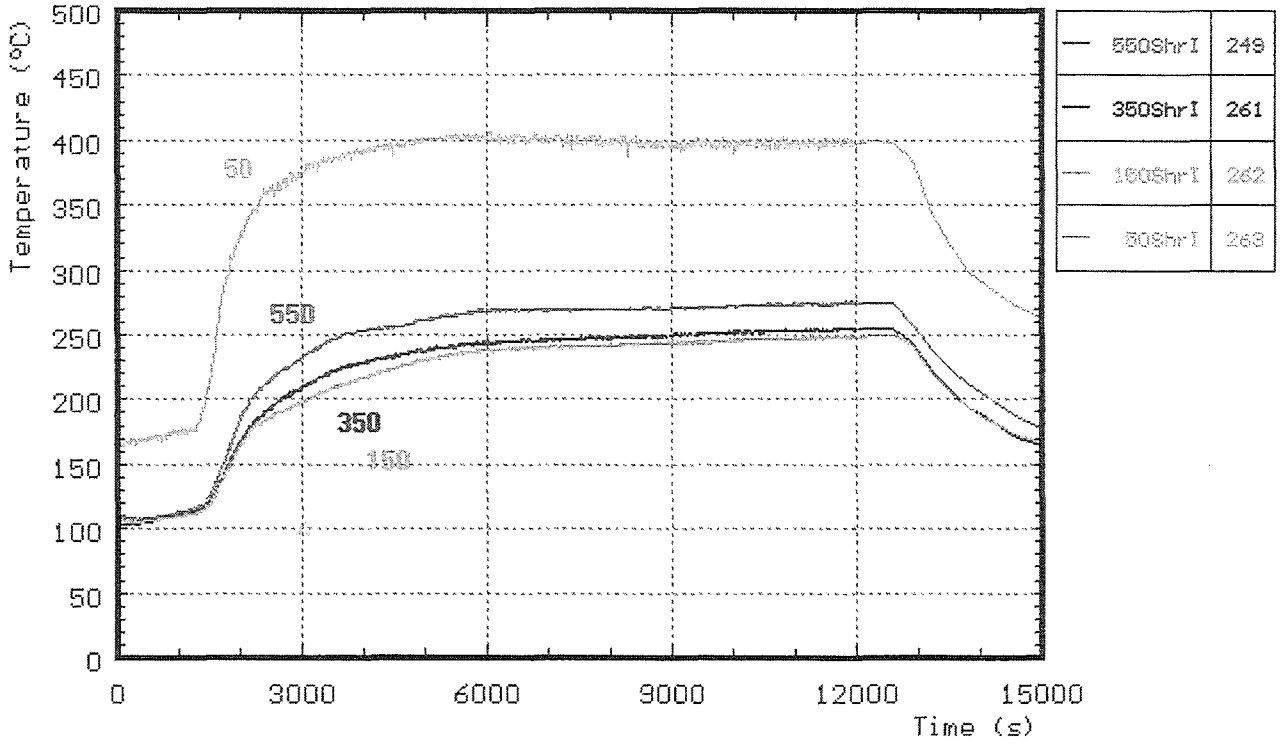

Fig. C13: Temperatures of the shroud insulation during pre-oxidation (CORA-29 P)

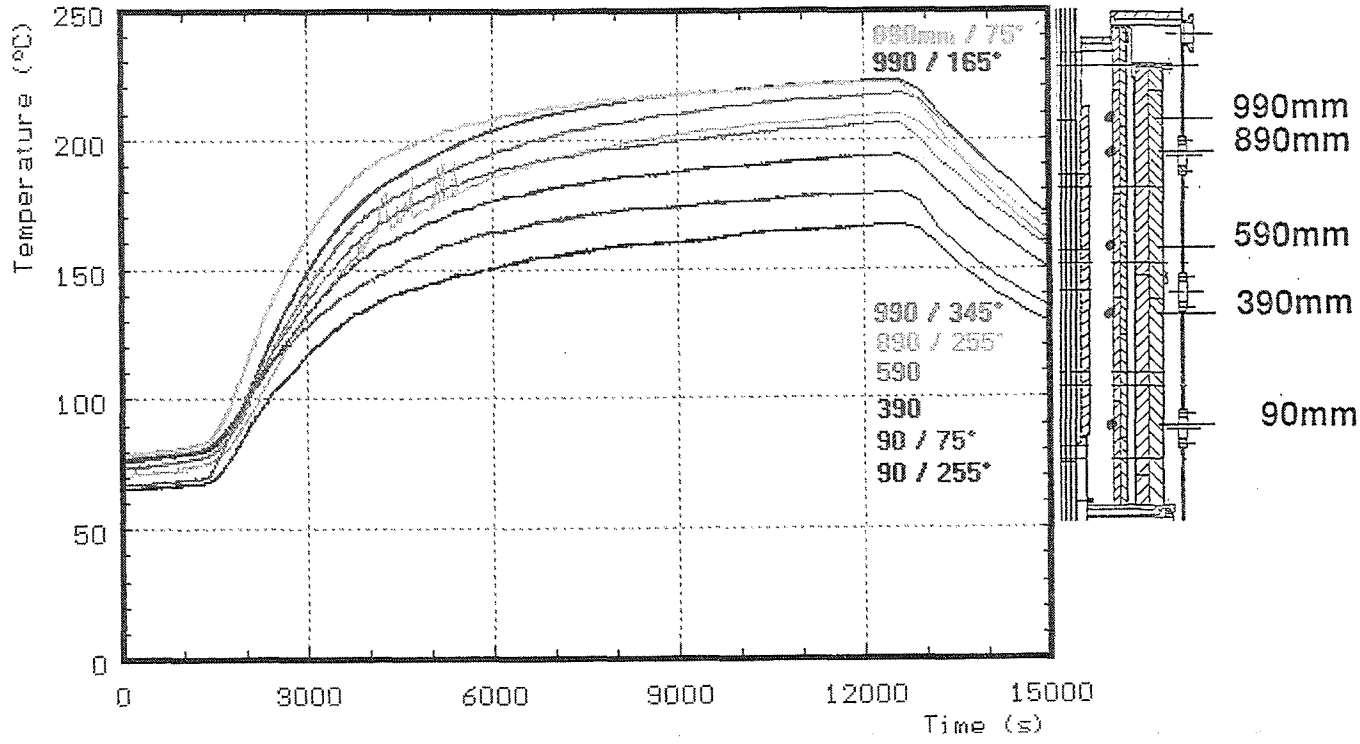

Fig. C14: Temperatures of HTS, inner surface at 153 mm radius during pre-oxidation (CORA-29 P)

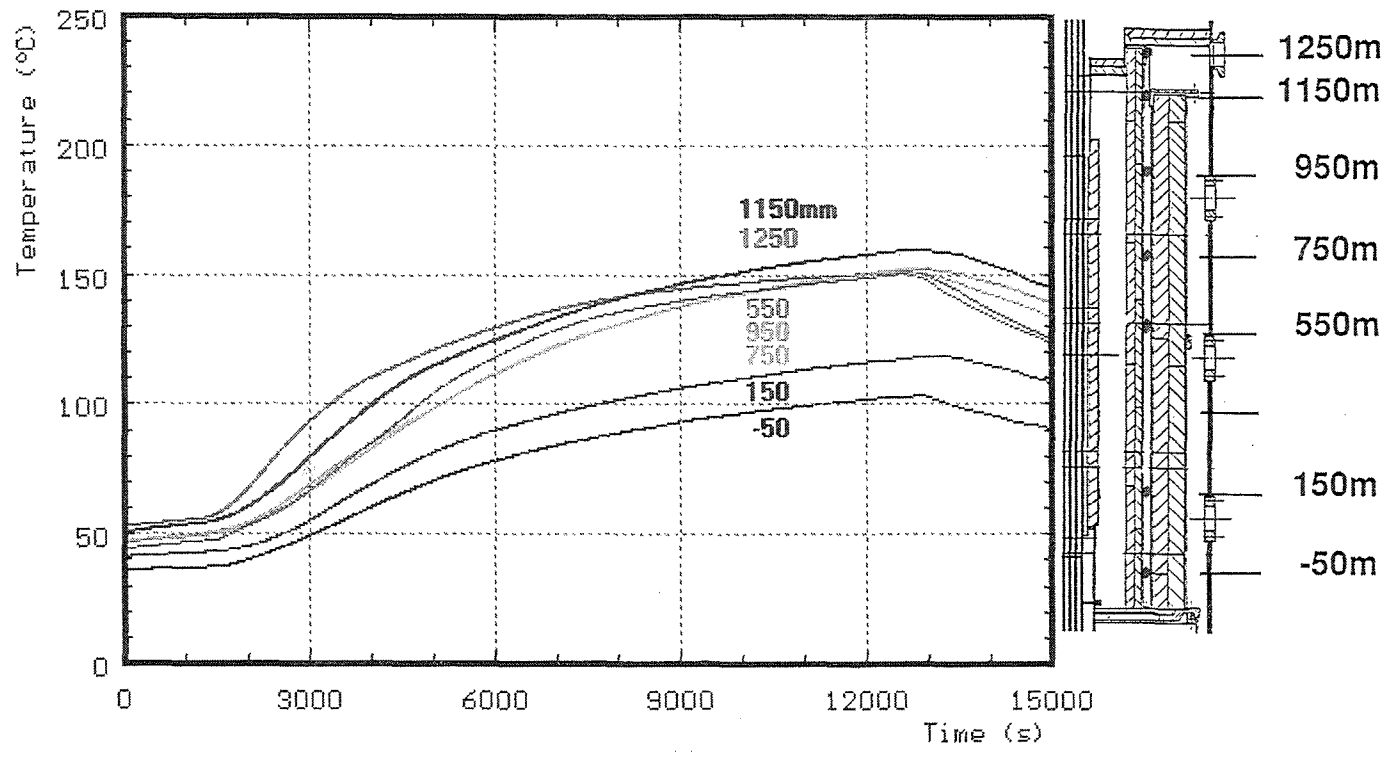

Fig. C15: Temperatures of HTS at 192 mm radius, 345° during pre-oxidation (CORA-29 P)

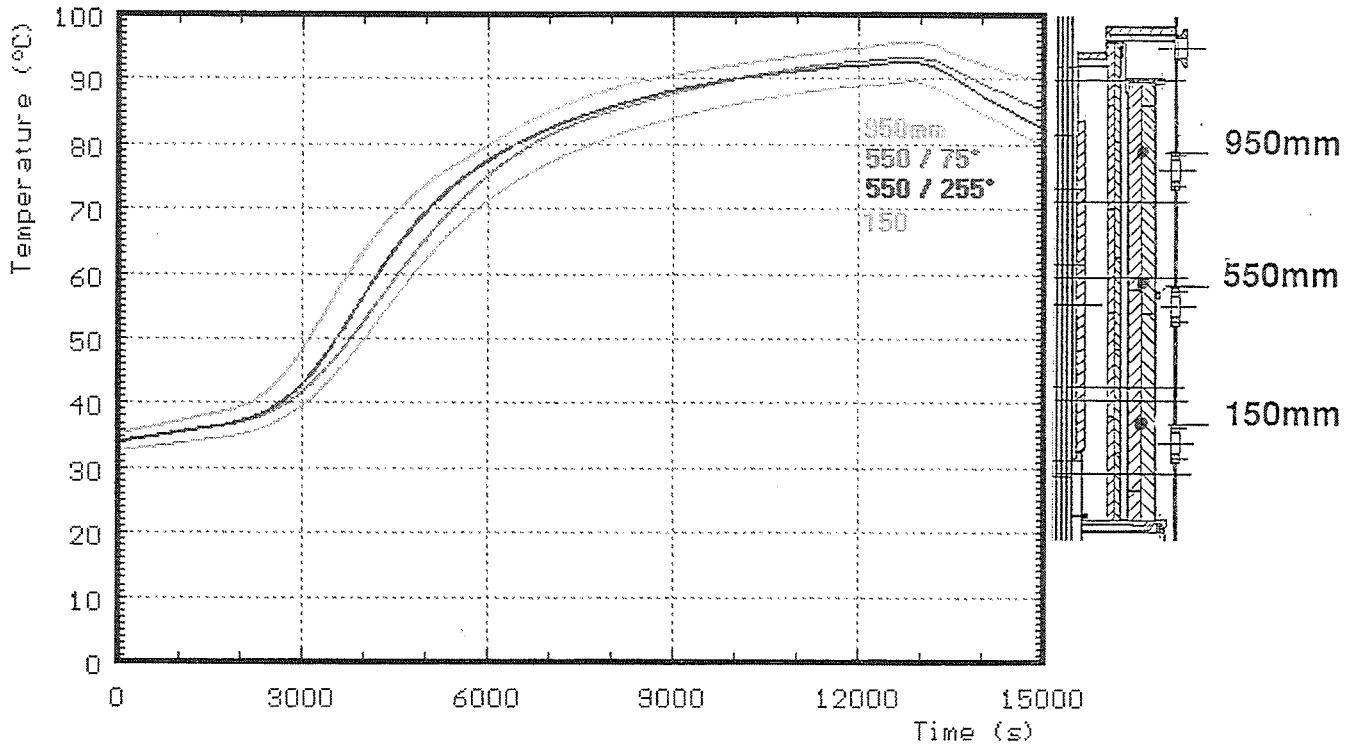

Fig. C16: Temperatures of HTS at 255 mm radius during pre-oxidation (CORA-29 P)

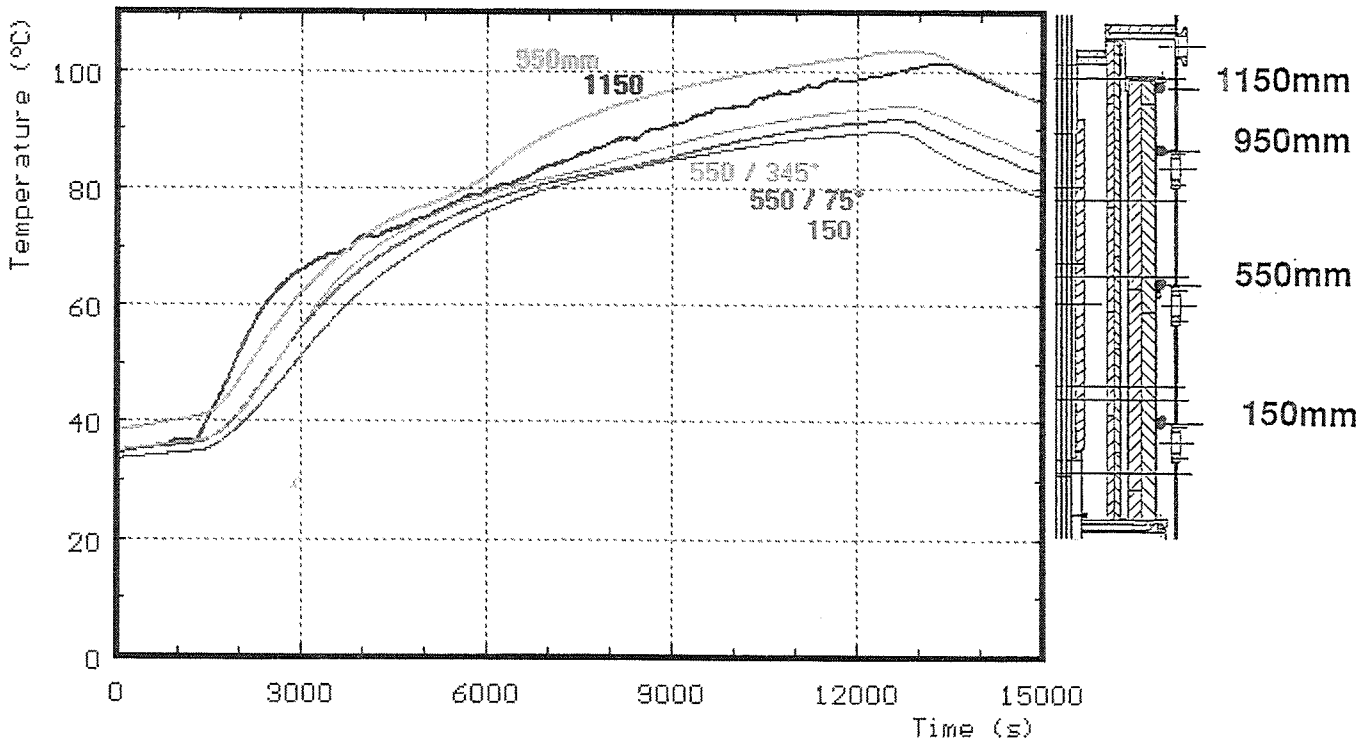

Fig. C17: Temperatures of HTS at 293 mm radius during pre-oxidation (CORA-29 P)

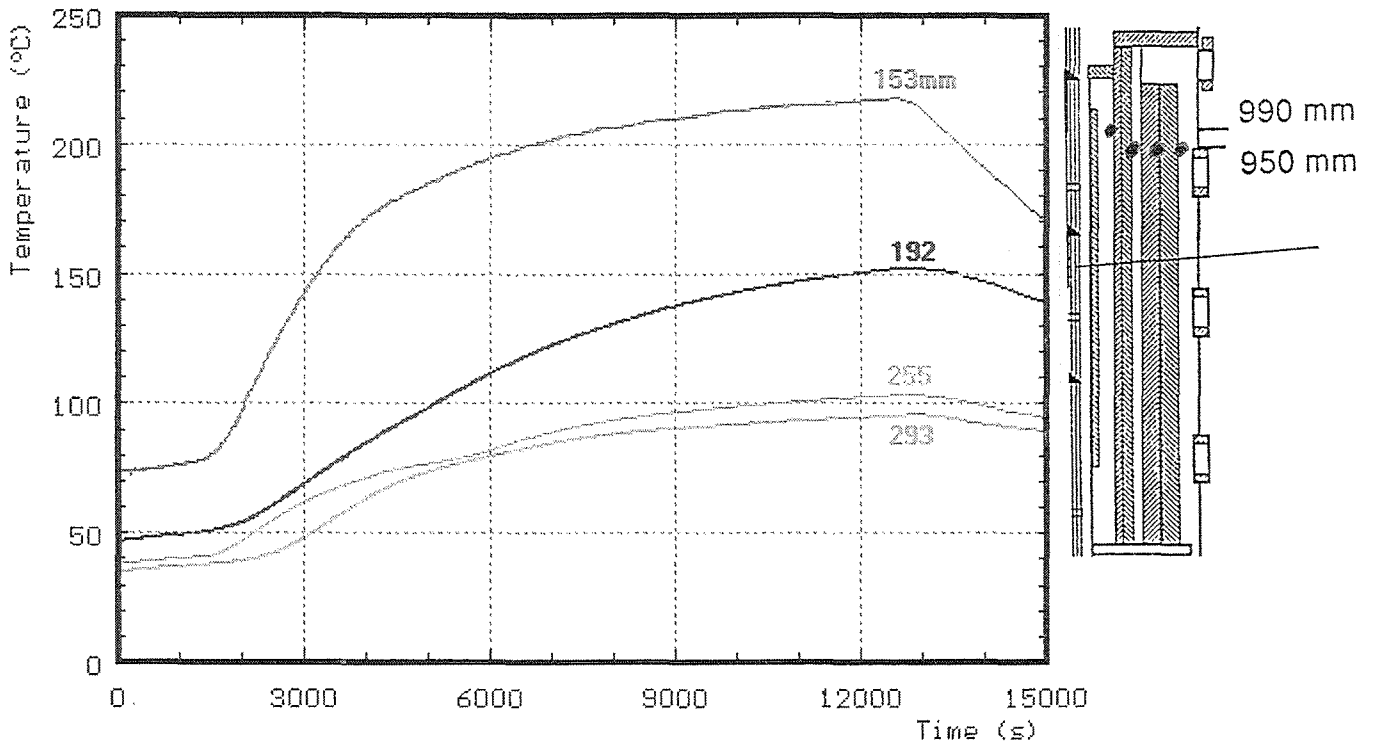

Fig. C18: Temperatures of HTS, radial dependence at about 950 mm elevation during pre-oxidation (CORA-29 P)

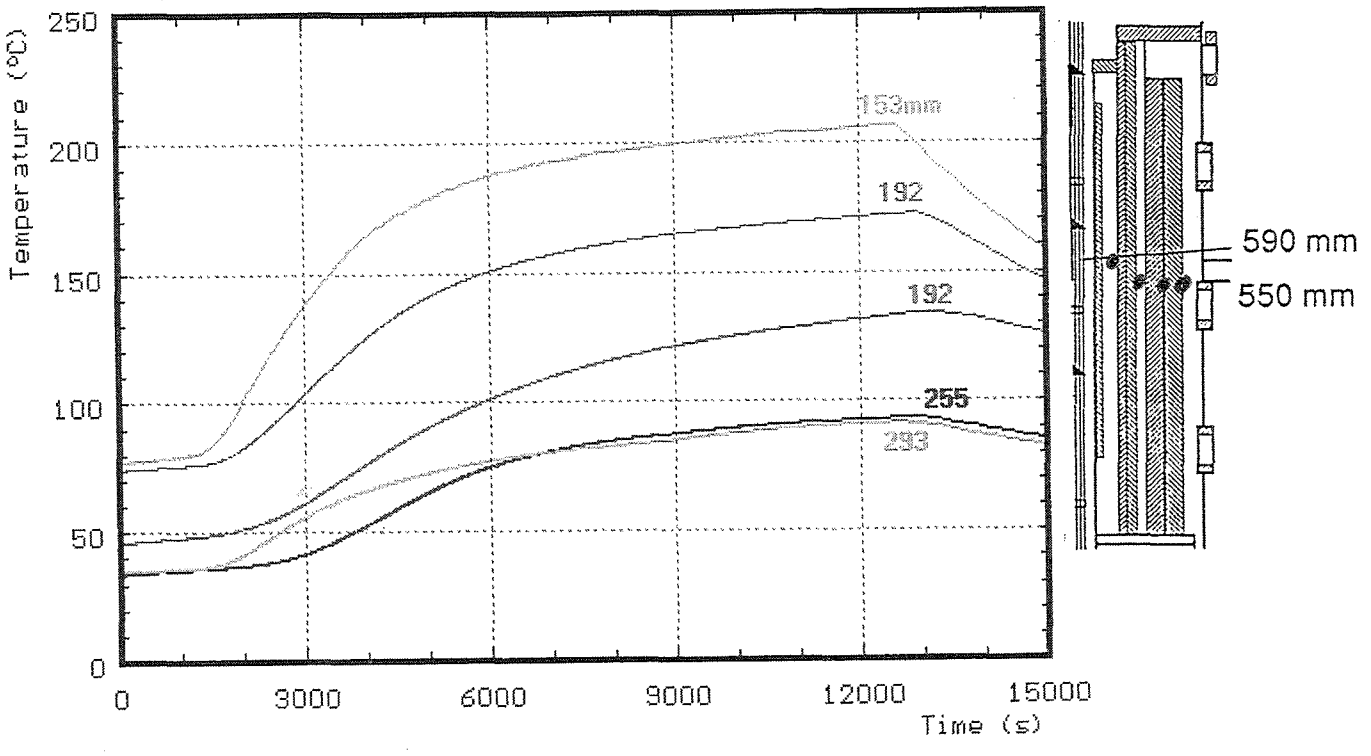

Fig. C19: Temperatures of HTS, radial dependence at about 550 mm elevation during pre-oxidation (CORA-29 P)